

AD AD A070623



NATIONAL BUREAU OF STANDARDS

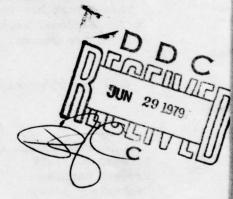


MDA070623

COMPRESSOR RESEARCH FACILITY AERODYNAMIC ANALYSIS

G. DAVID HUFFMAN

INDIANAPOLIS CENTER FOR ADVANCED RESEARCH, INC. INDIANAPOLIS, INDIANA 46202



DOC FILE COPY

APRIL 1979

TECHNICAL REPORT AFAPL-TR-79-2021
FINAL REPORT FOR PERIOD OCTOBER 1974 to JULY 1978

Approved for public release; distribution unlimited.

AIR FORCE AERO PROPULSION LABORATORY
AIR FORCE WRIGHT AERONAUTICAL LABORATORIES
AIR FORCE SYSTEMS COMMAND
WRIGHT-PATTERSON AIR FORCE BASE, OHIO 45433

NOTICE

When Government drawings, specifications, or other data are used for any purpose other than in connection with a definitely related Government procurement operation, the United States Government thereby incurs no responsibility nor any obligation whatsoever; and the fact that the government may have formulated, furnished, or in any way supplied the said drawings, specifications, or other data, is not to be regarded by implication or otherwise as in any manner licensing the holder or any other person or corporation, or conveying any rights or permission to manufacture, use, or sell any patented invention that may in any way be related thereto.

This report has been reviewed by the Information Office (OI) and is releasable to the National Technical Information Service (NTIS). At NTIS, it will be available to the general public, including foreign nations.

This technical report has been reviewed and is approved for publication.

RICHARD B. RIVIR

Project Engineer Technology Branch Welke A Mitchell

WALKER H. MITCHELL Chief, Technology Branch Turbine Engine Division

FOR THE COMMANDER

ERNEST C. SIMPSON

Director, Turbine Engine Division

AF Aero Propulsion Laboratory

"If your address has changed, if you wish to be removed from our mailing list, or if the addressee is no longer employed by your organization please notify AFAPL/TBX __,W-PAFB, OH 45433 to help us maintain a current mailing list".

Copies of this report should not be returned unless return is required by security considerations, contractual obligations, or notice on a specific document.

AIR FORCE/56780/7 June 1979 - 81

(19) REPORT DOCUMENTATION PAGE	READ INSTRUCTIONS BEFORE COMPLETING FOR
V .	N NO. 3. RECIPIENT'S CATALOG NUMBER
AFAPL TR-79-2021	(9)
	5. TYPE OF REPORT & PERIOD COVI
4. TITLE (and Subtitle)	
COMPRESSOR RESEARCH FACILITY	Technical Final Technical
AERODYNAMICS ANALYSIS	Oct 1974 to Jule 1978
	4 FDL-78-005
7. AUTHOR(e)	8. CONTRACT OR GRANT NUMBER(*)
2 2 11 11 15	/F33615-75-C-2008/
O G. David Hurrman	
	(15)
9. PERFORMING ORGANIZATION NAME AND ADDRESS	10. PROGRAM ELEMENT, PROJECT, T AREA & WORK UNIT NUMBERS
Indianapolis Center for Advanced Research, Inc.	AREA G WORK ON I NOME ON
1219 W. Michigan Street \ t/uid Algas also	(16) 3066b420 4 P
Indianapolis IN 46202	1 (16) 3000 120
11. CONTROLLING OFFICE NAME AND ADDRESS	12. REPORT DATE
Air Force Aero Propulsion Laboratory (TBX)	(//) April 1979
Wright-Patterson Air Force Base OH 45433	NUMBER OF PAGES
14. MONITORING AGENCY NAME & ADDRESS(II different from Controlling Off	348 (ice) 15. SECURITY CLASS. (of this report)
MONITORING AGENCY NAME & AUDRESS/II different from Controlling Off	UNCLASSIFIED
	ONCLASSIFIED
13/90	15a. DECLASSIFICATION DOWNGRAD
to mineral and the second of t	
Approved for public release; distribution unl	imited.
Approved for public release; distribution unl	
- summer days are a great and of the contract of the	ent from Report)
Approved for public release; distribution unl	
Approved for public release; distribution unl	ent from Report)
Approved for public release; distribution unl 17. DISTRIBUTION STATEMENT (of the abstract entered in Block 20, if different supplementary notes	for (from Report)
Approved for public release; distribution unl 17. DISTRIBUTION STATEMENT (of the abstract entered in Block 20, if different to the abstract entered in Block 20, if different entered in Bl	ent from Report) 6 2 2 0 3 F
Approved for public release; distribution unl 17. DISTRIBUTION STATEMENT (of the abstract entered in Block 20, if different 18. SUPPLEMENTARY NOTES 19. KEY WORDS (Continue on reverse side if necessary and identify by block not compressor testing, turbulence reduction, ven compressor transient performance.	mnt (rom Report) 6 2 2 0 3 F mmber) turi discharge coefficients,
Approved for public release; distribution unl 17. DISTRIBUTION STATEMENT (of the abstract entered in Block 20, if different 18. SUPPLEMENTARY NOTES 19. KEY WORDS (Continue on reverse side if necessary and identify by block not Compressor testing, turbulence reduction, ven	mnt (rom Report) 6 2 2 0 3 F mmber) turi discharge coefficients,
Approved for public release; distribution unl 17. DISTRIBUTION STATEMENT (of the abstract entered in Block 20, if different 18. SUPPLEMENTARY NOTES 19. KEY WORDS (Continue on reverse side if necessary and identify by block not compressor testing, turbulence reduction, ven compressor transient performance. 20. ABSTRACT (Continue on reverse side if necessary and identify by block not compressor.)	mnt (rom Report) 6 2 2 0 3 F mmber) turi discharge coefficients,

SECURITY CLASSIFICATION OF THIS PAGE (When Date Entered)

410 273

SECURITY CLASSIFICATION OF THIS PAGE(When Date Entered)

This report documents a series of aerodynamic studies carried out jointly by AFAPL and ICFAR personnel in support of the design and development of the AF Aero Propulsion Laboratory Compressor Research Facility (CRF). The CRF is a non-return compressor test facility with air extracted from the atmosphere, compressed and then discharged to the atmosphere. In order to reduce compressor power requirements and simulate flight conditions at elevated altitudes, the compressor is mounted in a large tank or test chamber. The tank pressure is regulated with control valves with the compressor itself supplying the exhauster capability. The mass flow rate is measured downstream of the compressor using a series of venturis. The CRF utilizes automated data handling procedures and is capable of simulating some compressor transients. The cost of the facility coupled with its status as a national laboratory, dictated that every effort be made to ensure the viability of data produced. With this objective in mind, aerodynamic studies were initiated with a review of the measurement and flow quality capabilities of existing compressor test facilities. This information, in conjunction with a review of the sensitivity of compressors to inlet distortion, was then used to formulate a series of flow quality requirements for the CRF. Having determined flow quality requirements, flow conditioning elements for the facility were designed in conjunction with the AFAPL and the Cadre Corporation. A series of configurations were evaluated experimentally at AFAPL by AFAPL personnel in a 1/10 scale model of the facility. The final configuration - meeting all the flow quality requirements - employs an auxiliary test chamber, honeycomb flow straightener and a series of turbulence damping screens. One of the most critical measurements in compressor testing is the mass flow rate through the compressor. Transient compressor testing dictates that the steady-state mass flow rate be measured downstream using subsonic venturis. In an effort to maximize flow rate measurement accuracy without compromising facility usefulness, a study of the compressor research facility subsonic venturis was carried out. The effects of Mach number, Reynolds number, turbulence level and facility data taking procedures on venturi measurement procedures were recommended and have been incorporated in the flow measurement system. One of the attributes of the CRF, heretofore unavailable, is the ability to evaluate compressor transient performance. Tests of this type dictate new methods of mass flow rate measurements, data acquisition, and analysis as well as stringent requirements on the more conventional temperature, pressure and speed measurements. A pilot program utilizing an existing J-85 engine test facility at AFAPL was initiated to explore and develop the measurement technology required in transient compressor testing.

PREFACE

This final report documents investigations performed over a four-year period by the Indianapolis Center for Advanced Research (ICFAR), in conjunction with the AF Aero Propulsion Laboratory (AFAPL). Without the direct technical assistance of Dr. F.R. Ostdiek, Dr. R.B. Rivir and Mr. D. Rabe of AFAPL, many of these tasks reported herein could not have been completed. I would also like to acknowledge the assistance of my colleague at ICFAR, Dr. G.W. Haering.

The Purdue University School of Science at Indianapolis recently established in conjunction with ICFAR, Master of Science Programs in Applied Mathematics and Applied Computer Science. During the four year tenure of the research investigations, Mr. Edward Turner, Mr. Steven Mosher, Mr. David Kovalcin and Ms. Susan Chong assisted in various phases of the AFAPL studies as a part of their graduate degree programs. In addition, Mr. Dennis Adams, Mr. Michael Chainyk, and Mr. Jeffrey Clendenon carried out work elements with their undergraduate studies.

The typing of the final report and the preparation of the illustrations was carried out by Ms. Barbara Bowen, Ms. Susan Bourke, Ms. Mary Ann Graf, and Ms. Carol Gemignani. Their assistance is gratefully acknowledged.

TIS O		N.
nannou	inced	
ustif:	ication	
y		
	bution/	
	ability	
AVALL	Availand	
ist	specia	1

TABLE OF CONTENTS

SECTION			PAGE
I	FLO	W QUALITY REQUIREMENTS	1
	A.		1
	В.		6
		1. Introduction	6
		Survey of Flow Distortion Parameters	6
		3. Recommended Flow Parameters	16
		4. Measurement Accuracy	18
	C.	Survey of Compressor Facilities	19
		 Characteristics of Existing Compressor Test Facilities 	
		Flow Quality in Existing Compressor Test Facilities	19
	D.	Flow Quality Standards for the Compressor Research Facility	25
		 Recommended Flow Quality Standards 	25
		Impact of the Flow Quality Standards on the Compressor Research Facility	26
		Test Chamber	
11		PRESSOR RESEARCH FACILITY (CRF) 1/10 LE MODEL FLOW TESTS	28
	A.	Introduction	28
	B.	Scaling and Flow Model Tests	28
	c.	Reynolds Number Similarity for the Flow Conditioning Elements	34
	D.	The Flow Model Configuration	36
	E.	Measurements within the Compressor	42
		Research Facility 1/10 Scale Model	
	F.	Instrumentation Systems for the Compressor Research Facility 1/10 Scale Model	53
	G.	Data Reduction	56
		1. Introduction	56
		2. Computer Systems	56
		3. Calibration of Pressure Transducers	56
		4. Calibration of the Hot Wire Anemometer	58
		 Calculation of Total Pressure and Velocity 	64
		6. Mass Flow Rates	64
		7. Flow Quality Parameters	66
		8. Data Reduction Computer Program	67
	H.	Testing of the Baseline Configuration	67
		1. Introduction	67
		2. Test Program	67
		3. Data Accuracy	70
		4. Flow Conditioning Elements	72
		5. Maximum Flow Rate Bellmouth with	74
		Jet Deflectors, Flow Straightener,	
		Derforated Diate and Garage Tretalled	

TABLE OF CONTENTS (Cont'd)

SECTION			PAGE
	н.	Testing of the Baseline Configuration (Cont'd)	
		6. J-79 Bellmouth with Jet Deflectors, Flow	79
		Straightener, Perforated Plate and Screens Installed	
		 The Effect of Flow Conditioning Elements on Flow Quality 	83
		8. Summary of the Experimental Results for the Baseline Configuration	85
	I.	Modification of the Compressor Research Facility	86
		1/10 Scale Model to Accommodate a Compressor Simulator	
		1. Introduction	86
		2. Design of the Sonic Plate	86
		3. The Modified Bellmouth Units	87
		4. Test Program	94
		5. Experimental Results	94
	J.	Comparison of a Flow Centering Device and	100
		Auxiliary Test Chamber for Controlling Flow	
		Development	
		1. Introduction	100
		2. Test Program	100
		3. Experimental Results	110
	K.	Optimum Flow Conditioning System	150
III	-	CHARGE COEFFICIENTS FOR THE UNIVERSAL VENTURIS	155
	EMP	LOYED IN THE CRF FLOW MEASUREMENTS SYSTEM	
	A.		155
	В.	Objectives of the Venturi Analysis	155
	c.	Flow System Geometry	159
	D.	1 - 프라이크 및 프로젝터 특히 보고 프로젝트 및 프로젝트 (트라크로) (C. 1988) (C. 1988) (C. 1987) (C. 1988) (C. 1988) (C. 1988) (C. 1988)	161
	E.	Inviscid-Boundary Layer Matching	162
	F.	Inviscid Flow Model	166
	G.	Boundary Layer Models	168
	н.	The Discharge Coefficients	170 171
	I.		171
	J.	Computed Universal Venturi Discharge Coefficients	173
		1. Axial Variation of Boundary Layer Parameters	1/3
		2. Discharge Coefficients for the 12.5 in.	178
		Venturi	180
		Discharge Coefficients for the 30.0 in. Venturi	
	K.	Experimental Calibration of the CRF Venturis	185
	L.		191
	M.	Summary	191

TABLE OF CONTENTS (Cont'd)

SECTION			PAGE
IV	-	RIVATION OF AN IMPROVED MATHEMATICAL MODEL FOR	211
	A.	Introduction	211
	В.	Variable Grid Finite-Difference Module	212
	c.	Equations of Motion	213
	D.	Finite-Difference Form of the Equations of Motion	215
	E.	Solution Procedure	217
	F.	Normal Velocity Calculation	219
	G.	Initial Velocity and Shear Stress Profile	219
	H.	Boundary Layer Integral Properties	222
	I.	Transition Prediction	225
	J.	Empirical Functions	231
	K.	Program Structure	237
	L.	Results	237
V		PERIMENTAL EVALUATION OF COMPRESSOR TRANSIENT	240
	A.		240
	В.		243
		1. The Equations of Motion	243
		2. Summary of Governing Equations	247
		3. Application of Governing Equations to a Turbomachine	248
		4. Structure of the J-85 Digital Simulation Computer Program	251
		5. Compressor Mapping Using a J-85 Turbine Engine	255
		6. Compressor Transient Performance as	266
	_	Determined with a Mathematical Model	266
	c.	Design and Fabrication of the Pressure and Temperature Instrumentation	
		1. Introduction	266
		2. Frequency Response for the Temperature and Pressure Measuring Systems	295
		3. Probe Design	302
		4. Fabricated Probes	308
	D.	Aerodynamic Analysis of the Bellmouth Flow	308
		Measuring System	318
	E.	Data Processing and Analysis Program	318
		1. Data Analysis Variables	318
		2. Fluid Properties	322
		3. Mach Number and Velocity Calculation	326
		4. Five-Ported Cone Probe	327
		5. Recovery Factors for Thermocouple Probes	329
		6. Mass-Averaging	333
		7. Effective Wall Velocity	334
		8. Program Structure	336
	F.	Summary	342
	REF	PERENCES	343

LIST OF ILLUSTRATIONS

FIGURE		PAGE
1	Diagram of the Auxiliary Air System	3
2	Compressor Research Facility Air Flow Conceptual Formulation	4
3	Compressor Research Facility Schematic Diagram	5
4	Inlet Measuring Stations	8
5	Comparison of Flow Quality Parameters	12
6	Comparison of Flow Quality and Flow Distortion Parameters	15
7	Geometric Scale Factor as a Function of Temperature and Pressure	32
8	Scaled Mass Flow Rate as a Function of Temperature and Pressure	33
9	Compressor Research Facility 1/10 Scale Model	37
10	Inlet Flow Control Valves	38
11	Test Chamber Jet Deflectors	40
12	Facility Control and Monitoring System	41
13	Compressor Bellmouth Installed in the Test Chamber	43
14	J-85 and Maximum Flow Rate Bellmouths	44
15	Forward Portion of Test Chamber Showing a Honeycomb Straightener	45
16	Test Chamber Axial Measurement Stations	47
17	Inlet Valve Locations Relative to the Plane of the Measurements	48
18	Maximum Flow Rate Bellmouth Installed in the Test Chamber	49
19	J-79 Model Bellmouth with the Total Pressure Rakes	50
20	J-79 Model Bellmouth Total Head Tube Radial Locations	51

FIGURE	I	PAGE
21	Maximum Flow Rate Bellmouth with Total Pressure Rakes	52
22	Maximum Flow Rate Bellmouth Total Head Tube Radial Locations	54
23	Pressure Instrumentation Systems	55
24	Hot Wire Anemometry System	57
25	Hot Wire Probe Calibration Data Nu $\frac{\text{tm}}{\text{tf}}$ -0.17 versus Re	60
26	Hot Wire Probe Calibration Nu $\frac{\text{tm}}{\text{tf}}$ -0.17 versus Re ^{0.45}	61
27	Calibration of Hot Wire Probe 8709	62
28	Test Chamber Schematic	69
29	Mass Flow Rate Comparison	71
30	Modified 1/10 Scale Model with the 6" Bellmouth	88
31	Modified 1/10 Scale Model with the 12" Bellmouth	89
32	Bellmouth Unit Disassembled	90
33	Perforated Plate (Compressor Simulator)	90
34	Rear Bulkhead, Perforated Plate and Bellmouth Transition Section	91
35	Rear Bulkhead Assembly with Traversing Mechanism Installed	91
36	Rear Bulkhead Assembly with the Compressor Bellmouth Installed	92
37	Rear Bulkhead Assembly Showing the Location of the Hot Wire Anemometer Probe Relative to the Perforated Plate	92
38	Perforated Plate Support System Seen from Downstream	93

FIGURE		PAGE
39	Six-Inch Bellmouth Unit Assembled	93
40	Prediction of Turbulence Levels in 1/10 Scale Model	99
41	Schematic of Barrel Flow Conditioning Device	102
42	Barrel Assembly as Installed	103
43	Schematic of Flow Centering Device	104
44	Entrance Cone and Perforated Plate of Flow Centering Device	106
45	Flow Centering Device Showing Diffuser of Nested Cones	106
46	Lateral View of Flow Centering Device, Modification 2	106
47	Mean Velocity & Turbulence Profile in Test Chamber & Bellmouth; Test No. 3045	115
48	Mean Velocity & Turbulence Profile in Test Chamber & Bellmouth; Test No. 3046	119
49	Mean Velocity & Turbulence Profile in Test Chamber & Bellmouth; Test No. 3047	123
50	Mean Velocity & Turbulence Profile in Test Chamber & Bellmouth; Test No. 3048	127
51	Mean Velocity & Turbulence Profile in Test Chamber and Bellmouth; Test No. 3065	131
52	Mean Velocity & Turbulence Profile in Test Chamber and Bellmouth; Test No. 3066	135
53	Mean Velocity & Turbulence Profile in Test Chamber and Bellmouth; Test No. 3067	139
54	Mean Velocity & Turbulence Profile in Test Chamber and Bellmouth; Test No. 3068	143
55	Recommended Flow Conditioning System	151
56	Flow Measurement System Operating Envelope	157
57	Flow Measurement System Overall Geometry	159

FIGURE		PAGE
58	30" and 12.5" Venturis	160
59	Flow Field Schematic	165
60	Convergence Path for the Inviscid Boundary Layer Calculations	167
61	Convergence Behavior	172
62	Venturi Mach Numbers	174
63	Venturi Skin Friction Coefficients	175
64	Venturi Displacement Thickness	176
65	Venturi Boundary Layer Thickness	177
66	Discharge Coefficients for the 12.5" Venturi	179
67	Discharge Coefficients for the 30" Venturi. l=60", Tu=0.5%	181
68	Discharge Coefficient for the 30" Venturi. l=60", Tu=2.5%	182
69	Discharge Coefficient for the 30" Venturi. $\ell=792$ ", Tu=0.5%	183
70	Discharge Coefficient for the 30" Venturi. l=792", Tu=2.5%	184
71	Calculated Discharge Coefficients for the 30" Venturi. l=60", Tu=0.5%	186
72	Calculated Discharge Coefficients for the 30" Venturi. \$\ell=60\colon, Tu=0.5\cdot\cdot\cdot\cdot\cdot\cdot\cdot\cdot	187
	$P_{inlet} = 20 lb_f/in^2$ and $\Delta t = -40^{\circ}$	
73	Calculated Discharge Coefficients for the 30" Venturi. &=60", Tu=2.5%,	188
	$P_{inlet} = 20 lb_f/in^2 and \Delta t = 40^{\circ}$	
74	Calculated Discharge Coefficients for the 30" Venturi. l=60", Tu=2.5%,	189
	$p_{inlet} = 20 lb_f/in^2$ and $\Delta t = -40^{\circ}$	

FIGURE		PAGE
75	Measured and Correlated Discharge Coefficient. Venturi 48901-1 Tap Set 1 - 2	192
76	Measured and Correlated Discharge Coefficient. Venturi 48901-1 Tap Set 3 - 4	193
77	Measured and Correlated Discharge Coefficient. Venturi 48901-1 Tap Set 5 - 6	194
78	Measured and Correlated Discharge Coefficient. Venturi 48901-1 Tap Set 7 - 8	195
79	Measured and Correlated Discharge Coefficient. Venturi 48901-2 Tap Set 1 - 2	196
80	Measured and Correlated Discharge Coefficient. Venturi 48901-2 Tap Set 3 - 4	197
81	Measured and Correlated Discharge Coefficient. Venturi 48901-2 Tap Set 5 - 6	198
82	Measured and Correlated Discharge Coefficient. Venturi 48901-2 Tap Set 7 - 8	199
83	Measured and Correlated Discharge Coefficient. Venturi 48901-3 Tap Set 1 - 2	200
84	Measured and Correlated Discharge Coefficient. Venturi 48901-3 Tap Set 3 - 4	201
85	Measured and Correlated Discharge Coefficient. Venturi 48901-3 Tap Set 5 - 6	202
86	Measured and Correlated Discharge Coefficient Venturi 48901-3 Tap Set 7 - 8	203
87	Measured and Correlated Discharge Coefficient. Venturi 48901-4 Tap Set 1 - 2	204
88	Measured and Correlated Discharge Coefficient. Venturi 48901-4 Tap Set 3 - 4	205
89	Measured and Correlated Discharge Coefficient. Venturi 48901-4 Tap Set 5 - 6	206
90	Measured and Correlated Discharge Coefficient. Venturi 48901-4 Tap Set 7 - 8	207
91	Experimentally Determined Discharge Coefficients	208

FIGURE		PAGE
92	Finite - Difference Module	213
93	Velocity Profile Generated with the "Starting" Routine	223
94	Shear Stress Profile Generated with the "Starting" Routine	224
95	Neutral Stability Point as a Function of Pressure Gradient	228
96	Position of Self-Excited Transition as a Function of Average Pressure Gradient	229
97	Effect of Free-Stream Turbulence on Transition Location	230
98	A^{+} as a Function of $< \partial \tau^{+}_{\tau \ell} \partial y + >$	233
99	The Dissipation Length Scale as a Function of Position	234
100	The Diffusion Function Versus Position	235
101	The Gradient of the Diffusion Function Versus Position	236
102	Flow Chart for the Boundary Layer Computer Program	238
103	Volume Element Showing the x-Component of Momentum and Energy Transport	244
104	J-85 Exhaust Nozzle Design Area Variation	257
105	J-85 Compressor Performance as Determined with the Digital Simulation	260
106	J-85 Compressor Performance	262
107	J-85 Compressor Operation at a Corrected Speed of 82.5%	265
108	J-85 Compressor Performance. 70% Speed	267
109	J-85 Compressor Performance. 72.5% Speed	269

FIGURE		PAGE
110	J-85 Compressor Performance. 75.0% Speed	271
111	J-85 Compressor Performance. 77.5% Speed	273
112	J-85 Compressor Performance. 80.0% Speed	275
113	J-85 Compressor Performance. 82.5% Speed	277
114	J-85 Compressor Performance. 85.0% Speed	279
115	J-85 Compressor Performance. 87.5% Speed	281
116	J-85 Compressor Performance. 90% Speed	283
117	J-85 Compressor Performance. 92.5% Speed	285
118	J-85 Compressor Performance. 95.0% Speed	287
119	J-85 Compressor Performance. 97.5% Speed	289
120	J-85 Compressor Performance. 100% Speed	291
121	J-85 Compressor Transient Performance	293
122	Resonant and Nonresonant Measuring Systems	296
123	Aspirated Probe 107	299
124	Shielded Thermocouple Probe	299
125	Recovery Factors for the Shielded Thermocouple Probe	301
126	Miniature Thermocouple Response Times	303
127	Overall Instrumentation Location	304
128	Pressure and Temperature Detection Assembly	306
129	Transducer Mounting Block	307
130	Redesigned Probes for Circumferential Positions C3 and C4	309
131	Probe Assembly for Position Cl	310
132	Probe Assembly for Position Cl Installed in Compressor Case	311

FIGURE		PAGE
133	Sensor Locations for Position Cl	312
134	Probe Assembly for Position C2	313
135	Probe Assembly for Position C3	314
136	Probe Assembly for Position C4	315
137	Bellmouth Assembly	316
138	Computed Discharge Coefficients for the Bellmouth System	319
139	Measured and Computed Discharge Coefficients	320
140	Five-Ported Cone Probe	328
141	Recovery Ratio as a Function of Mach Number	331
142	Recovery Ratio Function Variability with Flow Angle	332
143	Grid System for Numerically - Averaging Variables	335
144	Data Analysis Program Flow Chart	337
145	Typical Test Data Plot. Polar Coordinates	340
146	Typical Test Data Plot. Annular Polar Coordinates	341

LIST OF TABLES

TABLE		PAGE
1	Flow Quality Parameters	17
2	Existing Compressor Test Facilities	20
3	Compressor Test Facilities Flow Quality Standards	21
4	Design Valve Schedules	39
5	Calibration Constants of Hot Wire Probes	63
6	Baseline Test Program	68
7	Flow Conditioning Element Geometric Characteristics	73
8	Compressor Research Facility 1/10 Scale Model with Maximum Flow Bellmouth (Measured Pressures)	75
9	Compressor Research Facility 1/10 Scale Model with Maximum Flow Bellmouth (Measured Velocities)	76
10	Compressor Research Facility 1/10 Scale Model with Maximum Flow Bellmouth (Flow Quality Parameters)	77
11	Compressor Research Facility 1/10 Scale Model with J79 Bellmouth (Measured Pressures)	80
12	Compressor Research Facility 1/10 Scale Model with J79 Bellmouth (Measured Velocities)	81
13	Compressor Research Facility 1/10 Scale Model with J79 Bellmouth (Flow Quality Parameters)	82
14	Summary of the Test Conditions Used in the Evaluation of a Sonic Plate or Compressor Simulator	95
15	Compressor Research Facility 1/10 Scale Model Test Results with the Compressor Simulation. Measured Pressures and Velocities	96
16	Compressor Research Facility 1/10 Scale Model Test Results with the Compressor Simulator. Flow Quality Parameters	97
17	Compressor Research Facility 1/10 Scale Model Test	108

LIST OF TABLES (Cont'd)

	PAGE
Compressor Research Facility 1/10 Scale Model Test Program-Modified Auxiliary Test Chamber Configuration	109
Experimental Results for the Basic Barrel Configurations	111
Experimental Results for the Modified Barrel Configurations	112
Recommended Flow Conditioning System	152
Core Flow Measurement System	156
12.5 Inch Venturi Aerodynamic Parameters	163
30.0 Inch Venturi Aerodynamic Parameters	164
Statistical Analysis of the Venturi Calibration Data	190
Results of Newton-Raphson Iteration	256
Engine Parameters and Component Exit Conditions	261
J-85 Component Operating Conditions	263
J-85 Component Operating Conditions	264
J-85 Transient Component Operating Conditions	294
Bellmouth Aerothermodynamic Parameters. Steady State Values	317
Data Analysis Variables	321
Scanivalve Channel and Pressure Designation	323
	Test Program-Modified Auxiliary Test Chamber Configuration Experimental Results for the Basic Barrel Configurations Experimental Results for the Modified Barrel Configurations Recommended Flow Conditioning System Core Flow Measurement System 12.5 Inch Venturi Aerodynamic Parameters 30.0 Inch Venturi Aerodynamic Parameters Statistical Analysis of the Venturi Calibration Data Results of Newton-Raphson Iteration Engine Parameters and Component Exit Conditions J-85 Component Operating Conditions J-85 Transient Component Operating Conditions Bellmouth Aerothermodynamic Parameters. Steady State Values Data Analysis Variables

LIST OF SYMBOLS

Symbol	Description	Units *
a contracts	Sonic velocity	ft/sec
a ₁ ,G,L	Empirical functions for the turbulent boundary layer	
a _i ,b _i ,c _i ,d _i ,e _i	Coefficients for the turbulent shear stress equation	
A	Area	ft ²
A,B,n	Hot wire calibration constants	
Ar	Area ratio	
A _o ,A _i ,c,C	Arbitrary constants	
A _i ,B _i ,C _i ,D _i ,E _i	Coefficients for the momentum equation	
An'an'bn	n-th Fourier coefficients	
В	Bias	
B _w	Wake parameter	
cď	Discharge coefficient	
c _f	Skin friction coefficient	
c _p	Specific heat at constant pressure	BTU 1b _m - °R
Cr	Courant number	
dr	Orifice to pipe diameter ratio	
D,d	Diameter	ft

^{*} Unless otherwise specified

Symbol	Description	Units
E	Voltage	volts
En	Total Energy, i.e., Internal and Kinetic	BTU/lb _m
fair	Fraction by mass of mixture of water vapor and air that is dry air	
f, φ,F, Φ	Generalized function or property	
Fr	Applied force per unit length	lb _f /ft
Fa	Orifice thermal expansion factor	
g _c	Gravitation conversion constant	$\frac{1b_{m} - ft}{1b_{f} - \sec^{2}}$
g _i	General coefficient	
G	Skin friction parameter	
Gr	Grashof number	
h	Streamtube thickness	ft
h _t	Heat transfer coefficient	ft ² - °R - sec
Н	Laminar boundary layer parameter	
Ĥ	Enthalpy, $\hat{H}_o + \int_{t_o}^{t} C_p dt$	BTU/1bm
H _f	Heat transfer rate	BTU/sec

Symbol	Description	Units
H _{t1}	Total Enthalpy	BTU/lb _m
i,j,n	Indices	
I	Rotor Moment of Inertia	lb _f -ft-sec ²
J	Mechanical equivalent of heat	ft-lb _f /BTU
k	Screen drag coefficient	
k ₀ ,k _r	Distortion factor	
Kf'Ko'Ke'a	Orifice flow coefficients	
K	Thermal conductivity	BTU ft-sec-°R
£	Length Scale	ft
2 *	Wall variables mixing length	
L _m	Dimensionless mixing length	
	Mass	1b _m
ń	Mass flow rate	lb _m /sec

Symbol	Description	Units
М	Mach number	
M _i ,N _i	Recursive parameters used in the solution of the tridiagonal equations	
n	Boundary layer profile exponents	
N	Rotor speed	rev/min
Nu	Nusselt number	
•	Area ratio parameter, 1 - Ar ⁻³	
p	Static pressure	lb _f /in ²
P	Total pressure	lbf/in2
Pr	Prandtl number	
q	Dynamic head	lb _f /in ²
q ^(t)	Turbulent energy flux	BTU ft ² - sec
Q	Heat flux	BTU ft ² - sec
r	Radius	ft
r _f	Recovery factor	
r _r	Recovery ratio	

Symbol	Description	Units
R	Gas constant	ft - lb _f lb _m - •R
Rp	Pressure ratio	
Rt	Temperature ratio	
Re	Reynolds number	
8	Entropy	1b _m - *R
s	Precision	
t	Static temperature	°F, °R
^t 95	95 percentile point for the two-tailed Students t distribution	
T	Total temperature	°F, °R
Tu	Turbulence level	
u ^(t)	Root-mean-square turbulent or fluctuating velocity	ft/sec
ΰ	Internal energy per unit mass	BTU/1bm
υ ⁺	Dimensionless velocity, U/U_{τ}	
U,V,W	Velocity in Cartesian or cylindrical coordinates	ft/sec or dimensionless
Uc	Measurement uncertainty	

Symbol	Description	Units
ua,va,wa	Dimensionless velocity	
v_{τ}	Wall friction velocity	ft/sec
z,r,0	Axial, radial and circumferential cylindrical coordinates	
x,y,z	Cartesian coordinates	ft
X,Y,Z	Dimensionless position	
y ⁺	Dimensionless distance normal to surface, $yU_{\tau}^{/\nu}$	
Y	Orifice expansion factor	
α,β,γ*	Flow angles	degrees
$\alpha_{i}, \beta_{i}, \gamma_{i}, \delta_{i}$	Coefficients in the finite- difference form of the turbulent shear stress	
$A_i, B_i, \Gamma_i, \Delta_i$	Coefficients in the finite- difference form of the momentum equation	
$\alpha, \beta, \gamma, x_k, y_k, z_k$	Arbitrary variables	
Y 10 Sec\22	Ratio of specific heats	
δ	Boundary layer thickness	ft

Symbol	Description	Units
δ*	Displacement thickness	ft
δ ⁺	Boundary layer thickness, $\delta U_{\tau}/V$	ft
Δ*	Dimensionless displacement thickness	
Δx,Δy	Nominal finite-difference steps	ft
Δθ	Angular distance between circum- ferential measuring stations	
ε	Implicit-explicit parameter	
ζ	Flow control device open area ratio	
ζ _i	Parameter in the finite-difference approximation to the second derivative	
η	Normal direction finite-difference grid scale factor	
$\eta_{\mathbf{n}}$	n-th stage efficiency	
$\theta_{\mathbf{m}}$	Momentum thickness	ft
Θ _m	Dimensionless momentum thickness	
λ	Turbulent velocity profile parameter Damping factor	
•	bamping ractor	

Symbol	Description	Units
μ	Viscosity	1h ft-sec
ν	Dynamic viscosity	ft ² /sec
$\xi_{\mathbf{i}}$	Parameter in the finite- difference approximately to the first derivative	
ρ	Fluid density	lb _m /ft ³
σ	Profile distortion function	
τ	Time	sec
τ ⁺	Dimensionless shear stress, $\tau/\tau_{_{\mathbf{W}}}$	
τ _c	Probe time constant	sec
^τ d	Dimensionless turbulent shear stress	
τ _w	Wall shear stress	1b _m ft - sec
τ ^(t)	Turbulent momentum flux	ft ² /sec ²
$\phi_{ extbf{i}}$	Flow coefficient	
φ ^(v) , φ ^(t)	Viscous and turbulent dissipation	BTU ft ² - sec
Ψ ^P _i	Pressure coefficient	
Ψ ₁ ^T	Temperature coefficient	
ω	Frequency	hz

LIST OF SUBSCRIPTS

Description Symbol Average a Actual act Adiabatic adb air Dry air Ambient amb Bellmouth b Boundary Layer В Bleed bl Combustor br c,C Compressor Circumferential ca Calibration cal d Design Dew point đр Fluid f Gas g i Inlet i,j,k,nIndices Inviscid I Mean m Maximum value max Model mdl Measured mea Minimum value min n Neutral

LIST OF SUBSCRIPTS

Symbol	Description
nz	Nozzle
P	Total pressure
r	Radial
ref	Reference value
rp	Reference radial value
R	Rotor
S	Screen
st	Static
t	Throat
tb	Free-stream turbulence induced condition
tc	Test chamber
th	Theoretical
tl	Total
tr	Turbine
ts	Self-excited condition
Tu	Turbulence level
U	Velocity
v	Vapor
w	Wire
wl	Wall
x,y,z	Cartesian coordinates or arbitrary variables
θ	Circumferential
5	Turbine nozzle
8	Exhaust or afterburner nozzle
0	Zero
σ.	Free-stream
	xxvi

LIST OF SUPERSCRIPTS

Symbol	Description
n	Current x-station
0	Previous z-station
t	Turbulent
v	Viscous
1,2,3	Indices
•	Fluctuating
	Time-averaged

SECTION I

FLOW QUALITY REQUIREMENTS FOR THE COMPRESSOR RESEARCH FACILITY

A. Introduction

The Compressor Research Facility (CRF) consists of a test system which emphasizes automated procedures and data handling with the expressed objectives of enhancing increased testing by means of reduced costs. Furthermore, the facility offers the capability of simulating some compressor transients.

The facility is configured in the open loop mode, i.e., air is extracted from the atmosphere, compressed, and then discharged to atmospheric conditions. In order to reduce compressor power requirements and simulate flight conditions at elevated altitudes, the compressor will be mounted in a large tank or test chamber. A series of control valves will be utilized to regulate the tank pressure and/or mass flow with the compressor itself supplying the exhauster capability. This concept -- while offering a minimum cost approach -- poses problems when compressor cooling, bleed, and flow quality are considered.

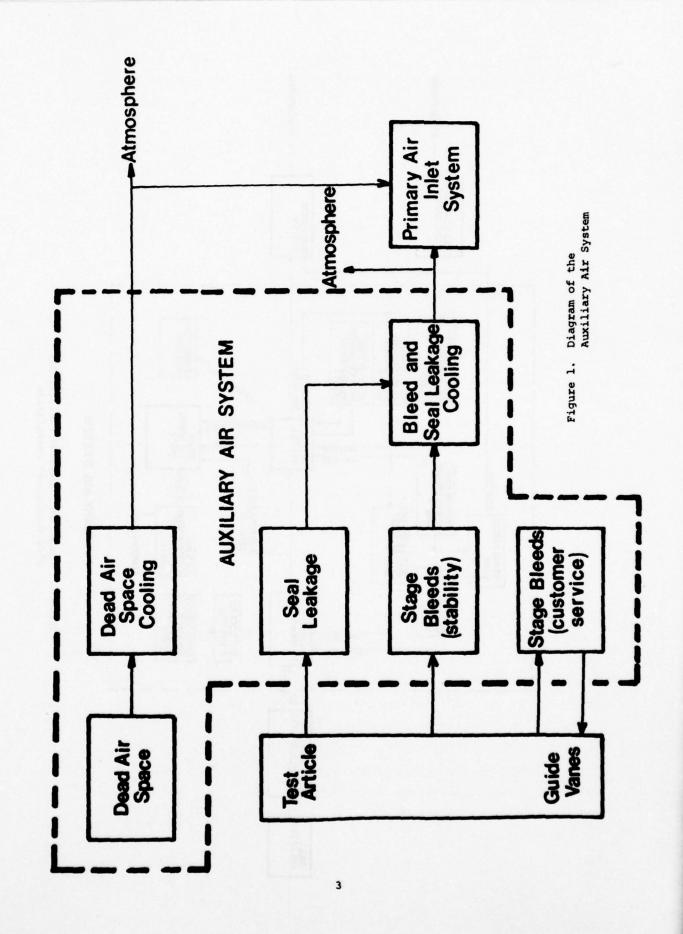
The compressor cooling air, stability and bleed air and seal leakage are lumped together in the auxiliary air system. The purposes of the auxiliary air system are:

- Maintain the temperature of the test chamber dead air space at levels commensurate with the instrumentation temperature limits.
- Provide cooling for the test compressor outer case.
- 3) Provide a means for disposing of the air which is bled from the various compressor stages.
- 4) Provide a means for controlling the compressor gas path seal leakage flows.

In essence, the auxiliary air can be returned to the primary air inlet system or to the atmosphere. A block diagram showing both these options is presented in Figure 1. After considerable study of both these options, the facility contractor elected to return the auxiliary air to the inlet system. The overall facility with the auxiliary air returned to the inlet is shown in Figures 2 and 3.

The National Academy of Science - National Research Council Advisory Committee to the AFSC³ and subsequent panels⁴ felt that the transient aerodynamic performance of the Compressor Research Facility might be severely compromised by the reingestion system. Furthermore, acquisition of data during compressor transients is one of the major reasons for constructing the facility and, thus, this might present an unacceptable risk. The potential dynamic coupling between the compressor inlet system and the compressor stability bleeds might make it difficult to maintain the correct back pressure for the bleed ports as well as the correct compressor inlet conditions. Moreover, if the reingested air differed from the ambient air temperature, the compressor inlet temperature would vary temporarily during a transient. In addition, insufficient mixing could also result in a spatially varying temperature field.

Degradation in flow quality was also a potential outgrowth of the reingestion system. Since recent operational experience has shown that distorted inlet flow can impact compressor and, thus, engine performance, a test facility must be able to provide -- as a baseline -- a high quality undistorted flow. Distortions may be either spatially or time variant involving parameters such as the pressure, temperature, velocity or flow direction. Since the existing facility contract did not incorporate any flow quality specifications, the committees recommended that specifications be incorporated which quantitatively limit the maximum allowable steady state and dynamic distortion levels both within the test chamber and the compressor bellmouth. Furthermore, it was felt that aero dynamic testing was vital to insure compliance with the aforementioned objectives.



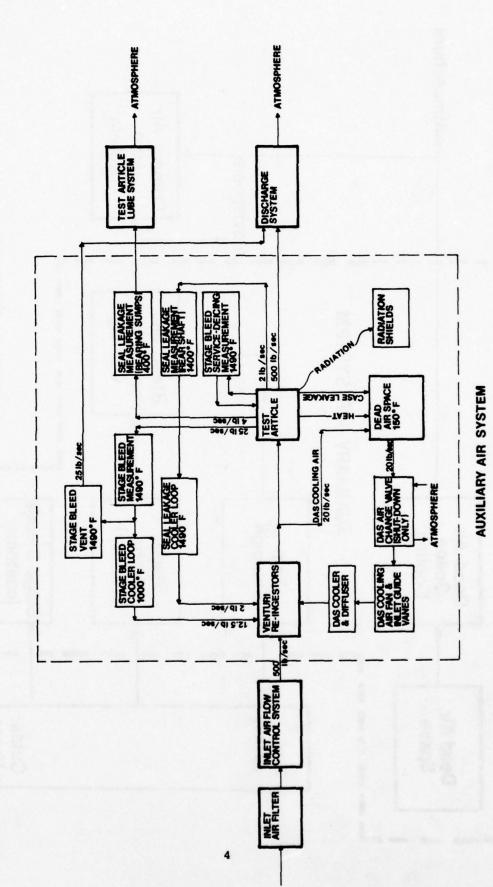


Figure 2. Compressor Research Facility Air Flow Conceptual Formulation

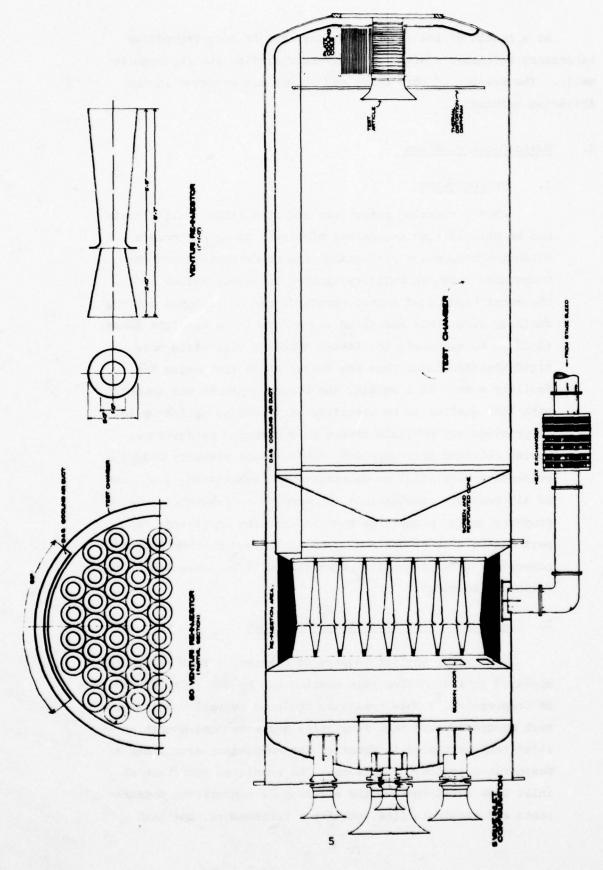


Figure 3. Compressor Research Facility Schematic Diagram

As a result of the recommendations, the AF Aero Propulsion Laboratory initiated a study of compressor airflow quality requirements. The results of this study and survey are reviewed in the following sections.

B. Basic Considerations

1. Introduction

Flow distortion parameters and/or airflow quality goals can be defined from two points of view. Those parameters affecting compressor performance can be determined and the Compressor Research Facility limited to lesser values. On the other hand, wind tunnel standards can be employed and the facility flow field specified as uniform in an absolute sense. As might be expected, the latter approach will yield more rigid specifications than the former while increasing the facility cost. As a result, the former approach was chosen with flow quality to be specified at values sufficiently low to preclude any possible impact on compressor performance. Having selected this approach, the relevant property and/or properties must still be determined and quantified, i.e., out of all possible combinations of aerodynamic parameters the property and/or properties most influencing compressor flow performance must be defined. The survey and recommendation of compressor flow distortion parameters will be presented in the following sections.

2. Survey of Flow Distortion Parameters

One of the earlist reviews of compressor test procedures appeared in 1946 having been carried out by the NACA Subcommittee on Compressors. This committee reviewed overall compressor test procedures and test facilities and recommended that an inlet tank be placed in front of the compressor even under atmospheric operating conditions. The committee felt that an inlet tank would improve the accuracy of temperature measurements and eliminate flow rotation. Furthermore, the tank

diameter should be at least 1-1/2 times the compressor diameter with 3 times the compressor diameter preferred. A bell-mouth inlet should be provided to insure a smooth transition at the compressor face with the bellmouth inlet diameter being 1-1/2 to 2 compressor diameters. Compressor inlet measurements should be made at least 1 compressor diameter ahead of the bellmouth inlet with

$$\frac{q_{\text{max}} - q_a}{q_a} < 0.01 \left(\frac{d_{\text{tc}}}{d_c}\right)^2 \tag{1}$$

$$T_{\text{max}} - T_{\text{a}} < 1^{\circ}F \tag{2}$$

where q denotes the dynamic head, d the diameter and T the total temperature. The measuring stations are shown in Figure 4. Moreover, at the compressor entrance any rotation should cause less than a 3° deviation in the flow from the axial direction, i.e.,

$$\beta < 3^{\circ}$$
 (3)

The method of determining the average dynamic head and total temperature is not specified in reference 6 although an area averaged value is probably intended.

The NACA Subcommittee on Compressors felt that the standards of equations 1, 2, and 3 could be achieved by utilizing one or more reinforced screens and a honeycomb straightener with the last screen or straightener 2 compressor diameters ahead of the bellmouth inlet. Moreover, screens with 50% open area were found to produce the maximum improvement in flow uniformity.

A similar study has been carried by the Aerodynamics Subcommittee of the Gas Turbine Collaboration Committee of the Aeronautical Research Council of Great Britain. The results of this survey are considerably more recent and are reported in reference 6. In this reference the following flow quality

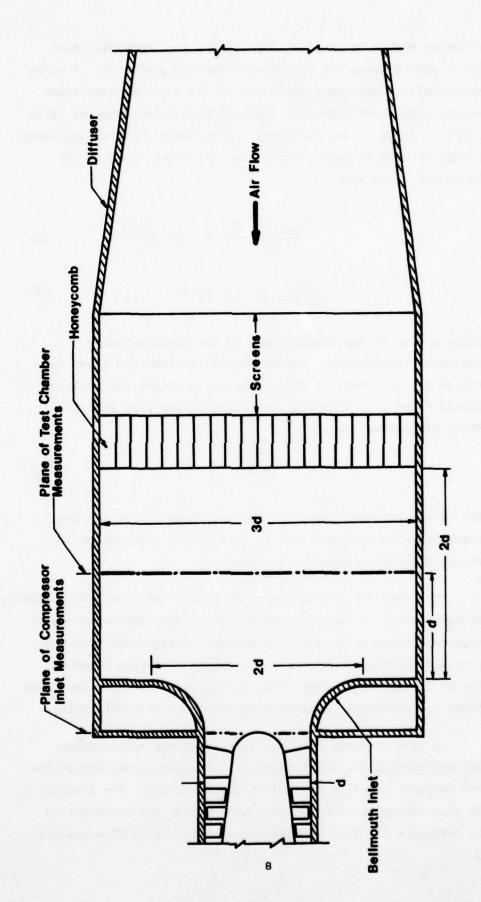


Figure 4. Inlet Measuring Stations

standards are proposed

$$T_{\text{max}} - T_{\text{a}} < 1^{\circ}\text{C} \quad (1.8^{\circ}\text{F})$$
 (4)

and

$$\frac{P_{\text{max}} - P_{\text{a}}}{P_{\text{a}} - P_{\text{a}}} < 0.05 \tag{5}$$

where P and p denote the total and static pressure respectively and the subscript a denotes an area-averaged value. Equation 5 is selected over a velocity relationship, e.g., equation 2, since it appears that the compressor influences the flow upstream such that the approach velocity is made more uniform and a corresponding static pressure variation remains.

Note that the bellmouth contraction is very effective at reducing the velocity non-uniformity. Prandtl⁸ has shown that the percentage variation in kinetic energy is reduced to $1/Ar^2$ times its original value in passing through a contraction of area ratio Ar; consequently an area ratio of 3 would reduce $(u_{max} - u_a)^2/u_a^2$ by a factor of 9.

One of the most recent documents defining flow quality standards has been published by the Arnold Engineering Development Center. These specifications are directed toward engine rather than compressor testing; however, since the AEDC standards are directed toward turbine engine stability which is strongly dependent on compressor surge margin, the values are relevant. In particular, reference 9 states that

$$\frac{P_{\text{max}} - P_{\text{min}}}{P_{\text{a}}} < 0.1, \tag{6}$$

$$\sqrt{\frac{(P')^{\frac{2}{max}} - \sqrt{(P')^{\frac{2}{min}}}}{P_a}} < 0.01$$
 (7)

$$\frac{T_{\text{max}} - T_{\text{min}}}{T_{\text{a}}} < 0.01, \tag{8}$$

and

$$\sqrt{\frac{\left(\mathbf{T'}\right)^2_{\max} - \sqrt{\left(\mathbf{T'}\right)^2_{\min}}}{\mathbf{T_a}}} < 0.01 \tag{9}$$

are sufficient to establish baseline performance values. $\sqrt{(P')^2} \text{ and } \sqrt{(T')^2} \text{ terms denote the total pressure and total temperature time-variant spatial inlet distortion. Note that equations 6 through 9 differ from equations 1 through 3 and 4 and 5 in two important respects. First, the steady-state spatial pressure distortion is non-dimensionalized with the total pressure rather than the dynamic head and, secondly, time-dependent standards have now been introduced.$

The above criteria have been derived by considering two specific mechanisms as the major cause of compressor stall. The first theory postulates that the engine and/or compressor is sensitive to distortion patterns -- primarily those that change rapidly with time. 10 The rate at which the total pressure and total temperature can change and still be sensed by the rotor is a function of the engine or rotor speed. The second theory speculates that surge margin reduction can be correlated with the root-mean-square level of the time-variant component of total pressure at the compressor face. Furthermore, the unsteady flow properties must be characterized statistically using the rms level, frequency spectra, and correlation properties. The two theories can be generalized as either frequency 10 or amplitude dependent. 11 In either event, the inequalities of equations 6 through 9 will assure base-line or maximum compressor surge margin and performance.

In addition to the above 3 reviews, an in-depth study on inlet flow quality has been carried out by H. C. Melick. 12

The objective of this program was to establish the feasibility of a concept by which the improvement of an inlet could be monitored from the standpoint of inlet flow quality. Melick screened 24 candidate flow quality definitions and selected

$$Q = 1 - \frac{\int_{A} (P_{a} - P_{min}) dA}{A q_{a}}$$
 (10)

with all properties defined at the compressor face. Q is a flow quality parameter and is essentially an area weighted pressure difference and can be related to the previously defined parameters. Equation 10 can be extended to fluctuating flows by redefining P_{\min} as a function of both position and time, 12 i.e., $P_{\min} = P_{\min}(r, \theta, \tau,)$ where the r dependence is implied in equation 10.

The flow parameter, Q, can be directly related to $(P_{max} - P_{min})/P_a$ by considering

$$\frac{\int_{\mathbf{A}} (P_{\text{max}} - P_{\text{min}}) dA}{\int_{\mathbf{A}} PdA} \quad \text{and} \quad \frac{\int_{\mathbf{A}} (P_{\text{a}} - P_{\text{min}}) dA}{\int_{\mathbf{A}} (P_{\text{-}} - P_{\text{)}} dA}$$

where the two expressions are now recast in integral form. Melick ¹² has compared both of the above expressions using the data of reference 13. These results are shown in Figure 5. The relationship between the two parameters is linear indicating that either is an acceptable representation of flow distortion.

Circumferential and radial distortion factors are also currently in use. The factors are defined in terms of coefficients which are generated by fitting the measured profiles with a Fourier expansion. 14 The circumferential distortion factor \mathbf{k}_{A} is defined as

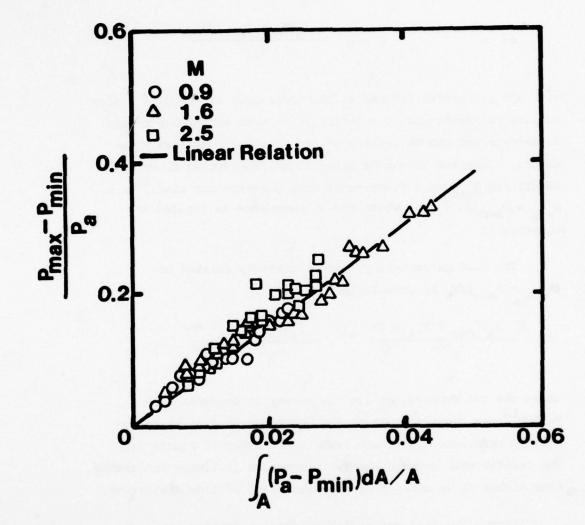


Figure 5. Comparison of Flow Quality Parameters

$$k_{\theta} = \frac{\sum_{j=1}^{J} \left[\left(\frac{A_{n}}{n^{2}} \right)_{max} \right]_{j}^{J}}{\sum_{(q/P)_{ref}}^{J} \sum_{j=1}^{(1/d_{j})}}$$
(11)

where the subscript j denotes the j-th radial ring. The coefficient \mathbf{A}_{n} is

$$A_n = \sqrt{a_n^2 + b_n^2}$$
 $n = 1, 2, 3...$ (12)

where

$$a_{n} = \frac{\Delta\theta}{180} \sum_{i=1}^{I} \frac{P/P_{ref}(i\Delta\Theta)}{P_{a}/P_{ref}} \cos(ni\Delta\Theta)$$
 (13)

and

$$b_{n} = \frac{\Delta \theta}{180} \sum_{i=1}^{I} \frac{P/P_{ref}(i\Delta \theta)}{P_{a}/P_{ref}} \sin(ni\Delta \theta)$$
 (14)

Note that $P/P_{ref}(i\Delta\theta)$ is the total pressure recovery at the angle $i\Delta\theta$ and P_a/P_{ref} is the area averaged recovery.

The radial distortion factor is defined in a similar manner and

$$k_{r} = \frac{\sum_{j=1}^{J} \frac{(\Delta P)}{P_{aj}} \left(\frac{1}{(d_{j})^{2.8}}\right)}{(q/P)_{ref} \sum_{j=1}^{J} 1/(\Delta j)^{2.8}}$$
(15)

with

$$\left(\frac{\Delta P}{P_{a}}\right)_{j} = \left|\frac{\left(\frac{P_{ca}}{P_{ref}}\right)_{j}}{\left(\frac{P_{a}}{P_{ref}}\right)} - \left(\frac{P_{rp}}{P_{a}}\right)\right|\left(\frac{P_{a}}{P_{rp}}\right)$$
(16)

where P denotes a reference radial pressure which is a function of q/P. The circumferential average is generated by integrating

over the variable θ at a constant value of radius, i.e.,

$$\phi_{ca}(r) = \frac{1}{2\pi r} \int_{0}^{2\pi} \phi(r,\theta) r d\theta \quad \text{where } r = \text{constant} \quad (17)$$

 \mathbf{k}_{θ} and $\mathbf{k}_{\mathbf{r}}$ can be combined into a distortion factor \mathbf{k} by

$$k = k_{\theta} + ck_{r} \tag{18}$$

where c is a radial distortion weighting factor.

Melick 12 has also compared the circumferential and radial distortion factors to 1-Q. These are similar to k_0 and are shown in Figure 6. Again, the parameters are linearly related. It would appear that Q, $(P_{max} - P_{min})/Pa$ or k are all capable of adequately representing flow distortion and its impact on turbine engine performance.

During the course of the investigations regarding flow quality for the CRF, a number of turbine engine and airframe manufacturers as well as government laboratories were contacted. The results of these visits are documented in references 15 through 22. A number of flow quality parameters were suggested by the organizations visited. In general, these consisted of the following:

$$\frac{P_{\text{max}} - P_{\text{min}}}{P_{\text{a}}} ,$$

(ii)
$$\frac{P_{\text{max}} - P_{\text{min}}}{q_{\text{a}}},$$

(iii)
$$\sqrt{(P')^2_{\max}} - \sqrt{(P')^2_{\min}}$$
,

(v)
$$\sqrt{\left(\mathbf{T'}\right)^2_{\max}} - \sqrt{\left(\mathbf{T'}\right)^2_{\min}}$$

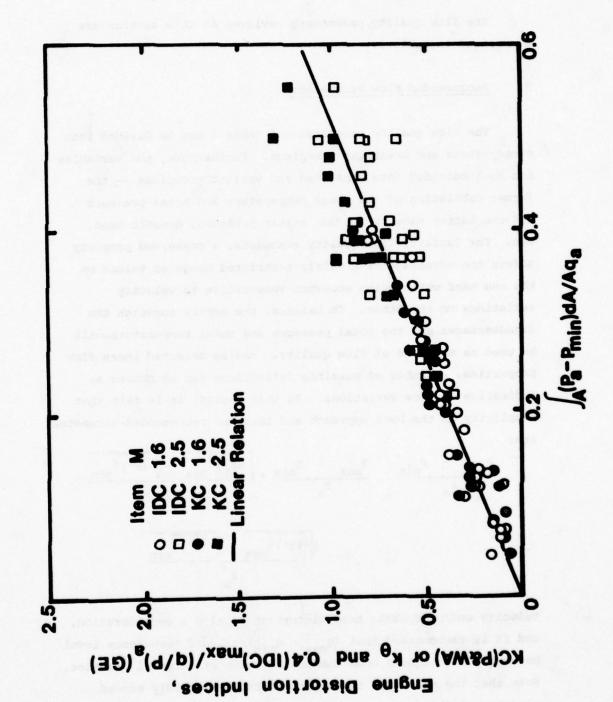


Figure 6. Comparison of Flow Quality and Flow Distortion Parameters

(vi)
$$\sqrt{\overline{(U')}^2}_{max} / U_a$$

as well as k_{θ} and k_{r} .

The flow quality parameters reviewed in this section are summarized in Table 1.

3. Recommended Flow Parameters

The flow quality parameters of Table 1 can be divided into steady-state and transient groupings. Furthermore, the variables can be subdivided into conserved and variant groupings — the former consisting of the total temperature and total pressure and the latter made up of the static pressure, dynamic head, etc. For facility flow quality standards, a conserved property offers the advantage of a fairly restricted range of values on the one hand while being somewhat insensitive to velocity variations on the other. On balance, the merits outweigh the disadvantages and the total pressure and total temperature will be used as measures of flow quality. Having selected these flow properties, a number of possible definitions can be chosen as indicative of flow variations. In this regard, it is felt that simplicity is the best approach and thus the recommended parameters are:

$$\frac{P_{\text{max}} - P_{\text{min}}}{P_{\text{a}}}, \frac{T_{\text{max}} - T_{\text{min}}}{T_{\text{a}}}, \sqrt{\frac{(P')^2_{\text{max}} - \sqrt{(P')^2_{\text{min}}}}{P_{\text{a}}}},$$

$$\sqrt{\frac{(T')^2_{\text{max}} - \sqrt{(T')^2_{\text{min}}}}{T}}$$

Velocity and/or dynamic head distortion is also a consideration, and it is recommended that $(q_{max} - q_{min})/q_a$, and turbulence level be employed to ensure come commonality with wind tunnel practice. Note that the values of these parameters may markedly exceed wind tunnel standards.

TABLE 1
FLOW QUALITY PARAMETERS

Steady	y-State	Time-Dependent		
q _{max} - q _{min}	P _{max} - P _{min}	$\frac{\sqrt{(P')^2}_{\text{max}} - \sqrt{(P')^2}_{\text{min}}}{P_a}$		
Pmax - Pa Pa - Pa	$1 - \frac{\int_{\mathbf{A}} (\mathbf{P_a} - \mathbf{P_{min}}) d\mathbf{A}}{\mathbf{q_a}^{\mathbf{A}}}$	\frac{\overline{\text{T'}}^2}{(\text{T'})^2} \tag{(\text{T'})}^2 \text{min}		
k ₀	k _r			
T - Ta	Tmax - Ta	Ua Ua		
В				

(1) The spatially-averaged value of the property $\boldsymbol{\varphi}$ is defined as

$$\phi_{\mathbf{a}} = \frac{1}{A} f_{\mathbf{A}} \phi(\mathbf{r}, \theta) d\mathbf{A}$$

(2) The root-mean-square value of the property ϕ is defined as $\phi_{\rm rms} = \{\frac{1}{\tau} \int_{\tau} [\phi({\bf r},\theta,\tau) - \phi({\bf r},\theta)]^2 d\tau\}^{1/2} \text{ where } \phi({\bf r},\theta) = \frac{1}{\tau} \int_{\tau} \phi({\bf r},\theta,\tau) d\tau$

Note that the subscript max or min denotes the spatial and not the temporal maximum or minimum value of a property.

4. Measurement Accuracy

Prior to specifying values for each of the recommended flow parameters, a brief review of pressure and temperature measurement accuracy will be presented. This review will furnish sufficient background such that the attainability of the standards can be assessed.

All temperature and pressure measurements are inaccurate to some extent. These errors are the differences between the measured and the true value as defined by the National Bureau of Standards. The measurement error or uncertainty consists of a fixed and random error. The fixed or systematic error is also known as bias. The bias is always the same in a given measurement and can only be determined by comparing the measured and true value of a quantity. Large unknown biases are eliminated by calibration processes. The random or precision error is the variation of repeated measurements of the same quantity. Precision can be defined statistically with the standard deviation normally utilized for this purpose. The uncertainty is the combination of bias and precision and

$$Uc = + (B + t_{95}S)$$

where Uc is the uncertainty, B is the bias, S the precision, and t_{95} is the 95th percentile point for the two-tailed students t distribution. ²³

Pressure measurement error sources are primarily due to calibration errors, data acquisition and reduction errors and probe errors. The calibration errors are the result of the cumulative effect of a series of calibrations tracing back to the National Bureau of Standards. Data acquisition errors are caused by uncertainties in excitation voltage, electrical simulation, signal conditioning, recording of information, etc. Data reduction errors stem from calibration curve fits and computer resolution. Probe errors are due to extraneous aerodynamic effects and when combined with calibration, data acquisition, and data

reduction errors yield uncertainties of from 0.3 - 0.78. This amounts to 0.04 - 0.10 lb_f/in² for atmospheric pressures. Note that probe errors may be markedly influenced by turbulence level.

Temperature measurement errors are due to the same sources as noted above for pressure measurements, i.e., calibration, data acquisition and data reduction errors. In this case, uncertainties amount to 0.5 - 0.6%. This is approximately 2.3 - 2.8°R for temperatures of 460°R.

C. Survey of Compressor Facilities

Characteristics of Existing Compressor Test Facilities

During the course of the investigations preceding this report, a survey of existing airbreathing engine and compressor test facilities was carried out. The overall characteristics of the compressor facilities are summarized in Table 2 where the information has been extracted from references 15 through 22 and 25 through 27. The table lists the organization, the maximum power available to drive the test compressor, the maximum compressor rotating speed, the maximum compressor flow rate, and the environmental conditions. The environmental conditions include the range of temperatures and pressures which can be controlled at the compressor inlet. An open system is limited to ambient temperatures and pressures unless a flow control system is utilized at the compressor inlet in conjunction with a pressure vessel. Under these conditions, subatmospheric pressures can be utilized in the test program.

2. Flow Quality in Existing Compressor Test Facilities

In addition to the overall facility characteristics, typical flow quality standards are presented in Table 3. This information is a compilation of data presented in reference 15 through 22. The data is divided into five major categories. These consist of the steady state total pressure and temperature variation, the flow angle, and the

TABLE 2
EXISTING COMPRESSOR TEST FACILITIES

Organization	Power hp	Speed rpm	Flow lb_/sec	Environment
NASA Lewis	15,000	18,000	100/75	60 to -20°F/15 to 2 lb _f /in ²
AEDC	3,000	5,000/ 17,000	24	Controlled/12 to 1 lb _f /in ²
Continental	4,000	11,000/ 30,000		Open system
	1,400	42,000/ 63,000		Open system
Lycoming	1,500	20,000/ 65,000	-	Open system
estalizati and and a Aligno america	2,500	20,000/ 65,000	egas povetnike en 1.5aulenn	Open system
Detroit Diesel Allison	36,000	25,000	440/100	105 to 0°F/30 to 3 lb _f /in ²
egit zrocen	20,000	15,000	140/42	60 to -70°F/30 to 3 lb _f /in ²
General Electric Full Scale	30,000	10,000	500	200 to -75°F/22 to 1 lb _f /in ²
Small Engine	13,000	20,000	70	200 to -30°F/30 to 2.5 lb _f /in ²
House Compressor	15,000	10,000	250	Open system
Pratt & Whitney X-204	21,000	15,000	400/60	200 to -40°F/22 to 14 lb _f /in ²
x-17	30,000	11,000	127	Open system
X-211	40,000	5,000/ 10,500	500	Open system
х-219	53,000	11,250/ 17,500		Open system

TABLE 3
COMPRESSOR TEST FACILITIES FLOW QUALITY STANDARDS

Organization		.1	4				Tata Tain' "F			(P') 2 - (P') 2 min	min (T') 2 - (T') 2
	Pacility	Pacility Accuracy Limit	Impacts Compressor Performance	Pacility Goal	Pacility	Facility Accuracy Limit	Impacts Compressor Performance	Pacility Goal		a.*	.•
WSA Levis	0.03		1	1		t ₁ (1)	l,	ı	1	1	1
Armold Engineering Development Center Engine Test Facilities	0.004	0.03	0.03-0.04	0.01	ı	ĩ	1	-	1	0.005-0.01 (2)	0.01(3)
3	0.002- (4)	ı	1	1	•	1	1	ı	6.6	ı	ı
Detroit Diesel	910.0	ı	0.04-0.10	ı	i	ı	1-15(5)	1		0.01-0.20(6)	1
General Electric	0.00	0.00	0.03	0.00	1	1	1	~	١	1	1
Pratt & Whitney	0.01-	0.0015	0.005- (7)	0.01	-	-	0.6(8)	-	0.5-1.0(9)	0.001 - 0.015 (10)	1
McDonald-Douglas	0.04-0.06	1	0.08-0.10	ı	ı	1	ı	1	1	0.16-0.24	I
Boeing	1.01-0.02	1	1	1	1	ı	1	1	ı	ı	

TABLE 3 (continued)

- (1) NASA notes that only a 3°F temperature difference exists between the operating and the surge line.
- (2) Frequencies from 0 700 hz
- (3) Estimated Value
- (4) $\frac{U_{\text{max}} U_{\text{min}}}{U_{\text{a}}} \simeq 0.02 0.03$
- (5) 15°F represents an extreme upper limit
- (6) 0.2 represents an extreme upper limit
- (7) The lower value corresponds to a l% loss in compressor efficiency with the upper value related to a l% loss in surge margin.
- (8) 0.6°F corresponds to a 1% degradation in efficiency. 3.5 4°F temperature difference between the surge and operating line is typical of modern compressors.
- (9) 0.5°F corresponds to approximately 1% change in efficiency
- (10) Frequencies from 0 1000 hz. with a goal of 0.01 for $\sqrt{\frac{(P')^2_{\text{max}} \sqrt{(P')^2_{\text{min}}}}{P_a}}$ over the same frequency range
- (11) These values are typical of engine inlets. The smaller values are for subsonic, under-the-wing, engine installations while the larger values correspond to a supersonic inlet.
- (12) Acoustic considerations dictate that $\frac{U_{\text{max}} U_{\text{min}}}{U_{\text{a}}} < 0.03$ with the acoustic energy less than 0.002 at any frequency and less than 0.01 over the entire frequency spectrum.

root-mean-square value of the time variant total pressure and temperature distributions. The first two categories are further subdivided into four additional areas. These are the current facility values, the minimum value of the parameter that can be measured in the facility which is denoted as the "Facility Accuracy Limit", the minimum value of the parameter impacting compressor performance which is entitled "Impacts Compressor Performance", and the value of the parameter to be used as a design goal in a new facility. The latter value was influential in the determination of the CRF specifications.

An examination of Table 3 indicates that most facilities currently have total pressure deviation, i.e., $P_{max} - P_{min}/P_a$, values of approximately 1 - 2%. Generally these values are consistent with measurement accuracies. Values of 2 - 4% are required before any change in compressor performance, i.e., degradation in efficiency or surge margin, can be detected. Facility goals of from 1/2 - 1% were most frequently quoted. It is important to note that modest non-uniformities in pressure impact measurement accuracy long before they impact compressor performance. The non-uniform flow field necessitates a substantial increase in the number of measuring stations. An averaging procedure must then be employed to obtain a "mean" compressor inlet condition. The uncertainty in this measurement increases rapidly with the non-uniformity of the flow field. As a consequence, modest non-uniform conditions will impact measurement accuracy while not influencing compressor performance.

Excessively high turbulence levels also markedly affect measurement accuracy. A very limited number of measurements 28, 29 indicate that turbulence levels at the compressor face should be less than about 1%. It is well known that a reduction in area will substantially alter both longitudinal and lateral turbulence levels. As a consequence, turbulence levels may be significantly higher in the test chamber itself. Batcheler 30 has shown that the turbulence reduction due to an area contraction can be written as

$$\frac{Tu_c}{Tu_{tc}} = \frac{1}{Ar^2} \sqrt{\frac{3}{4} \left[\frac{1+o^2}{2o^3} - \ln\left(\frac{1+o}{1-o}\right) - \frac{1}{o^2} \right]}$$

where Tu_{tc} denotes the turbulence level in the test chamber, Tu_{c} the level at the compressor face and $o = 1 - Ar^{-3}$. The reduction in level varies roughly as $1/Ar^{2}$ and thus a contraction ratio of 4 to 1 would produce a 16 fold decrease. Note that $Tu = \sqrt{\frac{1}{(U')^{2}}/U_{a}}$ in the present context.

Total temperature variations range from $1-5^\circ F$ in current facilities with $1-2^\circ F$ representing the measuring capabilities in most cases. Again, the impact of a non-uniform spatial and temporal distribution of temperature is more pronounced with regard to measurement accuracy than with compressor performance until large values of $T_{\text{max}} - T_{\text{min}}$ occur.

Swirl or non-uniform flow angularity generally varies from 1/2 - 1° and is not usually a major concern. In a similar vein,

$$\sqrt{\frac{(P')^2}{\max} - \sqrt{(P')^2}_{\min}} \quad \text{and} \quad \sqrt{\frac{(T')^2}{\max} - \sqrt{(T')^2}_{\min}} \quad \text{have not}$$

been extensively investigated. The very limited data sample indicates that these parameters are generally of the order of 1%. Some recent information 14 concludes, however, that temporal variations of pressure may be much larger particularly in supersonic applications. It appears that time-dependent variations will become more important in the future.

In summary, $(P_{max} - P_{min})/P_a$ values of approximately 1 - 2 are typical of current compressor facilities. Moreover, $T_{max} - T_{min}$ values of 2 - 4°F seem to represent the state of the art in temperature variations. Temporal variations of pressure and temperature are not as well documented as their steady-state counterparts; nevertheless,

values of
$$\frac{\sqrt{(P')^2}_{\text{max}} - \sqrt{(P')^2}_{\text{min}}}{P_{\text{a}}} \quad \text{and} \quad \frac{\sqrt{(T')^2}_{\text{max}} - \sqrt{(T')^2}_{\text{min}}}{T_{\text{a}}}$$

of about 1 - 2% would be expected in most facilities.

D. Flow Quality Standards for the Compressor Research Facility

1. Recommended Flow Quality Standards

The flow quality standards recommended for the Compressor Research Facility have been arrived at by considering the following:

- (i) The parameters which best represent the impact of flow distortion and/or non-uniformities on compressor performance and measurement uncertainties.
- (ii) The accuracy with which temperature and pressures can be measured. This information can be used to determine the minimum measurable flow distortion.
- (iii) The minimum value of flow distortion which influences compressor efficiency and/or surge margin.
 - (iv) The current industry-wide standards for flow distortion.

As a result of the previously discussed items, the following flow quality standards are recommended for the Compressor Research Facility.

$$\frac{P_{\text{max}} - P_{\text{min}}}{P_{\text{a}}} < 0.01 \tag{19}$$

$$\sqrt{\frac{(P')^2}{\max} - \sqrt{(P')^2}}_{\min}$$
 < 0.01 for frequencies (20)

from 0 - 1000 hz.

$$\frac{q_{\text{max}} - q_{\text{min}}}{q_{\text{a}}} < 0.01 \left(\frac{D_{\text{tc}}}{D_{\text{c}}}\right)^2$$
 (21)

$$\frac{T_{\text{max}} - T_{\text{min}}}{T_{\text{max}}} < 0.005 \tag{22}$$

$$\sqrt{(T')^2_{\text{max}}} - \sqrt{(T')^2_{\text{min}}} < 0.005 \text{ for frequencies}$$
(23)

from 0 - 1000 hz.

$$\sqrt{(u')^2}_a/v_a$$
 < 0.01 (24)

Relations (19) through (23) are to be satisfied one compressor diameter upstream of the inlet bellmouth with inequality (24) to be satisfied at the compressor face. Note that this standard can be translated upstream if an appropriate area contraction is specified.

2. Impact of the Flow Quality Standards on the Compressor Research Facility Test Chamber

Wind tunnel designers have used "settling chambers" to combat flow distortions since the early 1900's. A settling chamber or stagnation tank consists of a large diameter section wherein the flow is decelerated to very low velocities. As a result, the total pressure approaches the static pressure and values of P - P min/Pa would normally be small provided p is uniform. It thus follows that equation 21 is a more stringent requirement than equations 19 or 20 provided the velocity is sufficiently small and reasonably uniform. Since the test chamber for the Compressor Research Facility is to be 20 ft. in diameter with maximum compressor diameters at 10 ft., the velocities in the test chamber are small. Even when advanced compressors having high subsonic axial Mach numbers are considered, it is unlikely that the tank velocities would ever exceed 200 ft/sec. As a result, the dynamic head is approximately 2% of the total pressure; consequently, if the static pressure is uniform, the maximum value of Pmax - Pmin a would be 2%. If the test chamber velocities are reduced to 100 ft/sec, P_{max} - P_{min}/P_a is approximately 1%.

The same rationale can be used with regard to $q_{max} - q_{min}/q_a$. In this case even though the dynamic head is small, this flow parameter may be large since the difference $q_{max} - q_{min}$ is normalized with an average value of dynamic head rather than the total pressure.

The root-mean-square total pressure parameter is more difficult to quantify than $P_{max} - P_{min}/P_a$. Even so $\sqrt{\frac{(P')^2}{max} - \sqrt{(P')^2}_{min}}$

is probably roughly of the same order of magnitude as P - Pmin/Pa.

The temperature variations are functions of the inlet design in conjunction with recirculation and/or reingestion concepts. If the auxiliary air is returned to the inlet, provisions must be made to satisfy equations 22 and 23. It is recommended that reingestion be avoided if at all possible. The elimination of reingestion does not

automatically assure that
$$T_{max} - T_{min}/T_a$$
 and $\sqrt{\frac{(T')^2}{max} - \sqrt{(T')^2}}$

will be less than 0.005. Temperature stratifications adjacent to the facility inlet system may well produce variations which exceed the limits of equations 22 and 23. Provisions must be made to preclude the occurrence of any naturally developed temperature variations. Care must also be taken in the location of the inlet relative to other facility exhaust systems. The ingestion of hot exhaust gases or spent steam from other facilities must be avoided at all costs.

As has been stated above, total pressure variations will be nominal provided a reasonably uniform flow field exists. Since the Compressor Research Facility uses five control valves whose combined area is much less than the area of the tank (see Figure 3), provisions must be made to diffuse the high velocity jets issuing from the inlet valves. This can be accomplished by using deflector plates to diffuse and direct the jets radially outward. A perforated plate can then be employed for further diffusion both axially and radially. These two elements may be all that is required to satisfy the total pressure constraint, i.e., equation 19. Equations 20 and 21 are more stringent than equation 19 and further flow control devices may be required. These would consist of honeycomb and screens with the honeycomb removing any residual swirl and the screens promoting further radial diffusion as well as a reduction in the free-stream turbulence level.

In summary, plate deflectors, perforated plates and the honeycomb and screens will be required to meet the flow quality standards of equations 19 through 23. No insurmountable problems are anticipated and the selection of a 20 ft. diameter test chamber will be an immeasurable aid in achieving good flow quality.

SECTION II

COMPRESSOR RESEARCH FACILITY

1/10 SCALE MODEL

FLOW TESTS

A. Introduction

The magnitude of the investment associated with the Compressor Research Facility dictates that all reasonable effort be taken to assure compliance with the flow quality standards discussed in Section I. Investigations have been carried out in a scale model of the facility. By selectively employing Reynolds and Mach scaling for the various flow control elements utilized in the test chamber, the aerodynamic characteristics of the Compressor Research Facility have been reproduced in the model. As a result, flow quality development testing has been carried out in the model at a nominal cost and well in advance of utilization of the full-scale facility. The rationale for the test program as well as the experimental results of these investigations are discussed in the following sections.

B. Scaling and Flow Model Tests

Fluid mechanics -- unlike nuclear physics -- does not attempt to determine the absolute values of physical constants; consequently, most experimental results can be related to flows on a different scale or in a different fluid provided they are expressed in a non-dimensional form. The dimensionless quantities are generated by dividing by a reference parameter having the same units of mass, length, time, etc. This technique or process is often called dynamic similitude. The appropriate dimensionless properties can be determined by dimensional analysis or an inspection of the governing equations of motion. The latter course is more straightforward and will be followed in this work.

Consider the flow of a fluid through a three-dimensional bounded space.

$$\rho \frac{\partial U_j}{\partial x_j} = 0 \tag{25}$$

$$\rho(\frac{\partial U_{j}}{\partial \tau} + U_{i} \frac{\partial U_{j}}{\partial x_{i}}) = -\frac{\partial p}{\partial x_{i}} + \frac{\partial^{2} U_{j}}{\partial x_{i} \partial x_{i}} - \rho \frac{\partial}{\partial x_{i}} (\tau_{ij}^{(t)})$$
 (26)

$$\rho c_{\mathbf{p}} \left(\frac{\partial t}{\partial \tau} + \mathbf{U}_{i} \frac{\partial t}{\partial \mathbf{x}_{i}} \right) = \kappa \frac{\partial^{2} t}{\partial \mathbf{x}_{i} \partial \mathbf{x}_{i}} - \frac{\partial}{\partial \mathbf{x}_{i}} \left(\mathbf{q}_{i}^{(t)} \right) + \mu \left(\phi^{(v)} + \phi^{(t)} \right)$$
(27)

where U_i denotes the velocity, t the static temperature, x_i the i-th Cartesian coordinate, p the static pressure, ρ the density, μ the absolute viscosity, C_p the specific heat, K the thermal conductivity, $T_{ij}^{(t)}$ the turbulent momentum flux, $q_i^{(t)}$ the turbulent energy flux, and $\phi^{(v)}$ and $\phi^{(t)}$ the viscous and turbulent dissipation functions. Equations 25 through 27 are derived in reference 31. Note that equations 25 through 27 are for constant property fluids and a repeated subscript indicates a summation.

Equations 25, 26, and 27 can be recast in dimensionless form by referencing all lengths to a length scale ℓ , the velocities to U_{ref} , the turbulent velocities to $\sqrt{\frac{2}{(U')^2}}$, the pressure to ρu_{ref}^2 and the temperatures to t_{ref} . This yields

$$\frac{\partial U_{j}}{\partial x_{i}} = 0 \tag{28}$$

$$\frac{\partial U_{j}}{\partial \tau} + U_{i} \frac{\partial U_{j}}{\partial x_{i}} = -\frac{\partial p}{\partial x_{i}} + \frac{1}{Re} \frac{\partial^{2} U_{j}}{\partial x_{i} \partial x_{i}} - Tu^{2} \frac{\partial \tau_{ij}}{\partial x_{j}}$$
(29)

$$\frac{\partial t}{\partial \tau} + v_i \frac{\partial t}{\partial x_i} = \frac{1}{PrRe} \frac{\partial^2 t}{\partial x_i \partial x_i} - Tu \frac{\partial q_i^{(t)}}{\partial x_i} +$$

$$\frac{1}{(\gamma-1)\operatorname{ReM}} \left[\phi^{(v)} + \operatorname{Tu}\phi^{(t)}\right] \tag{30}$$

where γ is the ratio of specific heats and all terms are now dimensionless. The derived dimensionless groups can be defined as

$$Re = \frac{\rho U_{ref}}{\mu}$$

$$Reynolds number$$

$$Pr = \frac{\mu C}{K}$$

$$Prandtl number$$

$$M^{2} = \frac{U_{ref}^{2}}{C_{p}^{t}_{ref}^{2}}$$

$$Mach number$$

$$Tu = \frac{\sqrt{(U')^{2}_{ref}}}{U_{ref}^{2}}$$

$$Turbulence level$$

An inspection of equations 28 through 30 indicates:

- The system of equations is independent of scale provided Re, Pr, M, and Tu are the same and the boundary and initial conditions are identical
- 2) Any solutions to the aforementioned equations will take the form

$$U_i = f_1(x_i, Re, Pr, M, Tu)$$

$$t = f_2(x_i, Re, Pr, M, Tu)$$
(32)

The four dimensionless groups governing dynamic similitude can be linked to specific physical processes. For example, the Reynolds number represents the ratio of inertia to viscous forces, the Prandtl number depicts heat transfer effects, the Mach number is a measure of the importance of compressibility and the turbulence level is indicative of turbulence effects. For laminar, adiabatic, low speed flows, only the Reynolds number is important. The turbulence level is of particular significance when transitional conditions are encountered, i.e., the circumstances whereby a laminar boundary layer becomes turbulent.

The actual application of the scaling process consists of maintaining a constancy of Re, Pr, M and Tu between the actual case and the model. For situations involving the same fluid -- note that there is no requirement to test both the actual unit and the model in the

same fluid -- the pressure and temperature of the gas as well as the geometric scale factor can be varied.

The Compressor Research Facility can be modeled by assuring the equivalence of Re, Pr, M, and Tu for both the full-scale and scale model unit, i.e., Re mdl = Re act, Pr mdl = Pr act, M mdl = M act, and Tu act. The Prandtl number of air is reasonably constant over a wide range of temperatures and pressures and thus, Pr mdl = Pr act provided the model uses air as the operating fluid. If the Reynolds number and Mach number for both the actual and scale unit are equated, the following relationship can be derived

$$\frac{\ell_{\text{mdl}}}{\ell_{\text{act}}} \stackrel{p_{\text{mdl}}}{p_{\text{act}}} = \left(\frac{t_{\text{mdl}}}{t_{\text{act}}}\right)^2 \left(\frac{t_{\text{act}} + 198}{t_{\text{mdl}} + 198}\right)$$
(33)

where the subscripts act and mdl denote the full-scale and scale model respectively and Sutherland's rule 32 has been used to express the viscosity as a function of temperature. Both t and t act must be expressed in R. The ratio of mass flow rates is then

$$\frac{\dot{m}_{mdl}}{\dot{n}_{act}} = \left(\frac{\ell_{mdl}}{\ell_{act}}\right)^2 \left(\frac{p_{mdl}}{p_{act}}\right) \left(\frac{t_{act}}{t_{mdl}}\right)^{1/2}$$
(34)

Equations 33 and 34 are plotted in Figures 7 and 8 where $(l_{\rm mdl}/l_{\rm act})$ has been eliminated via equation 33. For an arbitrary geometric scale factor, Figures 7 and 8 can be used to determine the temperature and/or pressure ratio once either is specified. To maintain strict scaling, the turbulence parameter must also be maintained at the same value. This poses problems since the "actual" value is frequently unknown.

Figures 7 and 8 can be employed to determine the appropriate flow parameters for the Compressor Research Facility scale model. t_{act} is approximately 50°F in this case and if t_{mdl} is also maintained at this value, then (ℓ_{mdl}/ℓ_{act}) (p_{mdl}/p_{act}) is 1. This implies that the pressure ratio is inversely proportional to the geometric scale factor. By reducing t_{mdl} relative to t_{act} , the pressure

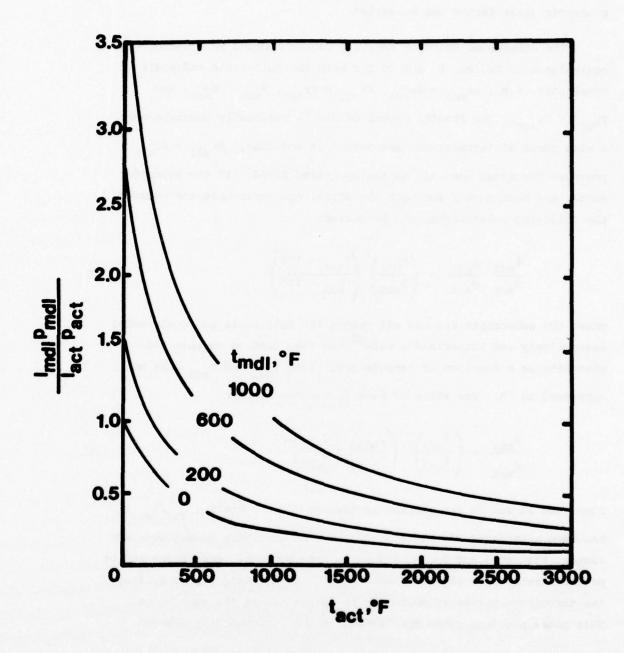


Figure 7. Geometric Scale Factor as a Function of Temperature and Pressure

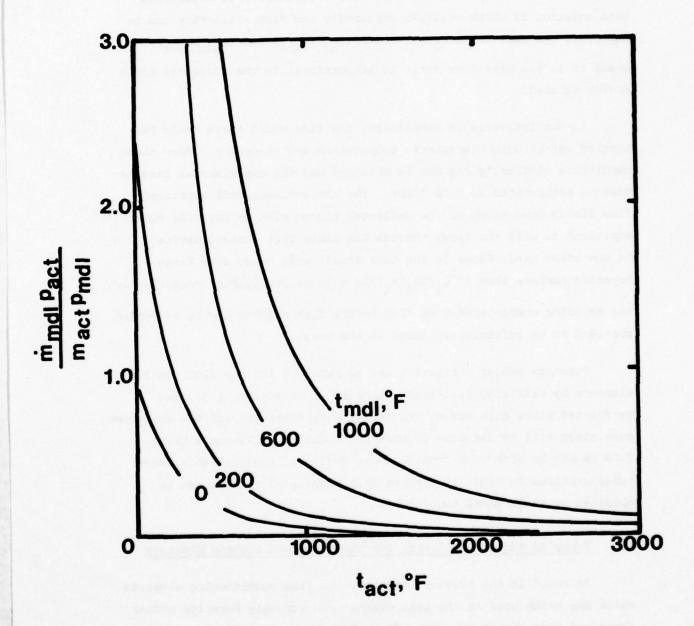


Figure 8. Scaled Mass Flow Rate as a Function of Temperature and Pressure

can be reduced. For $t_{act} = 50^{\circ}F$ and $t_{mdl} = 0^{\circ}F$, $p_{mdl}/p_{act} = 0.8808 \times (\ell_{act}/\ell_{mdl})$ and $\dot{m}_{mdl}/\dot{m}_{act}$ is 0.9134 (p_{act}/p_{mdl}) or 1.037 (ℓ_{mdl}/ℓ_{act}) . In either case, substantial pressure ratios are required to compensate for geometric scaling. If Reynolds number similarity is neglected, then equation 34 which utilizes continuity and Mach similarity can be employed. In this instance with both (p_{mdl}/p_{act}) and (t_{mdl}/t_{act}) equal to 1, the mass flow ratio is proportional to the geometric scale factor squared.

In the interests of simplicity, the flow model tests could be carried out at both atmospheric temperature and pressure. Under these conditions similarity can not be obtained and the experimental results must be interpreted in this light. The three-dimensional separated flow fields downstream of the deflector plates will be Reynolds number dependent as will the flows through the other flow control devices. On the other hand, flows in the tank itself will be at such large Reynolds numbers that $(\partial^2 \mathbf{U}_j/\partial \mathbf{x}_j \partial \mathbf{x}_j)/\mathrm{Re}$ will be negligible; consequently, the Reynolds number effect on flow in the test chamber can be neglected provided Re is sufficiently large in the model.

Reynolds number similarity can be obtained for the flow control elements by utilizing full-scale geometry in this case, i.e., the perforated plate hole sizes, the screen wire diameters and the honeycomb core sizes will be the same in both the model and full-scale tests. This cannot be done with regard to the deflector plates. With these considerations in mind, it appears that meaningful results can be obtained by scale model testing.

C. Reynolds Number Similarity for the Flow Conditioning Elements

As noted in the previous section, the flow conditioning elements which are being used in the test chamber are strongly Reynolds number dependent even though the gross flow through the tank itself is independent of the Reynolds number. In particular, the pressure loss in screens and honeycombs is a function of the wire Reynolds number, $\mathrm{Ud}_{\mathbf{S}}\rho/\zeta\mu$,

and the open area ratio , $(1-d_s/l_s)^2$. The screen drag coefficient, k can be written as $\Delta p/\frac{1}{2} \rho U$ and

$$\zeta^2 k/(1-\zeta) = 9Re_s^{-0.4}$$
 50 < Re_s < 200 (35)

$$\zeta^2 k/(1-\zeta) = 6.5 \text{ Re}_x^{-1/3} \quad 60 < \text{Re}_x < 600$$
 (36)

Equation (35) is given in reference 33 and equation (36) is presented in reference 34.

It has also been shown 35 that $\left(U'\right)^2$ and $\left(V'\right)^2$ can be reduced to about 0.15 and 0.30 of their initial values for k=2. As a consequence, both the screen pressure loss, the reduction in mean flow spatial variations and the reduction in turbulence levels is a function of screen Reynolds number and open area ratio. Similar relationships hold for honeycomb and perforated plates.

When the local screen Reynolds number exceeds about 80, the screen wire rakes will become turbulent. The turbulence is of a very small spatial scale and decays fairly rapidly -- about 500 wire diameters are sufficient for complete decay of the turbulence in most cases. This implies that both $\overline{(u^i)}^2$ and $\overline{(v^i)}^2$ are functions of x/d_s where x is the axial distance and d_s is the screen wire diameters. It thus follows that

$$k = \phi_1(Re_s, \zeta)$$

$$\frac{\Delta U}{U} = \phi_2(Re_s, \zeta)$$

$$\frac{\Delta (U')^2}{U^2} = \phi_3(Re_s, \zeta, \frac{x}{d_s})$$

$$\frac{\Delta (V')^2}{U^2} = \phi_4(Re_x, \zeta, \frac{x}{d_s})$$
(37)

where ϕ , denotes a functional dependence.

Equations (37) imply that Re_g , ζ , and x/d_g must be maintained at the same value for both the 1/10 scale model and the facility if dynamic similarity is to be obtained for the flow control elements. Mach similarity implies that

$$\mathbf{U}_{\mathbf{mdl}} = \mathbf{U}_{\mathbf{act}} \tag{38}$$

since t_{mdl} = t_{act} and thus the flow control elements, i.e., screens and honeycomb, must be geometrically the same in both cases. Note that the axial spacing between flow control elements must be equivalent to the full-size values. Since x/d_s will be 10 times the scale model values in the full-scale facility, turbulence damping should exceed the values obtained in the scale model and, thus, the scale model results do offer a degree of conservatism.

D. The Flow Model Configuration

The overall flow model is shown in Figure 9. Air flow is from left to right entering the 1/10 scale model through the five control valves. The flow model itself was fabricated by the Cadre Corporation in conjunction with an evaluation of air ejectors for use in the auxiliary air system. The ejectors and related items have now been removed with the model serving as a vehicle for flow quality studies.

The pressure level in the test chamber is controlled with the five inlet valves shown in Figure 10. The valves are scheduled to open and close as a function of both air flow rate and test chamber pressure level. Experiments have been carried out using the valve scheduling sequence of Table 4. The valve location and jet deflector geometry is shown in Figure 11.

The mass flow rate through the test chamber is controlled by means of the valve assembly of Figure 12. The test chamber pressure as well as the mass flow rate are monitored on the gauge unit which is

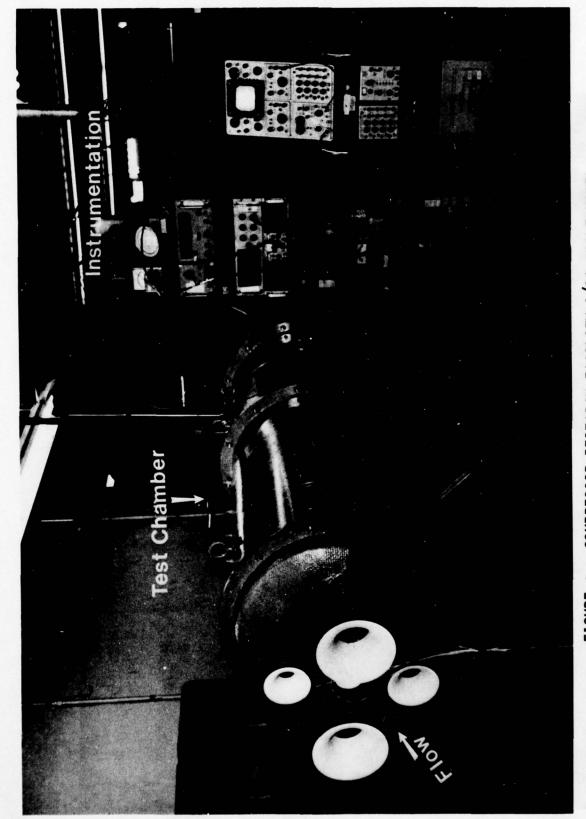


FIGURE 9. COMPRESSOR RESEARCH FACILITY 1/10 SCALE MODEL

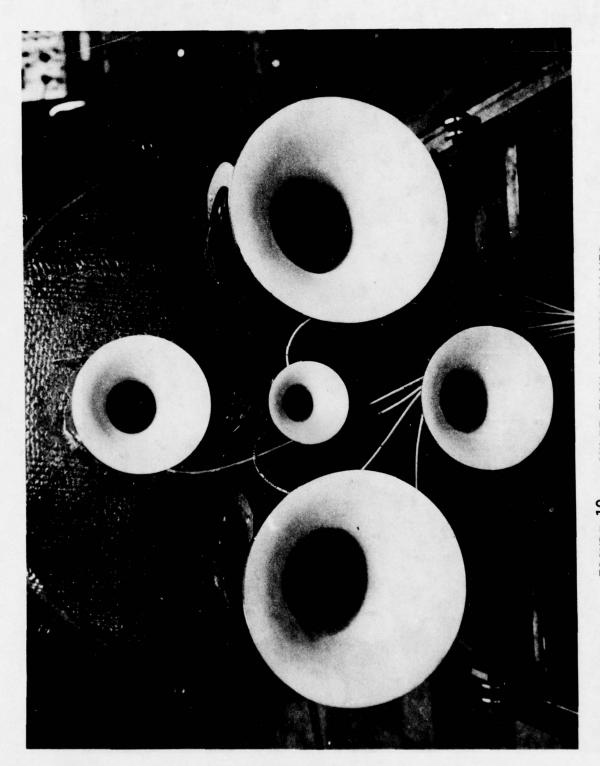


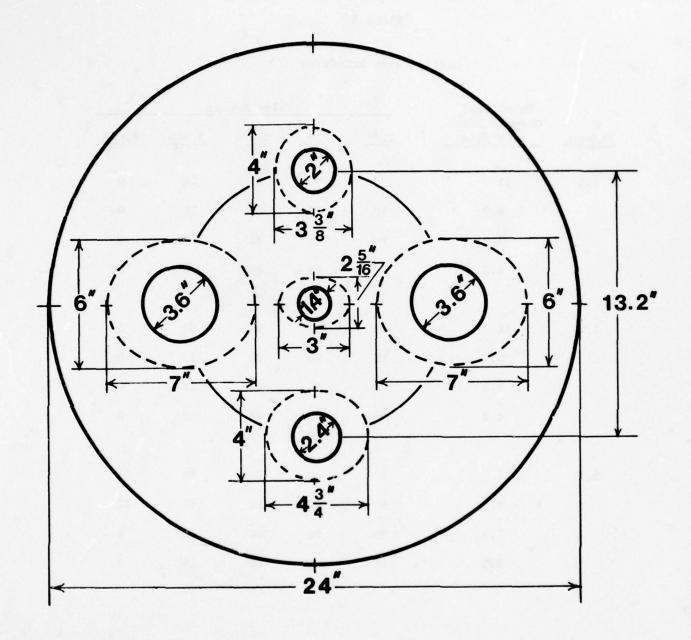
FIGURE 10. INLET FLOW CONTROL VALVES

TABLE 4

Design Valve Schedules

	Total Test Chamber Pres- sure psia	Valve Angles					
W lb/sec.		1.4"	2.0"	2.4"	3.6"L	3.6"R	
2.5	11	90*	90	71	26	o*	
	9.8	90	90	61	16	0	
	7.3	90	85	40	0	0	
	4.3	90	61	16	0	0	
3.5	11	90	90	90	50	5	
	9.8	90	90	80	35	0	
	7.3	90	90	62	17	0	
	4.3	90	76	31	0	0	
5.5	11	90	90	90	79	34	
	9.8	90	90	90	67	22	
	7.3	90	90	90	46	1	
	4.3	90	90	60	15	0	

^{* 90°} denotes the fully-open condition while 0° represents a fully-closed configuration.



COMPRESSOR RESEARCH FACILITY 1/10 SCALE MODEL SHOWING JET DEFLECTOR LOCATIONS

Figure 11. Test Chamber Jet Deflectors

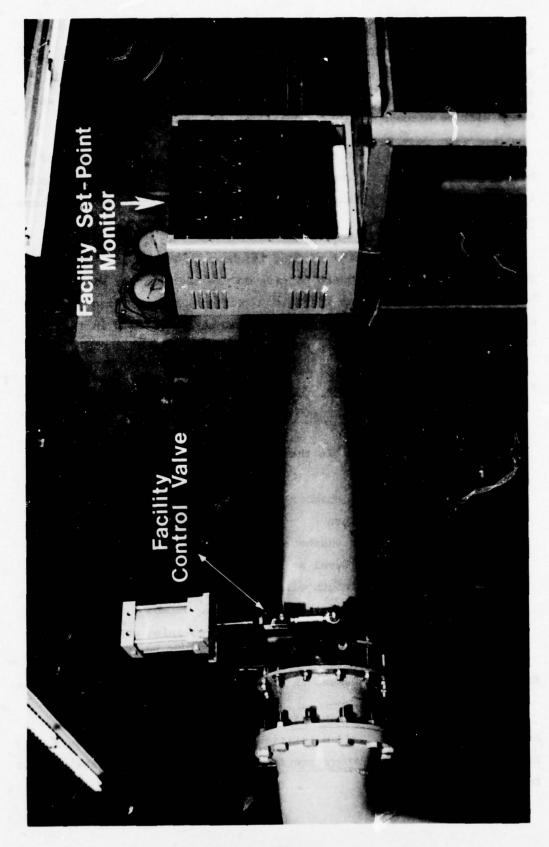


Figure 12. Facility Control and Monitoring System

also shown in Figure 12. The mass flow rate is measured by means of a sharp-edged orifice which is located behind the instrument panel. A number of redundant mass flow rate measurements are carried out and these will be discussed in more detail in Section II.G.

The compressor inlet flow field is simulated using a series of bellmouths. The J-79 bellmouth installed in the test chamber is shown in Figure 13. Two additional bellmouths have been fabricated and these are shown in Figure 14.

A typical flow control element is shown in Figure 15. This photograph depicts the forward portion of the test chamber with a honeycomb flow straightener installed. Screens, a perforated plate and core busters or deflector plates are or have been used in the test chamber to eliminate flow non-uniformities.

E. Measurements within the Compressor Research Facility 1/10 Scale Model

The measurements made in the 1/10 scale model consisted of:

- (i) The test chamber wall static pressure and total temperature
- (ii) The test chamber total pressure, velocity, and turbulence level at selected axial stations
- (iii) The bellmouth wall static pressure and total pressure distribution
- (iv) The orifice total temperature, inlet pressure and pressure drop.

Each of these will be discussed in more detail in the ensuing paragraphs.

The test chamber total temperature probe is shown in Figure 13. As a result of the low fluid velocities and relatively low pressure losses, the tank total temperature is approximately equal to the ambient temperature.

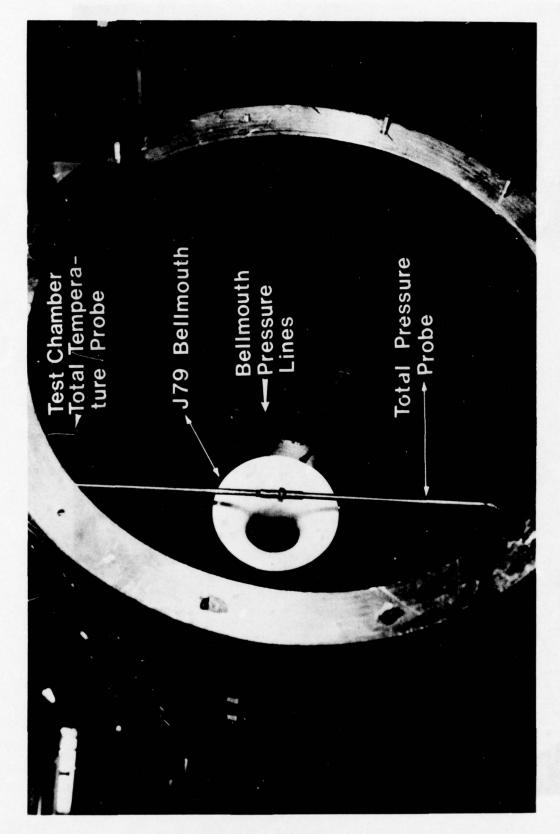


Figure 13. Compressor Bellmouth Installed in the Test Chamber

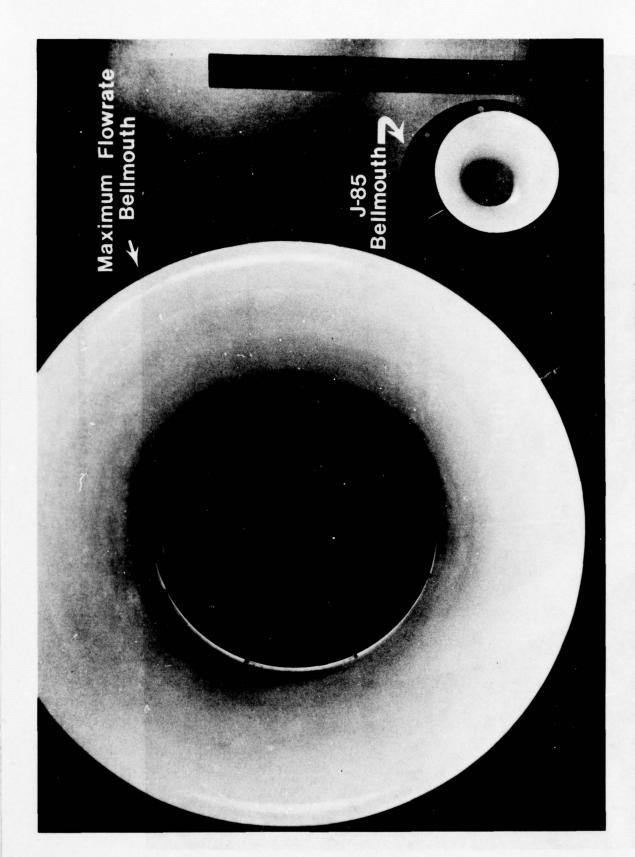


Figure 14. J-85 and Maximum Flowrate Bellmouths

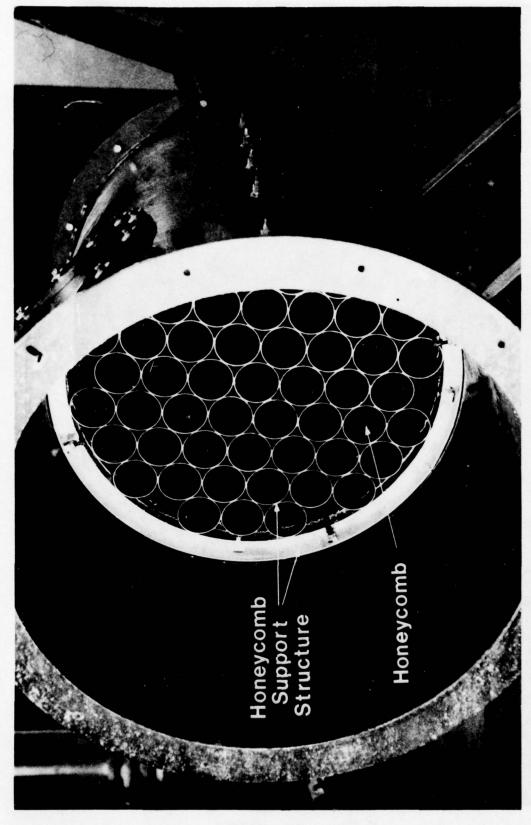


Figure 15. Forward Portion of Test Chamber Showing a Honeycomb Flow Straightener.

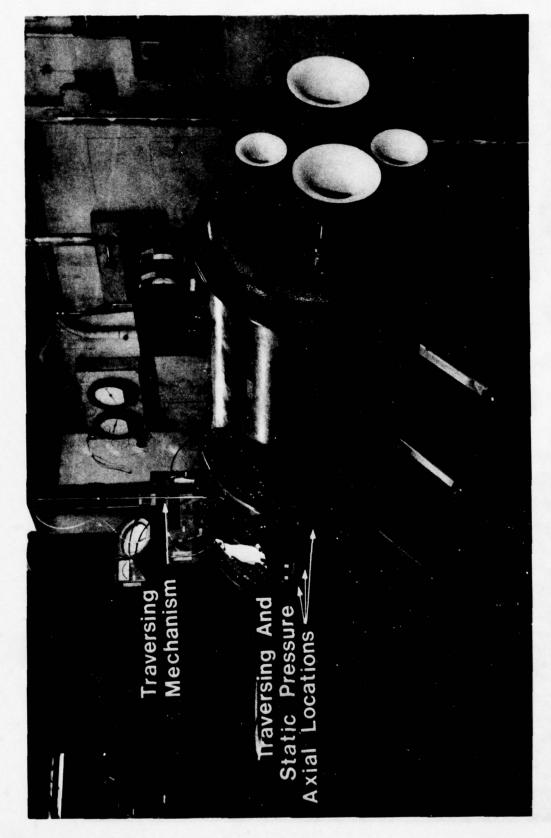


Figure 16. Test Chamber Axial Measurement Stations

The test chamber wall static pressures are measured at selected axial and circumferential locations corresponding to the total pressure and velocity measurements. In particular, three axial locations were chosen — one compressor diameter downstream of the appropriate bell—mouth. Four circumferential locations were chosen consisting of the 0°, 90°, 180°, and 270° positions. By assuming that the static pressure was uniform across the test chamber, i.e., the mean of the four circumferential values, the measured total pressure could be used to compute the velocity distribution. In a similar manner, the measured velocities and static pressure could be employed to determine the total pressure. The traversing and static pressure axial locations are shown in Figure 16.

The test chamber velocity and turbulence level were measured using a hot wire anemometer. The sensor was moved across the test chamber in the radial direction using a traversing mechanism. The locations of the traverse planes relative to the inlet valves are shown in Figure 17.

The hot wire anemometer probe is shown installed in the test chamber in Figure 18. The probe is supported from both ends to minimize flow distortion. In this instance, the radial traverse is carried out in the vertical direction. Mounting pads for the traversing mechanism are also located on the horizontal axis and traverses were also carried out in this direction.

The bellmouths were instrumented with total and static pressure probes so that the appropriate distortion factors could be ascertained. The J-79 model bellmouth with the total pressure rakes installed is shown in Figure 19. Because of the rather limited throat area, only four circumferential stations were employed in this case. This yielded a probe blockage value of 3.6% which is considered acceptable. The radial location of the rake elements relative to both the bellmouth wall and center-line is shown in Figure 20. Note that the rakes were located at the centroids of equal area segments.

The largest bellmouth, i.e., sized to accommodate the maximum facility flow rate, is shown in Figure 21. In this case eight circumferential locations were employed resulting in a probe blockage value of 1.9%.

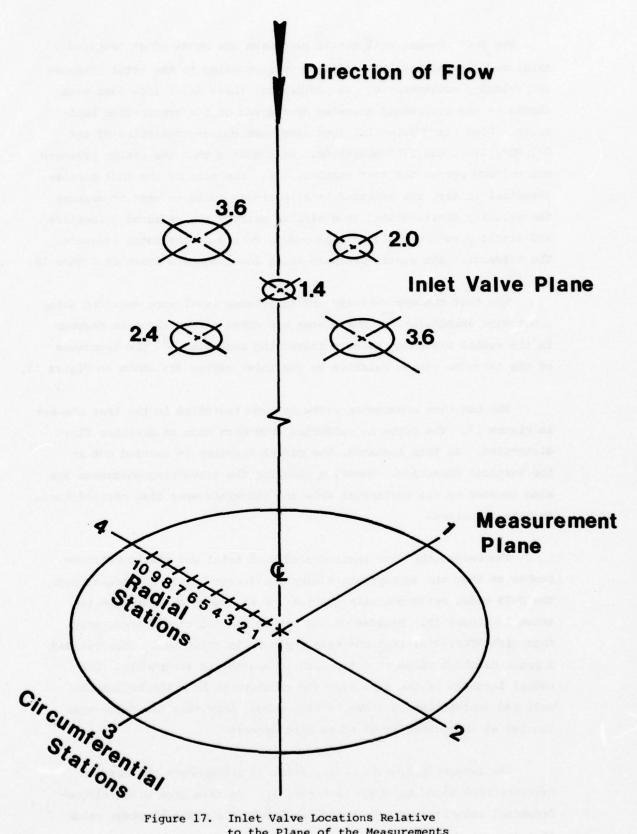


Figure 17. Inlet Valve Locations Relative to the Plane of the Measurements

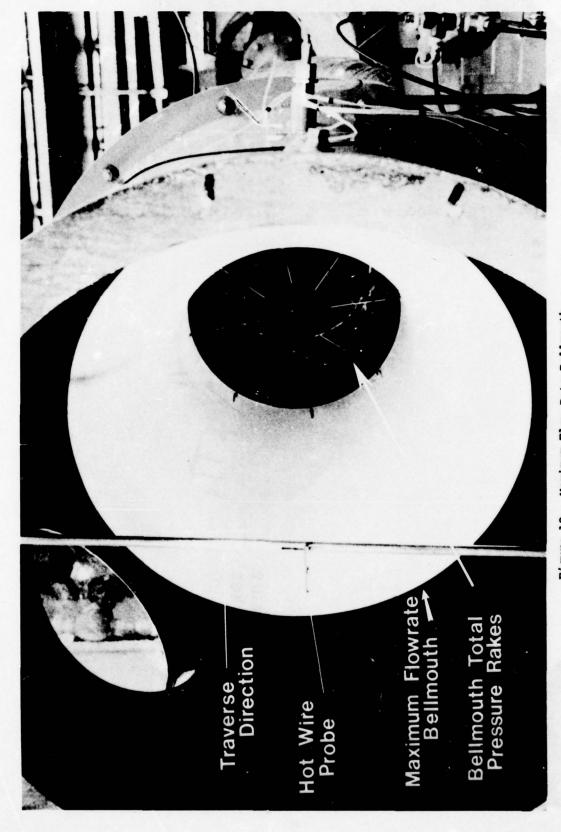


Figure 18. Maximum Flow Rate Bellmouth Installed in the Test Chamber

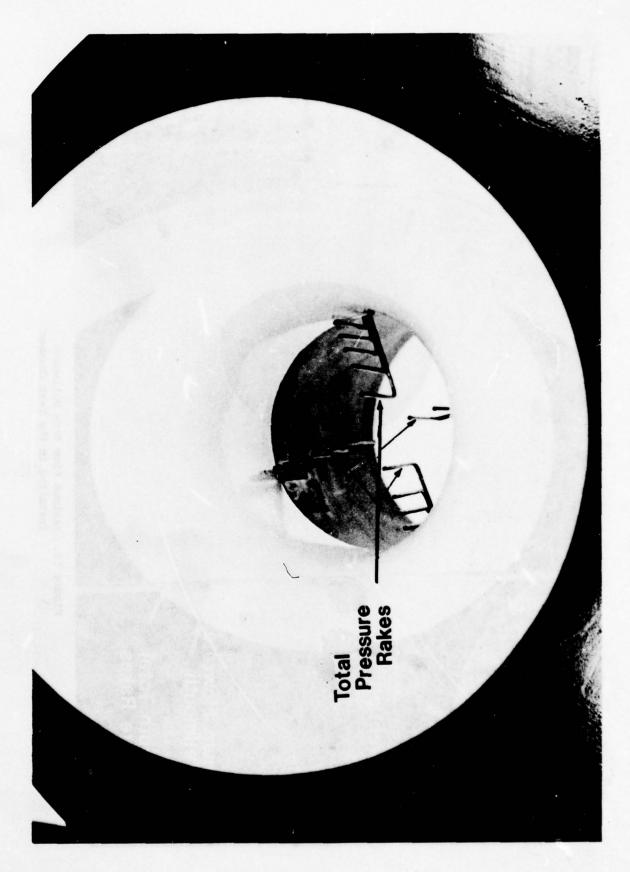
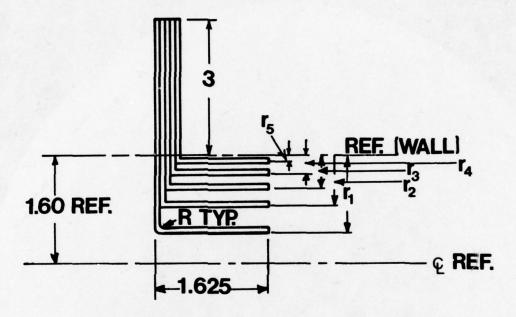


Figure 19. J79 Model Bellmouth with the Total Pressure Rakes

PRESSURE RAKE - TYPE I



 $r_1 = 1.123$

= .728

 $r_3 = .471$ $r_4 = .263$ $r_5 = .083$ r = 1/16 MIN.

MAT'L = 304 STN. STL

TUBING .065 O.D.

x .009 WALL

NO. REQ'D: 4

NOTES:

I. CU-BRAZE OR SILVER SOLDER

> Figure 20. J79 Model Bellmouth Total Head Tube Radial Locations

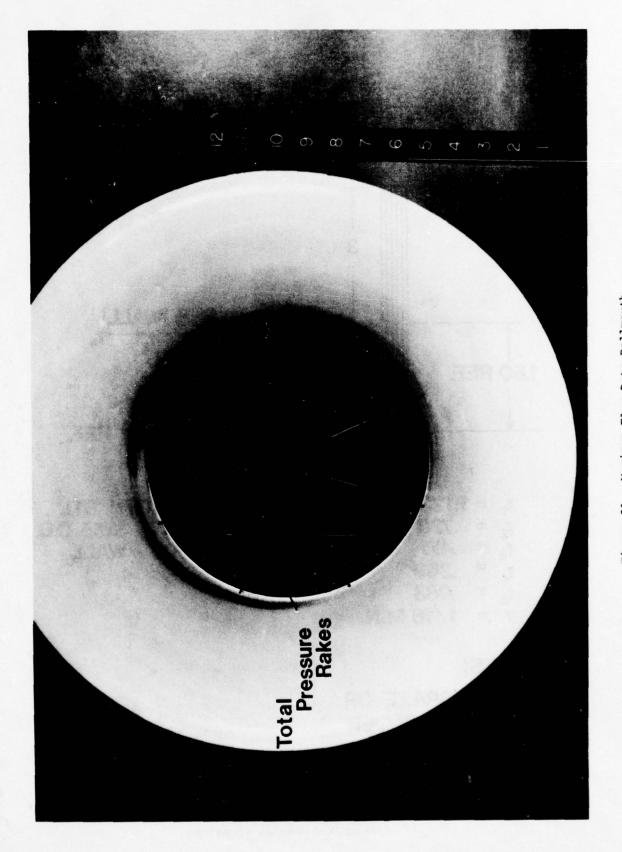


Figure 21. Maximum Flow Rate Bellmouth with Total Pressure Rakes

The radial locations of the individual total head tubes are shown in Figure 22. Wall static pressures are located adjacent to each of the total pressure rakes for both the instrumented bellmouths.

F. Instrumentation Systems for the Compressor Research Facility 1/10
Scale Model

The measurements carried out in the 1/10 scale model fall into three categories:

- (i) Steady-state pressures
- (ii) Steady-state temperatures
- (iii) Time-dependent and/or fluctuating velocities
 Each of the above were measured using different and/or independent techniques.

The steady-state pressures -- both totals and statics -- were measured using a rotary valve/pressure transducer unit. Two of these units were employed yielding a 128 channel measuring capability. Every other channel was supplied with a near vacuum pressure resulting in 64 active channels or 32 active channels per unit. Each unit employs a single strain gauge bonded pressure transducer which can be calibrated while installed in the unit. In particular, three known pressures, i.e., atmospheric, near vacuum, and sub-atmospheric, were supplied and the resulting voltages measured. The two sets of values were used to determine the calibration coefficients during the course of the experiment. The Scanivalve unit as described above is shown in Figure 23.

The channel selection process is governed by a Scanivalve controller. The controller not only activates the rotary valve mechanism, but it also indicates the selected channel. The transducers are both energized and conditioned by the power supplies and signal conditioning elements which are also shown in Figure 23. The transducer output was measured with the uppermost integrating digital valtmeter. The lower digital voltmeter was used for monitoring power supply voltage levels.

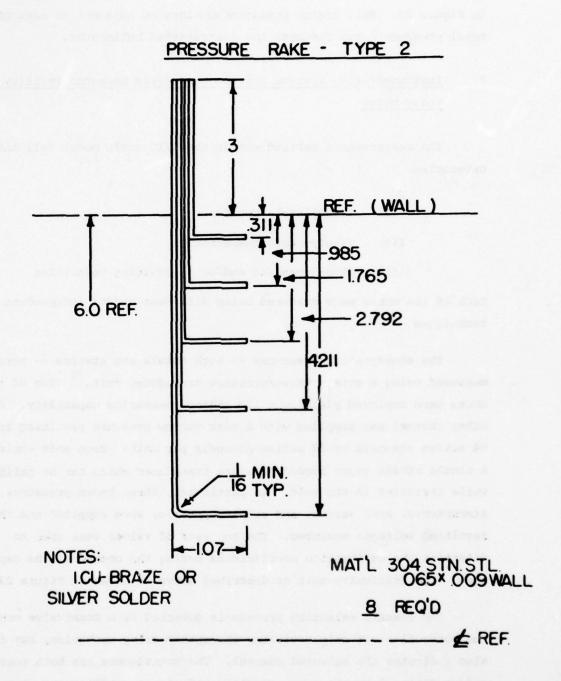


Figure 22. Maximum Flow Rate Bellmouth Total Head Tube Radial Locations

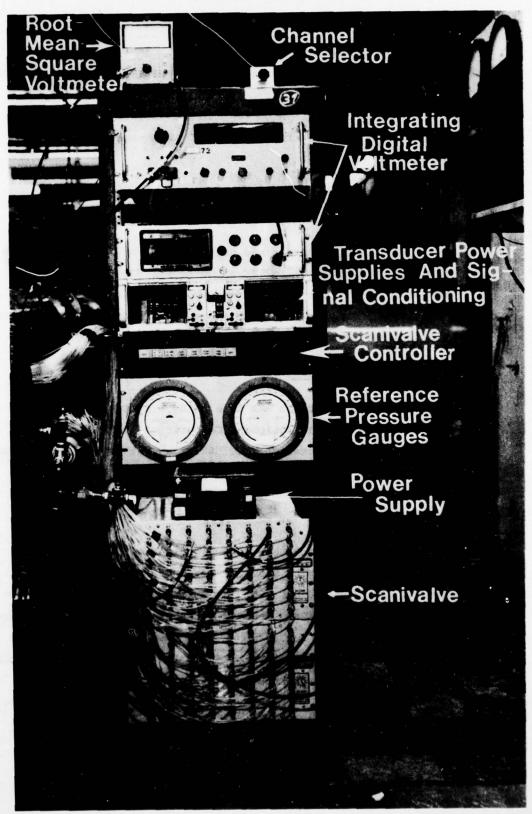


Figure 23. Pressure Instrumentation Systems

The hot wire anemometry system ³⁷ is shown in Figure 24. These units consist of a constant temperature anemometer, a signal conditioner, a linearizer, a power supply, an integrating digital voltmeter and a root-mean-square voltmeter. When maximum accuracy was required, the integrating digital voltmeters of Figure 23 were employed.

G. Data Reduction

1. <u>Introduction</u>

All data processing was done off-line using Indiana University or Indianapolis Center for Advanced Research computer systems. The raw data was recorded by hand and then transferred to computer cards. These were then processed with all calibrations, computations and plotting performed by the computer.

2. Computer Systems

The data reduction was done using a system of computers composed of a Digital Equipment Corporation (DEC) System 10, a Control Data Corporation (CDC) 6600, an International Business Machine (IBM) 370, and a DEC 11/70. The DEC-10 serves as both an independently functioning time sharing system as well as an input/output link to the batch oriented CDC 6600.

The DEC-10 is capable of supporting a large number of users in a time-sharing mode while concurrently manipulating data to and from the CDC 6600. Available peripheral units consisted of a card reader, magnetic tape drives, disc drives, line printer, paper tape reader/punch, a Calcomp compatible plotter and a Versatec dot-matrix printer/plotter. As a point in passing, the final data plots were generated using the latter device. Unlike Calcomp-type plotters, the Versatec does not draw lines, but rather deposits patterns of dots, 150 per inch, to form characters and drawings with superb resolution.

Calibration of Pressure Transducers

The pressure transducers were calibrated on-line as

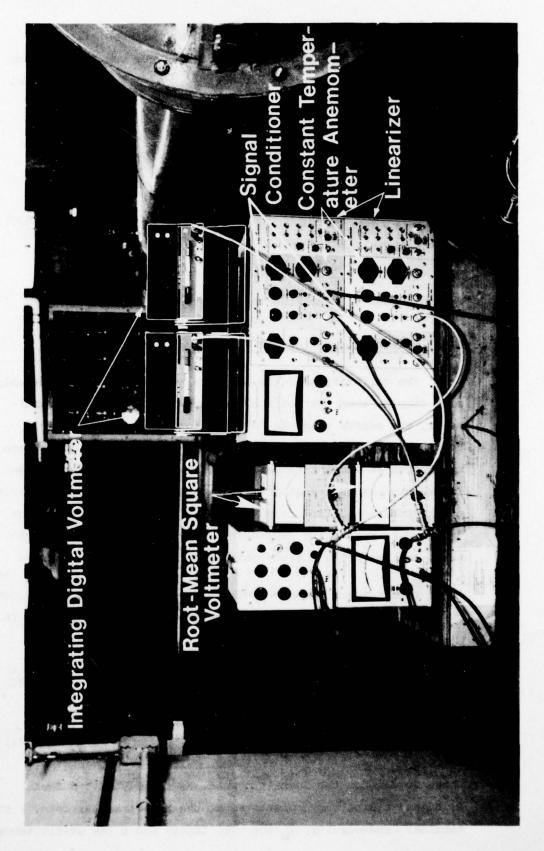


Figure 24. Hot Wire Anemometry System

described in Section II.F. Three known pressures, i.e., atmospheric, near vacuum and intermediate, were supplied to each transducer and the voltage outputs measured. This information in conjunction with

$$c = \frac{1}{2} \left\{ \frac{P_{\text{cal}_1} - P_{\text{cal}_2}}{E_{\text{cal}_1} - E_{\text{cal}_2}} + \frac{P_{\text{cal}_1} - P_{\text{cal}_3}}{E_{\text{cal}_1} - E_{\text{cal}_3}} \right\}$$
(39)

$$p = C(E - E_{cal_1}) + P_{cal_1}$$

was then used to determine the pressures p.

4. Calibration of the Hot Wire Anemometer

The calibration of the hot wire anemometer is considerably more complex than that of the pressure transducers. In particular, the sensor responds to variations in fluid velocity, temperature, and pressure or density. The hot wire probes were calibrated at ambient temperatures and pressures; however, the Compressor Research Facility 1/10 scale model testing was carried out at subatmospheric pressures and this must be accounted for in the data processing procedures. Temperature variations between calibration and test conditions must also be reconciled.

Both temperature and pressure variations can be determined by means of the relationships of references 40, 41, and 42. In particular,

$$Nu\left(\frac{t_{m}}{t_{f}}\right)^{-0.17} = A + B Re^{n}$$
 (40)

and

and

$$Nu = \frac{H_f/\ell_w}{\pi K_f(t_w - t_f)}$$
 (41)

where Nu denotes the Nusselt number, Re the Reynolds number, A, B, and n arbitrary constants, H_f the heat transfer rate, K the terminal conductivity, ℓ_{t} the wire length and t the static temperature.

Note that $t_m = \frac{1}{2} (t_w + t_f)$. The Reynolds number is

$$Re = \frac{\rho_f U_f d_w}{\mu_f}$$

with the fluid properties K_f , ρ_f and μ_f evaluated at t_m and the static pressure p. ρ and μ represent the density and viscosity respectively.

Figures 25, 26, and 27 illustrate calibration data obtained during the course of this investigation. Figure 25 shows the variation of $\mathrm{Nu(t_m/t_f)}^{-0.17}$ with Re while Figure 26 employs $\mathrm{Re^n}$ with $\mathrm{n} = 0.45$ as suggested by Collis and Williams. Note that the relationship of equation (40) adequately represents the data except for a few of the lower Reynolds number points. The empirical constants, A, B, and n are tabulated in Table 5 and agree fairly well with the values presented in reference 41 with the exception of A which is highly probe dependent.

Equation (40) is restricted to forced convection conditions and thus is valid only when

$$Re > 2Gr^{1/3} \tag{42}$$

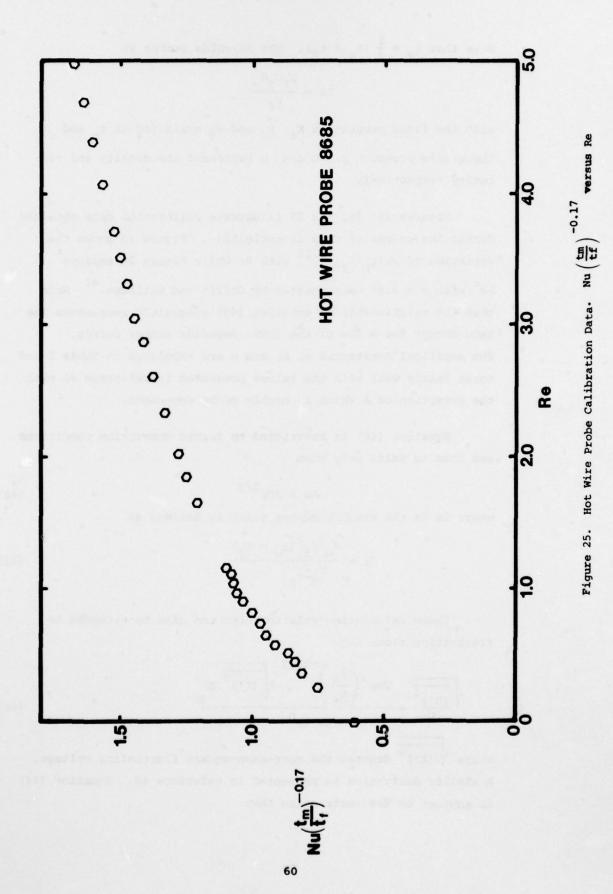
where Gr is the Grashof number which is defined as

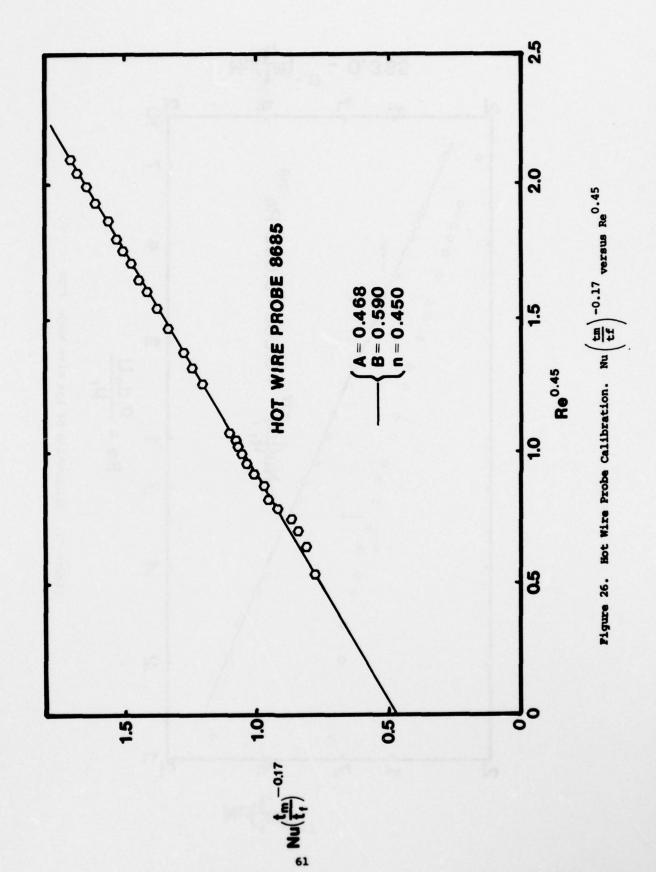
$$Gr = \frac{d_w^3 \rho_f^2 (t_w - t_f)}{\mu_f^2 t_f}$$
 (43)

These calibration relationships can also be extended to fluctuating flows and

$$\sqrt{\frac{\left(U'\right)^{2}}{U}} = \frac{2Nu \left(\frac{t_{m}}{t_{f}}\right)^{-0.17} \sqrt{\overline{\left(E'\right)^{2}}/E}}{nB Re^{n}}$$
(44)

where $\sqrt{(E')^2}$ denotes the root-mean-square fluctuating voltage. A similar derivation is presented in reference 42. Equation (44) is subject to the restriction that





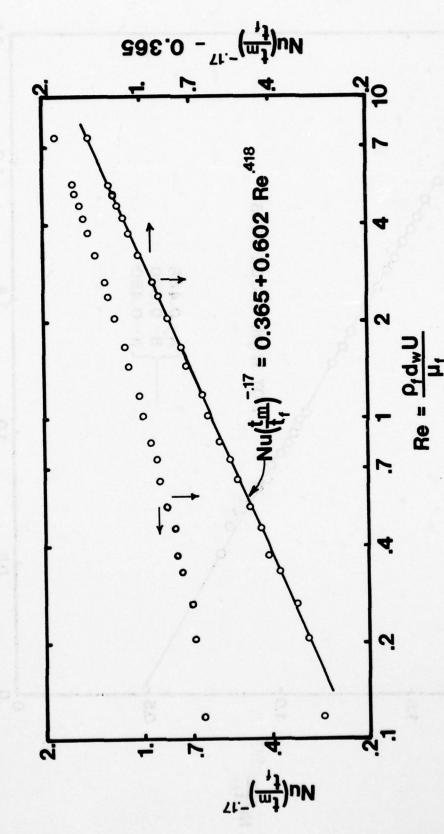


Figure 27. Calibration of Hot Wire Probe 8709

TABLE 5

CALIBRATION CONSTANTS OF HOT WIRE PROBES

	/t \	17				
Nu	Te	17	-	A	+	BRen
	/ 1/					

	\ /		
Probe Number	<u>A</u>	<u>B</u>	<u>n</u>
8477	.404	.756	.420
8709	.365	.602	.418
8710	.519	.516	.440
A766	.316	.616	. 382
B052	.386	.597	.432
B056	.695	1.292	. 392
B057	.304	.632	. 386
B060	.325	.644	.402
В63	.291	.502	. 396
B64	.433	.611	.414
8685	.470	.590	.450
8479	.430	.560	.450
Collis and Williams 41	.240	.560	.450

$$\frac{\text{Nu}\left(\frac{t_{\text{m}}}{t_{\text{f}}}\right)^{-0.17}\sqrt{(E')^{2}}}{\text{Nu}\left(\frac{t_{\text{m}}}{t_{\text{f}}}\right)^{-0.17}} < < 1$$
(45)

which is generally satisfied even for high turbulence levels. Note that the overbar denotes a time-averaged property, i.e.,

$$\overline{\phi^2} = \lim_{T \to \infty} \frac{1}{2T} \int_{\tau - T}^{\tau + T} \phi^2 d\tau \tag{46}$$

5. Calculation of Total Pressure

Since the velocities are measured in the test chamber and the total pressures in the compressor bellmouths, analytic relationships were used to calculate either the total pressure or the velocity. Following convention,

$$P = p + \frac{1}{2} \rho (U^2)$$

The bellmouth velocities were computed via

$$M^2 = \frac{2}{\gamma - 1} \left\{ \left(\frac{P}{P} \right)^{\frac{\gamma - 1}{\gamma}} - 1 \right\} = \frac{U^2}{\gamma Rt}$$
 (47)

where only mean values were considered.

6. Mass Flow Rates

Mass flow rates have been computed at three locations in the test chamber. These computations were carried out to both determine the test chamber operating point and serve as a guide to the data accuracy. The test chamber and bellmouth mass flow rates were computed from

$$\dot{m}_{i} = \int_{A} \int \rho_{i} U_{i} dA \tag{48}$$

with the orifice mass flow rate defined as

$$\dot{m}_5 = 75.551 \ d^2 \ Y_1 F_a K_f \sqrt{\rho (p_5 - p_6)}$$
 (49)

where d is the orifice diameter in ft , ρ is the fluid density at p_5 and t_5 in lb_m/ft^3 , p_5 and p_6 are the orifice upstream and downstream pressures in lb_f/in^2 and F_a is the orifice thermal expansion factor. K_f and Y_1 are the flow coefficient and expansion factor respectively. The expansion factor, Y_1 can be related to the orifice geometry and pressure drop via

$$Y_1 = 1 - (0.410 + 0.350 dr^4) \frac{\Delta P/P_1}{Y}$$
 (50)

which is valid for "flange taps", i.e., static pressure ports located in the flanges immediately adjacent to the square-edged, concentric orifice. 43

The flow coefficient can likewise be expressed in terms of the flow area, orifice geometry and Reynolds number, Re. For an installation using flange taps, K_f can be written as

$$\kappa_{f} = \kappa_{0} \left(1 + \frac{\alpha}{Re_{d}} \right) \tag{51}$$

$$\kappa_0 = \kappa_e \left(\frac{10^6 d}{10^6 d + 150} \right)$$
 (52)

$$K_e = 0.5993 + \frac{0.007}{D} + (0.364 + \frac{0.076}{\sqrt{D}}) dr^4 +$$

$$0.4(1.6 - \frac{1}{D})^5$$
 [(0.07 + $\frac{0.5}{D}$) - dr]^{5/2} -

$$(0.009 + \frac{0.034}{D})$$
 $(0.5 - dr)^{3/2}$ +

$$(\frac{65}{p^2} + 3) (dr - 0.7)^{5/2}$$
 (53)

$$\alpha = d(830 - 5000dr + 9000dr^2 - 4200dr^3 + \frac{530}{\sqrt{D}})$$
 (54)

where both d and D are expressed in inches and represent the orifice and pipe diameter respectively - dr = d/D. If any of

the last three terms in equation (53) produce an imaginary number, then that term is set to zero.

Note that Re can be written as

$$Re_{d} = \frac{4\dot{m}}{\pi d\mu}$$
 (55)

which produces an iterative solution, in that, $\mathring{\mathbf{m}}$ must be prescribed to define $\mathrm{Re}_{\mathring{\mathbf{d}}}$ which is in turn used in the calculation of $\mathrm{K}_{\mathring{\mathbf{f}}}$ and then $\mathring{\mathbf{m}}$. In practice, this process converges very rapidly.

7. Flow Quality Parameters

A series of flow quality parameters were reviewed in depth in Section I. All of these were computed during the course of the data reduction process; however, in the interest of consistency and conformance to standard practice, a profile variation factor was defined as

$$\sigma_{\phi} = \left\{ \frac{1}{A\phi_{\text{mean}}^2} \int_{A} \int (\phi - \phi_{\text{mean}})^2 dA \right\}^{1/2}$$
 (56)

where

$$\phi_{\text{mean}} = \frac{1}{A} \int_{A} \int \phi dA$$

Equation (56) minimizes the weighting of a few extreme points when compared to

$$\frac{\phi_{\max} - \phi_{\min}}{\phi_{\text{mean}}}$$

and yields values which are more representative of the property profile as a whole. As a result, the parameters of equation (56) were relied upon to characterize the profile variations.

8. Data Reduction Computer Program

The program embodying these concepts, as well as, various data plotting techniques, is presented in reference 43.

H. Testing of the Baseline Configuration

1. Introduction

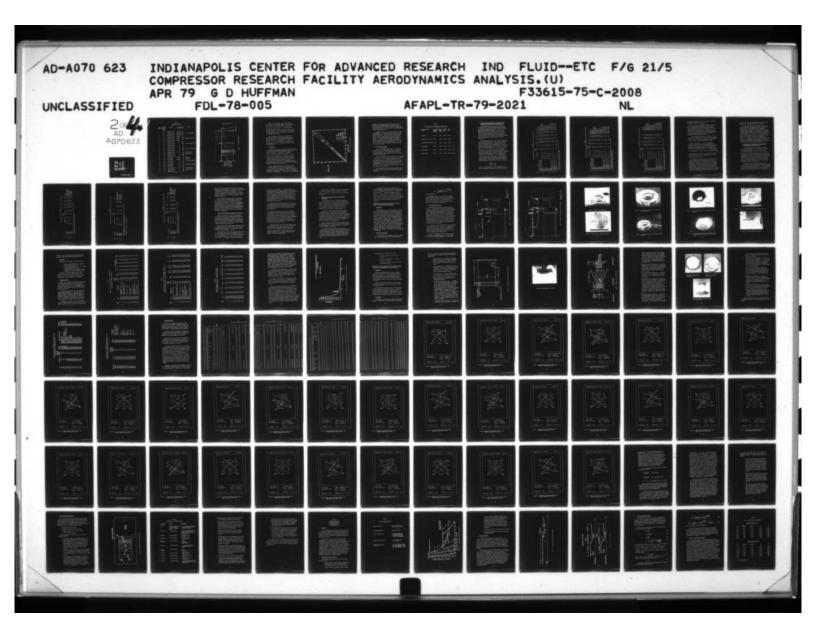
The overall objectives of the test program were:

- (i) To determine the flow quality and/or aerodynamic characteristics of the test chamber for a series of operating conditions
- (ii) To evaluate the performance of the various flow conditioning elements at representative operating points.

The characteristics of the baseline configuration are reviewed in this section.

2. Test Program

The test program is outlined in Table 6. Experiments were generally conducted in groups of threes with the first series of tests carried out with the inlet valves and bulkhead removed. This sequence of tests was to function as a baseline and the valve created flow disturbances. The second group of three tests, i.e., runs 4, 5, and 6, simulated the configuration of fully open valves. Tests 7, 8, and 9 utilized a tank pressure of 6.8 lb_f/in² and, thus, a valve Mach number of approximately 1. Tests 10, 11, and 12 were conducted at as low a test chamber pressure as possible subject to the limitations of the exhauster system. This resulted in pressures of approximately 3.8 lb_f/in² and valve Mach numbers of 1.5. Tests 1 through 12 employed all the available flow conditioning elements, i.e., jet deflectors, flow straightener, perforated plate, and screens. These elements and their axial locations are shown in Figure 28.



20F AD A070623



NATIONAL BUREAU OF STANDARDS MICROCOPY RESOLUTION TEST CHART

TABLE 6
BASELINE TEST PROGRAM

Test Number	Corrected Mass Flow Rate lb /sec	Bellmouth	Test Chamber Pressure, lb _f /in ²	Comments
1	7.50	Maximum Flow Rate	Atmospheric)	
2	5.63	Maximum Flow Rate	Atmospheric	Inlet Valves Removed
3	3.75	Maximum Flow Rate	Atmospheric	
4	7.50	Maximum Flow Rate	Maximum	
5	5.63	Maximum Flow Rate	Maximum	Atmospheric Simulation
6	3.75	Maximum Flow Rate	Maximum	
7	7.50	Maximum Flow Rate	6.8	
8	5.63	Maximum Flow Rate	6.8	Inlet Valves Transonic
9	3.75	Maximum Flow Rate	6.8	
10	7.50	Maximum Flow Rate	3.8	
11	5.63	Maximum Flow Rate	3.8	Inlet Valves Supersonic
12	3.75	Maximum Flow Rate	3.8	
13	7.50	Maximum Flow Rate	3.8	Flow Conditioning
14	7.50	Maximum Flow Rate	3.8	Elements Removed
15	7.50	Maximum Flow Rate	3.8	
16	1.70	J79 Bellmouth	Maximum }	Atmospheric
17	1.30	J79 Bellmouth	Maximum	Simulation
18	1.70	J79 Bellmouth	6.8	Inlet Valves Transonic
19	1.30	J79 Bellmouth	6.8	
20	1.70	J79 Bellmouth	3.8	Inlet Valves Supersonic
21	1.30	J79 Bellmouth	3.8	
22	5.63	Maximum Flow Rate	3.8	Flow Conditioning
23	5.63	Maximum Flow Rate	3.8	Elements Removed
24	5.63	Maximum Flow Rate	3.8	

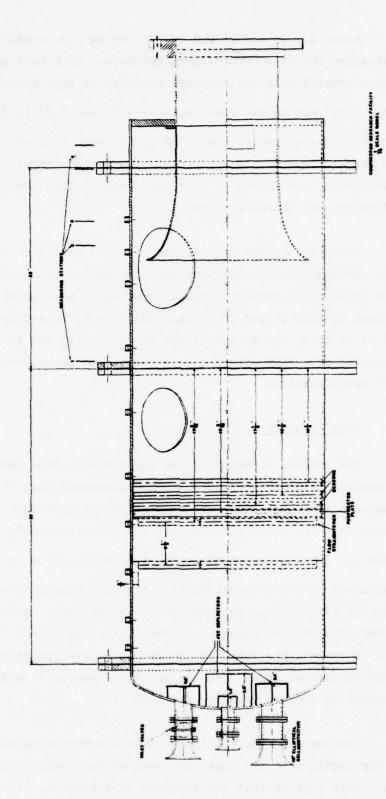


FIGURE 28. TEST CHAMBER SCHEMATIC

Tests 13, 14 and 15 and 22, 23 and 24 were aimed at evaluating the flow conditioning elements. Both test sequences were conducted at a test chamber pressure of approximately 3.8 lb_f/in² but at two flow rates -- 7.50 and 5.63 lb_m/sec corrected respectively. Tests 13 and 22 were carried out with the screens removed, 14 and 23 with the screens and flow straightener removed and 15 and 24 with the screens, flow straightener and perforated plates removed.

Tests 16 through 21 utilized the J-79 Bellmouth and were carried out with the same test chamber pressures which were employed previously. These experiments paralleled runs 4 through 12 with 16 and 17 corresponding to 4, 5, and 6; 18 and 19 to 7, 8, and 9; and 20 and 21 to 10, 11, and 12. The corrected mass flow rate has been reduced to correspond to the J-79 specifications.

3. Data Accuracy

The overall accuracy of the experimental data can be assessed by comparing the three independently determined mass flow rates, i.e., equations (48) and (49). The information is presented in Figure 29. The solid line denotes the relationship $\dot{m}_i = \dot{m}_5$ while the dotted lines indicate $\dot{m}_i = 1.1\dot{m}_5$ and $\dot{m}_i = 0.9\dot{m}_5$. A comparison of these equations with the data points shows that the bulk of the tests fell within the \pm 10% band. The majority of the data scatter occurred at the lower flow rates. The bulk of these tests were carried out at subatmospheric pressures. These conditions taxed both the hot wire anemometer and the pressure transducers from an accuracy point of view.

The test chamber total pressures are approximately equal to the static pressure since the test chamber velocities are low. This implies that the accuracy is a function of the pressure rather than the velocity measuring system. The pressure measurement uncertainty is approximately 0.1 - 0.25% using the on-line calibration

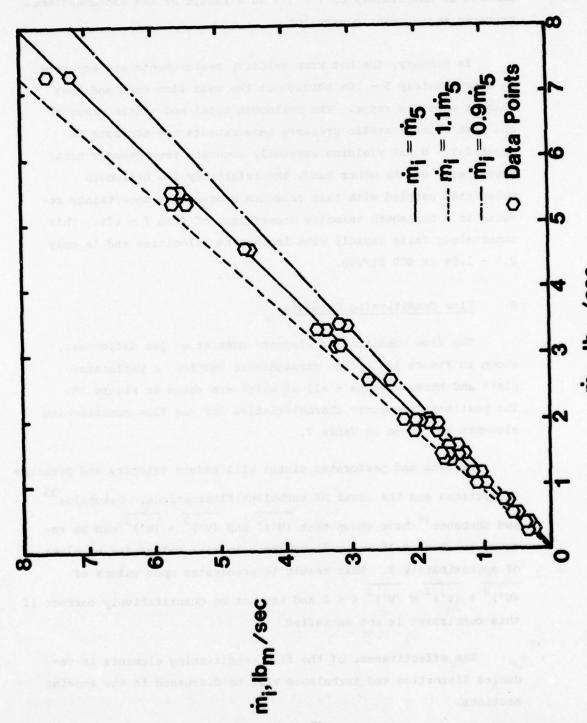


Figure 29. Mass Flow Rate Comparison

technique. 23 This yields extremely accurate values for the test chamber total pressure; however, velocities and mass flow rates computed from the bellmouth total and static pressures will exhibit an uncertainty of 7 - 17% as a result of the aforementioned pressure measurement constraint.

In summary, the hot wire velocity measurements are accurate to approximately 5 - 10% throughout the mass flow rate and test chamber pressure range. The bellmouth total and static pressure and test chamber static pressure measurements are accurate to about 0.1 - 0.25% yielding extremely accurate test chamber total pressures. On the other hand, the relatively low bellmouth velocities coupled with this pressure measurement uncertainty results in a bellmouth velocity uncertainty of from 7 - 17%. This uncertainty falls rapidly with increasing velocities and is only 0.5 - 1.5% at 400 ft/sec.

4. Flow Conditioning Elements

The flow conditioning elements consist of jet deflectors, shown in Figure 11, a flow straightener section, a perforated plate and three screens - all of which are shown in Figure 28.

The pertinent geometric characteristics for the flow conditioning elements are given in Table 7.

Screens and perforated plates will reduce velocity and pressure distortions and the level of turbulent fluctuations. Batchelor 35 and Shubauer 36 have shown that $(U')^2$ and $(V')^2 + (W')^2$ can be reduced to about 0.15 and 0.30 of their initial values for k values of approximately 2. This result is predicated upon values of $(U')^2 + (V')^2 + (W')^2 < 1$ and may not be quantitatively correct if this constraint is not satisfied.

The effectiveness of the flow conditioning elements in reducing distortion and turbulence will be discussed in the ensuing sections.

TABLE 7
FLOW CONDITIONING ELEMENT GEOMETRIC CHARACTERISTICS

Flow Conditioning Element	Wire Length or Plate Thickness in.	Hore or Wire Di- ameter in.	Length/ Diame- ter	Area Ratio	ζ
Honeycomb	5.500	0.5419	10.1495	0.8127	
Perforated Plate (Top)	0.0469	0.1090	0.4303	0.4055	
Perforated Plate (Bottom)	0.0469	0.1041	0.4505	0.4924	
Screen Number 1	0.0357	0.0130	2.7436	0.2720	0.4039
Screen Number 2	0.0374	0.0120	3.1181	0.5161	0.4614
Screen Number 3	0.0374	0.0120	3.1181	0.5161	0.4614

5. Maximum Flow Rate Bellmouth with Jet Deflectors, Flow Straightener, Perforated Plate and Screens Installed

The experimental program was initiated by evaluating the test chamber with all the flow conditioning elements installed. This series of experiments comprises tests 1 through 12 with the major parameters presented in Tables 8, 9, and 10. Table 8 summarizes the actual and corrected mass flow rates and the mean static and total pressures. Table 9 lists the mean velocities and turbulence levels and Table 10 gives the profile variation factors. All three tables list the inlet valve openings. Plots of the velocity and turbulence profiles are given in reference 44.

The first three tests, i.e., runs 1, 2 and 3, were carried out with the inlet valves removed. This was done to establish a baseline configuration from a flow distortion point of view. The mean test chamber velocities varied from 34 to 15 ft/sec with bellmouth velocities varying from 136 to 56 ft/sec. The turbulence level was approximately 1.5% in all cases with $\sigma_{\rm p}$ varying from 5 to 1 x 10 $^{-5}$ and $\sigma_{\rm U^2}$ about 7% in all three situations. It is important to note that the total pressure distortion or variation is negligible by any standard. The variation in squared mean velocity was substantially less in the bellmouth than in the test chamber in this case, i.e., $(\sigma_{\rm U}^{\ 2})$ was approximately 3 times less than the test chamber values. It should be noted, however, that the reduction was less than would be predicted by classical theories. These techniques postulate a reduction inversely proportional to the area ratio squared. This implies

$$\frac{\left(\sigma_{U^{2}}\right)_{b}}{\left(\sigma_{U^{2}}\right)_{bc}} = \frac{1}{Ar^{2}}$$

with Ar = 4 in the present case. The test chamber does not directly correspond to the theoretical case since the bellmouth

TABLE 8

COMPRESSOR RESEARCH PACILITY 1/10 SCALE MODEL WITH MAXIMUM PLOW BELLMOUTH (Measured pressures)

	P _b 1b _e /in Comments	14.397 Baseline Test	14.443 Baseline Test	14.489 Baseline Test	10.278 Atmospheric Simulation	12.033 Atmospheric Simulation	13.220 Atmospheric Simulation	6.727 Valves Transonic	6.700 Valves Transonic	6.652 Valves Transonic	3.700 Valves Supersonic	3.809 Valves Supersonic	3.831 Valves Supersonic	3.827 Flow Element Evaluation	3.794 Flow Element Evaluation	3.825 Flow Element Evaluation	3.683 Flow Element Evaluation	3.779 Flow Element Evaluation	3.712 Flow Element Evaluation
1				14.464 14.	10.165 10.	11.970 12.	13,186 13.	6.676 6.	9 099'9	6.628 6.	3.671 3.	3.790 3.	3.819 3.	3.791 3.	3.794 3.	3.787 3.	3.659 3.	3.752 3.	3.688 3.
	Ptc 1be/in ²		14.445	14.490	10.287	12.052	13,222	6.803	6.747	6,693	3.733	3.894	3.897	3.895	3.906	3.900	3.738	3.798	3.766
	Ptc 1b_/in ²		14.439	14.488	10.280	12.048	13.220	6.199	6.745	6.692	3.730	3.892	3.897	3.893	3.902	3,895	3.737	3.795	3.762
	m 1b_/sec	7.28	5.50	3.13	5.33	4.62	3.40	3.47	2.61	1.82	1.92	1.48	1.03	1.96	1.97	1.96	1.48	1.47	1.46
m/Rt ref	Rpref 1b /sec	7.47	5.59	3.15	7.59	95.5	3.71	7.49	5.64	3.92	7.59	29.6	3.89	7.51	7.49	7.52	5.91	5.65	89.5
	8, •	1	1	1	11	72	72	41	30	7	0	0	0	0	0	0	0	0	0
	Valve Settings,	1	1	1	02	89	69	4	59	50	10	21	0	01	10	10	0	0	0
	Lve Se	1	1	1	75	75	11	נג	נג	99	1	36	35	0,	0/	70	46	46	46
	VA 20	1	1	1	06 **06	90	90	90	96	90	90	90	75	96	96	90	90	90	06
	7	1	1	1	*06	06	90	90	90	90	8	06	90	90	90	8	90	96	90
	Configuration	Complete with Inlet Valves Removed	Complete with Inlet Valves Removed	Complete with Inlet Valves Removed	Complete	Complete	Complete	Complete	Complete	Complete	Complete	Complete	Complete	Jet Deflectors, Plow Straightener, Perforated Plate	Jet Deflectors and Perforated Plate	Jet Deflectors	Jet Deflectors, Flow Straightener, Perforated Plate	Jet Deflector and Perforated Plate	Jet Deflectors
	E S	-	~	3	*	•	9	1	8	6	9	=	12	13	7	15	22	23	24

*Complete implies jet deflectors, flow straightener, perforated plate and three screens installed.

** 90° denotes completely open and 0° denotes completely closed.

TABLE 9

COMPRESSOR RESEARCH FACILITY 1/10 SCALE MODEL WITH MAXIMUM FILM BELLMOUTH (Measured velocities)

	Comments	Baseline Test	Baseline Test	Baseline Test	Atmospheric Simulation	Atmospheric Simulation	Atmospheric Simulation	Valves Transonic	Valves Transonic	Valves Transonic	Valves Supersonic	Valves Supersonic	Valves Supersonic	Flow Element Evaluation	Flow Element Evaluation	Flow Element Evaluation	Flow Element Evaluation	Flow Element Evaluation	Flow Element Evaluation
	g to	0.0147	0.0144	0.0156	0.0391	0.0300	0.0243	0.0546	0.0513	1770.0	0.0822	0.0867	0.126	0.098	0.413	0.561	0.332	0.500	0.585
	Ub ft/sec	135.7	101.0	56.2	142.3	8.76	67.9	118.2	105.2	81.0	120.3	91.0	75.9	133.3	152.6	136.5	105.5	114.7	106.9
	Utc ft/sec	34.0	26.4	14.9	35.9	25.7	17.3	32.2	24.8	17.71	34.1	24.9	17.9	32.0	34.4	33.8	22.3	26.0	29.9
WRt ref	Poref 1b /sec	7.47	5.59	3.15	7.59	95.5	3.71	7.49	5.64	3.92	7.59	5.62	3.89	7.51	7.49	7.52	5.91	5.65	5.68
	36R	1	1	1	17	72	22	4	30	~	•	0	•	•	0	0	0	0	0
	ings, 36L	1	1	1	20	89	69	4	53	70	10	77	•	10	10	10	•	0	•
	Valve Settings, 20 24 36L	1	1	1	75	75	11	n	17	26	11	36	35	20	92	20	4	46	4
	7alve 20	1	1	1	06 .	9	9	96	8	90	6	8	75	8	9	90	8	6	8
	*	1	1	1	**06	8	96	96	96	8	8	8	8	8	9	90	90	90	96
	Configuration	Complete* with Inlet Valves Removed	Complete with Inlet Valves Removed	Complete with Inlet Valves Removed	Complete	Complete	Complete	Complete	Complete	Complete	Complete	Complete	Complete	Jet Deflectors, Flow Straightener, Perforated Plate	Jet Deflectors and Perforated Plate	Jet Deflectors	Jet Deflectors, Flow Straightener, Perforated Plate	Jet Deflector and Perforated Plate	Jet Deflectors

*Complete implies jet deflectors, flow straightener, perforated plate and three screens installed.

***See Appendix III for a discussion of turbulence scaling.

2 2 2 2

2 12 22

2 23

TABLE 10

COMPRESSOR RESEARCH FACILITY 1/10 SCALE MODEL WITH MAXIMUM FLOW BELLMOUTH (Flow quality parameters)

Comments	Baseline Test	Baseline Test	Baseline Test	Atmospheric Simulation	Atmospheric Simulation	Atmospheric Simulation	Valves Transonic	Valves Transonic	Valves Transonic	Valves Supersonic	Valves Supersonic	Valves Supersonic	Flow Element Evaluation	Flow Element Evaluation	Flow Element Evaluation	Flow Element Evaluation	Flow Element Evaluation	Flow Element Evaluation
ar S	0.181	0.176	0.166	0.0689	0.0722	0.103	0.0764	0.0587	0.126	1.0617	0.314	0.242	0.188	0.105	0.0837	0.305	0.136	0.0755
⁹ 2	0.0785	0.0582	0.0853	0.0841	0.0813	0.0951	0.0809	0.0985	0.208	0.104	0.244	0.138	0.541	0.320	0.365	0.725	0.682	0.633
o Ptc × 104	0.491	0.220	0.103	0.593	0.293	0.155	0.456	0.331	0.353	0.654	0.800	0.237	3.00	2.38	3.46	1.94	3.09	5.14
op to	0.0412	0.0240	0.0090	0.223	0.0785	0.0261	0.230	0.119	0.131	0.315	0.205	0.232	1.50	8.03	1.49	1.50	6.17	12.9
m/Rtref / Rpref lbm/sec	7.47	5.59	3.15	7.59	5.56	3.71	7.49	5.64	3.92	7.59	5.62	3.89	7.51	7.49	7.52	5.91	5.65	5.68
36R	1	1	1	11	72	72	41	30	7	0	0	0	0	0	0	0	0	0
Valve Settings, 20 24 36L	1	1	1	70	89	69	4	53	20	10	21	0	10	10	10	0	0	0
Sett 24	1	1	1	75	75	11	11	11	99	17	36	35	70	20	20	46	46	4
Valve 20	1	1	1	06 •	96	90	90	96	06	90	96	75	96	90	9	96	90	06
2	;	1	1	**06	96	90	90	90	90	96	90	90	96	90	90	06	90	96
Configuration	Complete with Inlet Valves Removed	Complete with Inlet Valves Removed	Complete with Inlet Valves Removed	Complete	Complete	Complete	Complete	Complete	Complete	Complete	Complete	Complete	Jet Deflectors, Flow Straightener, Perforated Plate	Jet Deflectors and Perforated Plate	Jet Deflectors	Jet Deflectors, Flow Straightener, Perforated Plate	Jet Deflector and Perforated Plate	Jet Deflectors
Mo.	-	7	•	4	5	9	7	80	6	10	11	12	13	14	15	22	23	24

*Complete implies jet deflectors, flow straightener, perforated plate and three screens installed.

** 90° denotes completely open and 0° denotes completely closed.

functions as a submerged inlet and this, coupled with measurement uncertainties, may explain the differences.

Tests 4, 5, and 6 were intended to simulate the condition where all 5 inlet valves were fully open. Since the valves used in the model are not identical to those used in the full scale facility the model with valves fully open did not yield the full-scale test chamber pressures. Consequently, the 2.4, 3.6R and 3.6L valves were adjusted to produce the desired pressure. As a result, these tests were carried out at the maximum test chamber pressures from a predicted point of view.

The major difference between tests 1, 2 and 3 and 4, 5 and 6 was in the mean turbulence leve. The Tu values were approximately double, i.e., 3%, with the profile variations at levels similar to that seen before. Again $\sigma_{\rm p}$ was negligible throughout.

Tests 7, 8 and 9 and 10, 11 and 12 were undertake to determine the effect of the valve created disturbances on the test chamber flow quality. As a result, the test chamber static pressures were chosen to produce valve exit Mach numbers which were transonic and supersonic respectively. The major change with test chamber pressure is again the turbulence level. $((U')^2/U)$ mean

is approximately 6% for transonic valve Mach numbers and about 10% for the supersonic case. $\sigma_U^{\ 2}$ increases to about 13% in the former and 16% in the latter case.

Note that all test chamber variables are more sensitive to changes in pressure level than to variations in flow rates. This is due to the dependence of the tank flow field on the initial conditions, i.e., the valve exit flow fields, which at transonic and supersonic conditions, tend to be Mach rather than Reynolds number dependent. It should also be noted that each operating condition differs in that the valve positioning is unique. This implies that each operating condition yields a separate test chamber flow field. Each measured flow field is unique on a macroscopic

basis, however, certain general features seem to prevail in most cases and, thus, limited flow similarity is maintained.

The effectiveness of the area contraction in removing the velocity variation is also diminished in these two cases. This is the result of large turbulence levels and length scales tending to negate the vortex stretching mechanism which is effective under normal circumstances. Note that the classic theories regarding turbulence dissipation via a reduction in cross-section area require that Tu << l/L, where l is a turbulent length scale and L is the length over which the area change takes place. This constraint is violated by about an order of magnitude for tests 7-12. Furthermore, recourse to experimental data for quantification of the dissipation of turbulence by area reduction is unlikely to prove fruitful since most information of this type has been generated for wind tunnel applications where Tu < 0.01.

J-79 Bellmouth with Jet Deflectors, Flow Straightener, Perforated Plate and Screens Installed

A series of tests similar to that described in Section II.H.5. was carried out using the J-79 bellmouth. The results of these tests are presented in Tables 11, 12 and 13. Two corrected mass flow rates, i.e., 1.7 and 1.3 lb_m/sec, were employed for each of three test chamber pressures. Again the maximum attainable test chamber pressures were computed using an inlet simulator and the full-scale valve geometry. This condition was generated on the 1/10 scale model by adjusting the five inlet valves. Following these two tests, runs 16 and 17, experiments were carried out with test chamber pressures yielding transonic and supersonic flows at the valve exhausts.

The tests utilizing the maximum test chamber pressure yielded turbulence levels of approximately 3.5%. This is comparable to tests 4, 5 and 6 with the larger bellmouth. The total pressure profile variations are again very small, e.g., of the order 10^{-5} ; however, the 0^{2} variations are much larger - approximately 40%.

TABLE 11

COMPRESSOR RESEARCH FACILITY 1/10 SCALE MODEL WITH 379 BELLMOUTH (Measured pressures)

						m/Rt ref /		۵	d	ď	ď	
Configuration	14	/alve 20	Valve Settings, * 14 20 24 36L 36R	ngs,	36R	Ppref lb/sec	in 1b/sec	lb _r /in ²	1bf/in ²	1bf/in ²	1b { 1n 2	Comments
Complete	*06	96	8	59	89	1.69	1.58	14.066	14.067			Atmospheric Simulation
Complete	0	0	0	90	06 06 0 0 0		1.22	14.141	14.141	13.444	14.137	Atmospheric Simulation
Complete	06	35	35	0	0	1.76	0.780	6.725	6.725		6.715	Valves Transonic
Complete	98	36	0	0	0		0.580	6.720	6.721		902.9	Valves Transonic
Complete	88	1	0	0	0		0.421	3.667	3.667		3.636	Valves Supersonic
Complete	58	0	0	0	0		0.323	3.708	3.708		3.680	Valves Supersonic

*Complete implies jet deflectors, flow straightener, perforated plate and three screens installed ** 90° denotes completely open and 0° denotes completely closed.

Run No.

TABLE 12

COMPRESSOR RESEARCH PACILITY 1/10 SCALE MODEL WITH 379 BELLMOUTH (Measured velocities)

Comments	Atmospheric Simulation	Atmospheric Simulation	Valves Transonic	Valves Transonic	Valves Supersonic	Valves Supersonic
T to	0.0389	0.0341	0.146	0.171	0.223	0.503
t,	399.9	303.8	433.2	316.6	443.2	325.2
n g	8.1	6.2	8.7	6.4	8.1	5.8
m/Rt ref / Rpref 1b / sec	1.69	1.27	1.76	1.27	1.76	1.30
36.	89	06	0	0	0	0
Valves Settings, *14 20 24 36L 36R	29	90	0	0	0	0
s Set 24	06	0	35	0	0	0
valve 20	06 **06	0	35	36	1	0
41	••06	0	96	98	88	28
Configuration	Complete*	Complete	Complete	Complete	Complete	Complete
Ru .	16	17	18	19	20	21

* Complete implies jet deflectors, flow straightener, perforated plate and three screens installed.

** 90° denotes completely open and 0° denotes completely closed.

*** See Appendix III for a discussion of turbulence scaling.

TABLE 13

COMPRESSOR RESEARCH FACILITY 1/10 SCALE MODEL WITH 379 BELLMOUTH (Flow quality parameters)

Coments		Atmospheric Simulation	Atmospheric Simulation	Valves Transonic	Valves Transonic	Valves Supersonic	Valves Supersonic
ئ ئو		1.850	0.864	0.390	0.311	0.354	0.276
ou ² tc		0.404	0.409	0.443	0.535	0.447	0.605
Ptc × 104		0.142	0.0843	0.179	0.124	0.207	0.197
°P tc x 10 €		0.0164	0.0082	0.108	0.0929	0.197	0.409
WRt ref		1.69	1.27	1.76	1.27	1.76	1.30
95		89	06	•	0	0	0
198	1	69	96	0	0	0	0
Valve Settings, *	:	90 59	0	35 35 0	0	7 0 0	0
alve	3	06 **06	0	35	36	1	0
3		••06	0	96	98	88	88
	Contiguration	Complete*	Complete	Complete	Complete	Complete	Complete
3	ė	16	11	18	19	20	21

* Complete implies jet deflectors, flow straightener, perforated plate and three screens installed.

^{** 90°} denotes completely open and 0° denotes completely closed.

The velocity profile is approximately parabolic in these cases leading to the large values of σ_{U^2} . The majority of this distortion is suppressed by the substantial area contraction - 0.0178. σ_{U^2} values within the bellmouth are approximately 1.2% yielding a reduction of about 40 to 1. Again this is less than would be predicted by equation (51) but is more than sufficient to yield acceptable flow quality.

Tests 18 through 21 show trends similar to those observed with the large bellmouth. The total pressure variation is low in all cases with the squared velocity profile variationat approximately the same level for all cases. The mean turbulence level increases from 3.6% for the low valve Mach number case to approximately 16% when the valve Mach number is approximately 1. This value increases to around 36% for the minimum test chamber pressure. All the mean turbulence levels are influenced by the predominantly large values near the tank walls. These values are plotted in reference 44.

7. The Effect of Flow Conditioning Elements on Flow Quality

Tests 13, 14 and 15 and 22, 23 and 24 were designed to yield information concerning the effectiveness of the flow conditioning elements in improving the overall flow quality. The two sequences of experiments were carried out at corrected flow rates of 7.5 and 5.63 lb_m/sec respectively. The test chamber pressure was approximately 3.8 lb_f/in^2 in all six cases yielding a supersonic flow field at the valve exit.

These tests were undertaken by serially removing each of the flow conditioning elements. The three screens (see Figure 28) were removed for tests 13 and 22. The integral and/or overall properties are shown in Tables 8, 9, and 10.

The impact of the screens on the aerodynamic characteristics of the test chamber can be ascertained by comparing tests 13 and 22 with experiments 10 and 11. In both cases, the turbulence level increases markedly - by a factor of 2.4 in one case and 3.8 in the other. The disparity in the increase in turbulence

level is due to the differences in screen Reynolds number which influences k and hence, the turbulence damping. At these velocities and pressures the screen Reynolds numbers are 108 for test 13 and 81 for test 22. This yields drag coefficient values of 3.50 and 3.93 respectively. Both the theoretical results of reference 35 and the data of reference 47 would indicate that more turbulence damping should occur; however, the cited references were both restricted to Tu < < 1 and this is not the case in the test chamber under these conditions.

The pressure profile variation increases by about an order of magnitude when the screens are removed but still is negligible. The dynamic head variations also increase markedly from 0.104 to 0.541 and from 0.244 to 0.725 in the high and low flow rate cases respectively.

Following the removal of the screens, the test sequence was repeated with the flow straightener removed. Surprisingly this resulted in a further increase in mean turbulence level with a slight decrease in velocity profile variation. The increase in turbulence levels could be the result of an ordered unsteadiness rather than truly random, i.e., turbulent, fluctuations. If this were the case, the honeycomb and/or flow straightener could have been partitioning the flow field, thus, largely removing the local zones of recirculating flow.

The final two tests, runs 15 and 24, were carried out with all the flow conditioning elements removed with the exception of the jet deflectors. These results are likewise presented in Tables 8, 9, and 10. Again both Tu and $\sigma_{\rm p}$ increased with $\sigma_{\rm U}^{\ 2}$ showing a slight decrease. The decrease in squared velocity variation is probably due to the enhanced turbulent diffusion resulting from the high turbulence levels.

Bellmouth velocity measurements indicate a moderate decrease in σ_{U^2} values as a result of the area contraction. Preliminary turbulence measurements in the bellmouth also indicate a diminution of Tu values.

8. Summary of the Experimental Results for the Baseline Configuration

The experimental results can be subdivided into two broad groups: those utilizing all the flow conditioning elements and those tests wherein the flow conditioning elements were sequentially removed. In the former case, the total pressure variation, i.e., $\sigma_{\rm p}$ is negligible in all cases. The dynamic head variation, on the other hand, increases from 0.0740 with the inlet valves removed to 0.1620 for the lowest test chamber pressure.

In addition to the σ_{U^2} values, the mean turbulence level increases from 0.0149 to 0.0983 with decreasing tank pressures for the large bellmouth. Both Tu and σ_{U^2} will be damped during the transition from the test chamber to the bellmouth. Unfortunately the magnitude of the reduction is less than would be predicted by either the classic theories or prior wind tunnel experiments. This may be due to both the magnitude and scale of the turbulence as well as the utilization of a submerged inlet.

Similar results were obtained for the test chamber with the J-79 bellmouth installed. Higher values of $\sigma_{\rm U^2}$ and Tu were obtained but greater damping - at least in the former case - was exhibited due to the substantial area reduction.

As the flow conditioning elements are removed, the total pressure variation, the squared velocity variation and the turbulence level increase markedly. The total pressure distortion is still well within compressor requirements. The dynamic head variation is now about 10 times greater than the treated test chamber values and exceeds the reference 48 recommendations by a factor of 10 to 15.

The turbulence levels also are extremely high and are clearly unacceptable for compressor testing. Turbulence levels in axial flow compressors have been measured by Schlichting and Das and deHaller. These works show maximum values of Tu from 6 - 8% with inlet values of 1% occurring in a multistage compressor. The test chamber sans flow conditioning would yield inlet values of Tu at least 10 - 20 times as great as the generated values. This would undoubtedly influence the performance of the compressor and degrade measurement accuracy and is thus unacceptable.

I. Modification of the Compressor Research Facility 1/10 Scale Model to Accommodate a Compressor Simulator

1. Introduction

As noted in Section II. D, the 1/10 scale model test conditions are controlled by means of a facility control valve and the five test chamber inlet valves. The former regulates the mass flow rate, while the latter controls the test chamber pressure. Under some conditions, the mass flow rate control valve is choked, i.e., sonic conditions exist, and disturbances cannot propogate upstream of the valve itself. Under other conditions -particularly low test chamber pressures -- the valve is operated in the subsonic regime and exhauster generated disturbances can possibly influence the test chamber and bellmouth flow fields. In an effort to eliminate any possibility of downstream influences on the bellmouth flow fields, a perforated plate or compressor simulator was designed for insertion between the bellmouth and rear test chamber bulkhead. The plate was operated at sonic conditions, thus eliminating the possibility of forward propogation of disturbances.

Design of the Sonic Plate

The perforated plate was designed on the basis of a choked orifice. The mass flow rate per unit area can be defined as

$$\frac{\dot{\mathbf{m}}}{\mathbf{A}} = c_{\mathbf{d}} \left\{ \frac{144P}{\sqrt{T}} \sqrt{\frac{\gamma g_{\mathbf{c}}}{R} \left(\frac{2}{\gamma + 1}\right)^{\frac{\gamma + 1}{\gamma - 1}}} \right\}$$

following reference 52.

The discharge coefficient is a weak function of Reynolds number and geometry, but has a value near 0.6 for sharp-edged orifices under normal conditions. Prior experience with perforated plates indicate that somewhat higher discharge coefficients result, i.e., in the range of 0.70 to 0.80. These values were employed in the design of the perforated plates.

The Modified Bellmouth Units

The modified bellmouth systems are shown in Figures 30 through 37. The perforated plate is bolted to the rear bulkhead. A cylindrical spacer occupies a short distance between the bellmouth and perforated plate and contains supports for the traversing system. The traversing system consists of a .250" diameter tube which passes through holes in the tank and cylindrical spacer. These holes are sealed around the tube. A slot three inches long, milled into the tube, allows the insertion of the hot wire probe and support. The position of the hot wire is slightly upstream of the bellmouth throat. There are two sets of holes in the spacer and tank to allow traverses at right angles to each other. This allows the measurement of turbulence and velocity uniformity at the location of the test item itself.

A one quarter inch thick disc supports the circular perforated plates, which can be up to 1/8 inch thick. Two bars support the perforated plates, Figure 38, to assure that no fragments pass into the air moving equipment downstream. These provide an additional blockage of slightly under 5% of flow cross sectional area, but are judged a useful safety feature.

The six inch bellmouth and exit cone as shown in Figure 39 were too long to be assembled as one unit. Provision was made to attach the exit diffuser independently to the test chamber

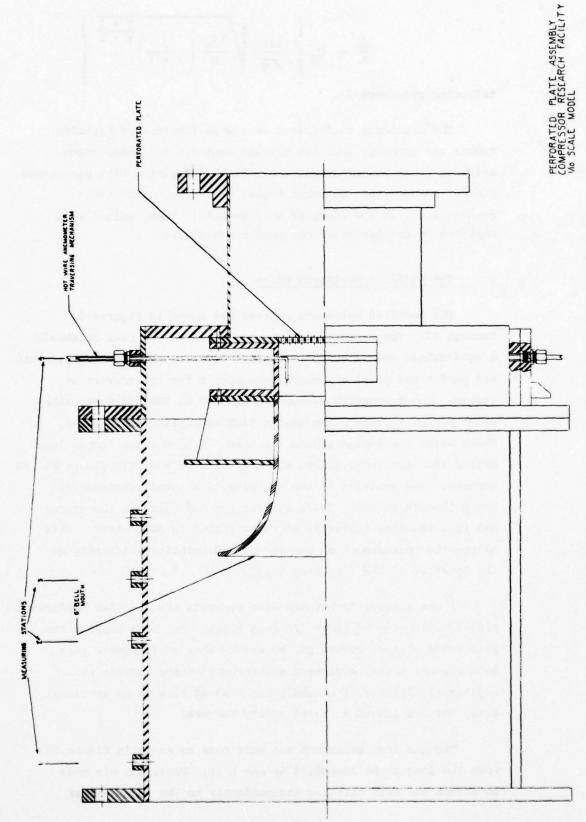


Figure 30. Modified 1/10 Scale Model with the 6" Bellmouth

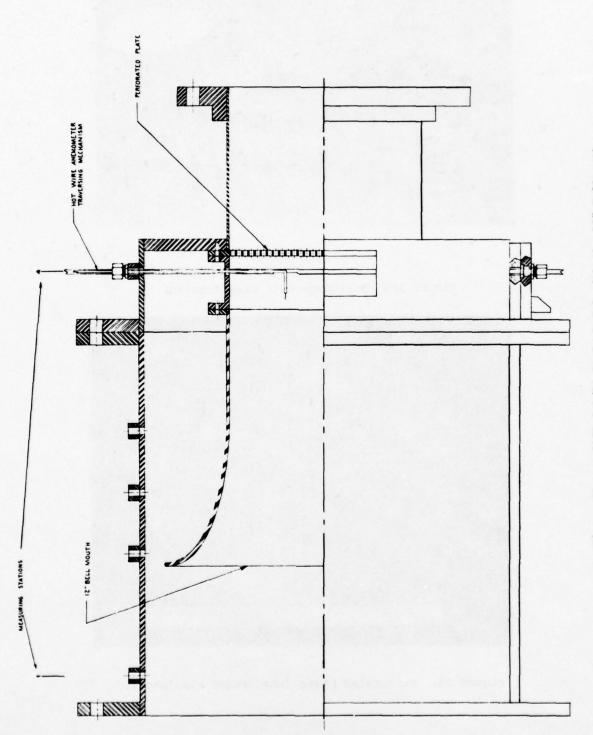


Figure 31. Modified 1/10 Scale Model with the 12" Bellmouth

PERFORATED PLATE ASSEMBLY COMPRESSOR RESEARCH FACILITY 1/10 SCALE MODEL

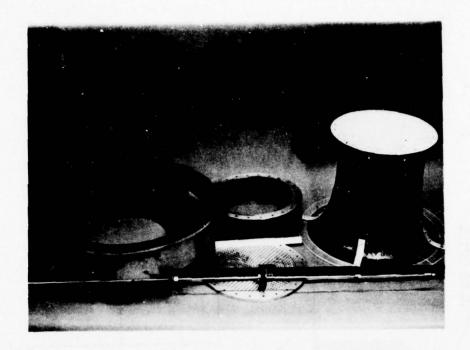


Figure 32. Bellmouth unit disassembled.

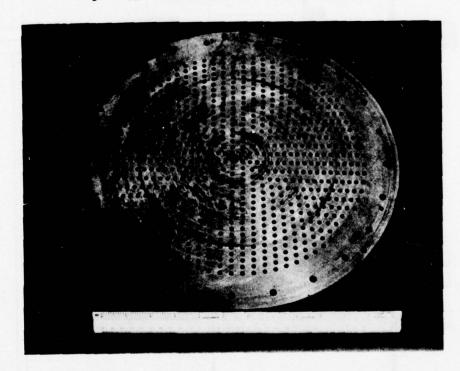


Figure 33. Perforated plate (compressor simulator).

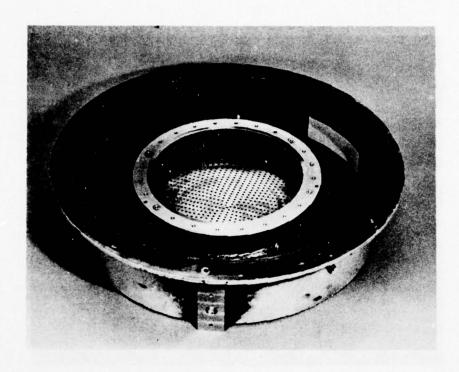


Figure 34. Rear bulkhead, perforated plate and bellmouth transition section.

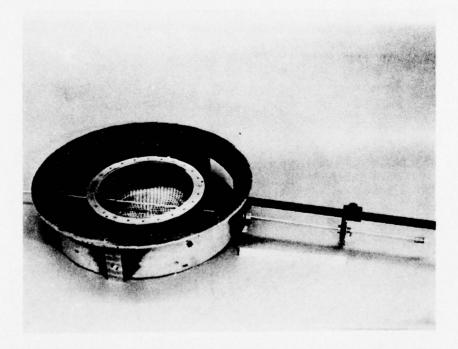


Figure 35. Rear bulkhead assembly with traversing mechanism installed.

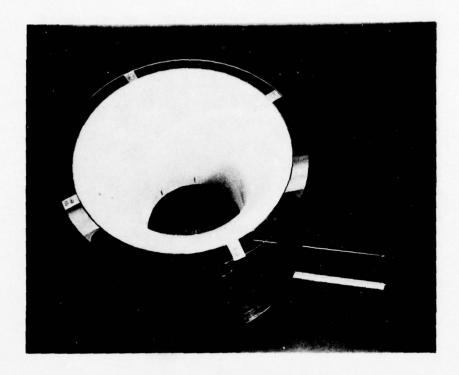


Figure 36. Rear bulkhead assembly with the compressor bellmouth installed.

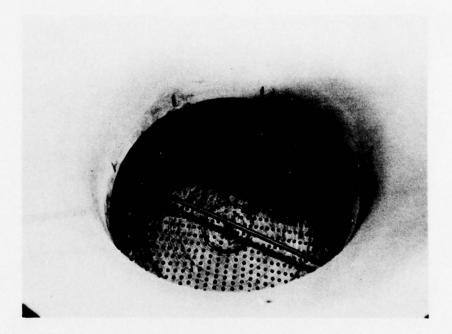


Figure 37. Rear bulkhead assembly showing the location of the hot wire anemometer probe relative to the perforated plate.

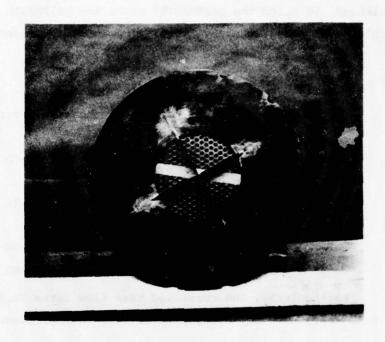


Figure 38. Perforated Plate Support System Seen from Downstream Direction

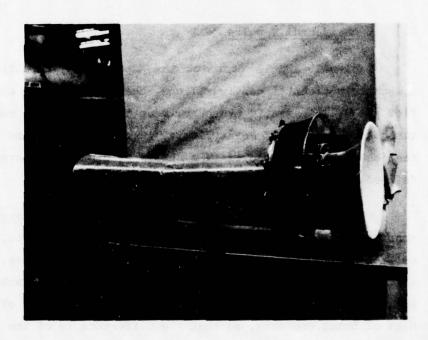


Figure 39. Six-Inch Bellmouth Unit Assembled

bulkhead, to which the perforated plate and bellmouth assembly could be attached, thereby simplifying assembly procedures.

4. Test Program

The objectives of this portion of the test program were:

- Evaluate the performance of test chamber both with and without a choke plane
- 2) Evaluate the flow quality in the 12 inch bellmouth with and without a choke plane
- Determine flow quality and aerodynamic characteristics for a series of operating conditions.

Particularly, two corrected mass flow rates (6.8 and 4.5 lb_m/sec) were employed, with several chamber pressures corresponding to each corrected mass flow. All tests used the 12 inch bellmouth. Table 14 summarizes the test program.

5. Experimental Results

Tables 15 and 16 document the experimental results. Listed are the experimental configurations, the corrected and actual flow rates, mean static pressure, mean total pressure, mean turbulence level, and mean velocity in the bellmouth and in the test chamber. Table 16 lists a series of distortion parameters defined in Section II.G.7.

The results as shown in Tables 15 and 16 are internally consistent regarding pressures. In a few cases, however, the bellmouth total pressure exceeds the tank total pressure, an improbable situation. One expects a small drop from tank to bellmouth. The difference is very small, on the order of 0.1% of total pressure, so that the difference is of the type normally associated with instrument error and normal scatter.

A comparison of tests number 1 through 4 (choke plane installed in bellmouth) with tests number 5 through 8 (open bellmouth, no choke plane) seems to indicate that the effect of the

TABLE 14

Cart .

SUMMARY OF THE TEST CONDITIONS USED IN THE EVALUATION OF

A SONIC PLATE OR COMPRESSOR SIMULATOR

			m'Rt ref						
to at			Poref	Ptc		Valv	Valve Settings	Sbi	
S .	Date	Configuration	1b /sec	1bf/in	1.4"	15	2.4"	3.6"L	3.6"R
-	1-16-76	Choke plane installed	4.63	13.34	06	06	06	06	96
7	1-16-76	Choked flow	4.58	12.38	06	06	06	09	9
e	1-16-76	Exhaust valve completely open	4.59	11.47	06	06	9	55	26
4	1-16-76		4.58	9.83	06	6	45	47	20
2	1-29-76	Choke plane removed	4.31	13.43	06	06	8	06	9
9	1-29-76	Exhaust valve flow control	4.37	12.36	90	06	96	26	28
1	1-29-76		4.34	11.47	06	90	54	55	54
00	1-29-76		4.33	9.83	06	90	45	44	44
6	1-29-76	Design valve schedule	4.29	12.43	06	90	96	82	15
10	1-29-76		4.30	11.57	90	90	90	63	15
11	1-29-76	_	4.37	17.6	90	96	96	45	10
12	2-05-76	Choke plane installed	4.82	12.25	06	96	96	06	90
13	2-05-76	Flow unchoked	4.85	11.63	06	06	96	73	89
14	2-05-76	THE RELEASE OF THE PERSON OF T	4.85	10.79	06	96	9	74	21
15	2-05-76		4.82	9.88	06	90	96	74	30
16	2-06-76	Choke plane installed	98.9	12.31	06	96	96	90	9
17	2-06-76	Choked flow	68.9	11.64	90	96	9	98	63
18	2-06-76	Exhaust valve completely open	6.88	10.83	06	96	9	79	47
19	2-06-76	_	98.9	9.91	90	06	6	72	37
20	2-13-76	Choke plane removed	6.72	12.41	96	8	8	90	6
21	2-13-76		6.70	10.71	90	96	9	75	48
22	2-13-76	Exhaust valve flow control	9.65	9.79	90	06	90	2	40

TABLE 15

COMPRESSOR RESEARCH FACILITY 1/10 SCALE MODEL TEST RESULTS WITH THE COMPRESSOR SIMULATION. MEASURED PRESSURES AND VELOCITIES

(U _b)m ft/sec	82.80	81.50	82.00	81.80	77.50	77.30	77.50	77.70	76.30	76.50	78.90	84.40	85.40	82.90	83.90	119.40	121.50	120.34	127.30	130.30	119.00	118.30
(U _{tc})m ft/sec	21.40	22.30	22.00	22.20	30.10	21.10	20.60	21.70	20.90	20.90	21.10	20.00	22.50	22.80	22.40	31.20	33.30	33.10	34.10	31.33	31.70	30.80
(Ptc) _m	13.348	12.383	11.473	9.833	13.432	12.365	11.473	9.835	12.434	11.577	9.715	12.257	11.630	10.794	9.882	12.316	11.638	10.827	806.6	12.416	10.709	9.794
(P _{tc}) _m 1b _f /in	13.343	12.379	11.469	9.830	13.428	12.361	11.470	9.832	12.430	11.573	9.711	12.253	11.626	10.793	9.878	12.308	11.629	10.819	9.901	12.408	10.702	9.788
in lb sec	4.31	3.96	3.67	3.14	4.03	3.76	3.46	2.96	3.72	3.46	2.95	4.05	3.86	3.58	3.26	5.80	5.50	5.11	4.66	5.74	4.93	4.48
m/Rt ref Rpref 1b / sec	4.63	4.58	4.59	4.58	4.31	4.37	4.34	4.33	4.29	4.30	4.37	4.82	4.85	4.85	4.82	89.9	68.9	6.88	98.9	6.72	6.70	6.65
Configuration	Choke plane installed				Choke plane removed				Design valve schedule			Choke plane installed			LExhaust valve partly open	Choke plane installed	Flow choked		7	Choke plane removed		Exhaust valve flow control
Date	1-16-76	1-16-76	1-16-76	1-16-76	1-29-76	1-29-76	1-29-76	1-29-76	1-29-76	1-29-76	1-29-76	2-05-76	2-05-76	2-05-76	2-05-76	2-06-76	2-06-76	2-06-76	2-06-76	2-13-76	2-13-76	2-13-76
Test No.																						

TABLE 16

COMPRESSOR RESEARCH FACILITY 1/10 SCALE MODEL TEST RESULTS WITH THE COMPRESSOR SIMULATOR. FLOW QUALITY PARAMETERS

Tub/Tute	.202	.156	.201	.152	861.	.332	.369	.258	.303	.192	.227	.279	161.	.156	171.	.321	.248	.169	.162	.256
(g 1, to	.063	.044	990.	660.	.067	.105	960.	.081	860.	.084	.612	.198	.147	.128	.140	.122	.145	860.	.268	.137
(q Tu to	.136	.160	.256	.140	.202	.251	.263	.128	.075	.229	.268	.323	.286	.163	.421	.359	.297	.219	.349	.197
(^Q p) _b ×10 ⁴	3.90	.72	2.71	1.38	1.34	1.14	3.28	2.94	06.0	2.12	4.21	2.21	2.07	2.95	4.57	7.08	80.8	5.54	6.40	60.6
(⁰ p) _{t,e} x10 ⁴	2.53	1.19	2.50	06.0	1.65	1.87	3.30	2.51	2.72	2.50	1.60	3.12	3.76	3.46	2.67	6.12	5.70	4.64	6.14	3.84
(⁰ ₁ , ²) _{tc}	.035	.018	.081	.041	.040	.034	.102	.091	.026	.054	.104	.058	.053	.037	.056	880.	060.	.070	.083	.119
(⁰ ₀ ²) _{tc}	1.017	.441	1.140	.355	902.	.725	1.406	1.059	.815	.943	.571	1.100	1.380	.643	.939	1.025	.892	.880	1.130	.745
(Tu _b)	8.53	4.91	8.56	5.62	7.98	13.50	16.10	11.90	15.10	6.30	6.78	10.60	8.76	5.31	6.67	10.30	10.60	6.30	6.40	9.10
(Tube)	42.3	31.4	42.5	36.9	40.2	40.7	43.7	46.1	49.9	32.9	29.9	38.0	46.1	33.9	39.1	33.1	42.9	37.3	39.4	35.6
Date	1-16-76	1-16-76	1-16-76	1-29-76	1-29-76	1-29-76	1-29-76	1-29-76	1-29-76	2-05-76	2-05-76	2-05-76	2-05-76	2-06-76	2-06-76	2-06-76	2-06-76	2-13-76	2-13-76	2-13-76
No.	7 7	е.	4. rv	9	7	8	6	10	77	12	13	14	15	16	17	18	19	50	21	22

choke plane gives a slight drop in turbulence both in the test chamber and bellmouth and slight improvement in uniformity of flow (a decrease in spatial variations). Tests numbered 1 to 8 all concerned a corrected mass flow of about 4.5 lb/sec. A comparison of tests numbered 16 through 19 with tests numbered 20 through 22 show the equivalent comparison at a corrected mass flow of about 6.8 lb/sec. No clear trend appears here with regard to turbulence level, either in the test chamber or bell-mouth. Overall, it appears that the presence of the choke plane has no significant effect on the flow in the test chamber or the bellmouth three inches upstream of the choke plane.

The contraction in area experienced by the flow from test chamber to bellmouth improved the flow significantly as expected. The reduction was not as great as predicted by Batchelor in reference 30, however, Batchelor's theory assumes low level homogeneous turbulence. Figure 40 details comparison of Batchelor's theory with test results.

Tests number 12 to 15 concern a configuration with choke plane installed but without choked flow. Comparison with tests number 1 to 4 shows that this unchoked mode of operation also has no significant effect on either turbulence or uniformity of flow.

each test number. These valve settings of the inlet valves for each test number. These valve setting schedules can have an effect on downstream flow, as they control the spatial variation of the flow in the upstream areas of the test chamber. Tests number 9 to 11 used the design valve schedule which opens some valves, while leaving others closed in such a manner as to introduce a large spatial variation of velocity. Tests number 9 to 11 may be compared directly to tests number 6 to 8, respectively. The design valve schedule caused significant increases in turbulence in the test chamber and bellmouth, and general loss of uniformity of flow parameters. The schedule of inlet valve opening appears to be an area of great improvement potential with regard to flow quality.



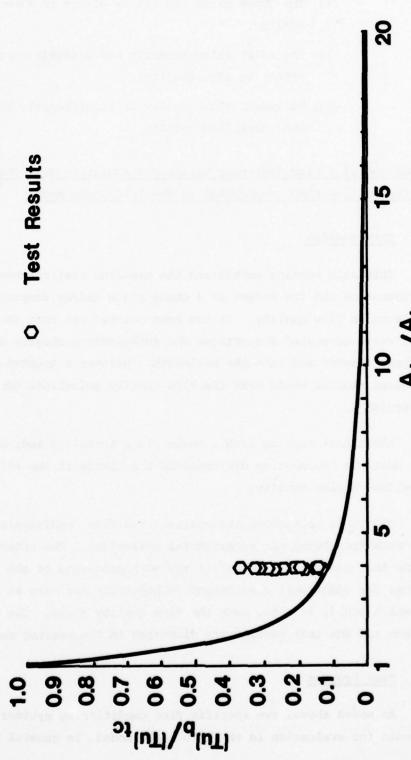


Figure 40. Prediction of Turbulence Levels in 1/10 Scale Model

The following general conclusions can be drawn:

- The choke plane had little effect on flow quality.
- 2) The inlet valve schedule had a significant effect on flow quality.
- 3) Bellmouth flow quality is significantly better than tank flow quality.

J. Comparison of a Flow Centering Device and Auxiliary Test Chamber for Controlling Flow Development in the 1/10 Scale Model

1. Introduction

Initially testing emphasized the baseline test chamber configuration and the effect of a choke plane and/or compressor simulator on flow quality. It has been pointed out that the inlet valve generated distortions and turbulence propogate down the test chamber and into the bellmouth. Neither a treated or untreated chamber would meet the flow quality guidelines discussed in Section I.

Additional testing with a choke plane installed indicated that upstream propogating disturbances had little if any effect on bellmouth flow quality.

With this background information, two flow conditioning systems were formulated for experimental evaluation. The objective of the test program was to select the more promising of the two devices for additional development -- hopefully arriving at a system which would, in fact, meet the flow quality goals. The two systems and the test results are discussed in the ensuing sections.

2. Test Program

As noted above, two specific flow conditioning systems were designed for evaluation in the 1/10 scale model. In general terms,

the systems consisted of an auxiliary test chamber or barrel and a flow centering device or diffuser. The specific configurations evaluated were:

- Barrel, Modification 1 a cylinder of 14.4 inches diameter and 20.4 inches length forms an aerodynamic path at the bellmouth inlet. The front face of the barrel supports a flow straightener and two screen holders.
- 2) Barrel, Modification 2 a configuration identical to Modification 1, except that two screens are now located in the barrel. Figure 41 indicates Modifications 1 and 2 to the barrel. Figure 42 is a photograph of the barrel with the screens installed.
- 3) Barrel, Modification 3 the same as Modification 2 with the addition of an inlet bellmouth on the barrel.
- 4) Barrel, Modification 4 Modification 3 with the barrel bellmouth smoothed in an attempt to lower boundary layer turbulence.
- 5) Flow Centering Device, Modification 1 an entrance cone of 120° included angle, leading to a cylindrical section, leading to an exit diffuser. The diffuser shown in Figure 43 consists of three nested cones, the largest of which has a 60° included angle. A flow straightening section in the cylindrical sections consists of packed 3/4" diameter thin wall conduit and six inch length and recessed from the inlet 1/2 inch. A perforated plate (1/8 inch diameter holes on 3/16 inch spacing in an equilateral triangular pattern) is located within the entrance cone as shown in Figure 44. The entire assembly sits in the test chamber aft of the front bulkhead, containing the inlet valves and corebusters.
- 6) Flow Centering Device, Modification 2 is the same as Modification 1 with the exception of the diffuser. The

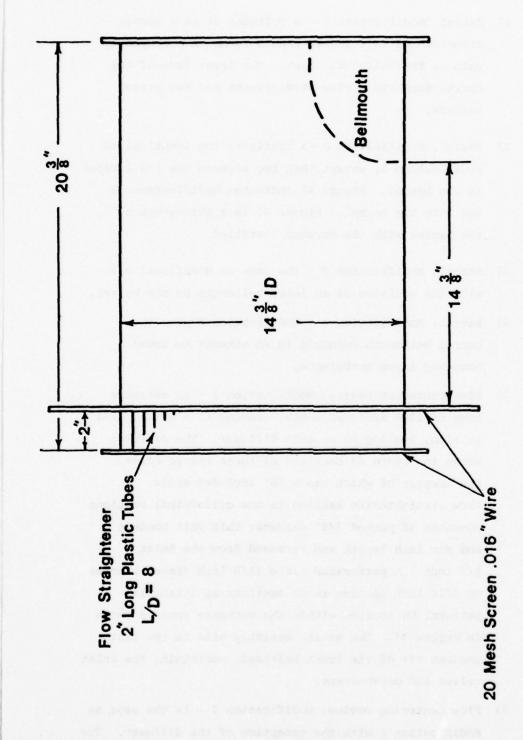


Figure 41. Schematic of Barrel Flow Conditioning Device

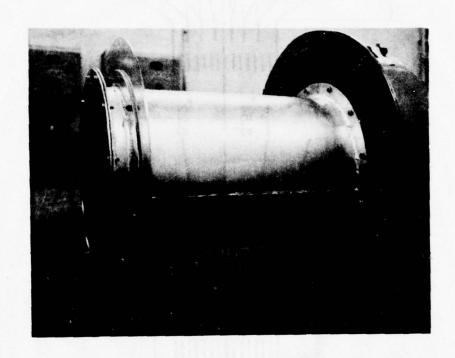


Figure 42. Barrel Assembly as Installed.

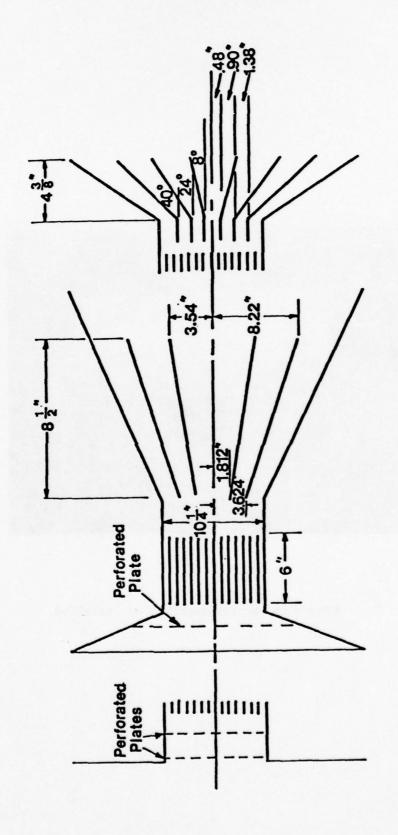


Figure 43. Schematic of Flow Centering Device

MODIFICATION 1

MODIFICATION 4

MODIFICATION 2

diffuser consists of four nested cones, the largest having an included angle of 112°. This arrangement has the advantage of being shorter, but the complication of an additional cone. Figure 43 gives details, Figure 45 an axial view, and Figure 46 a lateral view of the device. Tests were run with and without a perforated plate (of pattern described above) at the diffuser outlet.

- 7) Flow Centering Device, Modification 3 differs from Modification 2 only in the presence of two perforated plates (pattern described above) in the exit diffuser, and the removal of the inner cones. The first of these is at the 18" diameter location; the second at 23-1/4 inches.
- 8) Flow Centering Device, Modification 3a differs from Modification 3 only in the absence of a perforated plate at the 23-1/4 inch diameter location in the exit diffuser.
- 9) Flow Centering Device, Modification 4 differs from Modification 3a via the presence of a modified entrance section. The entrance cone has been replaced by a full face bulkhead with a hole in the center. A short cylinder connects the cone to the original flow straightener. This connecting cylinder contains two perforated plates of 0.161 inch hole diameter on 3/16 inch spacing in an equilateral triangle array, one at 1/4 inch, the other at 1-3/4 inch from the bulkhead. In addition, corebusters were removed from the inlet valves.
- 10) Flow Centering Device, Modification 5 Modification 3 with three perforated plates in the entrance cone, one perforated plate in the exit cone, and two screens downstream in the test chamber. The perforated plates in the entrance cone have diameters of 19, 15 and 11 inches. A perforated plate of 17 inch diameter

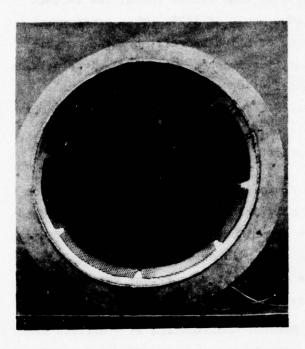


Figure 44. Entrance Cone and Perforated Plate of Flow Centering Device

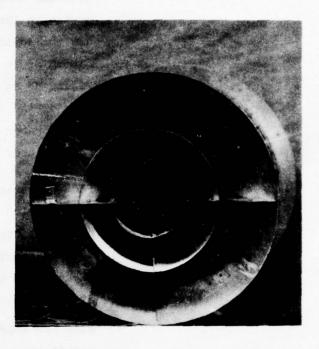


Figure 45. Flow Centering Device Showing Diffuser of Nested Cones



Figure 46. Lateral View of Flow Centering Device, Modification 2

- sits at the exit cone and the three inner cones are removed. Two screens are placed 6 and 9 inches downstream of the exit cone.
- 11) Flow Centering Device, Modification 6 Modification 5 with the exit cone of Modification 2. At the exit cone is placed a honeycomb straightener of 6 inch length and covering the entire tank diameter. The honeycomb is of hexagonal pattern with face-to-face dimension of 5/32 inch. Screens are placed 3 and 6 inches downstream of the honeycomb straightener.
- 12) Front End Device, Modification 1 consists of perforated plates covering the entire tank diameter at 5, 6 and 15 inches from the tank front bulkhead joint, the honeycomb mentioned above between 16 and 22 inches and screens at 22 and 25 inches from the joint.
- 13) Front End Device, Modification 2 consists of a venturi bank from 5 to 10 inches from the bulkhead joint and a perforated plate at 13 inches. The venturi banks consist of a supporting plate made up of 19 venturis of 2-9/16 inch inlet diameter on 2-3/4 inch spacing.
- 14) Front End Device, Modification 3 similar to Modification 2, but in addition contains another perforated plate and 2 screens downstream of the venturi bank.
- 15) Barrel, Modification 5 installation of a flow straightening element immediately downstream of the last screen. This provides a structural support for the final screen assembly and minimizes the chance of screen ingestion by the compressor in the event of a failure.

Tables 17 and 18 give an overview of this portion of the test program with regard to the flow conditioning element configuration.

TABLE 17 COMPRESSOR RESEARCH FACILITY 1/10 SCALE MODEL TEST PROGRAM BASIC AUXILIARY TEST CHAMBER CONFIGURATION

Bellmouth Treatment	Choke Plate	Choke Plate	Choke Plate	Choke Plate	Choke Plate	Choke Plate	Choke Plate	Empty	Empty	Empty	Empty	Empty	Empty	Empty	Empty	Empty	Empty	Empty	Empty	Empty	Empty	Empty	Empty	Empty	Empty
Test Chamber Treatment	Corebusters Only	Corebusters Only	Corebusters Only	Modification 1, Corebusters	Modification 1, Corebusters	Mod 1, Corebusters, Perforated Plate	Mod 1, Corebusters, Perforated Plate	Corebuster Only	Corebuster Only	Corebuster Only	Barrel, Corebusters	Barrel, Corebusters	Barrel, Corebusters	Modification 2	Modification 2	Modification 2	Modification 3	Modification 3	Modification 3	Modification 3a	Modification 3a	Modification 3a	Modification 4	Modification 4	Modification 4
Valve	Balanced	Balanced	Balanced	Balanced	Balanced	Balanced	Balanced	Design	Design	Design	Design	Design	Design	Design	Design	Design	Design	Design	Design	Design	Design	Design	Design	Design	Design
Approximate Corrected Mass Flow 1bm/sec	5.7	5.25	3.3	5.4	5.2	5.5	5.2	2.3	3.4	5.7	2.3	3.4	5.7	2.3	3.4	5.7	2.2	3.3	5.6	2.0	3.2	5.5	2.3	3.4	5.7
Test Numbers	1:	1-3	1-4	2-4	1-4	5-8	3-4	1025-8	1035-8	1045-8	2045-8	2055-8	2065-8	1085-8	1095-8	1105-8	1145-8	1155-8	1165-8	1318	1328	1328	1205-8	1215-8	1225-8
Date	3-22	4-19	3-18	3-25	4-08	3-25	4-08	4-28	4-26	4-28	5-03	5-03	5-03	5-13	5-13	5-13	5-17	5-17	5-17	5-17	5-17	5-17	5-27	5-27	5-27

TABLE 18
COMPRESSOR RESEARCH FACILITY 1/10 SCALE MODEL TEST PROGRAM MODIFIED AUXILIARY TEST CHAMBER CONFIGURATION

	Test Chamber Treatment	{FCD (Modification 5)	FCD 5 - do not confuse	with similarly numbered	runs on 5/17/76	(Barrel (Modification 3)			Barrel 4		Barrel 1 +	Front End 1	(Barrel 2 +	FCD 6		(Barrel 2 +	Front End 3		Front End 1	(Front End 3	~		Front End 2	~	
	Valve	Design	Design	Design	Design	Design	Design	Design	Design	Design	Design	Design	Design	Design	Design	Design	Design	Design	Design	Design	Design	Design	Design	Design	Design
Approximate Corrected	Mass Flow lbm/sec	2.3	3.4	5.8	2.2	2.3	3.4	5.7	2.2	3.3	2.2	5.7	2.2	3.4	5.7	2.3	3.3	5.4	2.5	2.4	3.3	5.8	2.3	3.5	5.9
	Date	6-21-76	6-21-76	6-21-76	6-21-76	6-28-76	6-28-76	6-28-76	7-22-76	7-22-76	92-2-9	9/-/-9	6-22-76	6-22-76	6-22-76	6-22-76	6-22-76	6-22-76	6-10-76	6-24-76	6-24-76	6-24-76	6-24-76	6-24-76	6-24-76
	Test Number	1265-8	1337-8	1347-8	1405-8	2165-8	2175-8	2185-8	2225-8	2235-8	3045-8	3065-8	3105-8	3115-8	3125-8	3165-8	3178	3188	4015-8	4075-8	4088	4098	4135-8	4148	4158

Experimental Results

Tables 19 and 20 summarize the experimental results. Listed are date, test number, configuration, corrected and actual mass flowrates, mean static and total pressures, mean turbulence levels and mean velocities in both the bellmouth and test chamber. Distortion parameters are also presented.

On several runs, data are incomplete. The installation of the flow conditioning devices in some cases precluded the possibility of a hot wire traverse of the test chamber. In these cases, the average chamber values are deleted.

Figures 47 through 54 show in detail the distribution of turbulence and velocity from the hot wire traverses. Data is presented for tests 3045 through 3048 and 3065 through 3068. Additional plots of all the data of Tables 19 and 20 are continued in references 53, 54, and 55.

Four figures correspond to each test point. The mean velocity and turbulence level are presented for the test chamber and bellmouth. The maximum value of each parameter is given in the figure legend. All variables are non-dimensionalized with maximum values and thus are scaled from 0 to 1. The station numbers are also noted. The parameter value, i.e., $\phi/\phi_{\rm max}$, at the outer most radial position is also presented on each figure. The valve location relative to the traverse is shown in Figure 17. Note that the velocity profiles in the test chamber are approximately parabolic while those in the bellmouth are fairly flat. The turbulence profiles are more irregular with a substantial reduction in mean value in the bellmouth.

Comparison of runs with an empty test chamber to those with flow conditioning elements shows that the elements do improve flow quality with regard to turbulence level in the bellmouth.

TABLE 19 EXPERIMENTAL RESULTS FOR THE BASIC BARREL CONFIGURATIONS

				m√Rt _{ref}											
-		Confin		Rp _{ref}		Val	ve Sett	ing		(Ptc)m	(Ptc)m	(p _b) _m	(P _b) _m	(Utc) m	(U _b) _m
Test No.	Date	Config- uration	lb_/sec	lb /sec	14	20	24	36L	36R	lbf/in2	lbf/in2	lbf/in2	lbf/in2	ft/sec	ft/sec
_	-				-	-	-	_	_		<u>-</u>				
1265	6-21-76	FCD	1.83	2.40	90	90	65	24	0	11.17	11.18	10.98	11.16	11.2	175 180
1266 1267	6-21-76	MOD 5	1.61	2.43	90	90	52 13	15	0	9.74 7.20	9.74 7.20	9.57 7.09	9.74 7.19	10.1	162
1268	6-21-76		0.65	2.18	90	40	15	0	0	4.38	4.38	4.32	4.38	9.8	160
1337	6-21-76	FCD 5 - Do not confuse with	0.94	3.47	90	90	49	20	0	7.17	7.17	6.92	7.16 4.29	16.0 14.9	252 234
1338	6-21-76	similarly num-	2.58	5.71	90	67 90	90	34	0	4.31 7.16	4.31 7.16	4.17 6.52	7.15	24.7	411
1348	6-21-76	bered runs on	1.57	5.85	90	90	47	16	0	4.27	4.27	3.87	4.26	25.8	418
1405	6-21-76	5/17/76	1.82	2.38	00		recor 52	ded 12	0	11.19 9.72	9.72	9.56	9.72	11.2	174 178
1407	6-21-76		1.61	2.43	90	90 75	22	0	0	7.49	7.49	7.39	7.49	9.8	155
1408	6-21-76	Barrel	0.60	2.02		not	recor			4.31	4.31	4.25	4.30	9.0	148
2165 2166	6-28-76	MOD 3	1.77	2.33	90	90	65 t recor	20	0	9.80		9.58	9.74		169 176
2167	6-28-76	MOD 3	1.07	2.17	90	75	26	0	0	7.30		7.15	7.24		158
2168	6-28-76		0.65	2.19	90	40	18	0	0	4.40		4.32	4.38		160
2175 2176	6-28-76		2.61	3.53 3.47	90	90	90	43	5	11.23 9.85		9.39	9.70		252 248
2177	6-28-76		1.63	3.42	90	90	82 49	20	0	7.22		6.90	7.12		247
2178	6-28-76		0.98	3.39	90	67	22	0	0	4.38		4.19	4.32		243
2185 2186	6-28-76		3.47	5.86 5.77	90	90 90	90	73 57	23 18	11.17 9.77		9.91 8.70	9.54		417
2187	6-28-76		2.57	5.73	90	90	90	33	0	7.28		6.49	7.09		405
2188	6-28-76		1.56	5.57	90	90	47	16	0	4.54		4.06	4.41		390
2225 2226	7-22-76		1.76	2.34	90	90	65 52	26 16	0	9.65		9.44	9.59		170 173
2227	7-22-76	Barrel	1.07	2.15	90	75	29	0	0	7.39		7.23	7.33		156
2228	7-22-76	MOD 4	0.54	1.80	90	40	20	0	0	4.41		4.32	4.36		131
2235 2236	7-22-76		2.55	3.49	90	90	90 82	43	5	9.86		9.43	10.98 9.72		248 238
2237	7-22-76		1.58	3.26	90	90	49	19	0	7.32		7.04	7.25		237
2238	7-22-76	Barrel 1	0.99	3.30	90	67	25	0	0	4.53		4.34	4.48	10.9	242 155
3045 3046	6-07-76	Front End 1	1.69	2.14	90	90	65 52	20.5	0	9.77	9.77	9.59	11.63 9.75	11.9	173
3047	6-07-76		1.07	2.19	90	75	21.5	0	0	7.20	7.20	7.07	7.17	10.8	158
3048 3065	6-07-76		3.99	1.80	90	40	15	0	0	4.42	4.42	4.35	4.39	10.2 26.6	130
3066	6-07-76		3.46	5.61	90	90	90 90	73 57	23 15.5	9.92	9.92	8.96	9.78	26.5	403
3067	6-07-76	Barrel 2	2.97	6.62	90	90	90	33	0	7.23	7.23	6.49	7.31	30.7	467
3068 3105	6-07-76		1.57	2.34	90	90	52 65	23	0	4.43	4.43	3.99 10.96	4.36	26.1	170
3106	6-22-76		1.51	2.28	90	90	52	13	0	9.79		9.58	9.73		166
3107	6-22-76	FCD 6	1.07	2.17	90	75	28	0	0	7.28		7.13	7.23		157
3108 3115	6-22-76		2.57	3.46	90	40 90	19 90	43	7	11.23		4.36	4.40		142 251
3116	6-22-76		2.22	3.42	90	90	82	20	ó	9.79		9.38	9.70		249
3117 3118	6-22-76		1.63	3.40	90	90	49	19	0	7.22		6.91	7.14		247
3125	6-22-76		0.95 3.97	5.75	90	90	18 90	73	37	11.19		10.00	4.35		232 411
3126	6-22-76		3.47	5.70	90	90	90	57	22	9.82		8.81	9.64		407
3127 3128	6-22-76	Barrel 2	1.51	5.66	90	90	90 47	31	0	7.25		6.48	7.07 4.26		402 405
3165	6-22-76		1.72	2.26	90	90	65	13	0	4.36		3.89 10.98	11.14		164
3166	6-22-76	Front End 3	1.60	2.43	90	90	52	12	0	9.78		9.54	9.70		179
3167 3168	6-22-76		0.60	2.27	90	75 40	21 15	0	0	7.25 4.40		7.11	7.21 4.37		160 145
3178	6-22-76		0.98	3.28	90	67	18	0	0	4.52		4.34	4.47		233
3188 4015	6-22-76	Front End 1		5.37	90	90	46	13	0	4.52		4.05	4.38		380
4017	6-10-76		1.88	2.48	90	90 75	66 23	21	0	7.64	7.64	7.53	7.63	11.6	181 155
4018	6-10-76		0.87	3.00	90	40	12	0	0	4.26	4.27	4.24	4.31	14.4	215
4075	6-24-76		1.83	2.40	90	90	65	21.5	0	11.19	11.20	11.00	11.18	11.5	174
4077	6-24-76	Front End 3	1.62	2.45	90	90	52 25	14	0	9.71 7.13	9.71 7.13	7.01	9.70 7.13	11.4	178 175
4078	6-24-76		0.66	2.21	90	40	19	0	0	4.36	4.37	4.29	4.35	10.8	154
4088 4098	6-24-76		0.95	3.26 5.78	90	67	20	0	0	4.35	4.35	4.21	4.33	15.6 24.6	234 398
4135	6-24-76		1.56	2.32	90	90	65	7.5	0	4.30	4.30	3.91 10.95	11.12	11.8	169
4136	6-24-76		1.62	2.46	90	90	52	15.5	0	9.71	9.71	9.54	9.71	12.1	178
4137	6-24-76	Front End 2	0.65	2.22	90	75 40	23.5	0	0	7.09 4.18	7.09 4.18	6.98 4.12	7.08 4.18	11.3	162
4148	6-24-76		0.96	3.52	90	67	21.5	0	0	4.07	4.07	3.93	4.07	17.2	252
4158	6-24-76		1.54	5.91	90	90	46.5	15	0	4.16	4.16	3.76	4.14	28.2	416

TABLE 19
EXPERIMENTAL RESULTS FOR THE BASIC BARREL CONFIGURATIONS

	Valv	ve Set			(p _{tc}) _m	(P _{tc}) _m	(p _b) _m	(P b) m	(U _{tc}) _m	(u ^p) ^m	(Tu _{tc}) _m	(Tu _b) _m	(o _U 2) tc	(σ ₁₁ 2) _b	Tutc	Tu	Tu /Tu
2	20	24	36L	36R	lb _f /in ²	lbf/in ²	1bf/in2	1bf/in2	ft/sec	ft/sec	<u>.</u>	•			tc	Tu _b	Tub/Tutc
0	90 90	65 52	24 15	0	11.17 9.74	11.18 9.74	10.98	11.16 9.74	11.2 11.3	175 180	6.9 18.2	0.6	.049	.016	.18	.31	.08
0	90	13	0	0	7.20	7.20	7.09	7.19	10.1	162	39.5	1.1	.120	.012	.07	.20	.06
0	40 90	15 49	20	0	4.38 7.17	4.38	4.32	4.38 7.16	9.8	160 252	30.9 32.7	1.8	.098	.014	.20	.12	.06
0	67	20	0	0	4.31	7.17 4.31	6.92 4.17	4.29	14.9	234	36.7	1.4	.283	.009	.08	.20	.04
10	90	90	34	0	7.16	7.16	6.52	7.15	24.7	411	5.5	1.3	.076	.017	.17	.28	.23
Ю	90 not	47 reco	16	0	4.27 11.19	4.27	3.87 11.00	4.26	25.8	418 174	24.8 5.3	0.5	.084	.008	.29	.13	.04
10	90	52	12	0	9.72	9.72	9.56	9.72	11.2	178	23.4	0.6	.084	.018	.17	.26	.03
ю	75	22	0	0	7.49	7.49	7.39	7.49	9.8	155	43.9	0.9	.127	.013	.05	.26	.02
0	90	reco 65	rded 20	0	4.31	4.31	4.25 11.00	4.30 11.17	9.0	148 169	36.1	0.4	.273	.019	.14	.13	.04
		reco			9.80		9.58	9.74		176		0.5		.022		.08	
0	75	26	0	0	7.30		7.15	7.24		158		0.8		.019		.13	
90	90	18	43	0	4.40		4.32	4.38		160 252		0.3		.016		.06	
00	90	82	20	0	9.85		9.39	9.70		248		0.4		.020		.10	
90	90 67	49	20	0	7.22		6.90	7.12 4.32		247 243		0.6		.020		.09	
90	90	90	73	23	4.38		9.91	10.89		417		0.9		.021		.15	
90	90	90	57	18	9.77		8.70	9.54		411		0.5		.013		.12	
90 90 90 90 90 90 90 90 90	90	90 47	33 16	0	7.28 4.54		4.06	7.09 4.41		405 390		0.5		.016		.18	
90	90	65	26	0	11.20		10.95	11.12		170		0.4		.022		.16	
00	90	52	16	0	9.65		9.44	9.59		173		0.5		.022		.10	
90	75 40	29	0	0	7.39		7.23 4.32	7.33 4.36		156 131		1.0		.020		.27	
90	90	90	43	5	11.09		10.60	10.98		248		0.4				.29	
90	90	82	22	0	9.86		9.43	9.72		238		0.4		.019		.32	
90	90 67	49	19	0	7.32 4.53		7.04	7.25 4.48		237 242		1.0		.019		.15	
90	90	65	20.5	0	11.67	11.67	11.48	11.63	10.9	155	7.2	0.7	.421	.022	. 37	.24	.10
90	90	52	11	0	9.77	9.77	9.59	9.75	11.9	173	9.4	1.3	.403	.022	.25	.60	.13
90	75 40	21.5	0	0	7.20 4.42	7.20 4.42	7.07 4.35	7.17 4.39	10.8	158 130	14.4 48.6	3.9	.724	.024	.63	.43	.20
90	90	90	73	23	11.26	11.26	10.12	11.07	26.6	407	5.2	1.3	.404	.020	.43	.46	.25
90	90	90	57 33	15.5	9.92 7.23	9.92	8.96	9.78 7.31	26.5 30.7	403 467	7.5 8.6	1.9	.419	.021	.27	.35	.25
90	90	52	14	0	4.43	7.23	6.49 3.99	4.36	26.1	407	11.0	2.1	.359	.019	.29	.14	.19
90	90	65	23	0	11.20		10.96	11.13		170		0.3		.018		.16	
90	90 75	52 28	13	0	9.79 7.28		9.58 7.13	9.73 7.23		166 157		0.3		.016		.18	
90	40	19	0	0			4.36	4.40		142		0.6		.015		.42	
90	90	90 82	43	7	9.79		10.75	11.12 9.70		251 249		0.3		.021		.21	
90	90	49	19	0	7.22		9.38 6.91	7.14		247		0.4		.012		.28	
90	67	18	0	0	4.42		4.23	4.35		232		0.6		.010		.22	
90	90	90	73 57	37 22	9.82		8.81	10.96 9.64		411 407		0.5		.042		.19	
90	90	90	31	0	7.25		6.48	7.07		402		0.5		.014		.30	
90	90	65	13	0	4.36		3.89	4.26		405		0.6		.013		.26	
90	90	52	12	0	11.22 9.78		10.98 9.54	9.70		164 179		0.3		.023		.10	
90	75	21	0	0	7.25		7.11	7.21		160		0.5		.019		.19	
90	40 67	15	0	0	4.40		4.32	4.37		145 233		0.8		.017		.19	
90	90	46	13	0	4.52		4.34	4.38		380		0.6		.018		.16	
90	90	66	21	0	11.20	11.20	11.00	11.20	11.6	181	19.2	0.7	.088	.021	.34	.17	.04
90	75 40	23 12	0	0	7.64 4.26	7.64 4.27	7.53 4.24	7.63 4.31	10.4	155 215	49.9 53.2	1.0	.217	.038	.18	.19	.02
90	90	65	21.5	0	11.19	11.20	11.00	11.18	11.5	174	5.5	0.9	.073	.022	.22	.54	.17
90	90 75	52	14	0	9.71	9.71	9.54	9.70	11.4	178	6.5	0.9	.163	.021	.17	.35	.13
90	40	25 19	0	0	7.13 4.36	7.13 4.37	7.01 4.29	7.13 4.35	11.7	175 154	10.7 12.1	1.5	.231	.018	.56	.35	.13
90	67	20	0	0	4.35	4.35	4.21	4.33	15.6	234	12.1	1.4	.162	.022	.42	.35	.12
90	90	65	7.5	0	4.30	4.30	3.91	4.27	24.6 11.8	398	8.8 23.2	7.7 1.52	.146	.023	.42	.19	.88
90	90	52	15.5	0	9.71	9.71	9.54	9.71	12.1	169 178	21.9	1.1	.622	.017	.32	.39	.05
90	75	23.5	0	0	7.09	7.09	6.98	7.08	11.3	162	20.2	1.8	.843	.020	.45	.38	.09
90	40 67	16.5	0	0	4.18	4.18	4.12 3.93	4.18	11.8	164 252	31.5 22.9	1.6	.610	.020	.28	.41	.08
90	90	46.5		0	4.16	4.16	3.76	4.14	28.2	416	20.5	1.2	.512	.020	.33	.23	.06
8																	

TABLE 20 EXPERIMENTAL RESULTS FOR THE MODIFIED BARREL CONFIGURATIONS

			m/Rt _{ref}		Va	lve Se	tting		(Ptc)m	(P _{tc}) _m	(Pb)m	(P _b) _m	(Utc) m	(U _b) _m	(TU _{tc}) _m
No.		fig- m tion lbm/sec	Rp _{ref} lb _m /sec	14	20	24	36L	36R	lbf/in2	1bf/in2	lb _f /in ²	lb _f /in ²	ft/sec	ft/sec	•
1 2	3-22-76 3-22-76	7 4.71 4.42	5.76	90 90	90 90	90 90	90 64	90 67	13.37 12.64	13.38 12.65	11.89 11.30	13.01 12.33	23.6 23.4	401 396	38.0 34.7
3 4	3-22-76 3-22-76	3.95	5.70 5.74	90	90	90	50 37	51 40	11.25	11.25	10.03	10.99	23.2 23.5	404 398	35.6 38.8
1 2	4-19-76 Empty, 4-19-76 busters	Core- 4.16	5.68	90	90	90	65 48	63 48	12.58 11.16	12.58 11.17	11.44	12.32	23.3	370 377	47.1 57.2
3	4-19-76 3-18-76 Choke F	3,20	5.27 5.23	90 90	90	90	34	40	9.69	9.69 13.84	8.84 13.33	9.55 13.75	23.8 14.9	377 237	51.8 47.7
2	3-18-76 3-18-76	3.09	3.32	90	90	90	40	44	12.40	12.40 11.49	11.89	12.27	15.3 15.8	240 239	46.0 41.7
4 2	3-18-75 3-25-76	2.08	3.31 3.21	90	90	87 78	0 71	0 71	9.57	9.57 12.48	9.29	9.55	15.0 22.7	225 384	47.5 32.5
3	3-25-76 Flow Ce 3-25-76 ing Dev		5.46 5.26	90	90	90	50	54 39	11.08	11.08	10.18	10.94	21.2	364 377	40.6
1 2	4-08-76 Mod 4-08-76 Choke P	1 4.31	5.45 5.18	90	90	90	90	90	13.02	13.02 12.59	12.07	12.91	21.1	355	47.7 37.5
3	4-08-76 4-08-76	3.65	5.18 5.19	90	90 90	90 90 90	68 50 36	51	12.59 11.16 9.65	11.16	10.34	12.54 11.10 9.57	21.1 20.8 21.0	364 361 359	33.6 40.0 44.7
5	3-25-76 Mod	3.19	5.18	90	90	90	37	39	9.60	9.60	8.80	9.55	22.6 22.8	385 384	10.6
7	3-27-76 Choke P	late 4.35	5.56	90	90	90	72	72 90	12.51	12.51 12.83	11.48	12.46 12.76	22.3	387	10.4
3	3-25-76 Perfora 4-08-76 Plate i	3.70	5.48	90	90	90	90 50	50	12.82	11.14	10.31	11.06	21.5	385 358	12.6
1045	4-08-76 Test Ch	7 4.05	5.20 5.74	90	90	90	36 48	37 59	9.69 11.27	9.69	10.24	9.61	22.1 25.1	355 400	14.4 39.5
1046	4-28-76 4-28-76	3.49 2.63	5.67	90	90	90	38 24	52 24	9.84 7.43	9.85 7.44	6.79	9.75	23.8	395 397	49.3 49.1
1048	4-28-76 Empty, 4-26-76 busters	Only 2.57	7.58 3.43	90 90	90 90	90	29	27	4.41 11.28	4.41	3.80 10.88	4.38	31.5 16.9	512 246	48.0 45.4
1036 1037	4-26-76	1.65	3.44 3.47	90	90	90 57	0	0	9.82 7.17	9.82 7.17	9.48 6.92	9.79 7.15	16.7	245 274	53.3
1038	4-26-76 4-28-76	1.18	3.19 2.38	90 90	90	72	0	0	4.45 11.29	4.45 11.29	4.30 11.10	4.43 11.28	15.0	228 171	51.1 52.0
1026	4-28-76 4-28-76	1.51	2.27	90	90	53 15	0	0	9.86 7.34	9.87 7.34	9.70 7.20	9.84 7.30	10.8	160	52.7 55.7
1028 2045	4-28-76 L 5-03-76 F	2.23	2.18	90	90	65	20	0	4.47 11.18	4.47	4.35	4.41	10.2	159 211	61.2 46.8
20 4 6 20 4 7	5-03-76 5-03-76	1.55	2.34	90	90 75	52 15	0	0	9.71 7.22	9.71	9.51 7.08	9.66 7.17	10.1	171 156	53.7 58.5
2048 2055	5-03-76 5-03-76	2.58	1.54 3.52	90 90	90	90	43	5	11.21	4.47	4.38 10.57	10.97	7.4 17.1	111 257	50.1 49.3
2056 2057	5-03-76 Barrel	1.65	3.48 3.44	90	90	82 49	16	0	9.77 7.20	9.77 7.21	9,38 6,91	9.70 7.14	17.2 16.8	250 244	48.8 51.8
2058 2065	5-03-76 5-03-76	4.03	2.65 5.78	90	67 90	90	73	25	5.82	5.82 11.23	5.66	5.77 11.06	12.7 25.9	189 410	49.3 42.5
2066 2067	5-03-76 5-03-76	2.56	5.88	90	90	90	57 33	15	9.60 7.22	9.60 7.23	8.56 6.48	9.42 7.07	26.9 26.4	418 400	40.4 50.7
2068 1085	5-03-76 L 5-13-76 C	1.52	2.30	90	90	65	20	0	4.34 11.16	4.34 11.16	3.89 10.98	11.15	9.0	400 167	50.3 37.0
1086	5-13-76 5-13-76	1.54	2.31	90 90	90 75	52 16	0	0	9.75 7.22	9.75 7.22	9.59 7.11	9.74 7.21	9.3	167 160	40.1 38.4
1088	5-03-76 5-13-76 Flow Cer		2.48	90 90	90	90	43	5	3.16 10.77	3.16 10.77	3.09 10.32	3.14	9.9	179 189	32.4 35.8
1096 1097	5-13-76 ing Dev 5-13-76	1.65	3.47 3.42	90	90	82 49	16	0	9.74 7.20	9.74 7.20	9.39 6.96	9.71 7.19	13.3	250 245	38.5 38.2
1098 1105	5~13-76 Mod 5~13-76	4.02	3.19 5.71	90 90	67 90	90	73	32	4.36	4.36	10.16	4.34	20.3	230 405	36.6 40.1
1106	5-13-76 5-03-76	2.60	5.68	90	90	90	58 30	18	9.73 7.13	9.73 7.13	8.85 6.48	9.67 7.10	20.4	406 410	42.7 38.9
1108	5-13-76 L 5-17-76 C	7 2.55	5.63 3.42	90	90	90	43	6	4.32 11.05	4.32 11.06	3.93 10.65	11.00	13.9	403 246	37.9 11.4
1156 1157	5-17-76 5-17-76	2.16 1.59	3.06	90	90	82 49	20 16	0	7.07	7.07	10.07 6.84	10.33 7.04	12.6	220 235	13.0
1158	5-17-76 Flow Cer 5-17-76 ing Dev	ce 3.99	3.16 5.68	90	90	90	74	33	4.19 11.06	4.19	10.05	11.03	14.0 21.7	217 412	19.6 10.8
1166 1167	5-17-76 Mod		5.64	90	90	90	33	0	9.65 7.08	9.65 7.09	8.77 6.44	9.69 7.04	21.9 22.1	404 405	11.2
1168	5-17-76 5-17-76	1.51	2.34	90	90	48 65	20	0	4.24 11.05	11.05	3.85 10.87	4.21	9.7	403 169	15.2
1146	5-17-76 5-17-76	1.46	2.21	90	90 75	19	0	0	9.63 7.12	9.64 7.12	9.47 7.01	9.60 7.10	9.3	161 156	12.1
1148	5-17-76 F	7 .514	1.97	90	40	11	0	0	4.26 3.76	4.26 3.76	4.20 3.70	4.25 3.74	9.6	147	20.3
1328	5-17-76 Mod :	1.50	3.15 5.51	90	90	12 48	10	0	4.21	4.21	4.08 3.88	4.19	15.6 24.1	231 391	23.7
1205 1206	5-27-76	1.84	2.28	90	90	65 52	10	0	9.84	11.25 9.84	9.67	9.85	9.3	165 172	9.3
1207 1208	5-27-76 5-27-76	1.14	2.29	90	75 40	16	0	0	7.30 4.38	7.30 4.38	7.20 4.33	7.30 4.39	9.7 9.9	163 159	12.6 22.6
1215 1216	5-27-76 Flow Cer		3.53	90	90	90	21	0	9.81	9.81	9.46	9.78	14.2	252 249	7.7 8.8
1217	5-27-76 ing Dev:	.958	3.39 3.23	90 90	90 67	14	0	0	7.32 4.44	7.32 4.44	7.07 4.30	7.30 4.43	14.1	243 235	13.1 17.6
1225	5-27-76 Mod 6	3.53	5.72 5.71	90	90	90	72 58	17	9.82	11.29 9.82	10.23 8.94	9.77	21.6	404 404	9.5
1227 1228	5-27-76 5-27-76	1.60	5.75	90	90	90 48	34 13	0	7.28 4.51	7.28 4.51	6.61 4.11	7.24 4.49	22.0	407 399	11.6

TABLE 20 EXPERIMENTAL RESULTS FOR THE MODIFIED BARREL CONFIGURATIONS

1bm/s 5.76 5.70 5.74 5.68 5.27 5.23 3.32 3.31 3.21 5.46 5.48 5.18 5.18 5.18 5.18 5.18 5.18 5.18 5.1	RP _{ref}
######################################	
000000000000000000000000000000000000000	
90 90 90 90 90 90 90 90 90 90 90 90 90 9	Va:
90 90 90 90 90 90 90 90 90 90 90 90 90 9	lve Se
90 64 50 37 65 48 34 90 40 20 0 71 50 8 90 68 50 367 50 72 90 50 36 48 38 24 0 29 8 0 0 0 0 0 0 0 0 0 0 0 0 0 0 0 0 0 0	etting 36L
90 67 51 40 63 48 40 90 44 24 0 71 54 39 90 69 51 36 95 27 16 0 0 0 0 0 0 0 0 0 0 0 0 0 0 0 0 0 0	36R
13.37 12.64 11.25 9.77 12.58 11.16 9.69 13.84 12.40 11.49 9.57 12.48 11.08 9.60 13.02 12.59 11.16 9.65 9.60 11.09 12.51 12.82 11.13 9.84 7.43 4.41 11.28 9.82 7.17 4.45 11.29 9.86 7.34 4.47 11.18 9.71 7.22 4.47 11.18 9.71 7.22 4.47 11.19 9.77 7.20 6.82 11.21 9.73 7.13 6.83 11.24 11.99 9.84 7.30 6.88 11.24	(Ptc)m
13.38 12.65 11.25 9.78 12.58 11.17 9.69 13.84 12.40 11.49 9.57 12.48 9.60 13.02 12.59 11.16 9.60 11.09 12.83 11.14 9.69 11.27 9.85 7.44 4.41 11.29 9.87 7.17 4.45 11.29 9.87 7.17 4.47 11.18 9.71 7.22 4.47 11.19 9.71 7.22 4.47 11.19 9.71 7.21 5.82 11.23 9.60 7.23 4.34 11.16 9.75 7.21 5.82 11.27 9.77 7.21 5.82 11.27 9.77 7.21 5.82 11.23 9.60 7.23 4.34 11.16 9.75 7.21 5.82 11.23 9.60 7.23 4.34 11.16 9.75 7.21 5.82 11.23 9.60 7.23 4.34 11.16 9.75 7.20 4.36 11.16 9.75 7.20 4.36 11.16 9.75 7.20 4.36 11.17 9.73 7.13 4.36 11.06 9.65 7.09 4.36 11.07 9.65 9.60 7.23 4.34 11.16 9.75 7.20 4.36 11.16 9.75 7.20 4.36 11.07 9.75 7.20 4.36 11.07 9.74 7.20 4.36 11.06 9.65 7.09 4.37 11.06 9.65 7.09 4.24 11.05 9.64 7.10 4.27 4.28 4.29 7.10 4.36 11.07 9.65 7.09 4.24 11.05 9.64 7.10 4.26 4.21 4.27 11.25 9.84 7.30 4.36 11.07 9.65 7.09 4.24 11.05 9.64 7.12 4.26 4.27 4.28 4.29 7.12 4.26 4.27 4.28 4.29 7.20 4.36 1.07 7.13 4.36 1.07 7.13 4.26 4.27 4.28 4.29 7.20 4.36 4.21 4.23 1.25 9.84 7.30 4.36 4.21 4.23 1.25 9.84 7.30 4.36 4.21 4.23 1.25 9.84 7.30 4.36 4.21 4.25 9.86 7.30 4.36 4.21 4.23 1.25 9.84 7.30 4.36 4.21 4.23 9.86 7.30 4.38 1.25 9.88 4.59 9.88 9.89	(P _{tc}) _m lb _f /in ²
11.89 11.30 10.03 8.73 11.44 10.14 8.84 13.33 11.89 11.16 9.29 11.43 10.18 8.79 12.07 11.67 10.34 8.93 8.80 10.05 11.48 11.77 10.31 8.97 10.34 8.96 6.79 3.80 10.88 9.48 6.92 4.30 11.10 9.70 7.20 4.35 10.95 9.51 7.08 4.38 10.57 9.38 6.91 5.66 6.48 3.89 10.98 9.59 7.11 3.09 10.32 9.39 10.16 8.85 6.48 3.89 10.96 9.59 7.11 3.09 10.32 9.39 10.32 9.39 10.42 10.16 8.85 6.48 3.89 10.96 9.59 7.11 3.09 10.32 9.39 10.32 9.39 10.42 10.16 8.85 6.48 3.89 10.96 9.59 7.11 3.09 10.32 9.39 6.96 4.22 10.16 8.85 6.48 3.89 10.96 9.59 7.11 3.09 10.32 9.39 6.96 4.22 10.16 8.85 6.48 3.89 10.98 9.59 7.11 3.09 10.32 9.39 6.96 4.22 10.16 8.85 6.48 3.89 10.85 10.87 9.47 7.01 4.20 3.88 3.88	(P _b) _m
13.01 12.33 10.99 9.53 12.32 10.94 9.55 12.27 11.51 9.55 12.39 10.94 9.50 12.91 11.10 9.57 9.55 11.08 11.10 9.75 11.08 11.10 9.75 11.08 11.11 9.75 11.08 11.12 9.84 11.12 9.84 7.39 4.38 11.24 9.79 7.15 4.38 11.24 9.79 7.15 4.38 11.28 9.84 7.30 4.41 11.22 9.66 7.17 4.41 11.09 7.19 11.09 7.19 11.09 7.10 11.11 11.12 9.84 7.30 4.41 11.22 9.66 7.17 11.09 9.70 7.14 5.77 11.06 9.70 7.14 5.77 11.06 9.70 7.14 11.15 9.74 7.17 11.06 9.70 7.14 11.15 9.74 7.19 4.34 11.15 9.74 7.19 4.34 11.11 9.67 7.19 4.34 11.11 9.67 7.19 4.34 11.11 9.67 7.19 4.34 11.11 9.67 7.10 4.24 11.15 9.74 7.21 3.14 10.97 9.70 7.14 5.77 7.14 5.77 11.06 9.70 7.14 5.77 7.19 4.34 11.11 9.67 7.10 4.21 11.03 9.69 7.04 4.21 11.04 9.69 7.04 4.21 11.07 9.70 7.04 4.10 9.69 7.07 4.21 11.04 9.69 7.07 4.21 11.04 9.69 7.07 4.21 11.07 9.70 7.10 4.21 11.07 9.70 7.10 4.21 11.03 9.69 7.04 4.21 11.07 7.04 4.21 11.07 7.07 4.21 11.07 7.04 4.21 11.07 7.08 4.21 11.07 7.09 4.21 11.04 9.69 7.00 4.21 11.04 9.69 7.00 4.21 11.04 9.69 7.00 4.21 11.04 9.69 7.00 4.21 11.04 9.69 7.00 4.21 11.04 9.69 7.00 4.21 11.04 9.69 7.00 4.21 11.04 9.69 7.00 4.21 11.04 9.69 7.00 4.21 11.01 9.69 7.00 4.21 11.21 9.85 7.30 4.43 11.21 9.77 7.30 4.43 11.21 9.77 7.30 4.43 11.21 9.77 7.30 4.43 11.21 9.77 7.30 4.43 11.21 9.77 7.30 4.43 11.27 9.77 7.24 4.49 4.49	(P _b) _m lb _f /in ²
23.6 23.4 23.2 23.5 23.8 14.9 15.3 15.8 15.0 22.7 21.1 21.0 21.1 20.8 21.1 22.6 22.8 22.0 21.5 22.1 23.8 25.2 31.5 16.9 16.5 16.7 16.5 15.8 10.6 10.8 10.6 10.8 10.6 10.8 10.6 10.8 10.8 10.9	(U _{tc}) _m
401 398 370 377 237 240 239 239 239 384 361 355 364 367 355 364 367 355 364 367 355 368 358 358 358 358 358 37 37 246 274 228 171 160 160 160 160 160 161 171 160 160 160 160 160 160 160 16	(U _b) _m
38.0 34.7 35.6 38.8 47.1 57.2 51.8 47.7 47.5 32.5 40.0 41.7 10.6 10.4 11.8 12.6 14.2 14.4 19.5 49.3 49.1 48.0 45.4 35.3 53.1 51.1 52.0 52.7 55.7 61.2 46.8 53.3 53.1 51.1 52.0 52.7 55.7 61.2 46.8 53.7 55.7 61.2 46.8 53.7 55.7 61.2 46.8 53.7 55.7 61.2 46.8 53.7 55.7 61.2 46.8 53.7 55.7 61.2 46.8 53.7 55.7 61.2 46.8 53.7 50.7	(TU _{tc}) m
3.5 4.0 4.4 4.5 7.6 8.1 7.1 3.2 4.4 8.6 8.3 8.9 6.4 4.9 4.1 4.1 4.9 4.1 4.1 4.9 4.1 4.1 4.9 4.1 4.1 4.9 4.1 4.1 4.1 4.9 4.1 4.1 4.1 4.9 4.1 4.1 4.1 4.9 4.1 4.1 4.1 4.9 4.1 4.1 4.1 4.9 4.1 4.1 4.1 4.1 4.1 4.1 4.1 4.1 4.1 4.1	(Tu _b) _m
.863 .516 .492 .664 .799 .542 .727 .785 .389 .411 .312 .702 .525 .923 1.030 .800 .569 .972 .239 .334 .364 .485 .330 .164 .605 1.480 .574 .1200 .611 .600 .574 .605 .1480 .628 .628 .628 .628 .628 .638 .638 .638 .638 .638 .638 .638 .63	(o _{u²}) _{tc}
.019 .038 .030 .026 .017 .022 .016 .118 .022 .031 .024 .026 .017 .010 .021 .020 .026 .022 .018 .021 .020 .026 .022 .019 .026 .027 .036 .026 .029 .021 .027 .036 .026 .029 .021 .027 .036 .026 .029 .021 .027 .036 .026 .029 .021 .027 .036 .026 .029 .021 .027 .036 .026 .029 .021 .027 .036 .026 .029 .021 .037 .027 .030 .026 .028 .029 .021 .030 .026 .029 .021 .030 .026 .029 .021 .030 .026 .029 .021 .030 .026 .029 .021 .030 .026 .029 .021 .030 .026 .029 .021 .030 .026 .029 .021 .030 .026 .029 .021 .030 .026 .029 .021 .030 .026 .029 .021 .030 .026 .027 .029 .030 .026 .027 .027 .029 .030 .024 .037 .027 .030 .026 .027 .027 .030 .027 .030 .027 .030 .027 .030 .026 .027 .027 .030 .027 .030 .027 .030 .030 .027 .037 .037 .037 .037 .037 .037 .037 .03	(o ₁₁₂)
101 to 229 250 219 250 219 2519 2117 235 208 257 246 2116 2137 208 216 217 208 217 216 217 217 217 217 217 217 217 217 217 217	T 1
Tub - 284 - 310 - 3217 - 257 - 358 - 162 - 214 - 408 - 308 - 291 - 233 - 264 - 213 - 251	T 11
Tub/Tute .09 .12 .12 .12 .12 .14 .04 .07 .11 .10 .11 .09 .10 .17 .15 .11 .10 .38 .47 .35 .22 .21 .23 .12 .08 .10 .13 .06 .06 .08 .07 .07 .10 .13 .10 .02 .02 .03 .09 .01 .04 .08 .07 .07 .07 .07 .08 .09 .01 .02 .04 .08 .09 .01 .02 .04 .08 .09 .01 .02 .04 .08 .09 .01 .02 .04 .08 .09 .01 .02 .04 .08 .09 .01 .04 .08 .09 .01 .05 .06 .08 .09 .01 .01 .06 .06 .08 .09 .01 .01 .06 .06 .08 .09 .01 .01 .02 .04 .08 .09 .01 .04 .08 .09 .01 .01 .04 .08 .09 .01 .04 .06 .08 .09 .07 .07 .07 .07 .08 .09 .09 .01 .09 .09 .01 .09 .09 .01 .00 .00 .00 .00 .00 .00 .00 .00 .00	The Attention

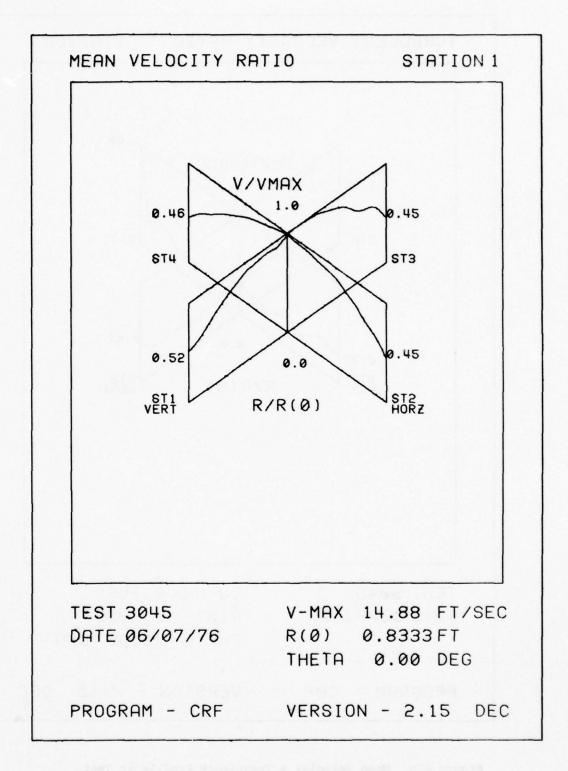


Figure 47a. Mean Velocity & Turbulence Profile in Test Chamber & Bellmouth; Test No. 3045.

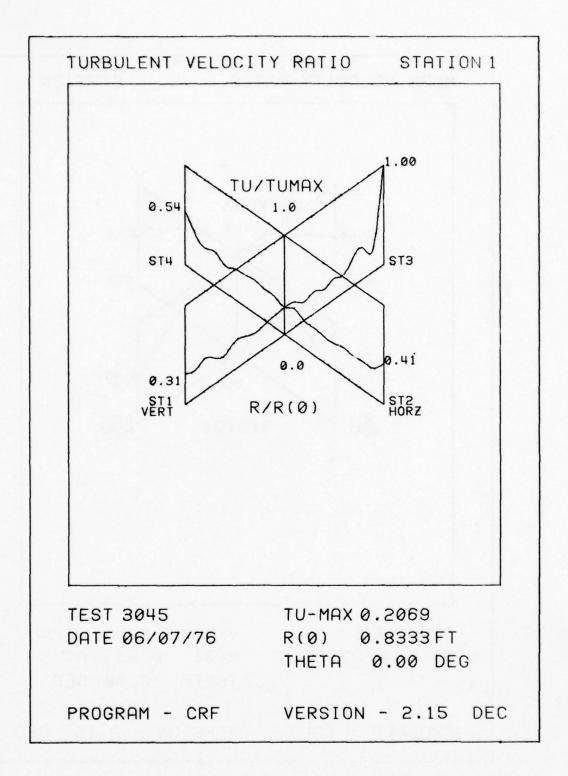


Figure 47b. Mean Velocity & Turbulence Profile in Test Chamber & Bellmouth; Test No. 3045.

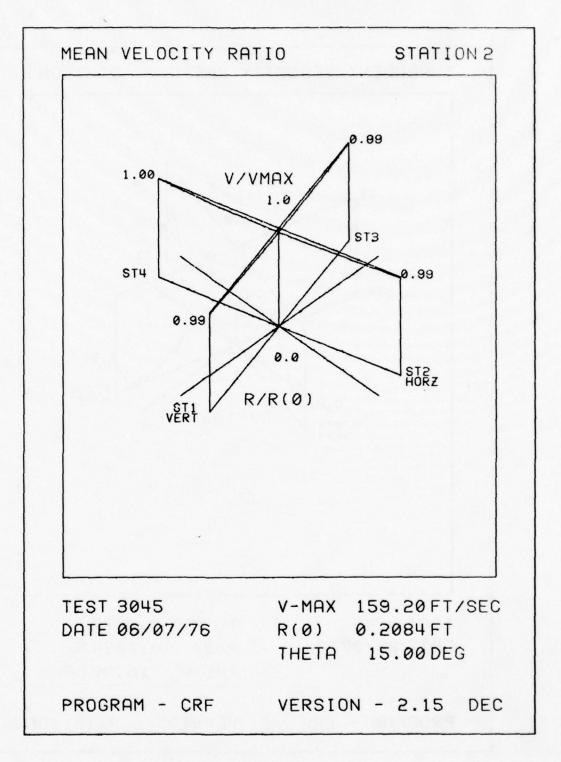


Figure 47c. Mean Velocity & Turbulence Profile in Test Chamber & Bellmouth; Test No. 3045.

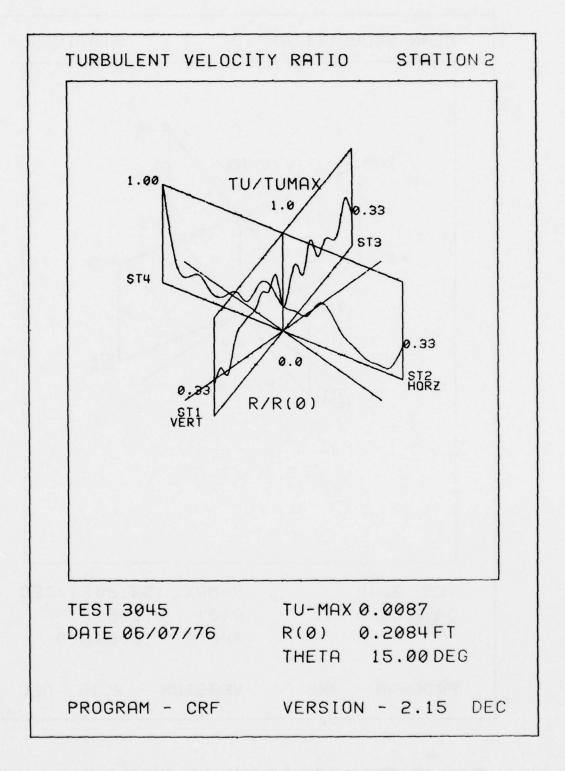


Figure 47d. Mean Velocity & Turbulence Profile in Test Chamber & Bellmouth; Test No. 3045.

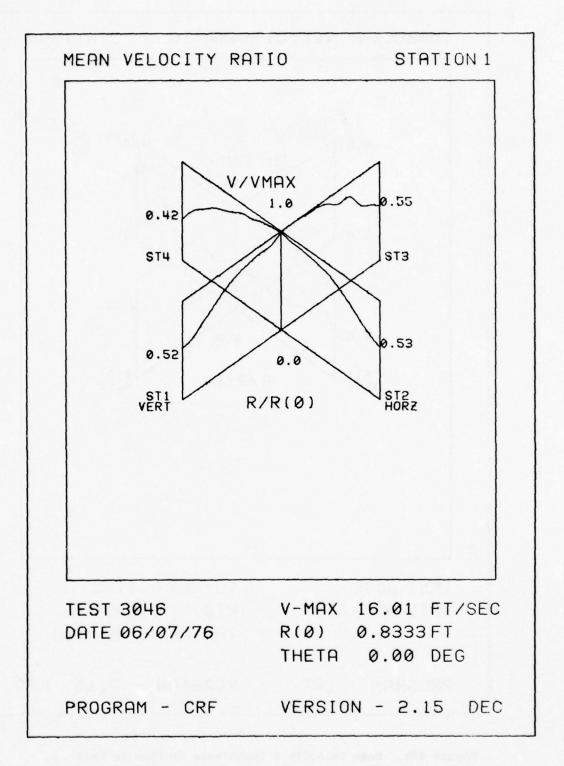


Figure 48a. Mean Velocity & Turbulence Profile in Test Chamber & Bellmouth; Test No. 3046.

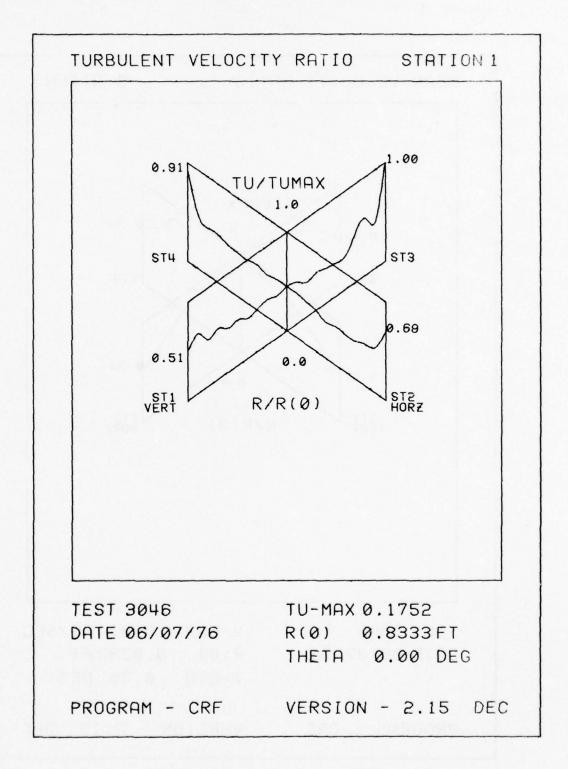


Figure 48b. Mean Velocity & Turublence Profile in Test Chamber & Bellmouth; Test No. 3046.

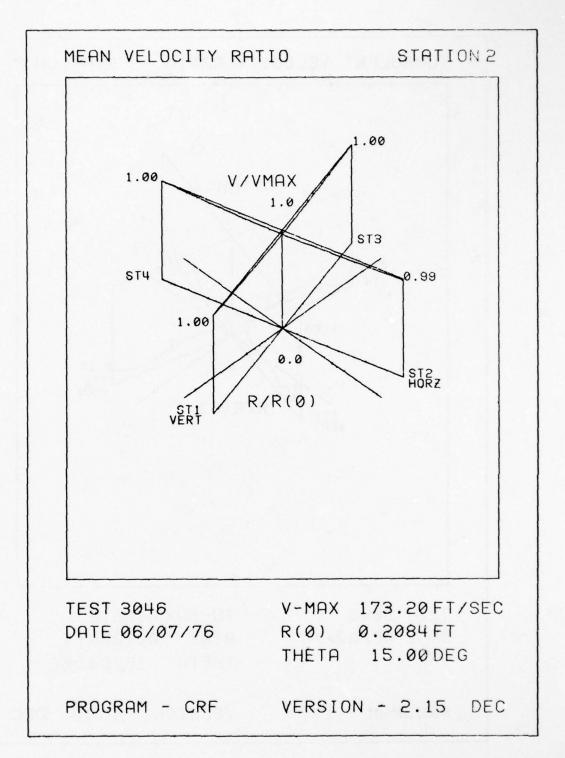


Figure 48c. Mean Velocity & Turbulence Profile in Test Chamber & Bellmouth; Test No. 3046,

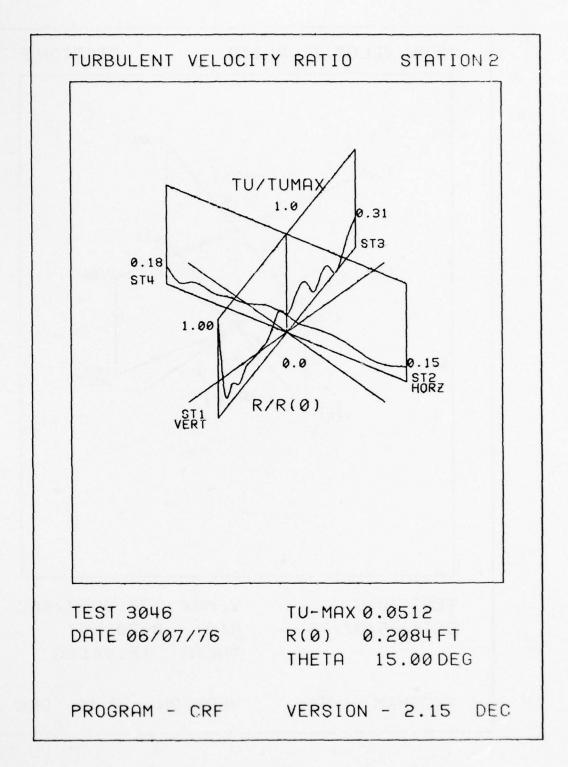


Figure 48d. Mean Velocity & Turbulence Profile in Test Chamber & Bellmouth; Test No. 3046.

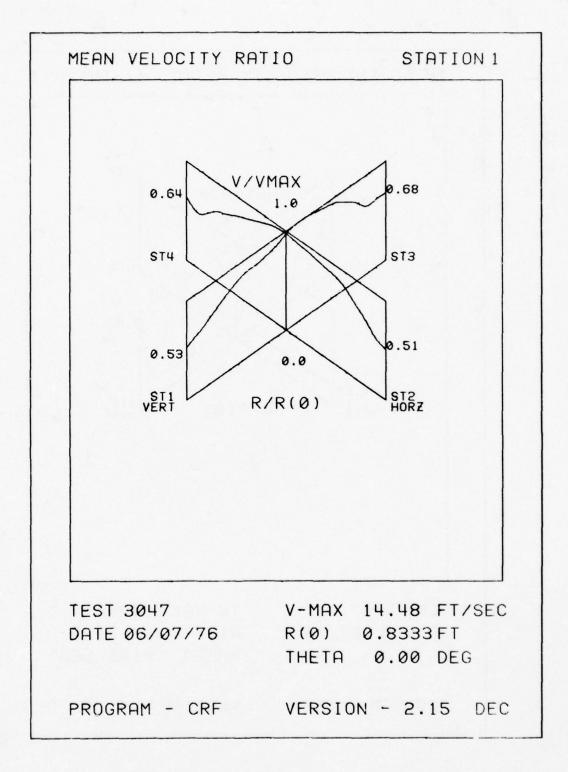


Figure 49a. Mean Velocity & Turbulence Profile in Test Chamber & Bellmouth; Test No. 3047.

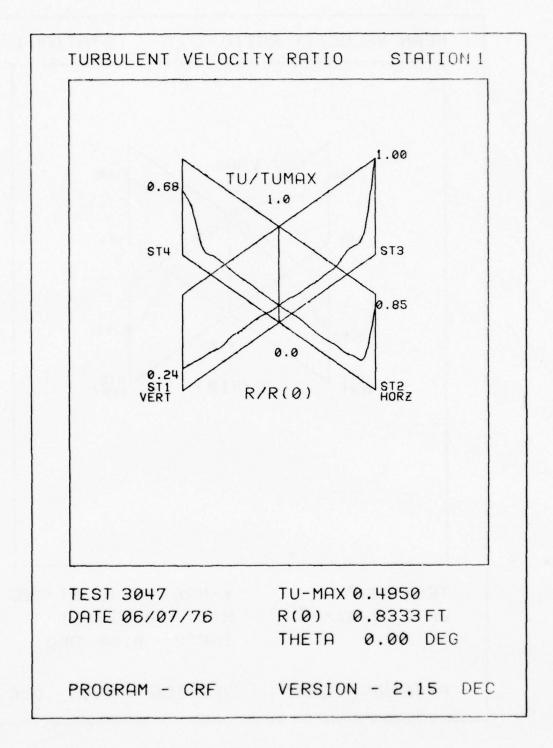


Figure 49b. Mean Velocity & Turbulence Profile in Test Chamber & Bellmouth; Test No. 3047.

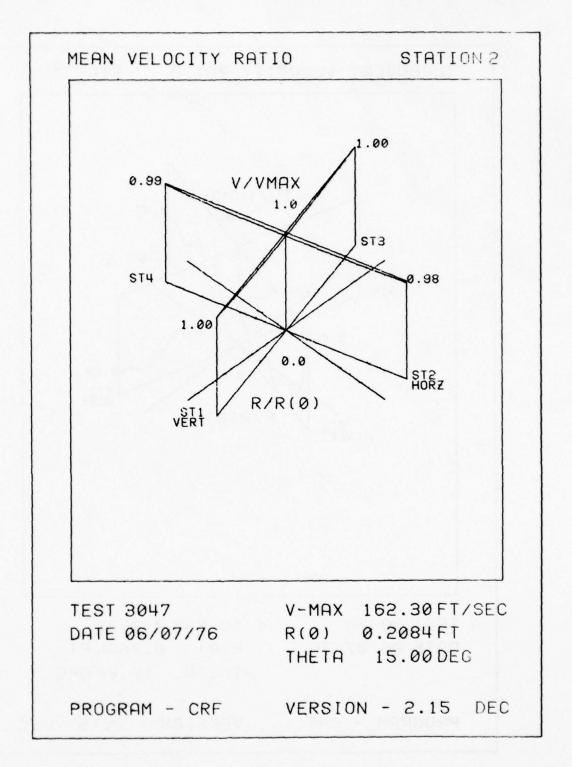


Figure 49c. Mean Velocity & Turbulence Profile in Test Chamber & Bellmouth; Test No. 3047.

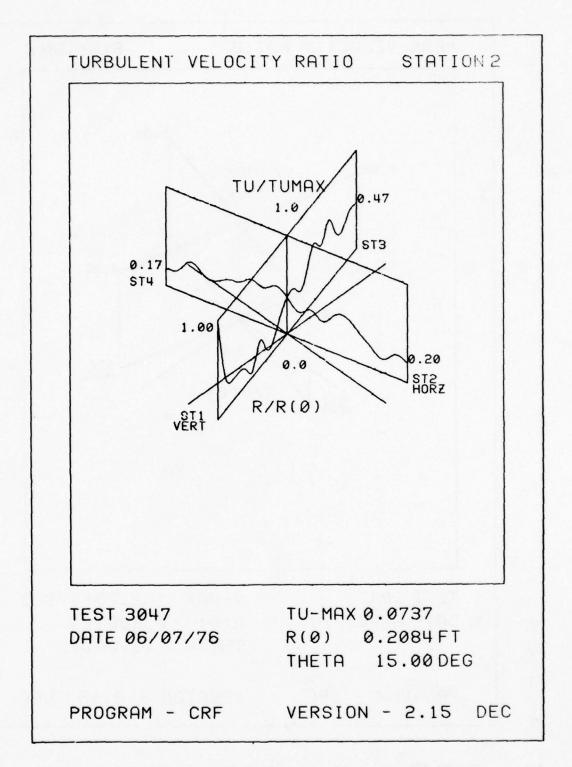


Figure 49d. Mean Velocity & Turbulence Profile in Test Chamber & Bellmouth; Test No. 3047.

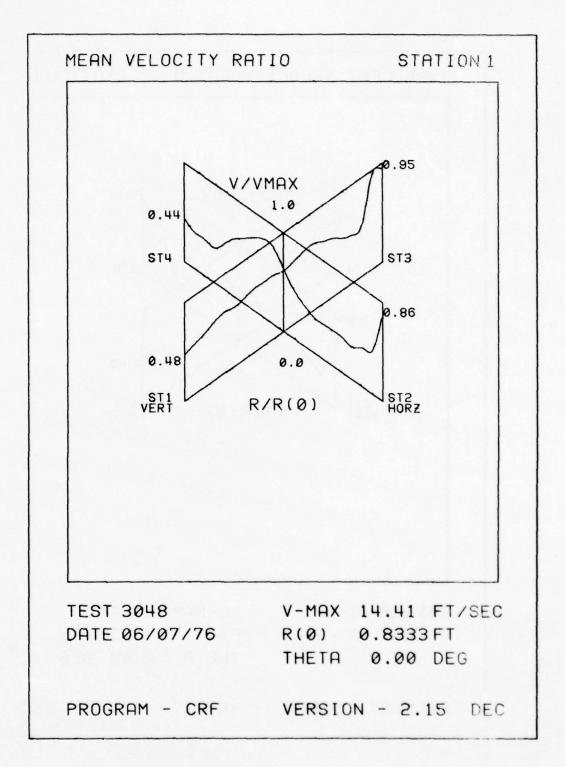


Figure 50a. Mean Velocity & Turbulence Profiles in Test Chamber & Bellmouth. Test No. 3048.

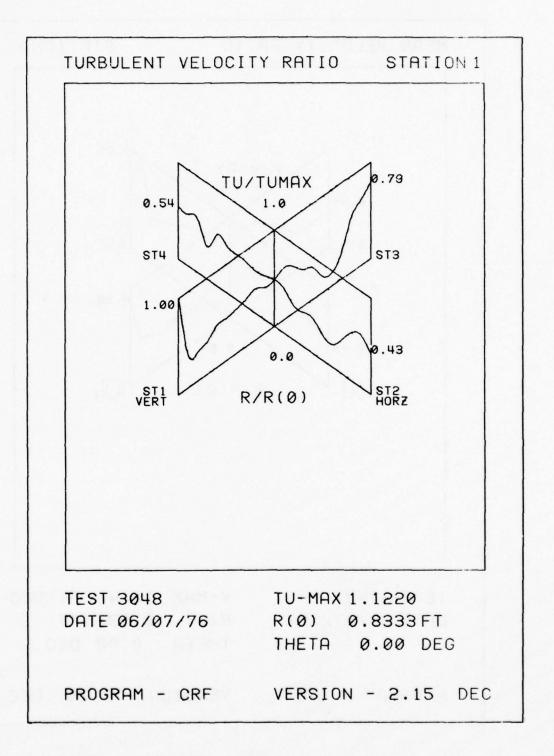


Figure 50b. Mean Velocity & Turbulence Profiles in Test Chamber & Bellmouth; Test No. 3048.

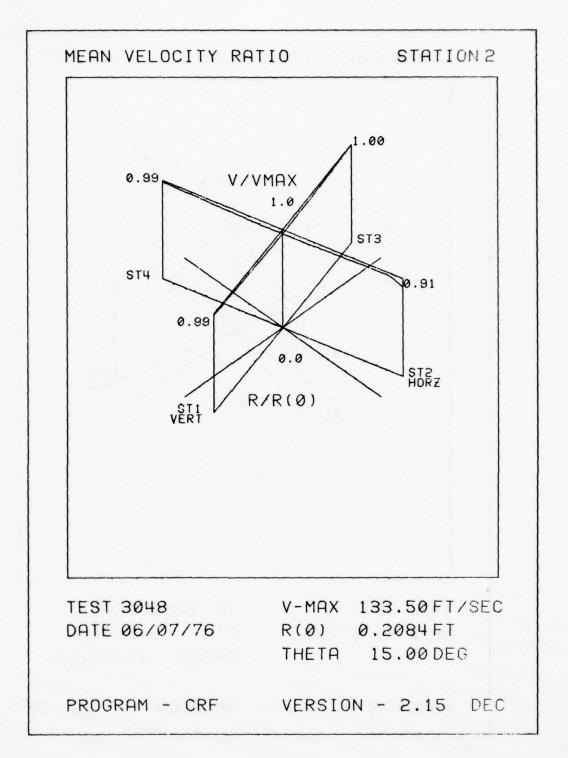


Figure 50c. Mean Velocity & Turbulence Profile in Test Chamber & Bellmouth; Test No. 3048.

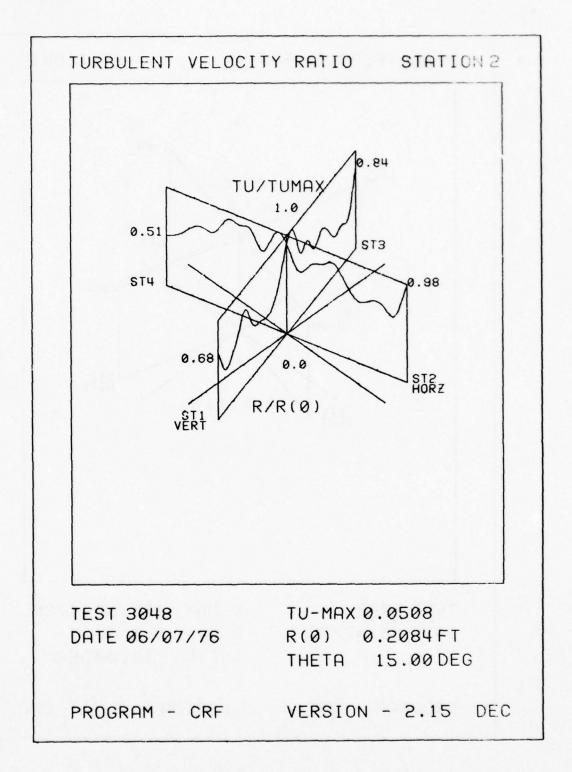


Figure 50d. Mean Velocity & Turbulence Profile in Test Chamber & Bellmouth; Test No. 3048.

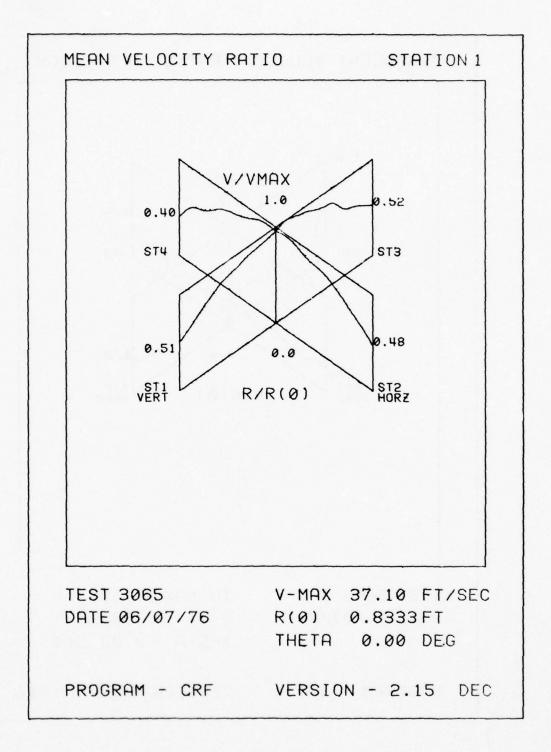


Figure 51a. Mean Velocity & Turbulence Profile in Test Chamber and Bellmouth; Test No. 3065.

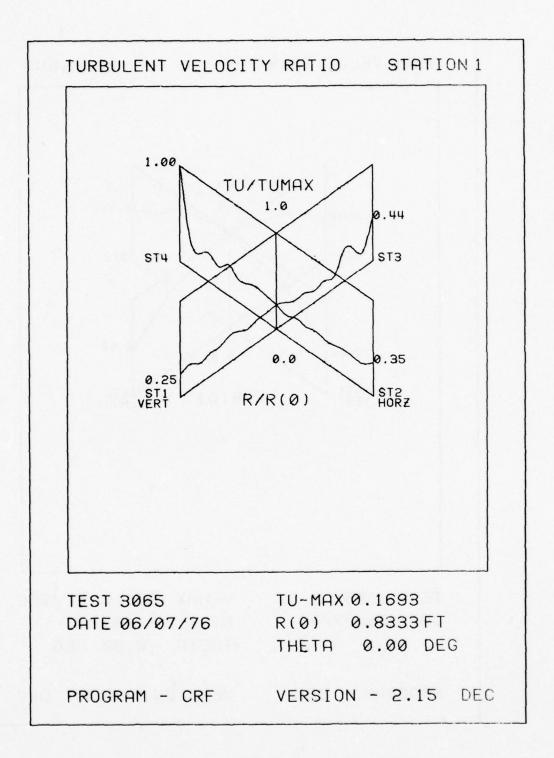


Figure 51b. Mean Velocity & Turbulence Profile in Test Chamber and Bellmouth; Test No. 3065.

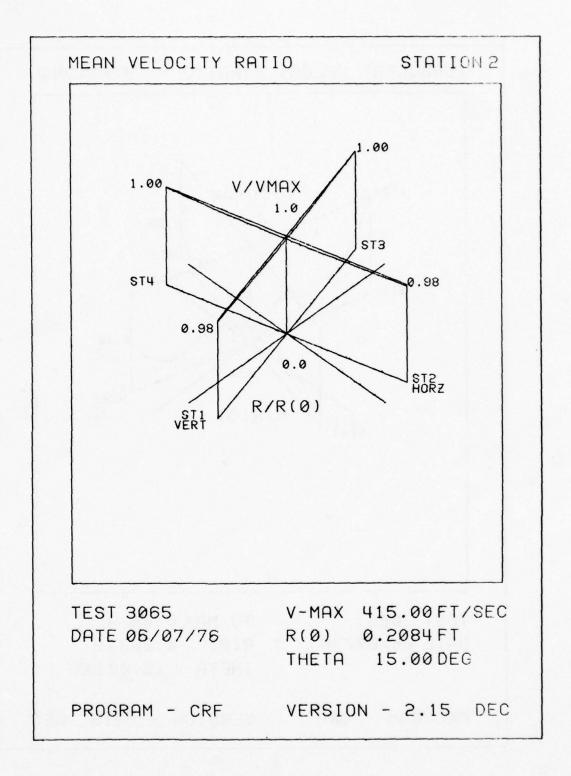


Figure 5lc. Mean Velocity & Turublence Profiles in Test Chamber & Bellmouth; Test No. 3065.

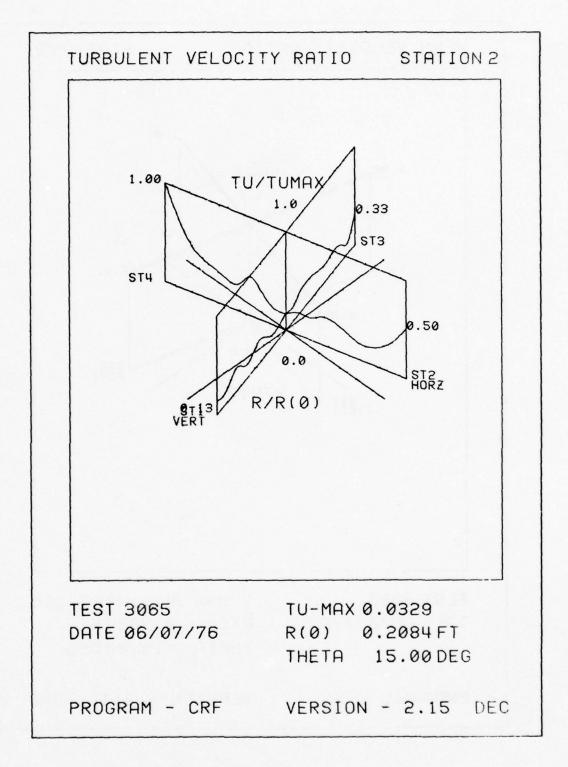


Figure 51d. Mean Velocity & Turbulence Profile in Test Chamber & Bellmouth; Test No. 3065.

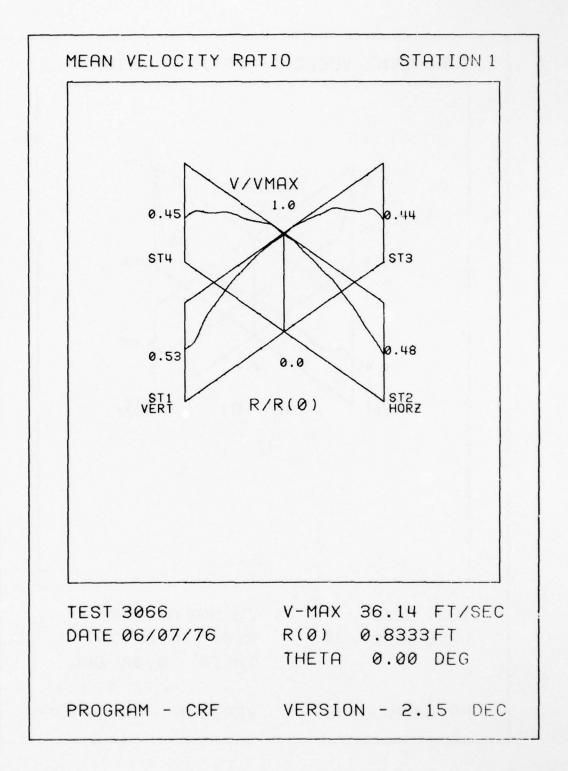


Figure 52a. Mean Velocity & Turbulence Profile in Test Chamber & Bellmouth; Test No. 3066.

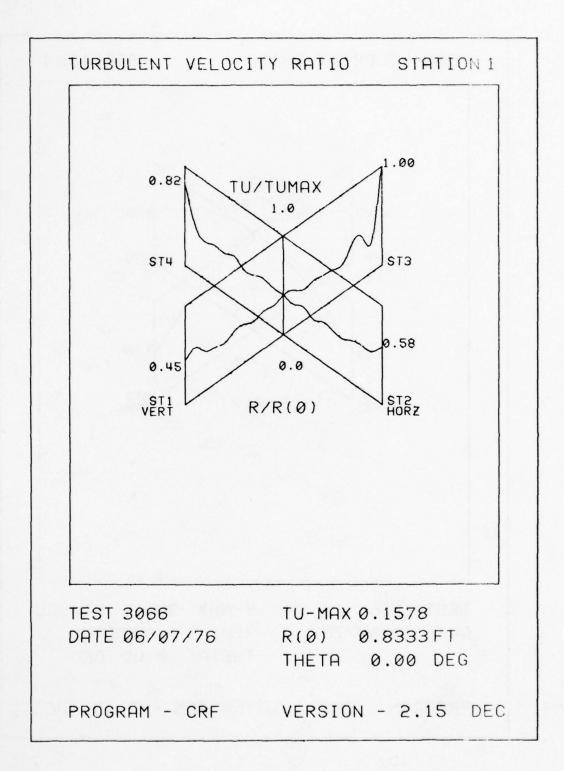


Figure 52b. Mean Velocity & Turbulence Profile in Test Chamber & Bellmouth; Test No. 3066.

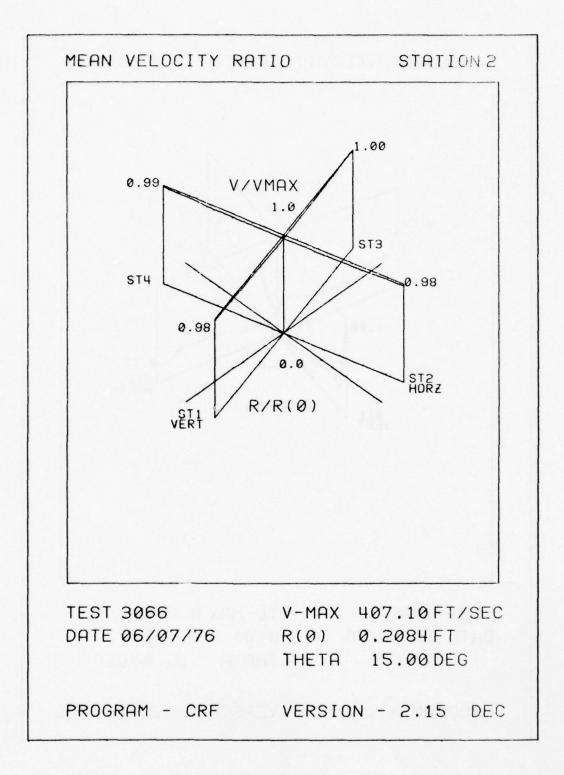


Figure 52c. Mean Velocity & Turbulence Profile in Test Chamber & Bellmouth; Test No. 3066

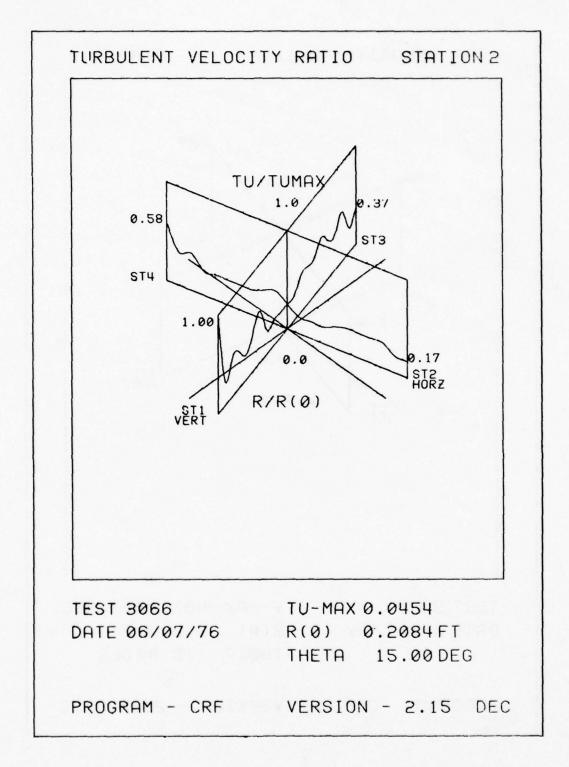


Figure 52d. Mean Velocity & Turbulence Profile in Test Chamber & Bellmouth; Test No. 3066.

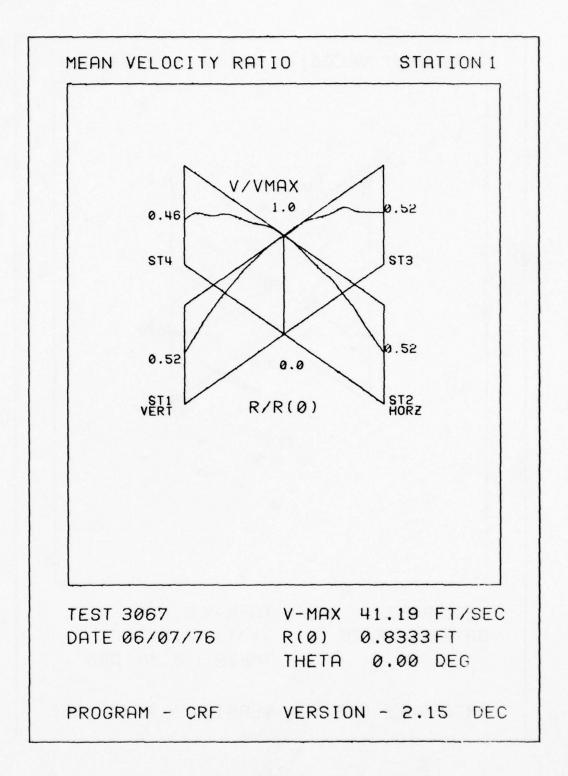


Figure 53a. Mean Velocity & Turbulence Profile in Test Chamber & Bellmouth; Test No. 3067.

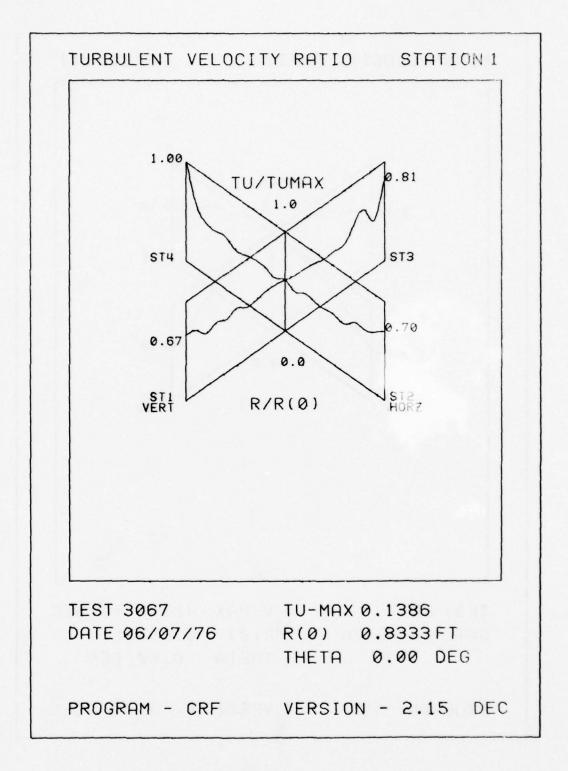


Figure 53b. Mean Velocity & Turbulence Profile in Test Chamber & Bellmouth; Test No. 3067,

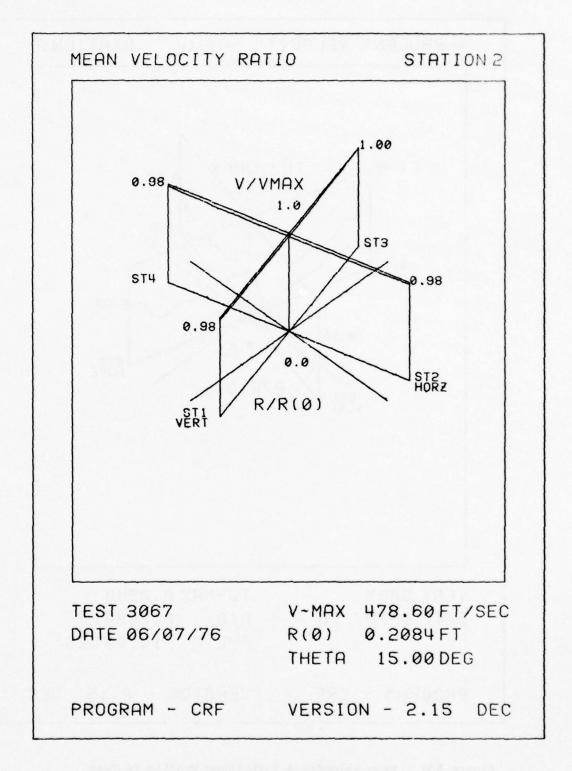


Figure 53c. Mean Velocity & Turbulence Profile in Test Chamber & Bellmouth; Test No. 3067.

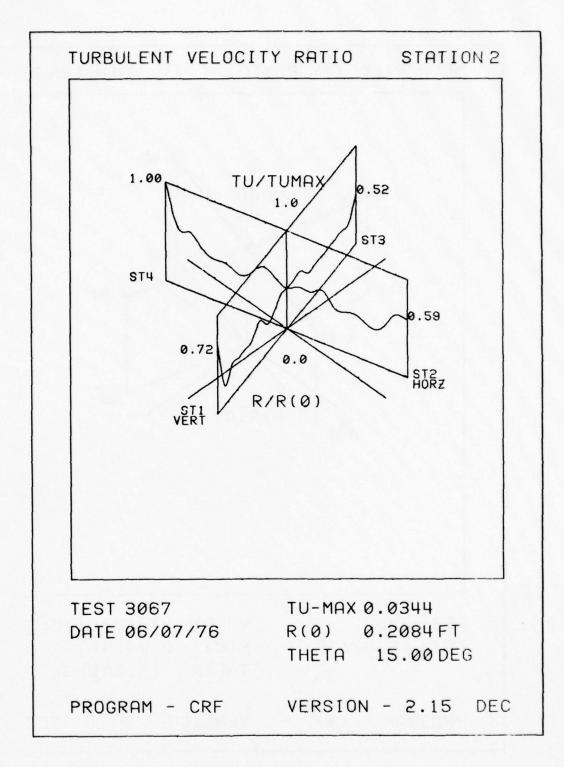


Figure 53d. Mean Velocity & Turbulence Profile in Test Chamber & Bellmouth; Test No. 3067.

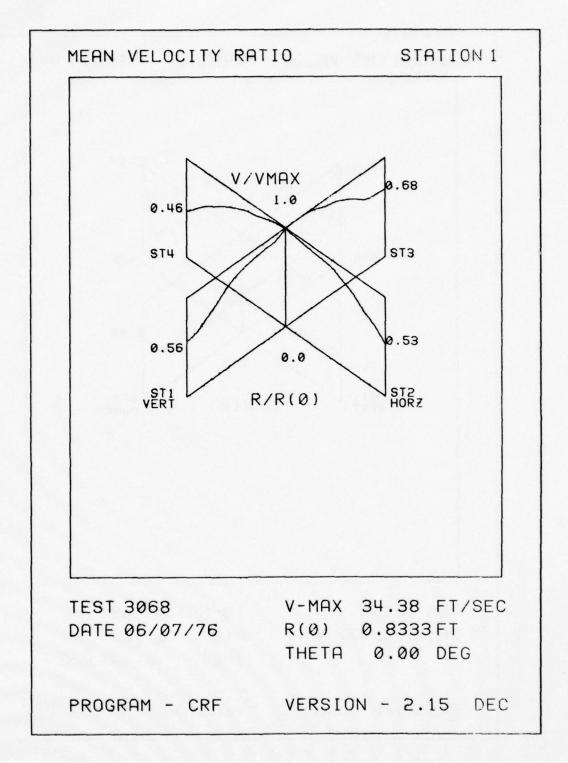


Figure 54a. Mean Velocity & Turbulence Profile in Test Chamber & Bellmouth; Test No. 3068.

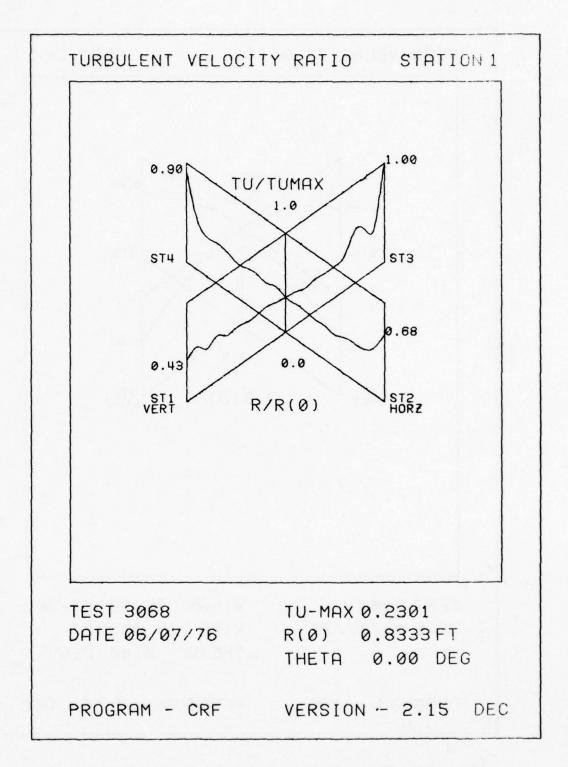
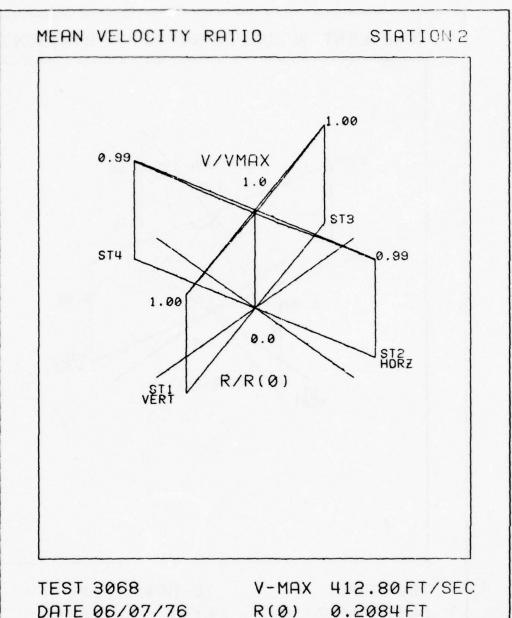


Figure 54b. Mean Velocity & Turbulence Profile in Test Chamber & Bellmouth; Test No. 3068.



THETA 15.00 DEG

PROGRAM - CRF VERSION - 2.15 DEC

Figure 54c. Mean Velocity & Turbulence Profile in Test Chamber & Bellmouth; Test No. 3068.

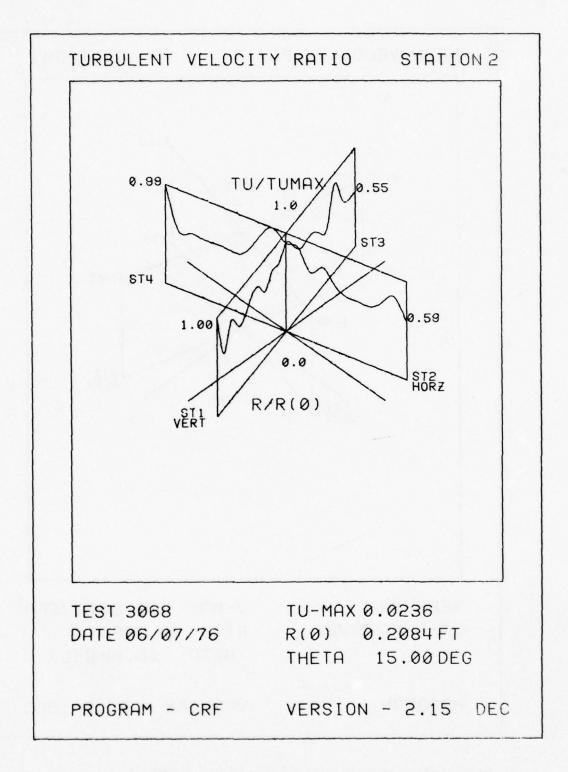


Figure 54d. Mean Velocity & Turbulence Profile in Test Chamber & Bellmouth; Test No. 3068.

The nonuniformity of velocity and turbulence level in the bellmouth (σ_U^2 and σ_{Tu}) do not seem to be affected in any consistent sense by the flow conditioning elements however. It should be noted that the velocity profile attained in this bellmouth throat for ideal flow is not flat because of the bellmouth design and location of the measuring station. This was shown in the open-to-atmosphere tests where the velocity near the wall is 1-2t higher than the centerline velocity depending on overall flow rate. The profile is smooth as expected and represents the standard of comparison which should be used rather than a flat velocity profile.

The flow conditioning requirements which this test program addressed were as follows:

$$\frac{P_{\text{max}} - P_{\text{min}}}{P_{\text{a}}} < 0.01 \text{ in the tank}$$

$$\frac{q_{\text{max}} - q_{\text{min}}}{q_{\text{a}}} < 0.01 \text{ in the bellmouth throat}$$

3) Tu < 0.01 in the bellmouth throat for ω < 1000 Hz

These flow quality standards do not apply to the boundary layer and will place the CRF on a par with or better than existing compressor test facilities. Conditions 1 and 2 were satisfied rather generally, if the comments above regarding the bellmouth velocity profile are taken into consideration.

The turbulence levels in the bellmouth (condition 3) show a large range in Tables 19 and 20. Turbulent energy for frequencies up to 10 KHz was included. This represents a more severe condition than was initially specified. The baseline CRF model has turbulence in the bellmouth in the 6 - 10% range. This has to be reduced by proper choice of flow conditioning elements to the level for

a free bellmouth, i.e., 1% or less. The first flow centering concepts still had turbulence levels in the 3 - 6% range, but this was reduced to 1 - 2% in Modification 6. Further effort with this type of flow device could reduce the turbulence level to less than 1%; however, this concept involves many cones, perforated plates, screens, etc., across the full face of the tank and would undoubtedly be expensive to construct. The front end configuration involving the venturi bank shows turbulence levels in the 0.5 - 3% range. However, the performance of all configurations which used the venturi bank (Front End Modifications 2 and 3, Combined Modification 3) was characterized by unsteady flow phenomena in both the tank and the bellmouth. Bursts of turbulence occurred at 1/2 - 2 second intervals which had an amplitude of up to two times the listed values. This type of performance could generate problems for the full-size CRF and consequently any configuration involving a venturi bank should not be used for flow conditioning. If inlet flow measurement is considered at a later date, a design and testing program will be required to satisfactorily eliminate this difficulty.

and 3 show turbulence levels in the 0.5 - 2.0% range. A detailed study of the data for Modification 2 of the barrel shows that the maximum value of turbulence occurs within 1.2 inch of the wall with the rest of the "turbulence profile" being less than the required 1%. The turbulence levels measured at this point may well be due to a probe-wall interaction. The hot wire probe and the related traversing system were not designed for boundary layer measurements and thus values in the near vicinity of the bellmouth wall are subject to some error. Preliminary measurements with specially designed boundary layer hot wire probe, reference 54, indicate a smooth variation in turbulence level from a maximum very near the wall to the free-stream values shown in Figures 47 through 54.

The data of this section indicates that the flow quality standards can be achieved by means of a properly designed auxiliary test chamber. The following points, however, must be noted:

- 1) The flow straightener section plus 2 screens in the barrel, have a total pressure drop of 0.61 inches of water for the high flow condition and less than 0.2 inches for the low flow. Experience in wind tunnels indicate pressure drops approximately three times as large should be used for maximum effectiveness. This would keep the pressure drop in the range (greater than 0.5 inches of water) where the large reduction in turbulence was noted.
- 2) The dead air space flow will be taken through the annulus formed by the barrel and the tank and will effectively be a secondary flow control system. If proper care is taken, the dead air space flow will remove much of the large turbulence producing eddies and will further reduce the overall turbulence level.
- 3) In this test, both the Mach number and Reynolds number have been simulated for the screens. However, much of the turbulence reduction (up to 50%) occurs through dissipation along a long flow path. Simulation of the long flow path was not possible in the model; however, we can expect the turbulence in the CRF to be lower than the model due to the increased length of the flow path.

K. Optimum Flow Conditioning System

On the basis of the data of Tables 19 and 20, an optimum flow conditioning system has been designed. The flow conditioning system is shown in Figure 55 with each element described in Table 21. The sizes and dimensions of the recommended elements have been chosen primarily on the basis of flow quality; however, the barrel or auxiliary test chamber is large so consideration was also given to:

- 11) Working space during test period
- 2) Personnel entry when the barrel is in place
- 3) Stowage of the barrel for test article removal
- 4) Loads on the barrel during test.

Specific constraints and considerations used in the design of the optimum elements are:

- 1) The internal diameter of all cylindrical elements in the complete barrel configuration should be the same with no change in diameter for screen or honeycomb holders and no lines, pipes, hooks, doors, lights, heaters, struts, or other protuberances are to be located downstream of the last flow element. Windows for test article observation should be contoured to the barrel inner wall and thus represent no change in flow path.
- 2) The overall length of the barrel is 24 feet, but the storage space available between the corebusters and the equipment door is approximately 19 feet. Therefore, the barrel inlet and one or more cylinders will have to be removed for forward storage.
- 3) The duct downstream of the screen section is specified as three cylinders so that for high flows the longest path can be chosen to allow maximum length for dissipation to occur and for low flows a short path can be chosen to prevent excessive boundary layer buildup. If all three cylinders are used, a maximum of 10 feet or two diameters for a five foot diameter compressor can be employed.

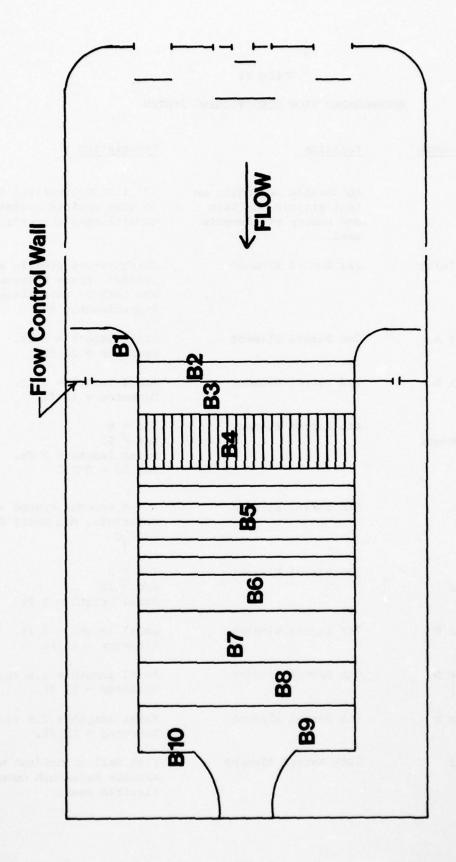


Figure 55. Recommended Flow Conditioning System.

TABLE 21
RECOMMENDED FLOW CONDITIONING SYSTEM

	Flow Element	Position	Description
	Barrel	Adjustable depending on test article position and number of elements used.	12' I.D. Cylindrical flow path to test article containing flow conditioning elements.
1.	Barrel Inlet	lst Barrel Element	Circular-arc profile with 2 ft radius. Space between outer lip and tank or tank structure is approximately 4".
2.	Cylinder A	2nd Barrel Element	Axial length = 1 ft. Diameter = 12 ft.
3.	Cylinder B	3rd Barrel Element	Axial length = 2 ft. Diameter = 12 ft.
4.	Flow Straightener	4th Barrel Element	$2/d \ge 8$ $D/d \ge 50$ Axial length = 3 ft. Max $\Delta P = 2^n H_2^0$
5.	Screens	5th Barrel Element	4 - 6 screens spaced at 6 - 12" intervals, Max Total ΔP = 12"H ₂ O
6.	Screen Retainer	6th Barrel Element	$2/d \ge 2$ $2/d \ge 20$ Axial Length = 2 ft.
7.	Cylinder C	7th Barrel Element	Axial length = 5 ft. Diameter = 12 ft.
8.	Cylinder D	8th Barrel Element	Axial length = 2.5 ft. Diameter = 12 ft.
9.	Cylinder E	9th Barrel Element	Axial length = 2.5 ft. Diameter = 12 ft.
10.	End Wall	10th Barrel Element	Flat wall coincident with test article bellmouth outer lip and flexible seal.

- 4) The screen spacing is specified as 200-500 wire diameters which is required for maximum screen effectiveness.
- 5) Flow straightener limits are consistent with standard practice with an \$\mathbb{L}/\text{d}\$ of at least 8 and a cell size of less than 2% of the barrel diameter. This section can be made of expanded metal pipe or corrugated metallic straps. The model was constructed with soda straws which suggests using plastic pipe to reduce the weight.
- 6) The elliptical corebusters located one valve diameter downstream of the valve outlet of diameter D should be constructed with a major axis of 2D and a minor axis of (4/3D).
- 7) The space between the barrel bellmouth and the tank must be small (approximately 4") so that the dead air space flow is taken from around the complete periphery of the barrel bellmouth. A 4" gap yields a velocity of only 13 ft/sec at 14.4 psia for 20 lbs/sec. Larger gaps might result in submerged inlet problems.
- 8) The dead air space flow is controlled by means of a wall and valve system located three feet axially downstream of the barrel inlet. Proper adjustment of the pressure drop should help smooth the overall flow. The flow control wall position was also chosen so that with a small test article, and with cylinders D and E removed, there is still access to the test article from the personnel doors.
- 9) The triangular duct below the barrel should be insulated.
- 10) The end wall of the barrel should be coincident with the lip of the test article bellmouth and attached with a flexible boot or joint so there is minimal air leakage.

 The early flow model tests indicated that large instabilities, unsteady flows, and separated flows can occur when a small

test article such as the J-85 is tested in the CRF if proper precautions are not taken to eliminate the submerged nature of the inlet in the CRF geometry. Secondary flow control systems could in part eliminate the submerged inlet and these could be readily accommodated with the flexible boot or joint.

11) The recommended flow conditioning system utilizes the dead air space flow as an integral part of the flow conditioning concept. There is adequate precedent and technical data in the literature to support this choice; however, this flow has not been simulated in the 1/10 scale model. To this extent the model test results are conservative with a slight improvement expected in the full-scale facility as a result of this factor.

Data collected in the 1/10 scale model test program indicates that the total pressure variation in the test chamber and the mean velocity variability and turbulence intensity in the bellmouth will all meet the flow quality criteria of 1% and that values in the facility itself may be slightly less.

SECTION III

DISCHARGE COEFFICIENTS FOR THE UNIVERSAL VENTURIS EMPLOYED IN THE CRF FLOW MEASUREMENT SYSTEM

A. Introduction

The core flow measurement system utilizes a subsonic venturi as the primary measuring element and is described in reference 56. The major aerodynamic features of the flow measurement system are given in Table 22. The operating envelope of the flow measuring system is shown in Figure 56. Note that high temperatures correspond to low flow rates and vice-versa.

The facility is to operate in both the steady-state and transient mode. The flow measurement system is to be used for steady-state test conditions with core flow measurements conducted with a calibrated bellmouth for transient experiments. "Steady-state" is normally construed to mean time invariant. This is not strictly the case with regard to the Compressor Research Facility testing since "steady-state" data is to be taken during the course of a "slow" compressor transient. As a result, the steady-state measuring system of Table 22 does in fact see time variant conditions. This has been investigated from a thermodynamic point of view in reference 57. The purpose of this study is to examine the system behavior from an aerodynamic point of view. The approach, as well as the results obtained, are discussed in the following sections.

B. Objectives of the Venturi Analysis

The aerodynamic analysis was carried out with the following objectives in mind:

- Quantify the effects of Reynolds number, Mach number and wall heating and/or cooling on the boundary layer development and, thus, the venturi discharge coefficient.
- 2) Determine the effect of entrance length and turbulence

TABLE 22

FLOW CORE MEASUREMENT SYSTEM

Overall configuration	Dual, lined ducts with removable venturi sections		
Flow metering elements	Universal venturi's		
Venturi instrumentation	6 airstream temperatures 6 inlet static pressures 4 differential pressures 4 throat wall temperatures		
Flow and temperature range	15 to 500 lbm/sec and -20°F to 1490°F		
Venturi size and maximum temperature	12.5" throat diameter, 1490°F 19.5" throat diameter, 1490°F 30.0" throat diameter, 1150°F 30.0" throat diameter, 1150°F		

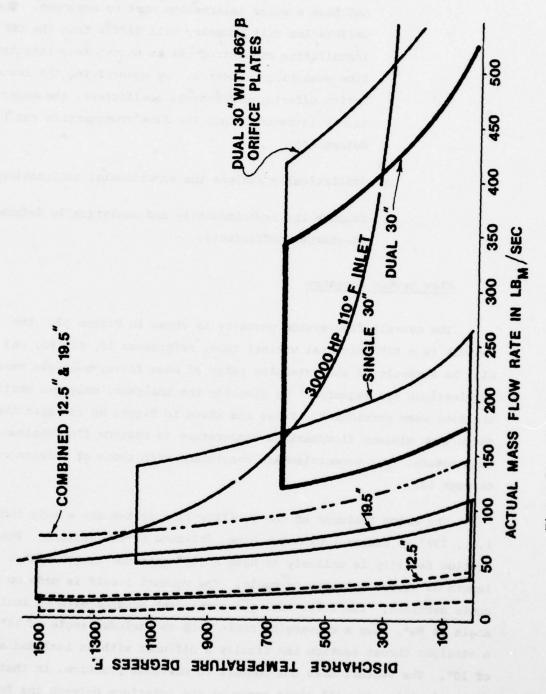


Figure 56. Flow Measurement System Operating Envelope

levels on the venturi discharge coefficients. The size of the venturis precludes a calibration in air and thus a water calibration must be employed. The calibration unit geometry will differ from the CRF installation and introduces an uncertainty into the flow measuring processes. By quantifying the installation effects on discharge coefficient, the uncertainty introduced into the flow measurements can be determined.

- 3) Statistically analyze the experimental calibration data.
- Compare the experimentally and analytically determined discharge coefficients.

C. Flow System Geometry

The overall flow system geometry is shown in Figure 57. The venturi is a BIF universal venturi tube, references 58, 59, 60, and 61. As a result of the extensive range of mass flows, multiple venturi combinations are required. To simplify the analysis, only two configurations were considered. These are shown in Figure 58 and span the range from minimum flow/maximum temperature to maximum flow/minimum temperature. The geometries are consistent with those of references 58 through 62.

The major features of the facility flow system are a long length, i.e., 792" of constant diameter pipe, followed by the venturi. The calibration facility is unlikely to have a 792" entrance length with a length of around 60" more probable. The venturi itself is made up of conic sections. The first having a convergent section with an included angle of 80°, then a converging conic with an included angle of 14°, a straight throat section and finally a diffuser with an included angle of 10°. The venturi does not conform to previous practice, in that, discontinuities in wall slope occur at the interface between the four conic elements. This has been a matter of considerable discussion; nevertheless, the units are now in wide use -- presumably with acceptable performance.

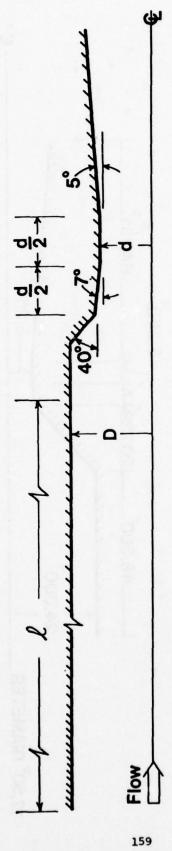


Figure 57. Flow Measurement System Overall Geometry.

UNIVERSAL VENTURIS

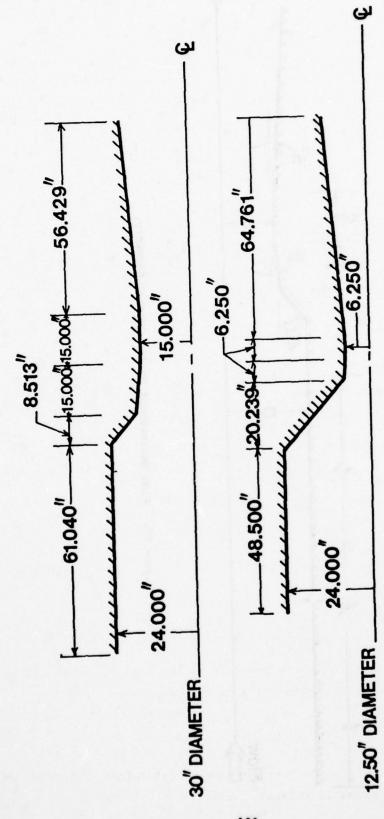


Figure 58. 30" and 12.5" Venturis

D. Facility Operating Conditions

As a result of the range of mass flow rates and temperatures encountered in the facility, each of the venturis must operate over a considerable range of Reynolds numbers, i.e., UDp/µ, where D denotes the pipe diameter and U the venturi inlet velocity. For example, the 12.5 inch venturi must span a Reynolds number range of from approximately 85,000 to 1,000,000.

The mass flow rate-temperature relations can be converted into Reynolds number-Mach number values via

$$Re = \frac{UD\rho}{u}$$
 (57)

$$\dot{\mathbf{m}} = \rho \left(\frac{\pi \mathbf{D}^2}{4} \right) \mathbf{U} \tag{58}$$

$$Re = \frac{4\dot{m}}{\pi D u} \tag{59}$$

$$\mu = \mu_{ref} \left(\frac{t}{t_{ref}} \right)^{1/2} \left(\frac{1 + 0.505}{1 + \frac{0.505}{(t/t_{ref})}} \right)$$
 (60)

where μ denotes the viscosity at temperature t, μ_{ref} is the viscosity evaluated at temperature t_{ref} . t_{ref} is normally taken as 492°R with $\mu_{ref} = 1.126 \times 10^{-5} \ lb_m/ft$ -sec. The Mach number can be defined as $U/\sqrt{\gamma Rg_c t}$. Note that the total and static temperatures are the same at the venturi inlet, i.e.,

$$t = T/(1 + \frac{k-1}{2} M^2)$$
 (61)

and t \simeq T for M < 0.05. The pressure at the venturi inlet can be related to the temperature and density by means of

$$p = \rho Rt$$
 (62)

The venturi throat Mach number can be determined from one-dimensional gas dynamic considerations and

$$\frac{A_{i}}{A_{a}} = \frac{1}{M_{i}} \left[\left(\frac{2}{\gamma+1} \right) \left(1 + \frac{\gamma-1}{2} M_{i}^{2} \right) \right]^{\frac{\gamma+1}{2(\gamma-1)}}$$
(63)

$$\frac{A_{t}}{A_{t}} = \frac{1}{M_{t}} \left[\left(\frac{2}{\gamma + 1} \right) \left(1 + \frac{\gamma - 1}{2} M_{t}^{2} \right) \right]^{\frac{\gamma + 1}{2 (\gamma - 1)}} = \left(\frac{A_{\underline{i}}}{A_{\underline{i}}} \right) \left(\frac{A_{\underline{t}}}{A_{\underline{i}}} \right)$$
(64)

from whence M_{+} can be determined iteratively.

With these relations the Reynolds numbers and Mach numbers can be determined for the various venturis. Information of the type for the 12.5 inch and 30.0 inch venturis are presented in Tables 23 and 24. Note that the Mach numbers have been determined using the venturi inlet and throat areas with no correction for boundary layer blockage. This restriction is removed in the following sections.

E. Inviscid - Boundary Layer Matching

The analysis was undertaken by subdividing the flow field into viscous and inviscid components. This is shown schematically in Figure 59. The two flow fields were aligned using the classic technique of matching the inviscid flow and boundary layer solutions. 64 The approach, in this case, including both inviscid and boundary layer domains is iterative in nature. The calculation is initiated by assuming that the boundary layers are nonexistant yielding an inviscid velocity distribution. This is used to compute the boundary layer development from whence the boundary layer displacement thickness can be determined. The displacement thickness is then added to the pipe and venturi surfaces and the inviscid flow calculation repeated. This approximates the viscous effects. 65 The process can be terminated at this point or continued until a converged solution is obtained. The speed of the convergence is directly proportional to the strength of the interaction, i.e., weak inviscid flow/boundary layer interactions converge rapidly with strong interactions requiring more calculations.

TABLE 23

12.5 in. VENTURI AERODYNAMIC PARAMETERS

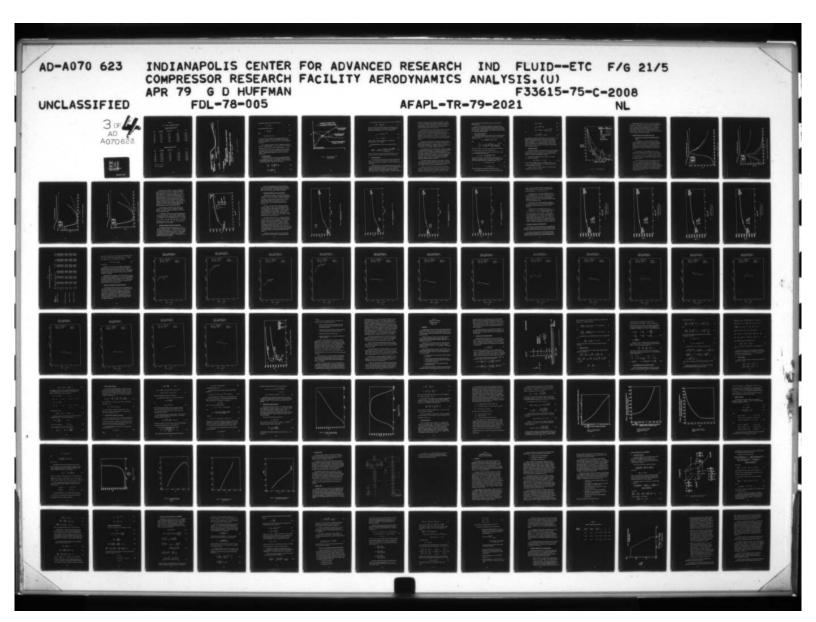
Minimum Flow Rate Limit (1)

t,°R	m,lb _m /sec	Re _i x 10 ⁻⁶	<u>M</u> i	M _t
560	15.55	0.395	0.0148	0.2230
760	13.04	0.261	0.0144	0.2170
960	11.72	0.198	0.0144	0.2190
1160	11.00	0.163	0.0150	0.2280
1360	10.05	0.134	0.0148	0.2250
1560	8.61	0.005	0.0136	0.2060
1760	8.25	0.101	0.0139	0.2100
1960	8.25	0.087	0.0146	0.2220

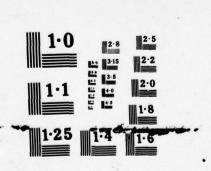
Maximum Flow Rate Limit (1)

t,°R	m,lb _m /sec	Re _i x 10 ⁻⁶	M _i	<u>M</u> t
560	39.59	1.006	0.0376	0.7830
760	33.73	0.676	0.0373	0.7670
960	30.02	0.508	0.0373	0.7670
1160	27.27	0.405	0.0372	0.7640
1360	24.16	0.373	0.0357	0.6930
1560	22.49	0.275	0.0356	0.6880
1760	22.25	0.272	0.0374	0.7740
1960	21.77	0.231	0.0386	0.8650

⁽¹⁾ $p = 15.00 lb_f/in^2$



30F/ADADA070623



NATIONAL BUREAU OF STANDARDS

TABLE 24
30.0 in. VENTURI AERODYNAMIC PARAMETERS

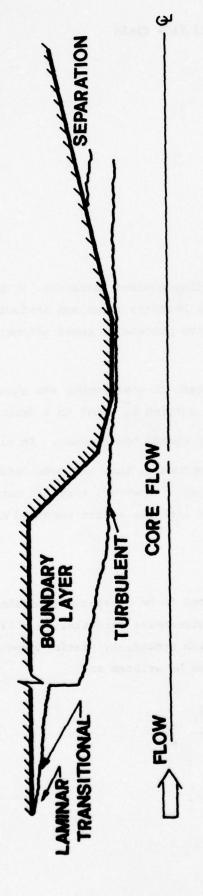
				(1)
Minimum	Flow	Rate	Limit	111

t,°R	m,lb _m /sec	Re _D x 10 ⁻⁶	<u> M</u> i	<u>M</u> t
560	85.32	2.169	0.0608	0.1577
760	73.49	1.474	0.0611	0.1583
960	64.85	1.098	0.0605	0.1570
1160	57.75	0.858	0.0593	0.1535
1360	53.49	0.715	0.0594	0.1540
1560	50.77	0.621	0.0604	0.1566
1607	49.82	0.598	0.0602	0.1560

Maximum Flow Rate Limit (1)

t,°R	m,lb _m /sec	Re _D × 10 ⁻⁶	M _i	M _t
560	238.94	6.073	0.1731	0.5053
760	206.62	4.144	0.1744	0.5107
960	185.56	3.141	0.1761	0.5175
1160	167.81	2.492	0.1750	0.5131
1360	153.37	2.049	0.1731	0.5056
1560	142.72	1.745	0.1725	0.5032
1607	139.76	1.677	0.1714	0.4989

 $⁽¹⁾_{p = 20.0 \text{ lb}_{f}/\text{in}^2}$



ASSUMPTIONS:

CONSERVATION OF MASS
TOTAL TEMPERATURE AND TOTAL PRESSURE CONSTANT CORE FLOW

CONSERVATION OF MASS, MOMENTUM AND ENERGY BOUNDARY LAYER FLOW and tw/tg= 1

Figure 59. Flow Field Schematic

as obtaining a solution to the inviscid flow field

$$\mathbf{U}_{\mathbf{I}} = \mathbf{U}_{\mathbf{I}}(\boldsymbol{\delta}_{\mathbf{I}}^{*}) \tag{65}$$

and the boundary layer flow field

$$\delta_{\mathbf{B}}^{\star} = \delta_{\mathbf{B}}^{\star}(\mathbf{U}_{\mathbf{B}}) \tag{66}$$

where

$$\delta_{\mathbf{B}}^{*} = \delta_{\mathbf{I}}^{*} \text{ and } \mathbf{U}_{\mathbf{I}} = \mathbf{U}_{\mathbf{B}}(\mathbf{y} = \delta)$$
 (67)

In the above relations δ^* denotes the displacement thickness, U the velocity and the subscripts B and I the boundary layer and inviscid flow fields, respectively. The iterative process is shown schematically in Figure 60.

Both an undamped and damped approach to convergence are shown in Figure 60. The damped approach, i.e., setting $\delta_{\rm I}^{\star}$ equal to a fraction of the previous $\delta_{\rm I}^{\star}$ and $\delta_{\rm B}^{\star}$ values, normally speeds convergence. It also prevents oscillation of the values. Approaches that are considerably more complex than this have been proposed; ⁶⁴ however, they did not appear to offer advantages commensurate with the effort required to implement them.

F. Inviscid Flow Model

The inviscid flow field was assumed to be quasi-two dimensional, i.e., a variation in flow area in the streamwise direction, A = A(x). Following Shapiro, reference 63, the Mach number, M, static temperature, t, and static pressure, p, variation can be written as

$$\frac{dM^2}{M^2} = -\frac{2(1 + \frac{Y-1}{2}M^2)}{1 - M^2} \frac{dA}{A}$$
 (68)

$$\frac{dt}{t} = \frac{(\gamma - 1)M^2}{1 - M^2} \frac{dA}{A} \tag{69}$$

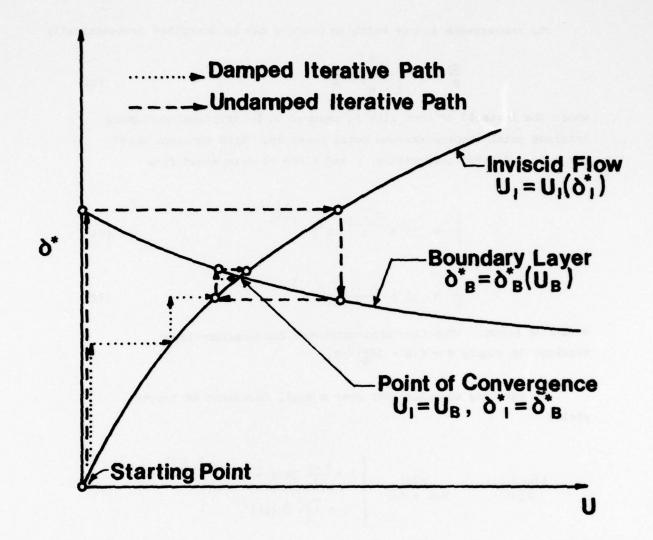


Figure 60. Convergence Path for the Inviscid Boundary
Layer Calculations

The convergence and/or matching process can be described mathematically

$$\frac{dp}{p} = \frac{\gamma M^2}{1 - M^2} \frac{dA}{A} \tag{70}$$

where the inviscid or core flow is assumed to be frictionless having constant total temperature and total pressure. With constant total pressure and total temperature, p and t can be determined from

$$\frac{p}{p} = (1 + \frac{\gamma - 1}{2} \text{ m}^2)^{-\frac{\gamma}{\gamma - 1}}$$
 (71)

$$\frac{t}{T} = \left(1 + \frac{\gamma - 1}{2} M^2\right)^{-1} \tag{72}$$

once M is known. The flow area corrected for boundary layer blockage is simply A = $\pi(d - 2\delta_B^*)^2/4$.

Integrating equation (68) over a small increment of length yields

$$\frac{A(x + \Delta x)}{A(x)} = \frac{M(x)}{M(x + \Delta x)} \begin{cases} \frac{1 + \frac{\gamma - 1}{2} \left[M(x + \Delta x)\right]^2}{1 + \frac{\gamma - 1}{2} \left[M(x)\right]^2} \end{cases} \frac{\frac{\gamma + 1}{2(\gamma - 1)}}{(73)}$$

which can be solved iteratively for $M(x + \Delta x)$ knowing A(x), $A(x + \Delta x)$ and M(x) from either the boundary conditions or the previous step.

G. Boundary Layer Models

The calculations were carried out with two separate boundary layer models. Both of these are well documented and in fairly wide use. As a result, the discussion will be limited to the critical elements of the two programs.

The investigation was initiated using the latest version of a boundary layer program developed by Bradshaw. This is a highly sophisticated program solving a momentum, continuity, turbulent shear stress and temperature equation. The governing relations are non-linear, first-order, hyperbolic partial differential equations. These are solved using

the method of characteristics as described in references 66, 67, and 68. This is an extremely versatile program and includes the capability to simulate wall roughness, longitudinal and transverse curvature and lateral divergence. The particular version of the program employed is valid for Mach numbers of less than about 5.

This program models only turbulent boundary layers and is normally initiated by presuming a boundary layer transition location or an initial boundary layer momentum thickness Reynolds number and skin friction coefficient. The program is terminated upon completion of the computation or upon boundary layer separation. In this instance separation is defined as the point at which the skin friction coefficient goes to zero or the out-going characteristic is directed inward toward the wall.

The previously described method is obviously complex, and since inviscid-boundary layer matching was to be carried out requiring multiple boundary layer computations, a less complex integral technique was also evaluated. This approach is described in reference 69 and consists of both a laminar and a turbulent boundary layer simulation.

The laminar boundary layer computations use the approach developed by Cohen and Reshotko, reference 70. The governing differential equations are expressed in terms of dimensionless parameters related to wall shear stress, surface heat transfer and the free-stream velocity gradient. This yields two equations with two unknowns. The system of equations is reduced to one first-order, ordinary, non-linear, non-homogeneous differential equation in terms of a free-stream velocity gradient parameter by employing Thwaites correlation.

The turbulent boundary layer model is also integral in nature and uses the momentum and moment-of-momentum integral boundary layer equations following Sasman and Cresci. This calculation is initiated with values supplied from the previously described laminar solution.

Boundary layer transition is specified following the methods of reference 32 extended via the data of reference 51 to account for the effects of free-stream turbulence. Separation is assumed to occur in the laminar calculation when $C_{\mathfrak{f}}$ passes from a positive to negative

value. The latter criterion has been chosen to be consistent with experimental data.

The bulk of the calculations discussed in the ensuing sections were carried out using the integral technique of reference 69. Selected cases were, however, analyzed using both the Bradshaw and integral methods with the results in general agreement. This verified the overall accuracy of the simplified integral approach.

H. The Discharge Coefficients

The discharge coefficient can be related to the flow field characteristics by utilizing the basic definition of the mass flow rate through the venturi, i.e., 52

$$\dot{m}_{t} = A_{t} Y \sqrt{2g_{c} \rho_{i} (p_{i} - p_{t})/(1 - dr^{4})}$$
 (74)

where

$$Y = \left[Rp^{2/\gamma} \left(\frac{\gamma}{\gamma - 1} \right) \left(\frac{1 - Rp^{\gamma}}{1 - Rp} \right) \left(\frac{1 - dr^4}{1 - dr^4 Rp^{2/\gamma}} \right) \right]^{1/2}$$
(75)

Note that dr = d/D, $A_t = \pi d^2/4$, $Rp = p_2/p_1$ and the subscript i denotes the inlet station and t the outlet or throat station.

The actual mass flow rate is related to the theoretical value by means of a discharge coefficient and

$$\dot{m}_{act} = C_d \dot{m}_t = C_d A_t Y \sqrt{2g_c \rho_i \Delta p / (1 - dr^4)}$$
 (76)

The discharge coefficient is normally determined empirically and is dependent on the Reynolds number, the Mach number, the diameter ratio and a heat transfer parameter for irreversible changes. 52 Thus

$$C_d = C_d(Re, M, dr, q_w)$$
 (77)

or

$$C_{d} = C_{d}(Re, M, dr)$$
 (78)

when no heat transfer occurs between the fluid and the pipe.

The mass flow rate through the venturi throat can be written as

$$\dot{\mathbf{m}}_{act} = \int_{\mathbf{A}} \int \rho \mathbf{U} d\mathbf{A}$$
 (79)

or

$$\dot{m}_{act} = 2\pi f_{t}^{d/2} \quad Urdr \tag{80}$$

$$\dot{\mathbf{m}}_{\text{act}} \approx \pi r_{\text{t}}^{2} \rho U_{\infty} C_{\text{d}} = \pi \rho U_{\infty} r_{\text{t}}^{2} \left(1 - \frac{\delta_{\text{t}}^{*}}{r_{\text{t}}} \right)^{2}$$
 (81)

and

$$c_{d} = \left(1 - \frac{\delta_{t}^{*}}{r_{t}}\right)^{2} \approx 1 - 4\delta_{t}^{*}/d$$
 (82)

As a consequence, the discharge coefficient can be directly related to the boundary layer displacement thickness. Note that the relationship of equation (82) presumes that the inviscid portion of the flow field is quasi-one-dimensional, i.e., at a given x-station the velocity field outside the boundary layer is independent of radius. This is not actually the case, and, thus, equation (82) represents the upper boundary for the discharge coefficient.

Convergence Procedure

The convergence procedure used in matching the inviscid and boundary layer solutions is discussed in Section II.D. This process consists of obtaining a solution to the inviscid flow field and boundary layer by means of the boundary layer displacement thickness.

$$\delta^{*}(\mathbf{x}) = \lambda \delta_{T}^{*}(\mathbf{x}) + (1 - \lambda) \delta_{B}^{*}(\mathbf{x})$$
 (83)

where λ denotes a damping factor which is bounded by 0 and 1, i.e., $0 \le \lambda \le 1$. The speed and stability of the convergence process can be influenced markedly by the λ value.

Figure 61 shows the convergence behavior for a typical venturi computation with a series of λ values.

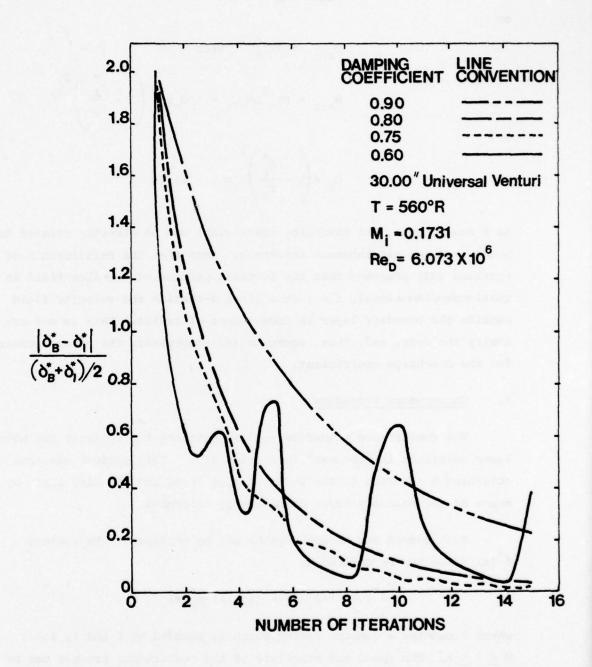


Figure 61. Convergence Behavior

Damping coefficients of from 0.6 to 0.9 are shown in Figure 61 with 0.6 being unstable and 0.75, 0.8 and 0.9 having increasing degrees of stability. The number of iterations required for a converged solution increases with increased damping factor. As a consequence λ must be large enough to prevent oscillations, but small enough to yield reasonable computing times. The computations discussed in the following section normally employed λ values of from 0.75 to 0.90 with 20 to 40 iterations required for convergence.

J. Computed Universal Venturi Discharge Coefficients

Axial Variation of Boundary Layer Parameters Within the Venturi

The computation of the venturi discharge coefficient entails integration of both the viscous and inviscid equations along the entire flow path length. As a consequence, the Mach number, skin friction coefficient, displacement thickness and boundary layer thickness are defined from the system inlet to the venturi exit, a distance of approximately 80 feet in some cases.

The variability of these parameters for the 12.5 inch venturi under the maximum flow rate conditions of $t_g = 1960^{\circ}R$ and $Re_i = 0.231 \times 10^6$, Table 23, are shown in Figures 62 through 65. Three heating and/or cooling conditions have been computed to illustrate this effect on boundary layer development and, thus, discharge coefficient.

The Mach number variation with axial location is shown in Figure 62. The venturi cross-section is superimposed on the plot with the peak value corresponding to the venturi throat. An unexpected result of the analysis was the predicted boundary layer separation in the diffuser for two of the three calculations. This is not, however, inconsistent with conventional diffuser practice since the included angle of 10° exceeds the normally recommended value of 7.5°.

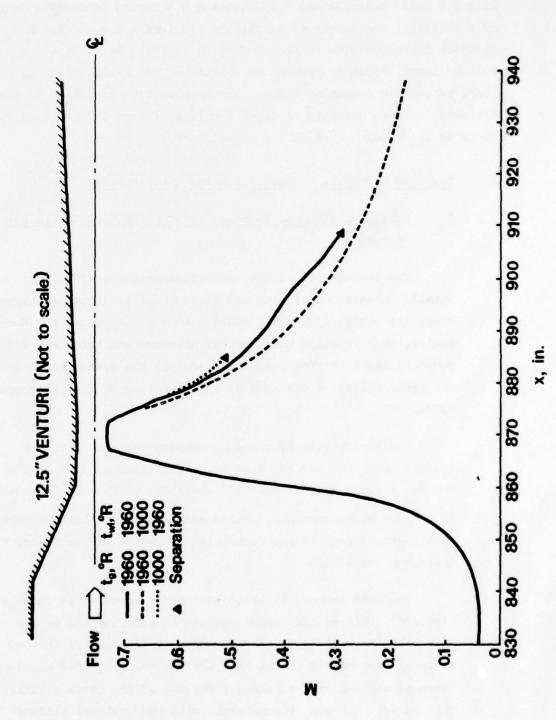


Figure 62. Venturi Mach Numbers

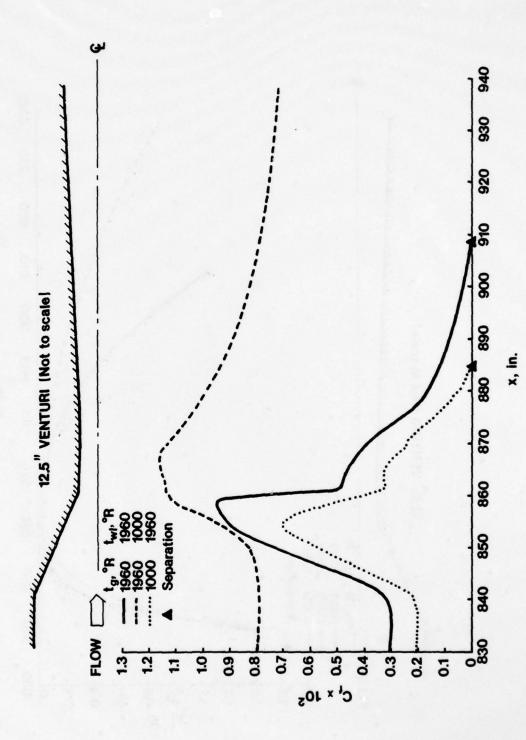


Figure 63. Venturi Skin Friction Coefficients

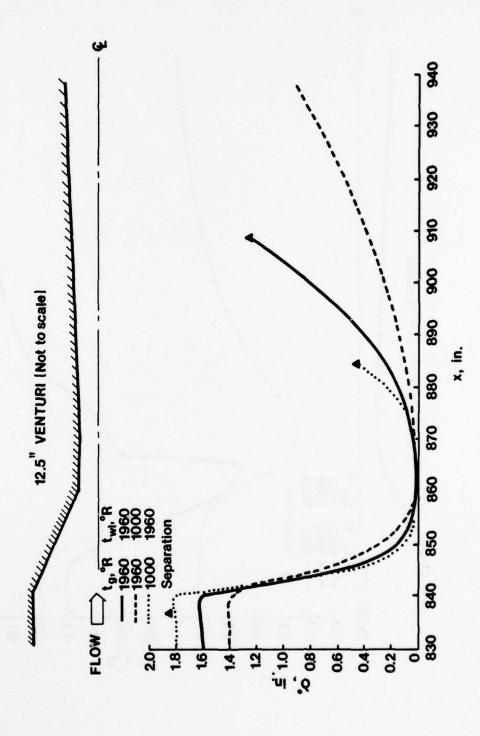
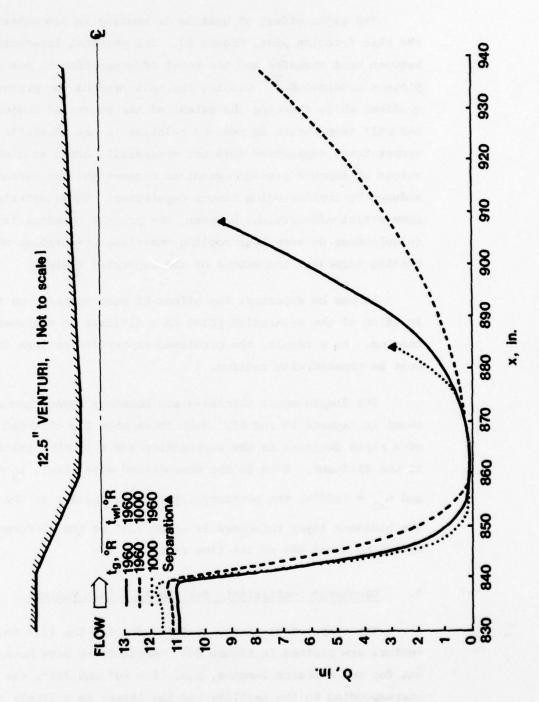


Figure 64. Venturi Displacement Thicknesses



The major effect of heating or cooling is demonstrated in the skin friction plot, Figure 63. The physical interaction between heat transfer and the onset of separation is not completely understood. Cooling the wall deepens the pressure gradient while reducing the extent of the separated region. If the wall temperature is reduced relative to the adiabatic wall temperature, separation does not necessarily occur at higher values of imposed pressure gradient because the gas viscosity is reduced by cooling which favors separation. These effects are to some extent off-setting; however, the present boundary layer calculations do show that cooling diminishes separation while heating increases the extent of the separated region.

As can be expected, the effect of heat transfer on the location of the separation point in a diffuser is extremely complex. As a result, the predicted separation or lack thereof must be treated with caution.

The displacement thickness and boundary layer thickness are shown in Figures 64 and 65. Both these show the expected trend of a rapid decrease in the contraction and a substantial increase in the diffuser. Even in the unseparated case, i.e., $t_g = 1960^{\circ}R$ and $t_{wl} = 1000^{\circ}R$, the boundary layer grows rapidly in the diffuser. The boundary layer thickness is about 7.5" at the diffuser exit making up about 65% of the flow field.

Discharge Coefficients for the 12.5 inch Venturi

The computed discharge coefficients for the 12.5 inch venturi are plotted in Figure 66. Computations have been carried out for two entrance lengths, i.e., $\ell = 60$ ° and 792°, the former corresponding to the facility and the latter to a likely calibration installation and for one turbulence level. Two diabatic conditions have also been considered – one corresponding to gas heating and the other to gas cooling.

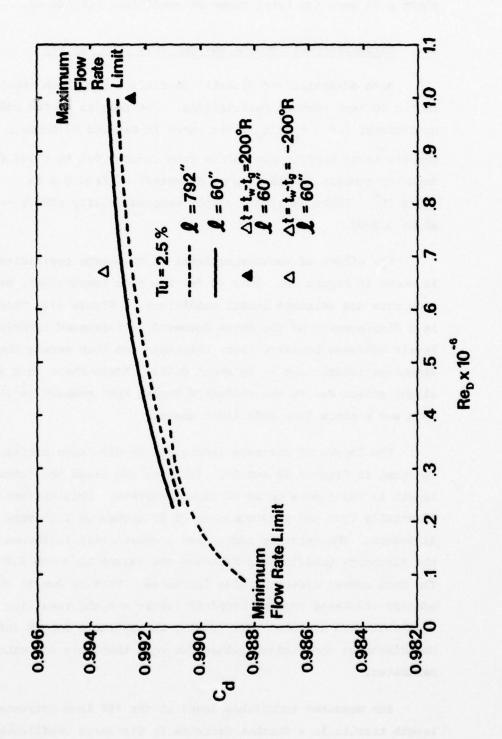


Figure 66. Discharge Coefficients for the 12.5" Venturi

As can be seen from Figure 66, the entrance length has less effect on the discharge coefficient than does the Reynolds number on heating/cooling. The discharge coefficient varies by about 0.5% over the total range of conditions considered.

3. Discharge Coefficients for the 30.0 inch Venturi

Both adiabatic and diabatic conditions have been employed in the 30 inch venturi calculations. The results of the adiabatic conditions, i.e., $t_g = t_{wl}$, are shown in Figures 67 through 70. The discharge coefficient varies from about 0.991 to 0.993 for Reynolds numbers (based on pipe diameter) of from 0.8 to 6.0×10^6 . There is a very slight compressibility effect —about 0.0002.

The effect of turbulence level on discharge coefficient is shown in Figure 68. This is for the same temperature, mass flow rate and entrance length conditions as Figure 67. There is a displacement of the curve downward -- increased turbulence levels increase boundary layer thickness and thus reduce the discharge coefficient -- by about 0.002. Again there is a very slight effect due to the different throat Mach numbers in the maximum and minimum flow rate limit cases.

The impact of entrance length, £, on discharge coefficient is shown in Figures 68 and 69. In these two cases the entrance length is 792 inches or 16.50 pipe diameters. This differs substantially from the previous case of 60 inches or 1.25 pipe diameters. The entrance length has a substantial influence on the discharge coefficients reducing the values by about 0.005. The Mach number affect is also increased. This is due to the greatly thickened venturi boundary layers and the resulting increase in throat Mach numbers. All in all, the entrance length influences the discharge coefficient values far more than does any other parameter.

The measured turbulence level at the 792 inch entrance length results in a further decrease in discharge coefficient

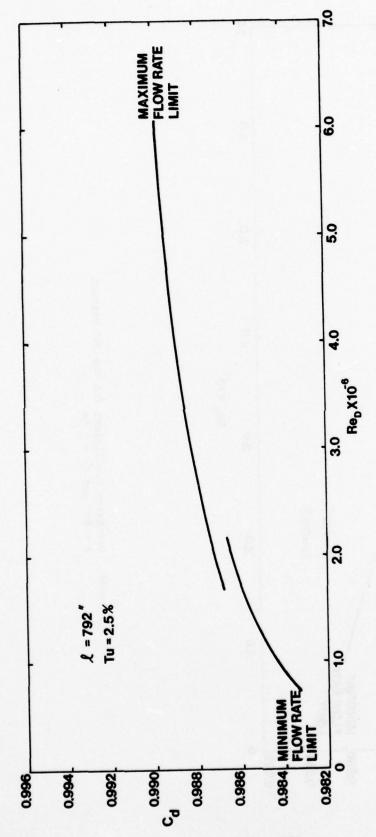


Figure 67. Discharge Coefficient for the 30" Venturi ℓ = 60" and Tu = 0.5%

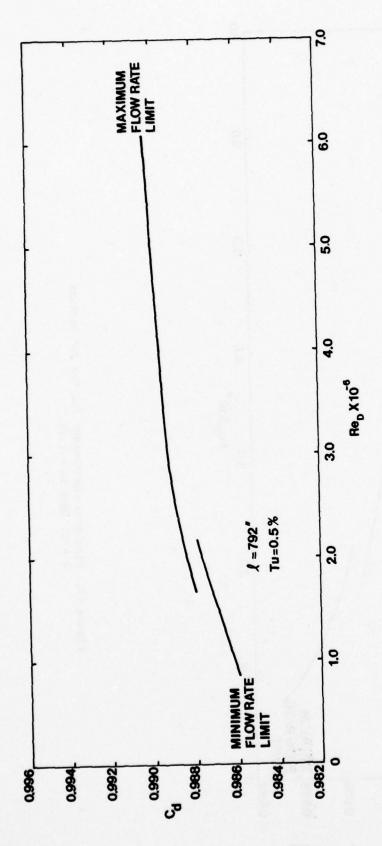


Figure 68. Discharge Coefficient for the 30" Venturi $\ell_{\rm s} = 60$ " and Tu = 2.5%

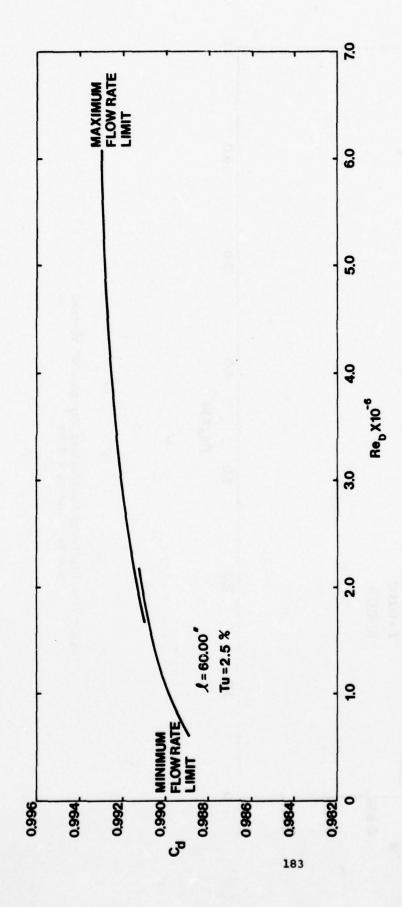
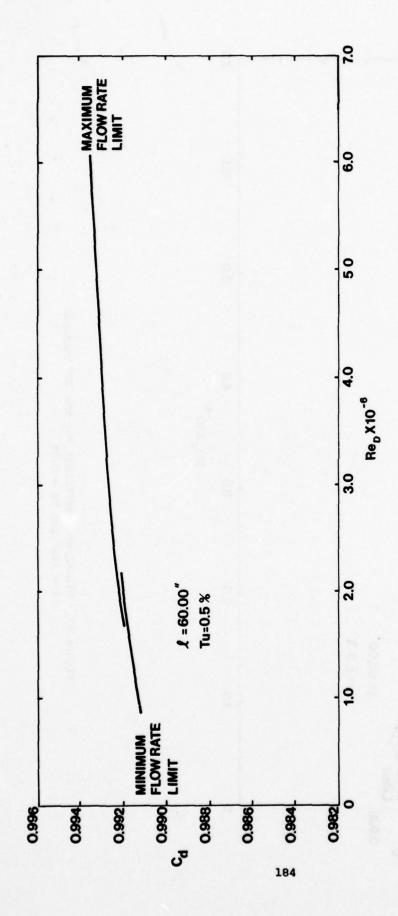


Figure 69. Discharge Coefficient for the 30" Venturi ℓ = 792" and Tu = 0.5%



1

Figure 70. Discharge Coefficient for the 30" Venturi $\ell = 792$ " and Tu = 2.5%

values. This is illustrated in Figure 69. Again note the effect of Mach number on the $C_{\rm d}$ values in the "overlap region" of Reynolds numbers, i.e., $1.7 < {\rm Re}_{\rm D} \times 10^{-6} < 2.2$.

The maximum variation in discharge coefficient is about 0.008 or approximately 1%. This occurs in comparing the $\ell=60$ in., Tu=0.5% to the $\ell=792$ in., Tu=2.5%. This illustrates the importance of calibrating the venturis in a facility having characteristics similar to that of the Compressor Research Facility mass flow rate measurement system.

Thermal effects have been investigated by calculating discharge coefficients for a series of wall and gas temperatures. The results of these calculations are plotted in Figures 71 through 74.

Calculations have been carried out for $\ell=60$ in., Tu = 0.5% and 2.5%, $\Delta t=\pm 40^{\circ}R$ and Reynolds numbers from 0.6 to 6 x 10^6 where $\Delta t-t_{wl}-t_{g}$. Discharge coefficients vary from a low of 0.9890 to a high of 0.9937 -- a range of about 0.0047 or approximately 0.5%. The bulk of this variability is due to Reynolds number and not to heating and/or cooling. The maximum deviation due to thermal effects, i.e., at this level $\pm 40^{\circ}R$, is about 0.0005 or 0.05%. It thus appears that as long as gas-wall temperature differences can be held to levels of less than 50°, the effect on the discharge coefficient is negligible.

K. Experimental Calibration of the CRF Venturis

The CRF venturis have been calibrated at the Alden Research Laboratories. Discharge coefficients as a function of Reynolds number have been obtained for four separate sets of pressure taps per venturi.

The venturi calibration data has been statistically analyzed using the techniques of reference 75. A linear correlation between Reynolds number and discharge coefficient has been developed and the

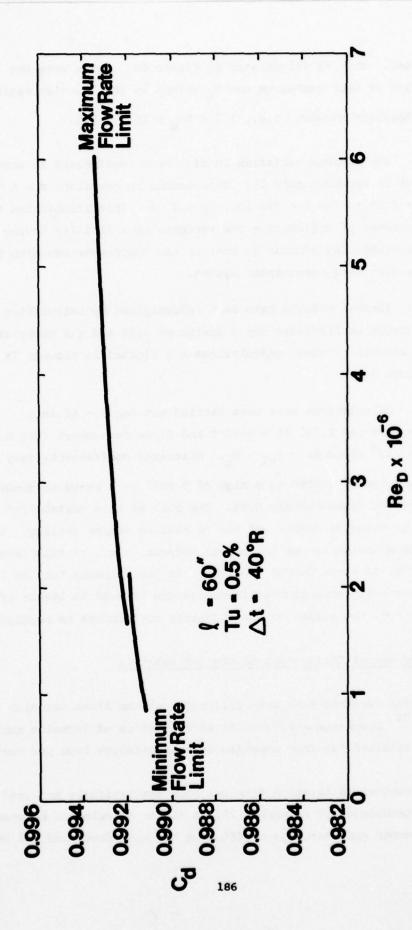
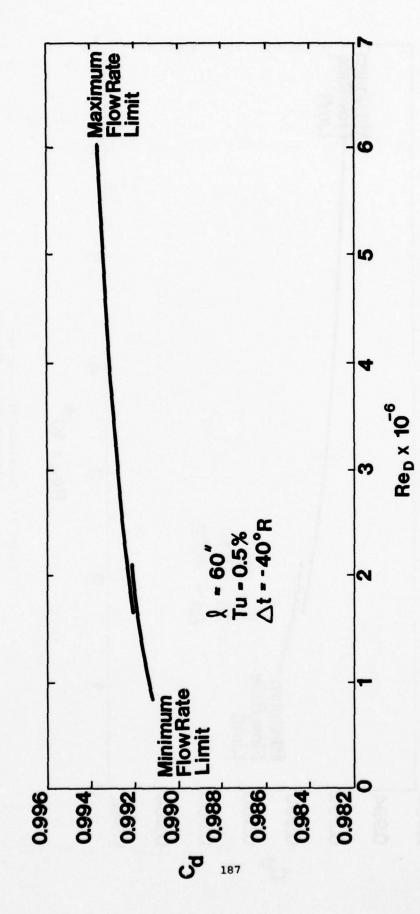
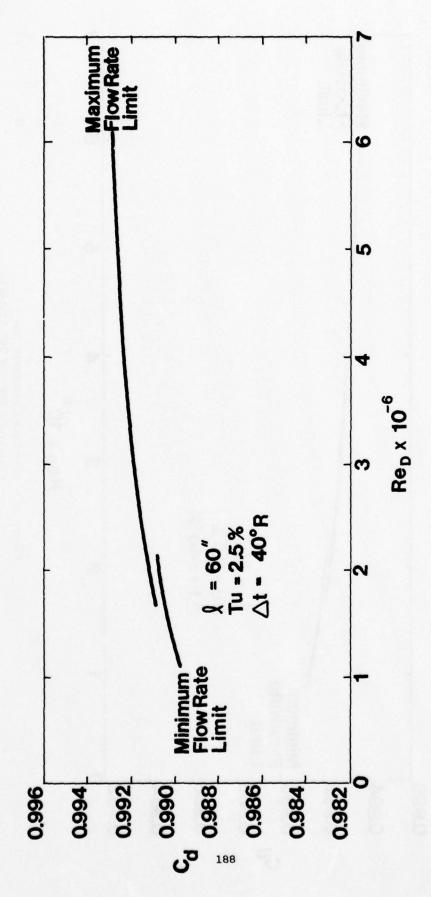


Figure 71. Calculated Discharge Coefficients for the 30" Venturi. $\ell = 60^\circ$, Tu = 0.5%, Pinlet = 20 lb_f/in and $\Delta t = 40^\circ$



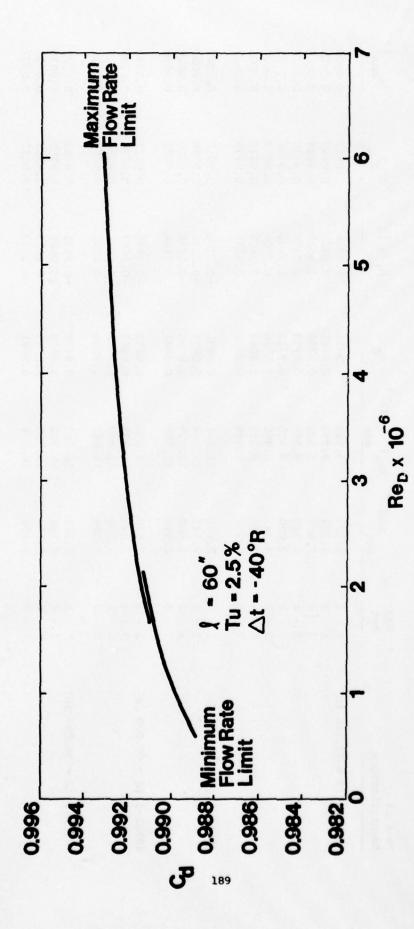
Carrie !

Figure 72. Calculated Discharge Coefficients for the 30" Venturi. $\lambda = 60^\circ$, Tu = 0.5%, Pinlet = 20 $1b_f/in$ and $\Delta t = -40^\circ$



一年 日本

Figure 73. Calculated Discharge Coefficients for the 30" Venturi. $\ell = 60$ ", $\tau_{\rm u} = 2.5$ %, $\rho_{\rm inlet} = 20~{\rm lb_f/in}^2$ and $\Delta t = 40^\circ$



(1)

Figure 74. Calculated Discharge Coefficients for the 30" Venturi $\ell = 60$ ", Tu = 2.5%, Pinlet = 20 lb_f/in and $\Delta t = -40$ °

TABLE 25

$$d = A_0 + A_1 Re$$

Venturi Identification	Tap	(Re _D) × 10 ⁻⁵ (min	(Re _D) × 10 ⁻⁵ max	o	A ₁ × 10 ⁸	(C _d)	max
48901-1 (d = 12.516 in)	1 - 2	2.028	3.521	0.9776	1.8310	0.9827	0.0002
	1 - 2	4.355	9.998	0.9841	0.0762	0.9847	0.0025
	3 - 4	2.027	3.522	0.9798	3.5010	0.9894	0.0018
	3 - 4	4.347	9.698	0.9973	0.0439	0.9955	0.0017
	9 - 9	2.030	3.520	0.9729	1.3170	0.9766	0.0002
	9 - 9	4.343	9.995	0.9790	0.3106	0.9812	0.0020
	7 - 8	2.030	3.525	0.9843	2.7460	0.9918	0.0005
	7 - 8	4.352	9.995	0.9958	0.2272	0.9974	0.0013
48901-2 (d = 19.479 in)	1 - 2	2.848	12.541	0.9831	-0.1706	0.9817	0.0027
	1	2.848	12.558	0.9824	-0.3176	0.9798	0.0023
	9 - 9	2.848	12.579	0.9796	-0.1945	0.9780	0.0026
	1	2.944	11.758	0.9847	0.1156	0.9855	0.0036
48901-3 (d = 30.099 in)	1 - 2	7.528	15.860	0.9850	-0.2526	0.9822	0.0033
	1	7.526	15.836	0.9843	-0.1047	0.9831	0.0025
	9 - 9	7.525	15.803	0.9911	-0.2422	0.9884	0.0017
	1	7.526	15.649	0.9864	-0.0326	0.9860	0.0031
48901-4 (d = 30.094 in)	1 - 2	8.164	16.750	0.9770	-0.2275	0.9743	0.0027
	3 - 4	8.164	16.731	0.9763	-0.0661	0.9755	0.0013
	9 - 9	8.157	16.728	0.9769	0.2693	0.9800	0.0033
	7 - 8	8.159	16.674	0.9881	-0.3173	0.9842	0.0037

results are given in Table 25. The mean value of the discharge coefficient, $(C_d)_m$, over the stated Reynolds number range, i.e., $(Re_D)_{min} \leq Re \leq (Re_D)_{max}$, as well as the maximum error or deviation

$$e = A_0 + A_1 Re_D - C_d(Re_D)$$
 (84)

is also given.

The data for the 12.5 inch venturi showed the analytically demonstrated trend of increasing discharge coefficient with Reynolds number and this data was piece-wise fit using two curve segments. The data for all other venturis was analyzed using one curve. The measured and correlated values for each venturi and pressure tap set are shown in Figures 75 through 90.

The maximum deviation between the least squares straight line and the experimental data is approximately 0.2 - 0.3%. This is considerably less than the deviation between the average discharge coefficient and the extremes of the data - a value of about 0.4 - 0.5%. This indicates that the discharge coefficient must be treated as a function of the Reynolds number and not as a constant value.

L. Comparison of Experimental and Theoretical Results

The calibration results of Section III.K can be compared to the theoretically determined discharge coefficients. Since both the turbulence level and entrance length were unknown in the calibration — the latter due to an elbow and flow straightening section upstream of the venturi, the envelope of the adiabatic calculations will be compared to the experimental results. Data from all four sets of pressure taps is shown in Figure 91. The analytic values bound most of the data; however, the data scatter makes it difficult to draw any definitive conclusions.

Figure 75. Measured and Correlated Discharge Coefficient. Venturi 48901-1. Tap Set 1 - 2

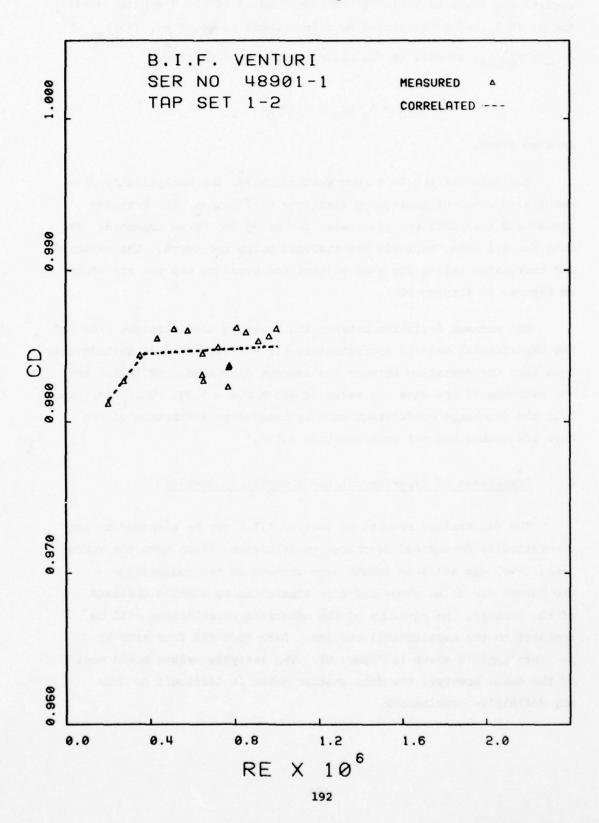


Figure 76. Measured and Correlated Discharge Coefficient. Venturi 48901-1. Tap Set 3 - 4

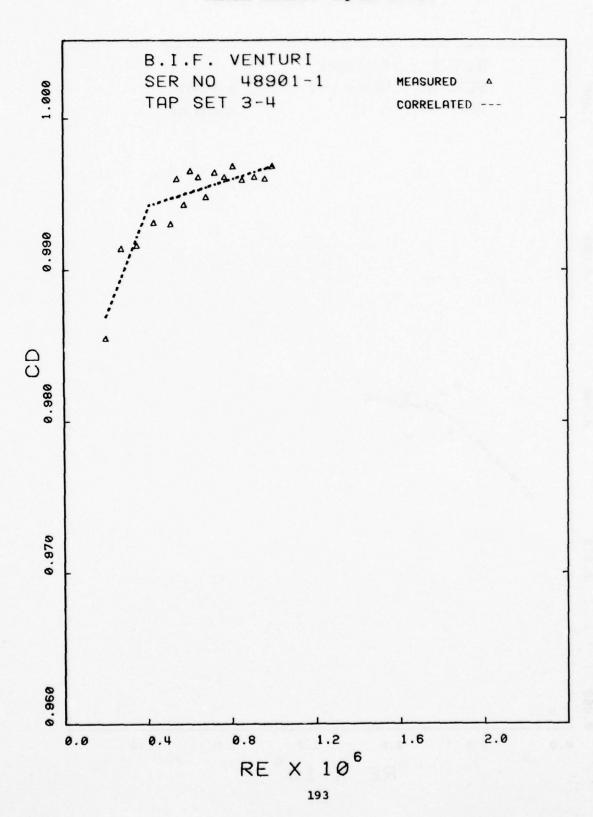


Figure 77. Measured and Correlated Discharge Coefficient. Venturi 48901-1. Tap Set 5 - 6

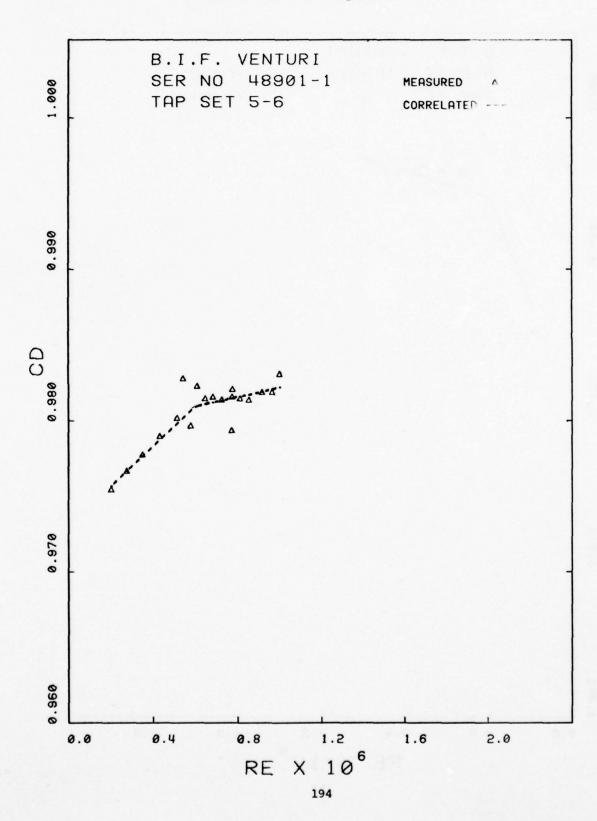


Figure 78. Measured and Correlated Discharge Coefficient. Venturi 48901-1. Tap Set 7 - 8

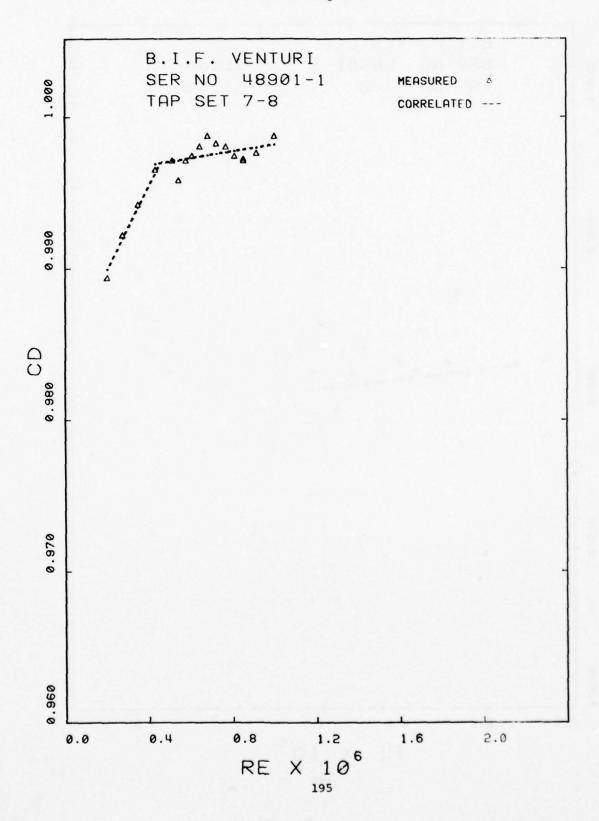


Figure 79. Measured and Correlated Discharge Coefficient. Venturi 48901-2. Tap Set 1 - 2

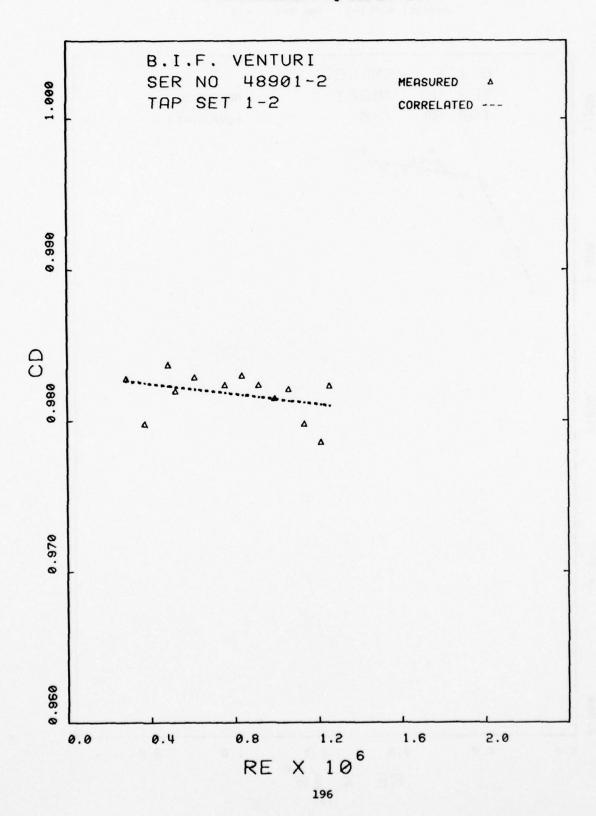


Figure 80. Measured and Correlated Discharge Coefficient. Venturi 48901-2. Tap Set 3 - 4

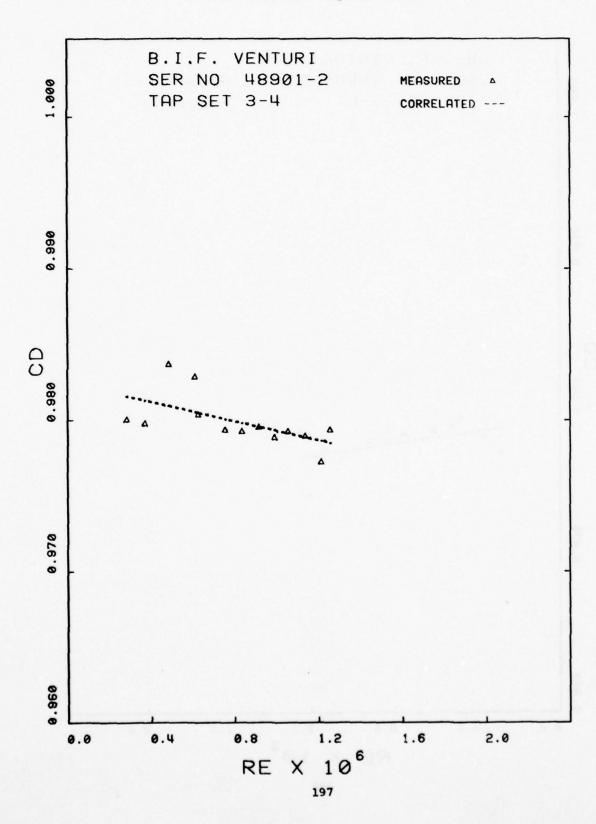


Figure 81. Measured and Correlated Discharge Coefficient. Venturi 48901-2. Tap Set 5 - 6

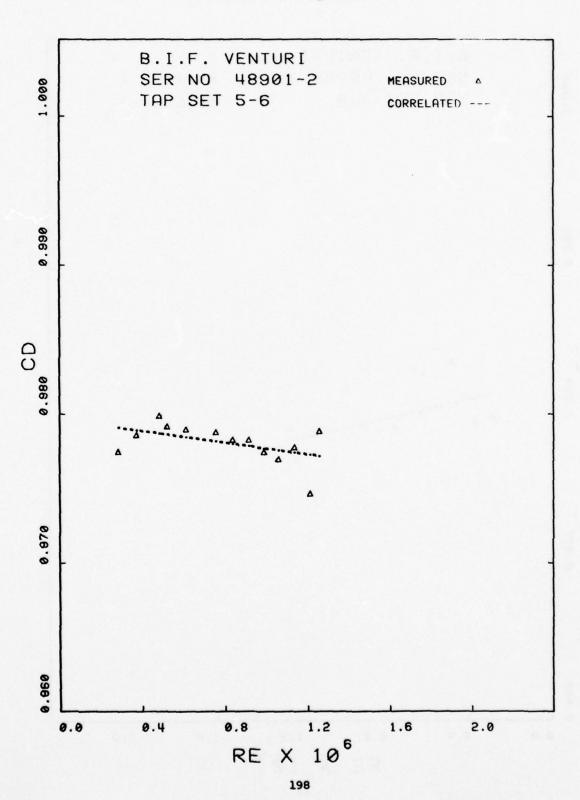


Figure 82. Measured and Correlated Discharge Coefficient. Venturi 48901-2. Tap Set 7 - 8

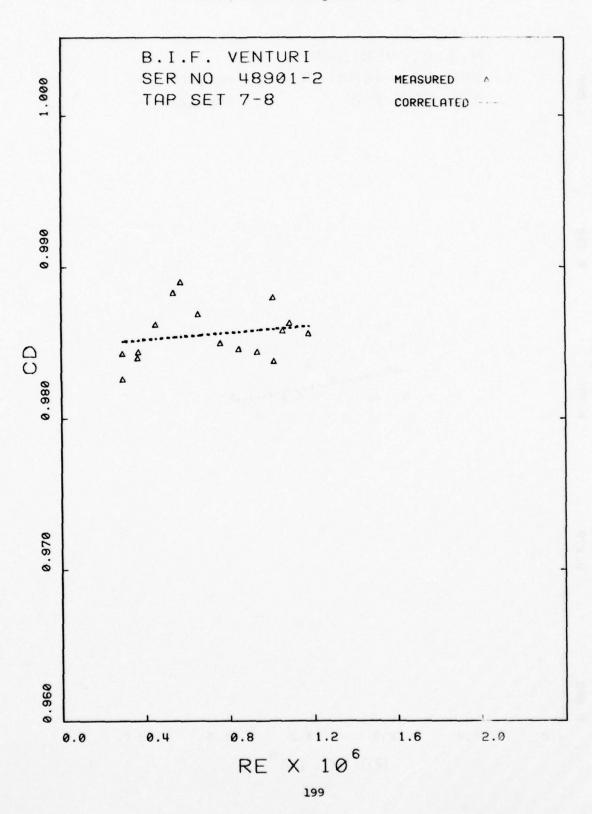


Figure 83. Measured and Correlated Discharge Coefficient. Venturi 48901-3. Tap Set 1 - 2

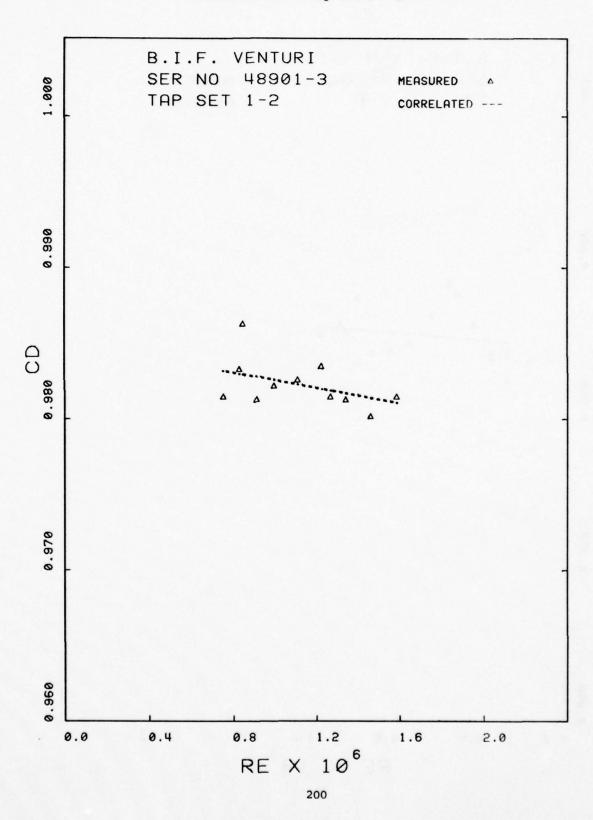


Figure 84. Measured and Correlated Discharge Coefficient. Venturi 48901-3. Tap Set 3 - 4

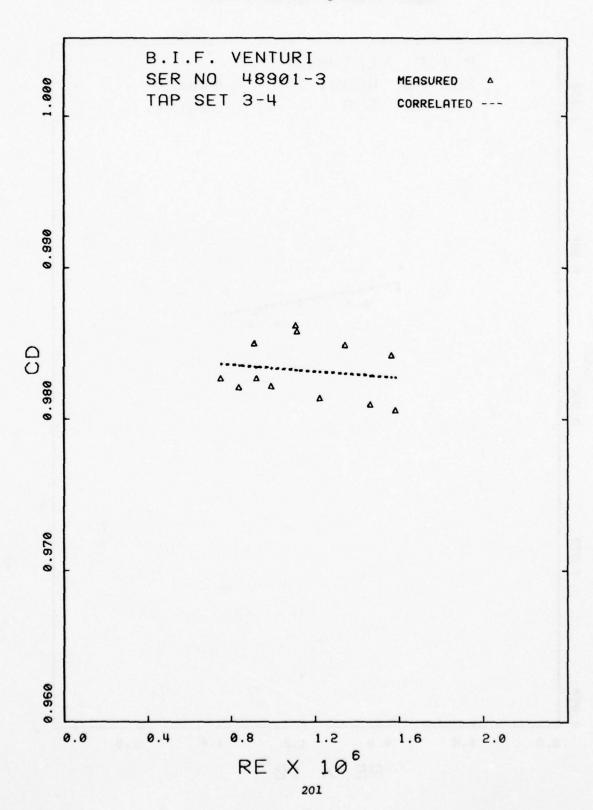


Figure 85. Measured and Correlated Discharge Coefficient. Venturi 48901-3. Tap Set 5 - 6

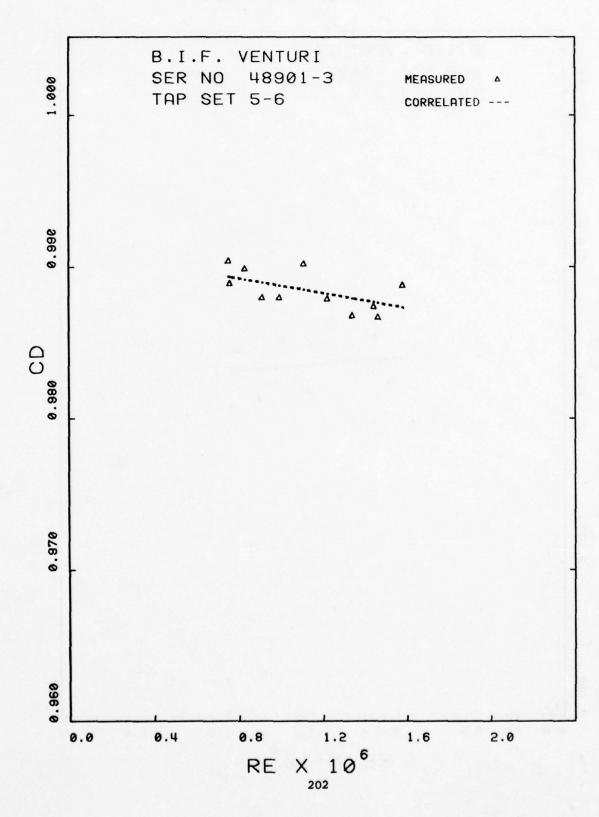


Figure 86. Measured and Correlated Discharge Coefficient.
Venturi 48901-3. Tap Set 7 - 8

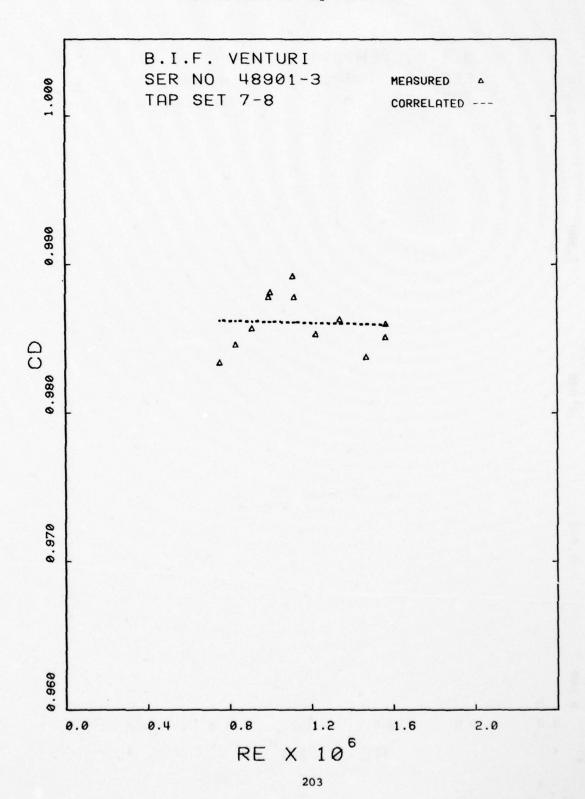


Figure 87. Measured and Correlated Discharge Coefficient.
Venturi 48901-4. Tap Set 1 - 2

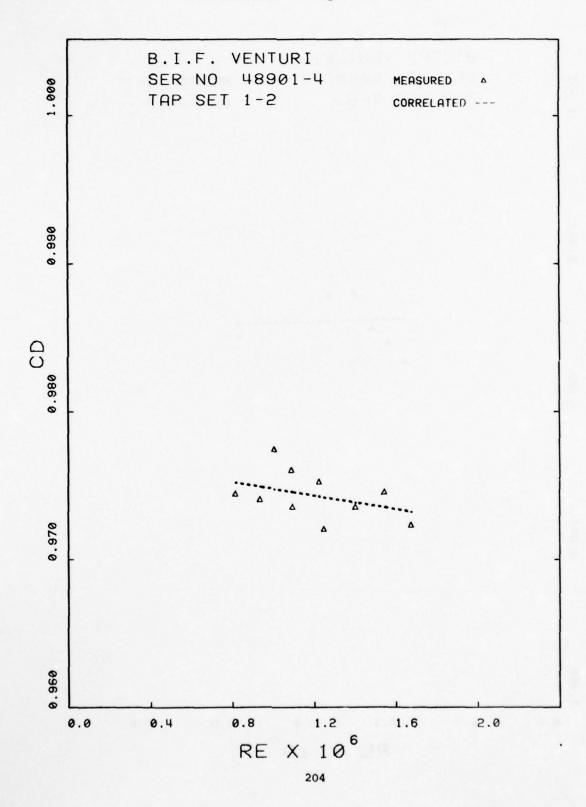


Figure 88. Measured and Correlated Discharge Coefficient. Venturi 48901-4. Tap Set 3 - 4

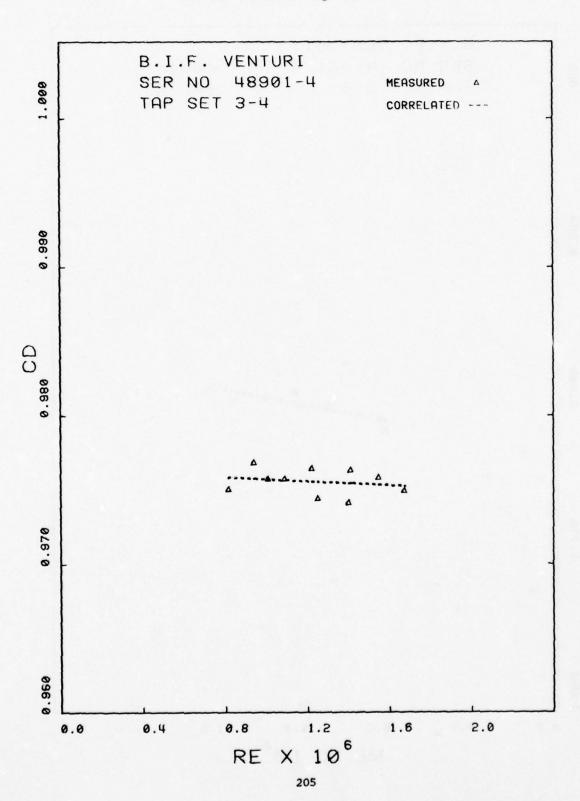


Figure 89. Measured and Correlated Discharge Coefficient. Venturi 48901-4. Tap Set 5 - 6

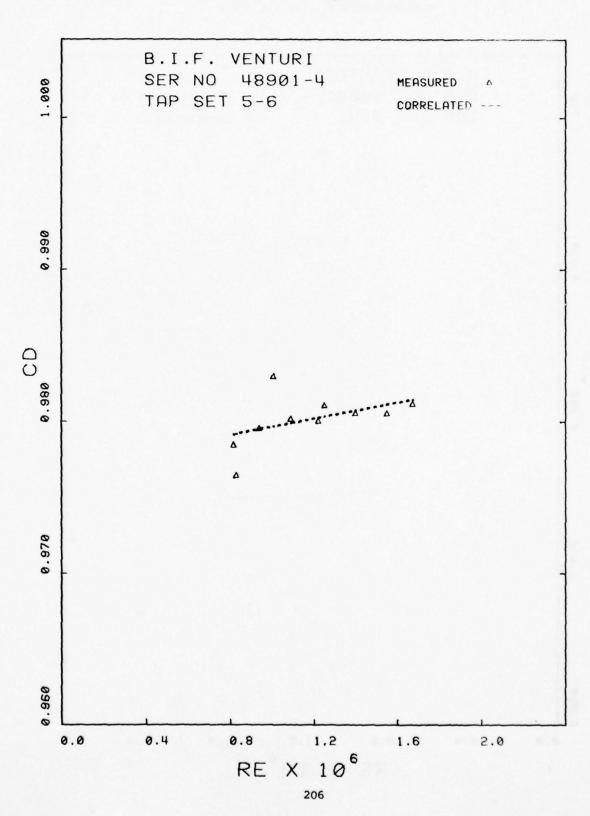
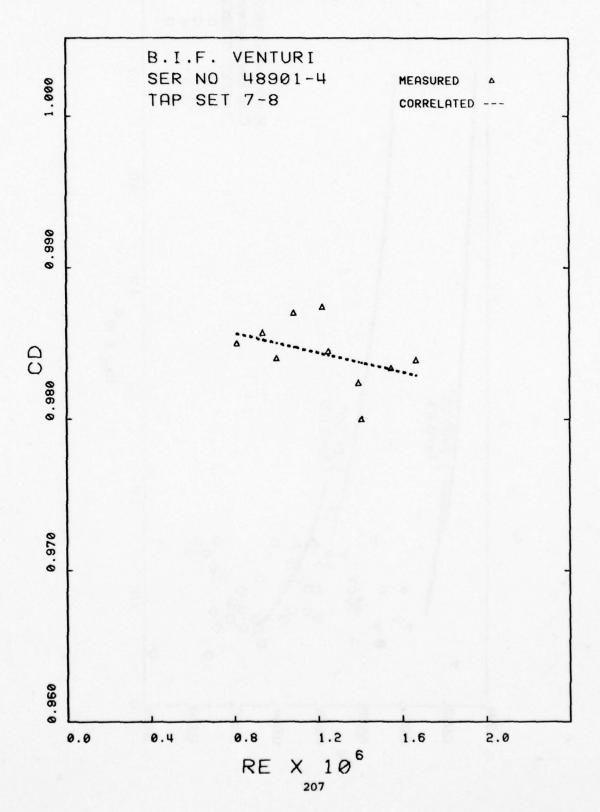


Figure 90. Measured and Correlated Discharge Coefficient. Venturi 48901-4. Tap Set 7 - 8



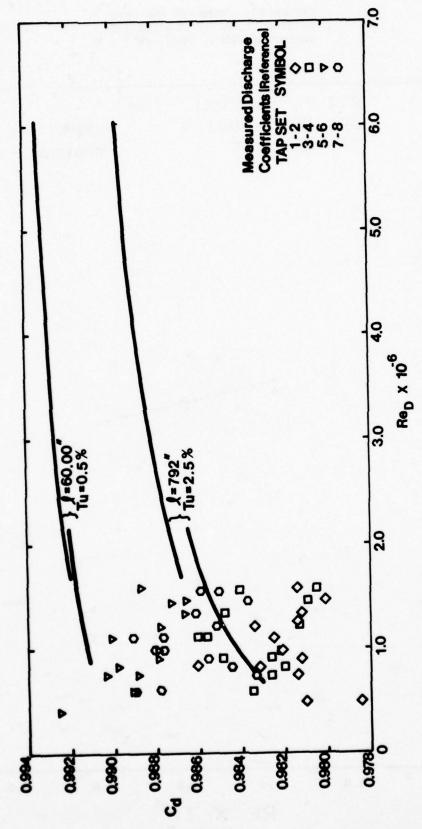


Figure 91. Experimentally Determined Discharge Coefficients

M. Summary

The objectives of the aerodynamic analysis of the Compressor Research Facility core flow measurement system were:

- Quantify the effects of Reynolds number and wall heating and/or cooling on boundary layer development and, thus, the discharge coefficient.
- 2) Determine the impact of calibration installation differences from the facility geometry on discharge coefficients.
- 3) Statistically analyze the calibration data.
- Compare the experimentally and analytically determined discharge coefficients.

The facility utilizes four venturis, two at a time, of three different sizes. Two configurations, 12.5 inch and 30.0 inch throat diameter, were chosen for analysis. The venturis operate over a range of temperatures and mass flow rates. The minimum and maximum flow rate conditions were employed in the calculation. This produced a Mach number effect as the two conditions corresponded to Mach numbers of approximately 0.2 and 0.8 for the 12.5 inch unit and 0.2 and 0.5 for the 30 inch unit. The variation in mass flow rate generated a Reynolds number range of from 8.7 x 10⁴ to 1.006 x 10⁶ for the 12.5 inch venturi and from 5.98 x 10⁵ to 6.073 x 10⁶ for the 30.0 inch universal venturi.

Computations for the 12.5 inch venturi showed that installation effects, i.e., entrance length changes of from 60 to 792 inches, had less influence on the discharge coefficients than did the Reynolds number. Furthermore, Mach number effects were clearly evident but of only 0.08% in magnitude.

Moreover, the results obtained for the 12.5 inch venturi also indicate that, under some conditions, the universal venturis have substantial regions of separated flow. The occurrence of separated flow in the diffuser does not necessarily imply measurement inaccuracies. It is certainly possible to determine a unique calibration for the device

with diffuser stall, e.g., an orifice operates with complete flow separation downstream of the element. This, however, presumes that all measurements are made upstream or in the venturi throat and not in the discharge. Measurements made downstream of the venturi will be uncertain and subject to time-dependent oscillations. In fact, the major detriment of diffuser stall is the generation of time-dependent pressure pulsations which can propogate upstream and influence the throat pressure measurements. This is of no consequence in an orifice since the pressure drop is relatively large when compared to a subsonic venturi. This is of sufficient magnitude - will increase the throat static pressure measurement uncertainty. In any event, calibration of the venturi with downstream pressure and temperature measurements is not recommended.

The results of the analysis of the 30.0 inch venturi show less dependence on Reynolds number than the 12.5 inch unit. The discharge coefficient varies by about 0.2% over the range of values considered. The Mach number effect is also smaller amounting to about 0.02%.

Analysis for different free-stream turbulence levels indicates that discharge coefficients are reduced by about 0.2% for an increase of from 0.5 to 2.5% in turbulence. There is also a very slight effect due to throat Mach number.

The entrance length has a substantial influence on the 30.0 inch venturi discharge coefficient reducing the values by about 0.5%, for length changes of from 60 to 792 inches. This is due to the thickened throat boundary layers developed over the greater length. Note that this effect is more important for the 30.0 than for the 12.5 inch unit.

Thermal effects for wall-gas temperature differences of \pm 40°R results in a variation in discharge coefficient of about 0.05%. Consequently, these can be ignored provided temperature difference can be maintained at levels of less than about 50°.

A comparison of experimental and theoretical results shows that the bulk of the calibration data falls within the envelope of analytic results. Note that the range of the calibration Reynolds numbers is much less than the actual operational envelope. This along with the data scatter, however, precludes any more definitive conclusions.

SECTION IV

DERIVATION OF AN IMPROVED

MATHEMATICAL MODEL FOR

VENTURI FLOWS

A. Introduction

The computations of Section III indicate that under some conditions the installation effects can alter venturi discharge coefficients by as much as 0.3 - 0.5% Since the overall flow measurement accuracy is to be 1%, this represents a significant uncertainty in the overall calibration/measurement process.

Calibrations carried out to date on the CRF universal venturis have not covered the complete operational Reynolds number range. Furthermore data scatter precludes any systematic extrapolation of the experimental results per se.

An estimate of the installation effects and a systematic extrapolation of the calibration data can be carried out with an improved mathematical model for venturi flows. As a consequence, a new technique has been developed.

The basic approach employed is similar to that of Section III in that inviscid and boundary layer solutions are serially combined via the boundary layer displacement thickness. The overall program contains the following elements:

- A routine to match the inviscid-viscous solution and control the iteration.
- 2) A laminar-transitional-turbulent boundary layer routine using the turbulence structural hypothesis ⁷⁶ and the transition computation of Section III.
- A quasi-three dimensional inviscid solution algorithm developed by AMO Smith.

The laminar-transitional-turbulent boundary layer routine has been generated by modifying a technique originated by Ferriss 77 and further

developed by Huffman. This technique employs an implicit-explicit numerical method in conjunction with the turbulence structural hypothesis. The extension of the method to laminar flows is fairly straightforward since provisions were made to include all the viscous terms in the equations of motion. Inclusion of a transition routine employing integral boundary layer properties is considerably more complex, but has been implemented.

The overall technique has now been developed and programmed. The mathematical framework, empirical functions for both transition and the turbulence model and the program logical structure are discussed in the ensuing sections.

B. Variable Grid Finite-Difference Module

Since boundary layer length scales differ by an order of magnitude, the axial and normal differences, i.e., Δx and Δy , must likewise differ. Furthermore, since property gradients tend to be greatest at the wall, Δy should also vary-being smallest at the wall and largest at the viscous-inviscid boundary. These characteristics are illustrated in Figure 92 where

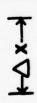
$$y_{i} = \Delta y \left(\frac{\eta^{i} - 1}{\eta - 1} \right)$$
 (85)

 Δy is the "nominal" grid spacing and η is a grid expansion factor, i.e., $\eta>1$. The effective Δy can be written as $\eta^{\dot{1}}\Delta y$ so that the grid expansion is due both to η and position. For η value of 1.1 and 25 grid points, the outermost spacing is 10.8 times the innermost. This approach yields a very "fine" inner mesh with a rather "coarse" outer spacing.

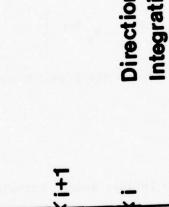
The first and second derivatives for an arbitrary property ϕ can be written in terms of a Taylor's series expansion as

$$\phi_{i-1} = \phi_{i} - \left(\frac{\partial \phi}{\partial y}\right)_{i} \left(y_{i} - y_{i-1}\right) + \left(\frac{\partial^{2} \phi}{\partial y^{2}}\right)_{i} \frac{(y_{i} - y_{i-1})^{2}}{2} + \dots$$

$$\phi_{i+1} = \phi_{i} + \left(\frac{\partial \phi}{\partial y}\right)_{i} \left(y_{i+1} - y_{i}\right) + \left(\frac{\partial^{2} \phi}{\partial y^{2}}\right)_{i} \frac{(y_{i+1} - y_{i})^{2}}{2} + \dots$$
(86)







Direction of Integration

1

213

$$y_i = \frac{\Delta y \left(\eta^i - 1\right)}{\eta - 1}$$



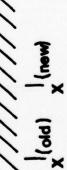
i = 2

n²∆y

-

ηΔy

Δy



~ Wall, y=0 Inner Boundary

Figure 92. Finite-Difference Module

which can be used to obtain $(\partial \phi/\partial y)_i$ and $(\partial^2 \phi/\partial y^2)_i$ in conjunction with equation (85). The resulting forms are

$$\left(\frac{\partial \phi}{\partial y}\right)_{i} = \frac{1}{\Delta y \eta^{i} (\eta + 1)} \left\{ \phi_{i+1} - (\eta^{2} - 1) \phi_{i} - \eta^{2} \phi_{i-1} \right\}$$
(87)

and

$$\left(\frac{\partial^{2} \phi}{\partial y^{2}}\right)_{i} = \frac{2\eta (\eta + 1)}{[\Delta y \eta^{i} (\eta + 1)]^{2}} \left\{\phi_{i+1} - (\eta + 1)\phi_{i} + \eta \phi_{i-1}\right\}$$
(88)

The differencing in the streamwise direction is more straightforward and

$$\left(\frac{\partial \phi}{\partial x}\right)_{i} = \frac{1}{\Delta x} \left\{ \phi_{i}^{(n)} - \phi_{i}^{(o)} \right\}$$
(89)

where the superscripts (n) and (o) denote the previous and current x stations.

C. Equations of Motion

The equations of motion for a laminar and/or turbulent boundary layer can be written as

$$U_{d} \frac{\partial U_{d}}{\partial X} + V_{d} \frac{\partial U_{d}}{\partial Y} = U_{d_{\infty}} \frac{\partial U_{d}}{\partial X} + \frac{1}{Re} \frac{\partial^{2} U_{d}}{\partial Y^{2}} + \frac{\partial \tau_{d}}{\partial Y} , \qquad (90)$$

$$U_{d} \frac{\partial \tau_{d}}{\partial x} + V_{d} \frac{\partial \tau_{d}}{\partial y} = 2a_{1}\tau_{d} \frac{\partial U_{d}}{\partial y} - 2a_{1}\sqrt{\tau_{d_{max}}} \frac{\partial G\tau_{d}}{\partial y} + \frac{1}{Re} \frac{\partial^{2}\tau_{d}}{\partial y^{2}} - 2a_{1}\sqrt{\tau_{d_{max}}} \frac{\partial G\tau_{d}}{\partial y} + \frac{1}{Re} \frac{\partial^{2}\tau_{d}}{\partial y^{2}}$$

$$(91)$$

$$\frac{\partial U_d}{\partial x} + \frac{\partial V_d}{\partial y} = 0 (92)$$

following Bradshaw and Ferriss $^{76}_{2\tau}$ with the viscous terms -- (1/Re)($\frac{\partial^2 U_d}{\partial x^2}$) and (1/Re)($\frac{\partial^2 U_d}{\partial x^2}$) -- now added. The addition of

these terms changes the basic nature of the equations from hyperbolic to parabolic and necessitates an alternate solution procedure. All the parameters of equations (90), (91) and (92) are dimensionless with

Equations (90) and (91) can be generalized by noting that each equation contains $\partial/\partial X$, $\partial/\partial Y$, $\partial^2/\partial Y^2$ and the first derivative with respect to Y of the other independent variable, i.e.,

$$A \frac{\partial \phi}{\partial x} + B \frac{\partial \phi}{\partial y} + C \frac{\partial^2 \phi}{\partial y^2} + D \frac{\partial F}{\partial y} = E$$
 (94)

where $D(\partial F/\partial Y)$ represents the coupling term and E the source term. Note that ϕ and F represent U and T with A, B, C, D, and E denoting the various coefficients, i.e.,

$$A = U_{d} B = V_{d} C = -1/Re D = -1$$

$$A = U_{d} b = V_{d} + 2a_{1}\tau_{d} \sqrt{\tau_{d}} G c = -1/Re d = -2a_{1}\tau_{d}$$

$$E = U_{d_{\infty}}dU_{d_{\infty}}/dX e = -2a_{1} \sqrt{\tau_{d_{max}}} \tau_{d}^{\partial G/\partial Y} - 2a_{1} \frac{\tau_{d}^{3/2}}{L} (95)$$

D. Finite-Difference Form of the Equations of Motion

The finite difference approximations of Section IV.B. can be extended to an implicit-explicit formulation by combining upstream

and downstream terms, 79 e.g.,

$$\left(\frac{\partial \phi}{\partial Y}\right)_{\mathbf{i}} = \left\{ \varepsilon \left(\frac{\partial \phi}{\partial Y}\right)_{\mathbf{i}} + (1 - \varepsilon) \left(\frac{\partial \phi}{\partial Y}\right)_{\mathbf{i}} \right\}$$
(96)

and

$$\left(\frac{\partial^2 \phi}{\partial y^2}\right)_{\mathbf{i}} = \left\{ \varepsilon \left(\frac{\partial^2 \phi}{\partial y^2} \right)_{\mathbf{i}} + (1 - \varepsilon) \left(\frac{\partial^2 \phi}{\partial y^2} \right)_{\mathbf{i}} \right\}$$
(97)

Note that the finite-difference approximations can be simplified considerably by defining

$$\xi_i = 1/[\Delta Y \eta^i (\eta + 1)]$$
 (98)

and

$$\zeta_i = 2\eta(\eta + 1)/[\Delta Y \eta^i (\eta + 1)]^2$$
 (99)

With equations (96) and (97) equation (94) takes the form

$$A_{i} \left\{ \frac{\phi_{i}^{(n)} - \phi_{i}^{(o)}}{\Delta x} \right\} + B_{i} \left\{ \varepsilon \left(\frac{\Delta \phi}{\Delta Y}^{(n)} \right)_{i} + (1 - \varepsilon) \left(\frac{\Delta \phi}{\Delta Y}^{(o)} \right)_{i} \right\} + C_{i} \left\{ \varepsilon \left(\frac{\Delta^{2} \phi^{(n)}}{\Delta Y^{2}} \right)_{i} + (1 - \varepsilon) \left(\frac{\Delta^{2} \phi}{\Delta Y^{2}} \right)_{i} \right\} + D_{i} \left\{ \varepsilon \left(\frac{\Delta F^{(n)}}{\Delta Y} \right)_{i} + (1 - \varepsilon) \left(\frac{\Delta F^{(o)}}{\Delta Y^{2}} \right)_{i} \right\} = E_{i}$$

$$(1 - \varepsilon) \left(\frac{\Delta F^{(o)}}{\Delta Y} \right)_{i} = E_{i}$$

$$(100)$$

where $(\Delta \phi/\Delta Y)_i$ denotes the finite-difference approximation to $\partial \phi/\partial Y$, etc.

Substitution of equations (87), (88), (98) and (99) for $\Delta\phi/\Delta Y$ and $\Delta^2\phi/\Delta Y^2$ respectively and collecting terms yields

$$\phi_{i+1}^{(n)} \left\{ B_{i} \varepsilon \xi_{i} + C_{i} \varepsilon \zeta_{i} \right\} + \phi_{i}^{(n)} \frac{A_{i}}{\Delta x} + B_{i} \varepsilon \xi_{i} (n^{2} - 1) - C_{i} \varepsilon \zeta_{i} (n + 1) + \phi_{i-1}^{(n)} \left\{ -B_{i} \varepsilon \xi_{i} n^{2} + C_{i} \varepsilon \zeta_{i} n \right\} = \phi_{i+1}^{(o)} \left\{ -B_{i} (1 - \varepsilon) \xi_{i} - C_{i} (1 - \varepsilon) \zeta_{i} \right\} + \phi_{i}^{(o)} \left\{ \frac{A_{i}}{\Delta x} - B_{i} (1 - \varepsilon) \xi_{i} (n^{2} - 1) + C_{i} (1 - \varepsilon) \zeta_{i} (n + 1) \right\} + \phi_{i-1}^{(o)} \left\{ B_{i} (1 - \varepsilon) \xi_{i} n^{2} - C_{i} (1 - \varepsilon) \zeta_{i} n \right\} + F_{i+1}^{(n)} \left\{ -D_{i} \varepsilon \xi_{i} \right\} + F_{i}^{(n)} \left\{ -D_{i} \varepsilon \xi_{i} (n^{2} - 1) \right\} + F_{i-1}^{(n)} \left\{ -D_{i} \varepsilon \xi_{i} (n^{2} - 1) \right\} + F_{i+1}^{(n)} \left\{ -D_{i} (1 - \varepsilon) \xi_{i} \right\} + F_{i+1}^{(n)} \left\{ -D_{i} (1 - \varepsilon) \xi_{i} \right\} + F_{i+1}^{(n)} \left\{ -D_{i} (1 - \varepsilon) \xi_{i} \right\} + F_{i+1}^{(n)} \left\{ -D_{i} (1 - \varepsilon) \xi_{i} \right\} + F_{i+1}^{(n)} \left\{ -D_{i} (1 - \varepsilon) \xi_{i} \right\} + F_{i+1}^{(n)} \left\{ -D_{i} (1 - \varepsilon) \xi_{i} \right\} + F_{i+1}^{(n)} \left\{ -D_{i} (1 - \varepsilon) \xi_{i} \right\} + F_{i+1}^{(n)} \left\{ -D_{i} (1 - \varepsilon) \xi_{i} \right\} + F_{i+1}^{(n)} \left\{ -D_{i} (1 - \varepsilon) \xi_{i} \right\} + F_{i+1}^{(n)} \left\{ -D_{i} (1 - \varepsilon) \xi_{i} \right\} + F_{i+1}^{(n)} \left\{ -D_{i} (1 - \varepsilon) \xi_{i} \right\} + F_{i+1}^{(n)} \left\{ -D_{i} (1 - \varepsilon) \xi_{i} \right\} + F_{i+1}^{(n)} \left\{ -D_{i} (1 - \varepsilon) \xi_{i} \right\} + F_{i+1}^{(n)} \left\{ -D_{i} (1 - \varepsilon) \xi_{i} \right\} + F_{i+1}^{(n)} \left\{ -D_{i} (1 - \varepsilon) \xi_{i} \right\} + F_{i+1}^{(n)} \left\{ -D_{i} (1 - \varepsilon) \xi_{i} \right\} + F_{i+1}^{(n)} \left\{ -D_{i} (1 - \varepsilon) \xi_{i} \right\} + F_{i+1}^{(n)} \left\{ -D_{i} (1 - \varepsilon) \xi_{i} \right\} + F_{i+1}^{(n)} \left\{ -D_{i} (1 - \varepsilon) \xi_{i} \right\} + F_{i+1}^{(n)} \left\{ -D_{i} (1 - \varepsilon) \xi_{i} \right\} + F_{i+1}^{(n)} \left\{ -D_{i} (1 - \varepsilon) \xi_{i} \right\} + F_{i+1}^{(n)} \left\{ -D_{i} (1 - \varepsilon) \xi_{i} \right\} + F_{i+1}^{(n)} \left\{ -D_{i} (1 - \varepsilon) \xi_{i} \right\} + F_{i+1}^{(n)} \left\{ -D_{i} (1 - \varepsilon) \xi_{i} \right\} + F_{i+1}^{(n)} \left\{ -D_{i} (1 - \varepsilon) \xi_{i} \right\} + F_{i+1}^{(n)} \left\{ -D_{i} (1 - \varepsilon) \xi_{i} \right\} + F_{i+1}^{(n)} \left\{ -D_{i} (1 - \varepsilon) \xi_{i} \right\} + F_{i+1}^{(n)} \left\{ -D_{i} (1 - \varepsilon) \xi_{i} \right\} + F_{i+1}^{(n)} \left\{ -D_{i} (1 - \varepsilon) \xi_{i} \right\} + F_{i+1}^{(n)} \left\{ -D_{i} (1 - \varepsilon) \xi_{i} \right\} + F_{i+1}^{(n)} \left\{ -D_{i} (1 - \varepsilon) \xi_{i} \right\} + F_{i+1}^{(n)} \left\{ -D_{i} (1 - \varepsilon) \xi_{i} \right\} + F_{i+1}^{(n)} \left\{ -D_{i} (1 - \varepsilon) \xi_{i} \right\} + F_{i+1}^{(n)} \left\{ -D_{i} (1 - \varepsilon) \xi_{i} \right\} + F_{i+1}^{(n)} \left\{ -D_$$

$$F_{i}^{(0)} = \{-D_{i}(1-\epsilon)\xi_{i}(\eta^{2}-1)\} + F_{i-1}^{(0)} = \{D_{i}(1-\epsilon)\xi_{i}\eta^{2}\} + E_{i}$$
 (101)

This relationship can be written symbolically as

$$A_{i}\phi_{i-1}^{(n)} + B_{i}\phi_{i}^{(n)} + \Gamma_{i}\phi_{i+1}^{(n)} = \Delta_{i}$$
 (102)

where A_i , B_i , Γ_i and Δ_i are known and $\phi_i^{(n)}$ is to be determined for all i.

Equation (101) is valid for both the momentum and shear stress equation with ϕ corresponding to U_d in the former and T_d in the latter. F then takes the other variable with a, b, c, d, and e replacing A, B, C, D, and E in the shear stress case.

E. Solution Procedure

Equation (102) denotes a system of relations since i takes on the values 1, 2, ..., I and

$$A_{1}\phi_{0}^{(n)} + B_{1}\phi_{1}^{(n)} + \Gamma_{1}\phi_{2}^{(n)} = \Delta_{1}$$

$$A_{2}\phi_{1}^{(n)} + B_{2}\phi_{2}^{(n)} + \Gamma_{2}\phi_{3}^{(n)} = \Delta_{2}$$

$$\vdots$$

: $A_{I}\phi_{I-1}^{(n)} + B_{I}\phi_{I}^{(n)} + \Gamma_{I}\phi_{I+1}^{(n)} = \Delta_{I}$ (103)

The subscripts o and I+1 denote the boundary conditions—inner and outer respectively—and thus these values, $\phi_O^{(n)}$ and $\phi_{I+1}^{(n)}$, are known. The coefficients can then be redefined as

$$\Delta_{1}' = \Delta_{1} - A_{1} \phi_{0}^{(n)} \qquad A_{1}' = 0$$

$$\Delta_{1}' = \Delta_{i} \qquad 1 \le i < I \qquad A_{i}' = A_{i} \qquad 1 < i \le I$$

$$\Delta_{1}' = \Delta_{1} - \Gamma_{1} \phi_{i+1}^{(n)}$$

$$B_{i}' = B_{i} \qquad 1 \le i \le I \qquad \Gamma_{i}' = \Gamma_{i} \qquad 1 \le i < I$$

$$\Gamma_{T}' = 0 \qquad (104)$$

and equation (103) becomes

$$A_{i}'\phi_{i-1}^{(n)} + B_{i}'\phi_{i}^{(n)} + \Gamma_{i}'\phi_{i+1}^{(n)} = \Delta_{i}'$$
 (105)

Equation (105) can be solved by means of the Thomas algorithm for tridiagonal matrices. The recursive relationships

$$M_{i} = B_{i}' - \frac{A_{i}'C_{i}'}{M_{i-1}}$$
 $M_{1} = B_{1}'$

$$N_{i} = [\Delta_{i}' - A_{i}'N_{i-1}]/M_{i}$$
 $N_{1} = \Delta_{1}'/B_{1}'$ (106)

are first computed and then $\phi_{i}^{(n)}$ is determined from

$$\phi_{I}^{(n)} = N_{I}$$
 $\phi_{i}^{(n)} = N_{i} - \frac{\Gamma_{i}^{*} \phi_{i+1}^{(n)}}{M_{i}}$
(107)

F. Normal Velocity Calculation

The linearization procedure employed in this and in other boundary layer solution techniques effectively "uncouples" the normal velocity from the shear stress and streamwise velocity. As a result the V_d velocity can be determined from the known U_d and T_d values. An independent relation for V_d can be derived by combining the momentum and continuity equations, i.e.,

$$\frac{\partial}{\partial Y} (U_{d}V_{d}) = -\frac{\partial U_{d}^{2}}{\partial X} + U_{d_{\infty}} \frac{dU_{d_{\infty}}}{dX} + \frac{\partial \tau_{d}}{\partial Y} + \frac{1}{Re} \frac{\partial^{2} U_{d}}{\partial Y^{2}} = \Phi$$
 (108)

This relationship can be solved for V_{d} by using a finite difference approximation. Thus

$$v_{d_{i+1}} = [\Delta Y \eta^{i} \phi_{i} + U_{d_{i}} V_{d_{i}}] / U_{d_{i+1}}$$
(109)

Note that a "two-point" expansion has been used for v_d . Since equation (109) represents a marching procedure, a three-point formulation would be unstable for all Δv .

G. Initial Velocity and Shear Stress Profiles

The calculation procedure of Section IV.E. must be initiated with known initial and boundary conditions, i.e., $\phi_i^{(o)}$ and $\phi_o^{(n)}$ as well as $\phi_{I+1}^{(n)}$ must be specified. Prescribed velocity and shear stress profiles can be used for this purpose or "equilibrium" solutions can be employed to initiate or start the solution procedure.

The laminar boundary layer calculation can be initiated with a Blasius solution, 32 i.e.,

$$u^{q} = u^{q^{\infty}} t_{\bullet}(H) \tag{110}$$

where

$$H = \frac{Y}{\sqrt{X}} \sqrt{ReU_{d_{\infty}}}$$
 and

$$f'(H) = 0.4696 \text{ H} - 9.189 \times 10^{-3} \text{ H}^4 + 2.260 \times 10^{-4} \text{ H}^7 -$$

$$5.026 \times 10^{-6} \text{ H}^{10} + 1.023 \times 10^{-7} \text{ H}^{13}$$
(111)

The latter relationship is derived in reference 82.

The boundary layer thickness Δ , i.e., δ/ℓ_r , can be written as

$$\Delta = 4.950 \sqrt{X_{eq}/Re}$$

or

$$x_{eq} = 0.0408 \Delta^2 \text{ Re}$$
 (112)

With Δ and Re specified, equation (112) can be used to determine X and the velocity profile determined from equations (110) and (111). Note that this "starting" solution is only valid for zero pressure gradient conditions.

The initial condition for a turbulent boundary layer follows the approach of Bradshaw extended to the inner region. In particular, the velocity profile takes the form

$$\frac{U}{U_{T}} = f(\frac{yU_{T}}{v}) + \frac{B_{W}}{2U_{T}} (1 - \cos\pi y/\delta)$$
 (113)

where yU_T/V denotes y^+ and $f(y^+)$ the inner layer or "log law" function. The second term denotes the outer or "wake" region.

The inner region solution can be obtained from 85

$$f(y^{+}) = \int_{0}^{y^{+}} \frac{\sqrt{1 + 4(\ell^{+}_{m})^{2} - 1}}{2(\ell^{+}_{m})^{2}} dy^{+}$$
 (114)

where l_{m}^{+} denotes the dimensionless mixing length and is given as

$$\ell_m^+ = (\kappa y^+) \left[1 - \exp(-y^+/A^+)\right]^2$$
 (115)

A is discussed in Section IV. J.

The velocity profile can be written in terms of dimensionless variables as

$$U_{d} = U_{d_{\tau}} [f(y^{+}) - f(\delta^{+})] + U_{d_{\infty}} - \frac{B_{w}}{2} [1 + \cos(\pi y/\delta)]$$
 (116)

The wake coefficient B_{W} is obtained in an iterative manner with the skin friction coefficient, C_{f} , and the momentum thickness Reynolds number, Re_{A} , specified. The parameter G is defined as

$$G = \frac{1}{\kappa} \sqrt{C_f/2}$$

where K is the log-law constant 0.41 and

$$B_w = 1 - G\{2.12 + \ln [\kappa G Re_{\theta}/(\theta/\delta)]\}$$
 (117)

with

$$\frac{\theta}{\delta} = \frac{G + B_w/2 - 2G^2 - 0.375B_w^2 - 1.59B_w^G}{1 + (49 - 297 G)/Re_A}$$
(118)

Furthermore

$$G = 1/\{2.12 + \ln [KGRe_{\theta}/(\theta/\delta)] \text{ when } B_{\psi} < -0.01$$
 (119)

The above system of equations is derived in reference 83 and is solved iteratively. A value for θ/δ is assumed and equations (117) and (118) solved. The new value of θ/δ is employed in the solution of equation (117) and the process continued until successive θ/δ values agree.

The shear stress profile is obtained from the velocity gradient and mixing length as

$$\tau_{d} = L_{m}^{2} \left(\partial U_{d} / \partial Y \right)^{2} \tag{120}$$

with $(\partial U_d/\partial Y)$ obtained from equation (116) and L defined as

$$L_{m} = \kappa Y \{1 - \exp(-y^{+}/A^{+})\} \sqrt{1 - 3.7(Y/\Delta)^{1.6}}$$

$$0 \le Y/\Delta \le 0.2$$

$$L_{m} = \kappa Y \{1.252 \exp(-1.95 Y/\Delta)\} \quad 0.2 < Y/\Delta \quad (121)$$

Velocity and shear stress profiles generated with the above relationships are plotted in Figures 93 and 94. The conditions correspond to those of Klebanoff⁸⁶ with the calculated and measured results in agreement.

H. Boundary Layer Integral Properties

The empirical length scales as well as the transition calculations employ boundary layer "integral" properties, i.e., skin friction coefficient, displacement thickness and momentum thickness. These can be readily calculated once the velocity profile is known. The boundary layer integral equation can itself be used to check the accuracy of the numerical technique. These calculations are outlined in the following paragraphs.

The skin friction coefficient is defined as

$$c_f = \tau \sqrt{(\frac{1}{2} \rho v_{\infty}^2)}$$
 (122)

where T denotes the wall shear stress, $\mu(\partial U/\partial y)_{wl}$. In terms of dimensionless variables, equation (112) becomes

$$\frac{c_f}{2} = \frac{1}{v_d^2} \frac{1}{Re} \left(\frac{\partial v_d}{\partial Y} \right)_{w1}$$
 (123)

The displacement and momentum thickness-both referenced to $\ell_{\mathbf{r}}$ -- are defined as

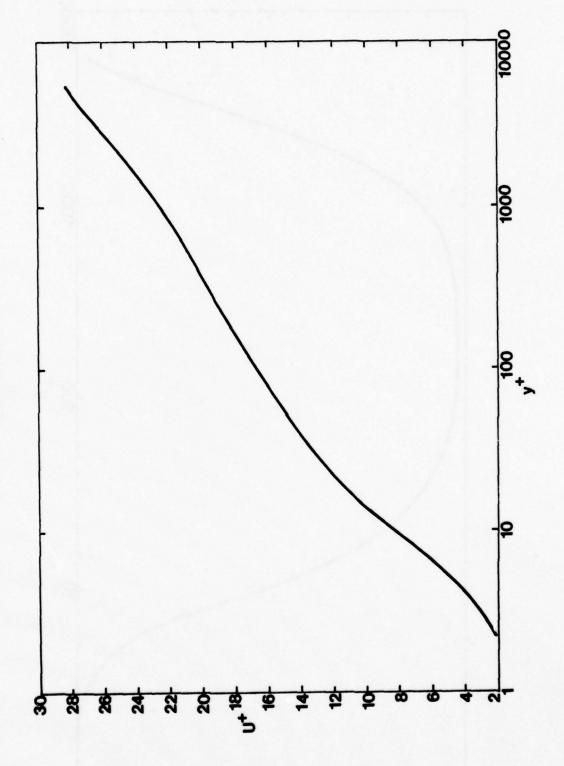


Figure 93. Velocity Profile Generated with the "Starting" Routine

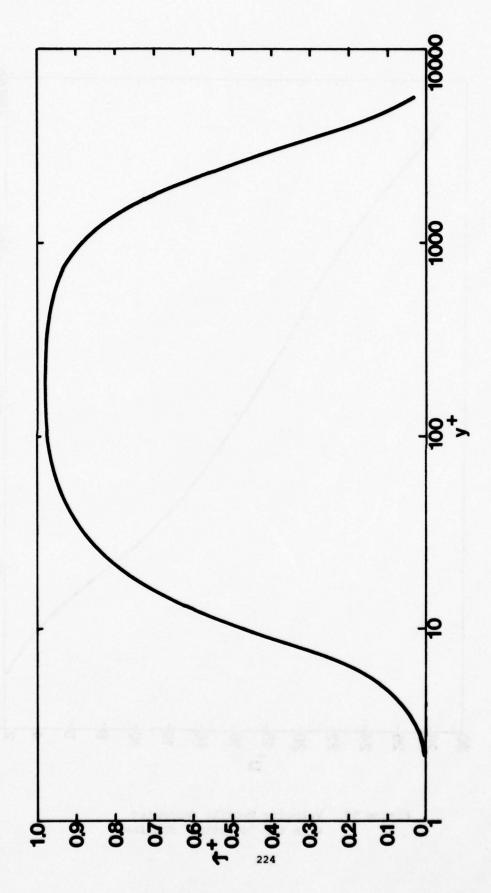


Figure 94. Shear Stress Profile Generated with the "Starting" Routine.

$$\Delta^* = \int_0^{\Delta} (1 - \frac{u_d}{u_{d_\infty}}) dy \qquad (124)$$

$$\Theta_{\rm m} = \int_0^{\Delta} \frac{v_{\rm d}}{v_{\rm d_{\infty}}} \left(1 - \frac{v_{\rm d}}{v_{\rm d_{\infty}}}\right) dy \tag{125}$$

where Δ denotes the boundary layer thickness, δ/ℓ_r . This is defined as the Y value at which $v_d/v_d=0.995$.

The uncertainty in the calculation can be estimated by independently computing both sides of the momentum integral equation and comparing the results. Any difference in these two values is indicative of momentum gain or loss. The momentum integral equation is

$$\frac{d\Theta_{m}}{dx} + \left(\frac{\Delta^{\star}}{\Theta_{m}} + 2\right) \frac{\Theta_{m}}{U_{d_{\infty}}} \frac{dU_{d_{\infty}}}{dx} = \frac{C_{f}}{2}$$
(126)

With all parameters independently computed, $\Theta_{\mathbf{m}}$, Δ^* , and $C_{\mathbf{f}}$, the error in the procedure can be estimated.

Note that the integrals of equations (124) and (125) are computed using the trapezoidal rule with $d\Theta_{\rm m}/dX$ and $dU_{\rm d_{\infty}}/dX$ determined using the differencing of Section IV.B.

Transition Prediction

While the governing system of equations, i.e., equations (90), (91) and (92) is formally capable of predicting transition given some initial shear stress perturbation, it was decided to use a more empirical technique. This model rather than a shear stress growth approach was chosen because of its demonstrated reliability and ability to reproduce experimental results. The use of a "phenomenologically" based transition prediction is certainly a worthwhile goal but undoubtedly a research project in itself.

As the boundary layer thickens in the downstream flow direction, the laminar flow tends to become unstable and undergoes transition to turbulent flow under the stimulus of disturbances in the flow. The transition zone extends from the point where the mean velocity profile of the laminar boundary layer begins to change to the point where the mean velocity profile of the turbulent boundary layer first appears. In general, the transition zone is short enough to be adequately represented by a transition point, i.e., the laminar flow model is employed until transition occurs and then the turbulent model is used. The position of transition depends largely upon the interaction of the boundary layer with random flow disturbances. The parameters most significantly affecting the transition position are:

- (i) the momentum thickness Reynolds number, Re₀;
- (ii) the pressure gradient in the flow direction, $U_{d_{\infty}}^{dU} d_{\infty}^{dX}$;
- (iii) the curvature of the surface.

The source of flow disturbances can be due to:

- (i) free-stream turbulence levels;
- (ii) surface roughness;
- (iii) noise being transmitted through the fluid.

As shown theoretically by numerous investigators, the laminar boundary layer exhibits stability characteristics which are largely governed by Reynolds number and pressure gradient. Transition then can be thought of as consisting first of a point of instability followed by a transition zone and finally by a point of transition. The point of instability being functionally dependent upon $\operatorname{Re}_{\theta}$ and $\operatorname{U}_{\operatorname{d}_{\infty}}\operatorname{dU}_{\operatorname{d}_{\infty}}\operatorname{dX}$ with the extent of the transition zone determined by $\operatorname{U}_{\operatorname{d}_{\infty}}\operatorname{dU}_{\operatorname{d}_{\infty}}\operatorname{dX}$ averaged over the length of the zone and the free-stream turbulence level.

The momentum thickness Reynolds number at the point of neutral stability, $\text{Re}_{\theta,n}$, has been correlated with the pressure gradient parameters, θ_m^2 dU/dx/ ν , in reference 89. This relationship is shown in Figure 95. Functionally, this can be written as

$$Re_{\theta,n} = Re U_{d_{\infty}}^{\Theta} m_{n} = f_{1} \left(\Theta_{m}^{2} Re \frac{dU_{d_{\infty}}}{dx} \right)$$
 (127)

As noted above, the extent of the transition region is a function of both pressure gradient and turbulence level. These two effects have been correlated separately and are shown in Figure 96 and 97 respectively.

The relationships of Figure 96 can be denoted as

$$(\Delta \operatorname{Re}_{\Theta})_{1} = \operatorname{ReU}_{d_{\infty}}(\Theta_{m_{t,s}} - \Theta_{m_{t}}) = f_{2}\left(\langle \Theta_{m}^{2} \operatorname{Re} \frac{dU_{d_{\infty}}}{dx} \rangle\right)$$
(128)

where

$$\langle \Theta_{m}^{2} \text{ Re } \frac{dU_{d_{\infty}}}{dX} \rangle = \text{Re } \frac{\int_{x_{n}}^{x_{ts}} \left(\Theta_{m}^{2} \frac{dU_{d_{\infty}}}{dX}\right) dX}{(x_{ts} - x_{n})}$$
 (129)

Figure 97 shows the effect of free-stream turbulence level on transition under conditions of zero pressure gradient. Functionally this becomes

$$(\Delta \text{Re}_{\Theta})_2 = \text{ReU}_{d_{\infty}} (\Theta_{m_{\text{tb}}} - \Theta_{m_n}) = f_3(\text{Tu})$$
 (130)

Equations (127) through (130) can be combined to compute the transition point in the presence of both free-stream turbulence and pressure gradients and

$$\Theta_{m_{tb}} = \Theta_{m_{n}} + (\Theta_{m_{ts}} - \Theta_{m_{n}}) \begin{cases} \frac{\Theta_{m_{tb}} - \Theta_{m_{n}}}{\Theta_{m_{ts}} - \Theta_{m_{n}}} \\ \frac{\Theta_{m_{tb}} - \Theta_{m_{n}}}{\Theta_{m_{ts}} - \Theta_{m_{n}}} \end{cases}$$
(131)

where the subscript 0 denotes a zero pressure gradient condition. All the parameters on the left-hand side of equation (131) can be computed as the boundary layer develops. When $\theta_{\rm m} \geq \theta_{\rm m}$, an unstable condition

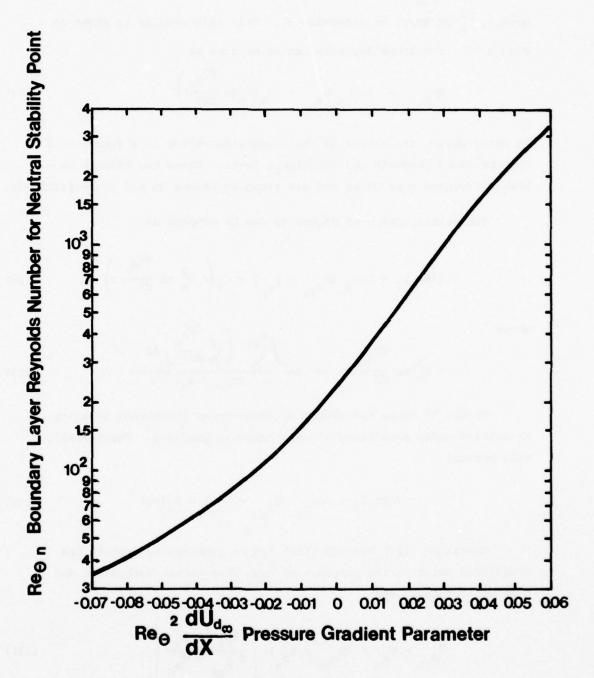


Figure 95. Neutral Stability Point as a Function of Pressure Gradient

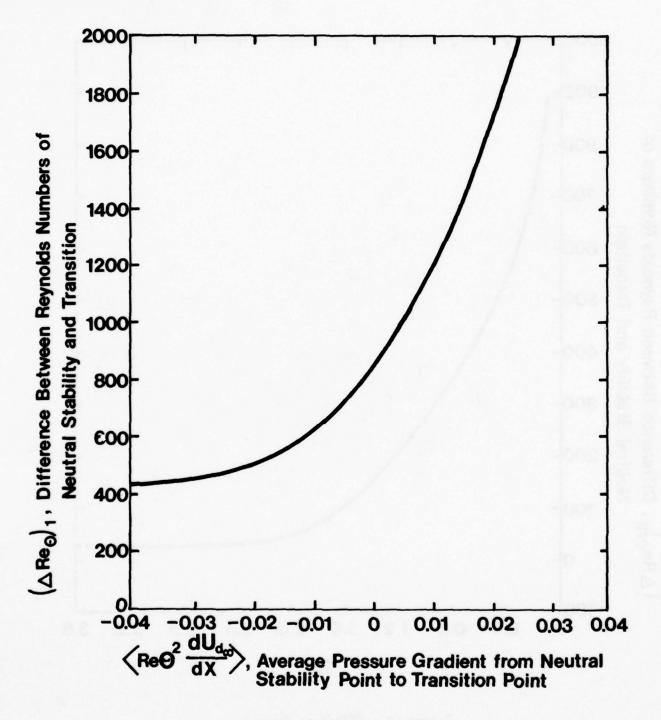


Figure 96. Position of Self-Excited Transition as a Function of Average Pressure Gradient.

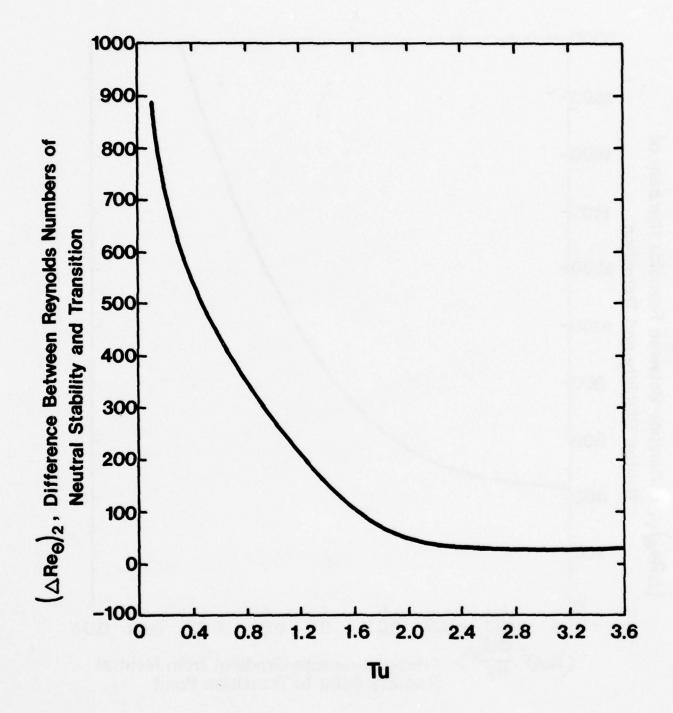


Figure 97. Effect of Free-Stream Turbulence on Transition Location

occurs and the computation of $<\theta_m^2 \text{Re } dU_{d_\infty}/dx>$ is initiated. θ_{m} the is then determined at each downstream station following equation (131) and Figures 95 through 97. The boundary layer is deemed turbulent when $\theta_{m} \geq \theta_{m}$. At this point, the turbulent boundary layer starting routine, Section IV.G., is used to generate a turbulent velocity and shear stress profile and the calculation continues.

J. Empirical Functions

The accuracy of the turbulent boundary layer calculations depends on the empirical functions a_1 , ℓ and G. These were originally formulated by Bradshaw, et.al. 66 as

$$a_1 = 0.15$$
 (132)

$$L/\Delta = f_1(Y/\Delta) \tag{133}$$

$$G = \sqrt{\tau_{d_{\text{max}}}/U_{d_{\infty}}^2} \quad f_2(Y/\Delta)$$
 (134)

with

$$f_{1}(Y/\Delta) = \kappa(Y/\Delta) \qquad 0 \le Y/\Delta < 0.18$$

$$f_{1}(Y/\Delta) = 0.095 - 0.055(2 \frac{Y}{\Delta} - 1)^{2} \quad 0.18 \le Y/\Delta < 1.1$$

$$f_{1}(Y/\Delta) = 0.016 \exp\{-10(Y/\Delta - 1.1)\} \quad 1.1 \le Y/\Delta \qquad (135)$$

and

$$f_{2}(Y/\Delta) = 17.5(Y/\Delta)^{1.86} \qquad 0 \le Y/\Delta < 0.63$$

$$f_{2}(Y/\Delta) - 09.0(Y/\Delta) - 49.75 \qquad 0.63 \le Y/\Delta < 0.89$$

$$f_{2}(Y/\Delta) = 18.7(Y/\Delta) + 14.85 \qquad 0.89 \le Y/\Delta \qquad (136)$$

In order to account for wall effects both L/Δ and G were modified by multiplication by a wall function f_{w_1} and f_{w_2} where

$$L/\Delta = f_1(Y/\Delta) f_{w_1}(y^+)$$

and

$$G = \sqrt{T_{\text{max}}/U_{d_{\infty}}^2} f_2(Y/\Delta) f_{W_2}(Y^+)$$

with y = YReU_T.

The dissipation length scale wall function, $f_{w_1}(y^+)$, was originally developed by van Driest⁹⁰ and extended by a number of investigators including Cebeci and Smith⁹¹ and Huffman and Bradshaw.⁹² Following the format of reference 92, $f_{w_1}(y^+)$ becomes

$$f_{w_1}(y^+) = 1 - \exp \left\{-\sqrt{\tau_{t\ell}^+}y^+/A^+\right\}$$
 (137)

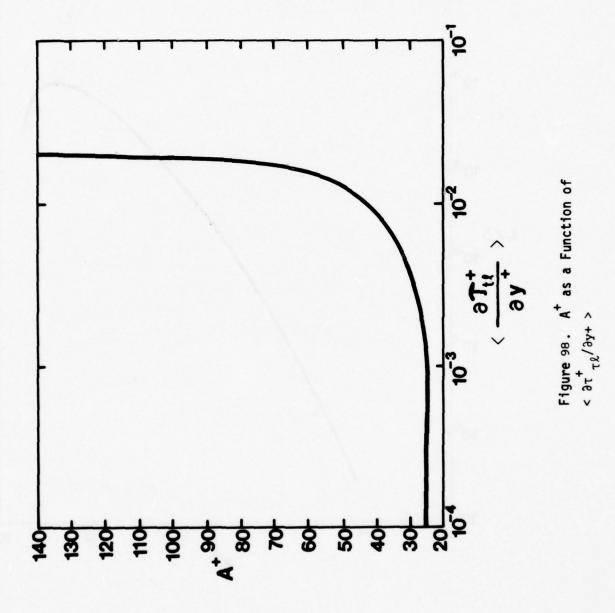
where $\tau_{\text{tl}}^{+} = [(\partial U/\partial Y)/\text{Re} + \tau_{\text{d}}]/[U_{\text{d}_{\infty}}^{-2}(C_{\text{f}}/2)]$ and A^{+} is a function of the average value of $\partial \tau_{\text{tl}}^{+}/\partial y^{+}$ in the wall region. The $A^{+} = A^{+}(<\partial \tau_{\text{tl}}^{+}/\partial y^{+}>)$ relation is shown in Figure 98 which is described in detail in reference 93.

In order to reproduce a mixing length formulation in the inner region, i.e., production equals dissipation, G is set to zero for $Y/\Delta < 0.18$ and

$$f_{W_2}(Y/\Delta) = 0 \qquad 0 \le Y/\Delta < 0.18$$

$$f_{W_2}(Y/\Delta) = 1 \qquad 0.18 < Y/\Delta \qquad (138)$$

The overall variation of L and G (using the wall function f_{w_1} rather than f_{w_2} for G, with position is shown in Figure 99 and 100. The gradient of G, $\partial G/\partial Y$, is shown in Figure 101.



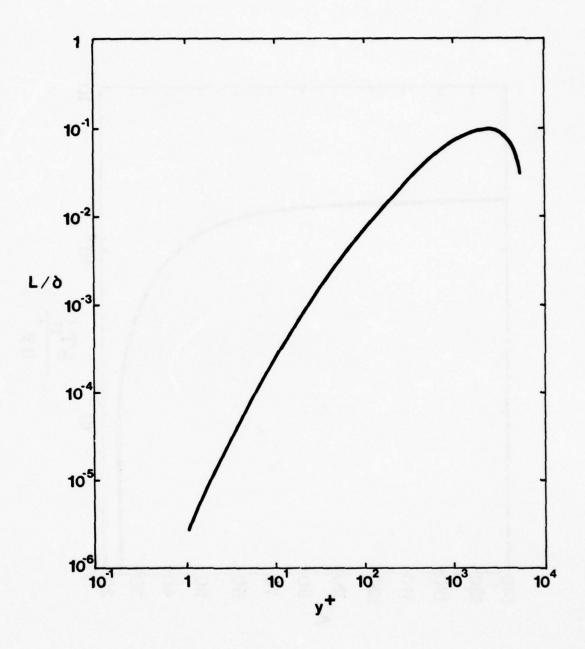


Figure 99. The Dissipation Length Scale as a Function of Position

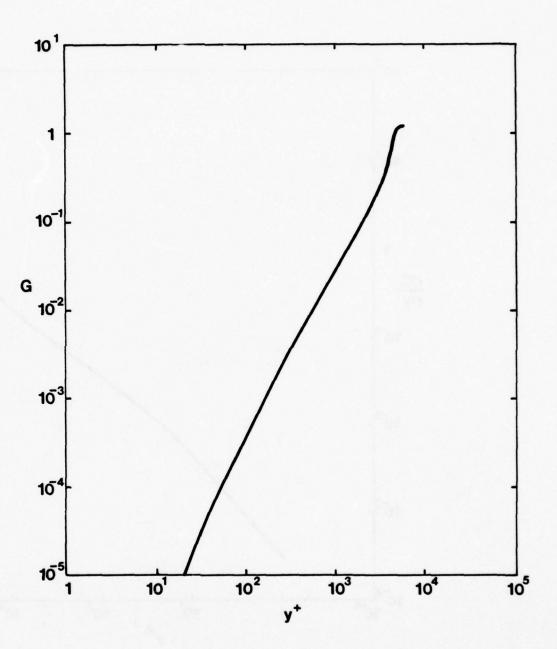


Figure 100. The Diffusion Function Versus Position

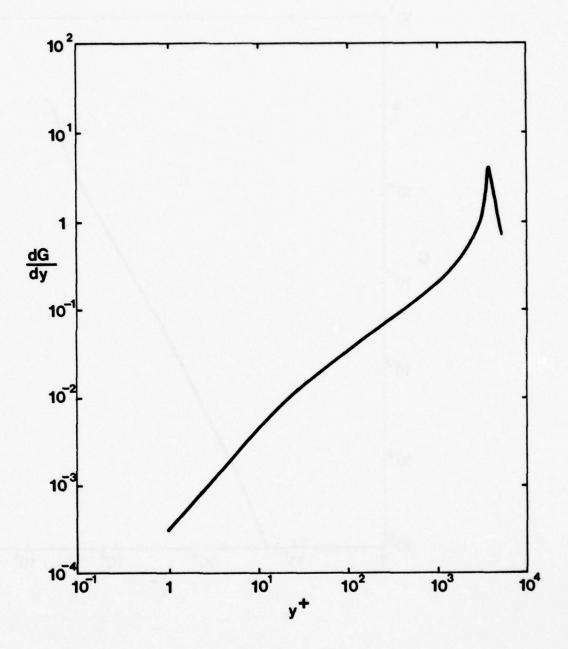


Figure 101. The Gradient of the Diffusion Function Versus Position

K. Program Structure

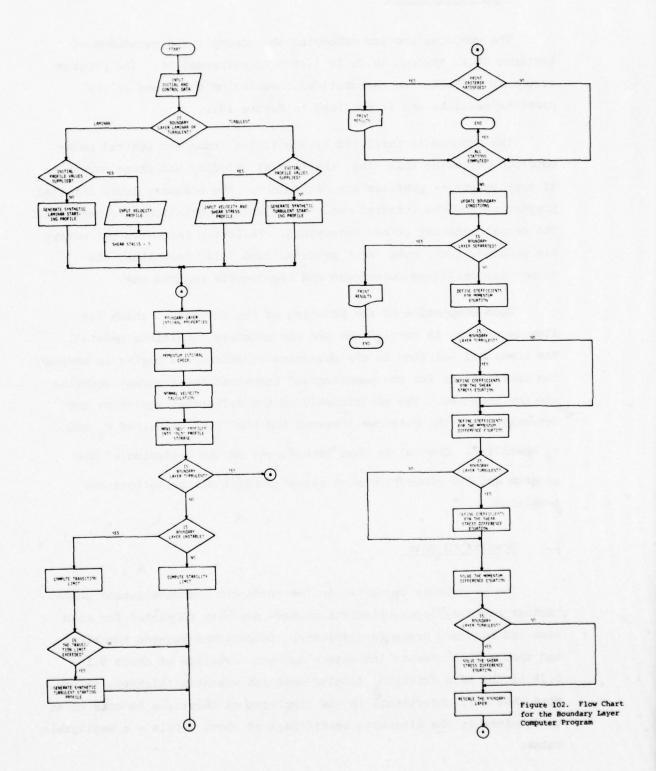
The computer program embodying the concepts and equations of Sections IV.A. through IV.J. is listed in reference 94. The program structure reflects the mathematical formulation described in the previous sections and is outlined in Figure 102.

The program is initiated by specifying input and control parameters. Following this step, the initial velocity and shear stress — if appropriate — profiles are determined. The boundary layer integral properties and the integral momentum balance calculations are performed. The normal velocity is now determined. Following this step the arrays are updated, i.e., move "new" profiles into "old" locations, the transition condition determined and the results printed out.

Upon completion of the printing of the results, a check for flow separation is carried out and the boundary conditions updated. The numerical solution to the governing equations now begins in earnest. The coefficients for the momentum and turbulent shear stress equation are now computed. The coefficients of the difference equations are determined and the matrices inverted and the "new" values of \mathbf{U}_d and \mathbf{T}_d specified. Control is then transferred to the beginning of the program and the above processes repeated until all x-stations are completed.

L. Results to Date

The program is currently in the check-out and development phase. Laminar boundary layer calculations have now been completed for both zero and non-zero pressure gradients. Comparisons between numerical and theoretical results indicate a maximum deviation of about 0.1 - 0.2% in the skin friction, displacement and momentum thickness values. Note that this uncertainty in the displacement thickness amounts to an uncertainty in the discharge coefficient of about 0.001% - a negligible value.



The calculation of all transition parameters has also been verified with results to date duplicating experimental measurements.

Both the laminar and turbulent "starting" routines are operational with results reproducing measured values.

SECTION V

EXPERIMENTAL EVALUATION OF

COMPRESSOR TRANSIENT PERFORMANCE

A. Introduction

As the performance of gas turbine engines has increased, the reliability of engine designs has become much more important. High performance aircraft undergoing violent maneuvers generate conditions which are difficult to envision in the engine design phase and even more difficult to analyze if predicted during development. As a result, advanced aircraft turbine engines are encountering operational compressor stalls. The bulk of the engine compressor stalls occur during throttle excursions, i.e., engine speed transients.

In addition, the operational mode and attitude of the aircraft can also influence compressor operation since flight at high angles of attack can result in severe inlet distortion and an accompanying compressor stall. There is obviously a complex interaction between engine operating condition, i.e., accelerating or decelerating, and aircraft attitude. It is virtually impossible to simulate all possible interactions between the engine inlet and the engine operating mode. As a result, new engines are designed to accept substantial inlet distortions with minimum degradations in compressor performance. This approach is likely to continue since it represents the division between the airframe and turbine engine manufacturer. This concept will be used in the discussions to follow with emphasis placed on compressor transient operation rather than on inlet distortion.

Turbine engines are nominally designed for steady-state operation with transient performance determined during the latter stages of the design program. Despite this apparent lack of emphasis on acceleration capabilities, the turbine engine has inherently good speed change characteristics as a result of low inertia and high power capabilities. These inherent characteristics frequently come into play during the operational life of an engine. If, as a result of transiently induced compressor stalls, the engine operational envelope is restricted, the value of the weapons system can be severely curtailed.

A number of mechanisms can be postulated for transiently induced compressor stalls. These can be grouped into three categories:

- 1) Inadequate control system capabilities
- 2) Time-dependent aerodynamic effects
- 3) Time-dependent thermal effects

Stalls encountered in variable geometry compressors are frequently blamed on control system malfunctions. These may consist of limited frequency response in sensors, usually thermocouples measuring compressor inlet temperatures, limited frequency response in variable vane actuation systems and/or excessive mechanical variation in vane actuators. The most common technique to eliminate operational compressor stalls is to reschedule the variable geometry stages. This may be accompanied by either a limitation in throttle excursion rate or compressor operating range. This is obviously a short-term solution resulting in satisfactory but compromised performance.

Time-dependent aerodynamic effects such as flutter, rotating stall, stationary distorted pressure profiles, secondary flow effects, and airfoil wake interactions have long been recognized as a second, i.e., lower order influence on compressor performance. In general, however, effects of this nature are not thought to be important in operational stalls -- aside from compressor inlet distortion as noted above. Note that the compressor operational envelope normally excludes the rotating stall and flutter regions and, thus, these effects should not influence transient performance unless the flutter and rotating stall boundaries change with acceleration rate.

The interaction between compressor aerodynamic performance and acceleration or deceleration rate is also a potential source of compressor stall. Historically, this mechanism has been neglected since the time scales and frequencies of the two phenomena differ markedly in most cases. The transit time of a fluid particle through a compressor is of the order of 4 - 6 μ sec while acceleration times are of the order of 2 - 4 sec. Maximum acceleration rates may approach 40% of the design speed and, thus, for the transit times quoted above, the compressor

speed would change by approximately 0.2% of the design speed. This is negligible from a steady-state point of view and aerodynamic interactions have been accordingly dismissed.

The final potential cause of transiently induced compressor performance changes can be traced to thermal effects. Speed changes result in changes in compressor pressure ratio and, thus, gas temperature. This in turn creates thermal growth or shrinkage in both the compressor case and rotor assembly. If a differential rate of thermal expansion exists between the case and rotor assembly, as is undoubtedly the situation, then the compressor airfoil tip clearances will change with the rate of speed change resulting in alterations in compressor performance. This impact of tip clearance changes on compressor performance will be a function of the specific compressor design.

The number and severity of operational compressor problems mandates an investigation of transient effects, and thus, an experimental evaluation of compressor transient performance is being carried out using an existing J-85 engine and test stand located at the AF Aero Propulsion laboratory. The program is made up of the following tasks:

- Utilization of a digital simulation program for the J-85 compressor.
- Modifications to the compressor and/or test facility to accommodate the transient testing.
- Design, fabrication and installation of the appropriate instrumentation.
- 4) Preliminary and final design of the experiment.
- 5) Development of a real time data processing system and the related computer programs.
- 6) Transient testing of the J-85 engine/compressor.
- 7) Data analysis.

These will be discussed in the following sections.

B. A Digital Simulation of the J-85 Compressor

1. The Equations of Motion

The governing equations for flow through a turbine engine can be derived by considering the flow element shown in Figure 103³¹. The momentum and energy transport is for the x component only; however, the sketch can be generalized to the y and z directions if desired.

The continuity relation can be derived by equating

which yields

$$\frac{\partial \rho h}{\partial \tau} + \nabla \cdot \rho h U = 0 \tag{139}$$

where h = h(x) and denotes the variable stream-tube thickness. Even though equation (139) was generated in Cartesian coordinates it can be generalized to any coordinate system using the appropriate definition of the vector operators.

The momentum equation can be obtained in a similar manner by considering

This yields

$$\rho \left[\frac{\partial \mathbf{u}_{\mathbf{x}}}{\partial \tau} + \mathbf{u}_{\mathbf{x}} \frac{\partial \mathbf{u}_{\mathbf{x}}}{\partial \mathbf{x}} + \mathbf{u}_{\mathbf{y}} \frac{\partial \mathbf{u}_{\mathbf{x}}}{\partial \mathbf{y}} + \mathbf{u}_{\mathbf{z}} \frac{\partial \mathbf{u}_{\mathbf{z}}}{\partial \mathbf{z}} \right] + \frac{\partial \mathbf{p}}{\partial \mathbf{x}} = \rho \mathbf{F} \mathbf{r}_{\mathbf{x}}$$
(140)

for the x-direction. In vector form

$$\rho \stackrel{\overrightarrow{DU}}{DT} + \overrightarrow{V} p = \rho \overrightarrow{Fr}$$
 (141)

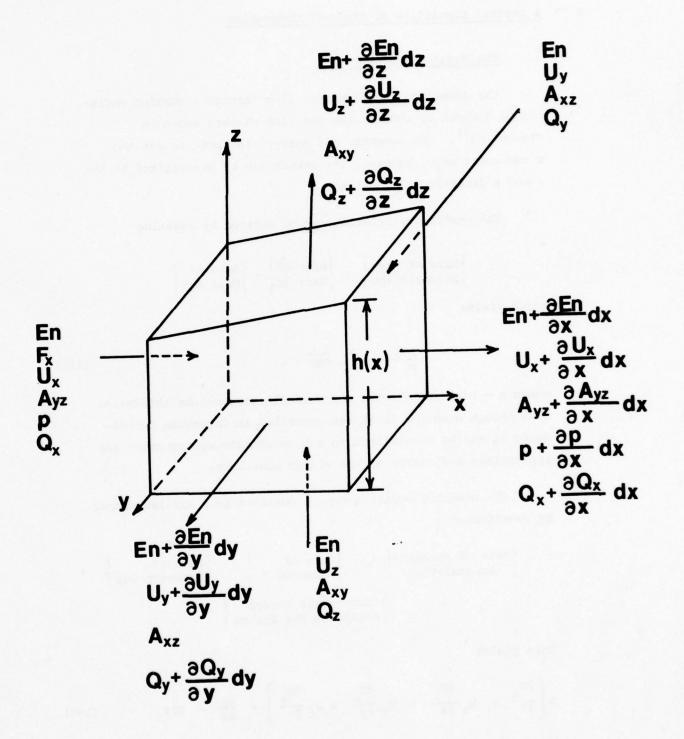


Figure 103. Volume Element Showing the X-Component of Momentum and Energy Transport.

where Fr denotes all forces acting on the control volume including the viscous and/or turbulent shear stresses.

Conservation of energy dictates that

which yields

$$\rho \frac{DEn}{DT} = -\frac{1}{h} \overrightarrow{\nabla} h\overrightarrow{Q} + \rho (\overrightarrow{U} \cdot \overrightarrow{Fr}) - \frac{1}{h} \overrightarrow{\nabla} \cdot ph\overrightarrow{U}$$
 (142)

where En denotes the total internal and kinetic energy, i.e., $\hat{\rho U} + \frac{1}{2} \rho U^2, \; \hat{U} \; \text{is the internal energy per unit mass and } U \; \text{is the magnitude of the local fluid velocity.}$

Equation (142) can be written in terms of the enthalpy \mathbf{H}_{+0} as

$$\frac{\partial \rho h E n}{\partial \tau} + \overrightarrow{\nabla} \cdot \rho h H_{t} \overrightarrow{U} = h \rho \overrightarrow{U} \cdot \overrightarrow{Fr} - \overrightarrow{\nabla} \cdot h \overrightarrow{Q}$$
 (143)

and as

$$\rho C_{p} \frac{Dt}{DT} - \frac{Dp}{DT} = -\frac{1}{h} \overrightarrow{\nabla} \cdot h\overrightarrow{Q} = -f \qquad (144)$$

for an ideal gas, where the divergence $\frac{1}{h} \overrightarrow{\nabla} \cdot h\overrightarrow{Q}$ has been replaced by the scalar function f.

The system of equations can be simplified considerably by averaging in the radial and circumferential directions. This process eliminates derivatives in all but the axial direction by virtue of boundary values or symmetry. This reduces the system of equations to

$$\frac{\partial \rho h}{\partial \tau} + \frac{\partial}{\partial x} (\rho h U_x) = 0 \tag{145}$$

$$\frac{\partial \rho U_{\mathbf{x}}^{h}}{\partial \tau} + \frac{\partial \rho h U_{\mathbf{x}}^{2}}{\partial \mathbf{x}} + h \frac{\partial p}{\partial \mathbf{x}} = \rho h F r_{\mathbf{x}}$$
 (146)

$$\frac{\partial \rho h E n}{\partial \tau} + \frac{\partial}{\partial x} (\rho h H_{tl} U_{x}) = h \rho U_{x} F r_{x} - f$$
 (147)

where the variables have been written in conservative form

Equations (145), (146) and (147) have been written with the overall objective of modeling turbine engine components. In this situation, hpu Fr and f denote the work and heat addition or removal occuring in the compression, combustion and expansion processes. From a fluid mechanics point of view, these terms represent an articifical viscous and thermal damping factor and equations (145) through (147) could be used for duct flows, etc.

The governing differential equations can be reformulated in terms of the mass flow rate, \dot{m} , as

$$\frac{\partial \rho}{\partial \tau} + \frac{1}{A} \frac{\partial \dot{m}}{\partial x} = 0 \tag{148}$$

$$\frac{\partial \dot{m}}{\partial \tau} + \frac{\partial}{\partial x} \left(\frac{\dot{m}^2}{\rho A} \right) + A \frac{\partial p}{\partial x} = \rho A Fr_x$$
 (149)

$$\frac{\partial \rho E n}{\partial \tau} + \frac{1}{A} \frac{\partial}{\partial x} \left(\dot{m} H_{tl} \right) = \frac{\dot{m}}{A} F_{x} - \frac{f}{A}$$
 (150)

where $\dot{m} = 2\pi r_a h \rho U_x$, $E = \hat{U} + \frac{1}{2} (\dot{m}/\rho A)^2$, $H_{tl} = \hat{H} + \frac{1}{2} (\dot{m}/\rho A)^2$, $\hat{U} = \hat{U}(t)$, $\hat{H} = \hat{H}(t)$, and $p = \rho Rt$. The major variables are thus ρ , \dot{m} and t. Note that p, En and H_{tl} can be defined in terms of these variables by means of an equation of state and the relations

$$\hat{U} = \hat{U}_0 + \int_{t_0}^{t} \frac{c_p}{\gamma} dt$$
 (151)

$$\hat{H} = \hat{H}_0 + \int_{t_0}^{t} C_p dt$$
 (152)

Summary of Governing Equations

The system of equations can be summarized as follows.

$$p = \rho Rt \tag{153}$$

$$En = \hat{U}_{O} + \int_{t_{O}}^{t} \frac{C_{p}}{\gamma} dt + \frac{1}{2} \left(\frac{\dot{m}}{\rho A} \right)^{2}$$
 (154)

$$\frac{\partial \rho}{\partial \tau} + \frac{1}{A} \left(\frac{\partial \dot{m}}{\partial x} \right) = 0 \tag{155}$$

$$\frac{\partial \dot{\mathbf{m}}}{\partial \tau} + \frac{\partial}{\partial \mathbf{x}} \left(\frac{\dot{\mathbf{m}}^2}{\rho \mathbf{A}} \right) + \mathbf{A} \left(\frac{\partial \mathbf{p}}{\partial \mathbf{x}} \right) = \rho \mathbf{AFr}_{\mathbf{x}}$$
 (156)

$$\frac{\partial \rho E n}{\partial \tau} + \frac{1}{A} \frac{\partial}{\partial x} \left[\dot{m} \left(E n + \frac{p}{\rho} \right) \right] = \frac{\dot{m}}{A} \left(F r_{x} \right) - \frac{f}{A}$$
 (157)

These equations are then subjected to a series of initial conditions of $\tau = 0$ and x = 0, i.e.,

$$\begin{array}{ccc}
\rho &=& \rho(\mathbf{x}) \\
\dot{\mathbf{m}} &=& \dot{\mathbf{m}}(\mathbf{x})
\end{array}$$

$$\tau &=& 0 \text{ for all } \mathbf{x} \qquad (158)$$

$$t &=& t(\mathbf{x})$$

3. Application of Governing Equations to a Turbomachine

The application of equations (153) to (157) to a turbomachine consists of defining the force and heat terms, F and f, by means of known steady state performance data. This by necessity limits the Δx step size, i.e., compressor stages are at a specified length — thus F and f can only be determined at specified locations. As a result, the differential equations must be written in terms of upwind differencing 95 and

$$p_{i}^{(n)} = R\rho_{i}^{(n)} t_{i}^{(n)}$$
 (159)

$$\operatorname{En}_{i}^{(n)} = \hat{\mathbf{U}}_{o} + \int_{t_{o}}^{t} \frac{c_{p}}{\gamma} \left(t_{i}^{(n)}\right) dt + \frac{1}{2} \left(\frac{\dot{\mathbf{m}}_{i}^{(n)}}{\rho_{i}^{(n)} \lambda_{i}}\right)^{2}$$
 (160)

$$\frac{\rho_{\mathbf{i}}^{(\mathbf{n+1})} - \rho_{\mathbf{i}}^{(\mathbf{n})}}{\Delta \tau} = \frac{1}{\mathbf{A}_{\mathbf{i}}} \frac{\left(\dot{\mathbf{m}}_{\mathbf{i}}^{(\mathbf{n})} - \dot{\mathbf{m}}_{\mathbf{i}=1}^{(\mathbf{n})}\right)}{\Delta \mathbf{x}_{\mathbf{i}}}$$
(161)

$$\frac{\dot{\mathbf{m}}_{\mathbf{i}}^{(n+1)} - \dot{\mathbf{m}}_{\mathbf{i}}^{(n)}}{\Delta \tau} = \rho_{\mathbf{i}}^{n} \mathbf{A}_{\mathbf{i}}^{\mathbf{F}} \mathbf{r}_{\mathbf{i}} - \mathbf{A}_{\mathbf{i}} \frac{\mathbf{p}_{\mathbf{i}}^{(n)} - \mathbf{p}_{\mathbf{i}-1}^{(n)}}{\Delta \mathbf{x}_{\mathbf{i}}} - \frac{[\dot{\mathbf{m}}^{2}/\rho \mathbf{A}]_{\mathbf{i}-1}^{(n)}}{\Delta \mathbf{x}_{\mathbf{i}}}$$
(152)

$$\frac{(En)_{i}^{n+1}-(En)_{i}^{(n)}}{\Delta \tau} = \frac{\dot{m}_{i}^{(n)}Fr_{i}}{A_{i}} = \frac{f_{i}}{A_{i}}$$

$$-\frac{1}{A} \left\{ \frac{\left[\dot{m} \, \operatorname{En} + \frac{p}{\rho} \right]^{(n)}_{i} - \dot{m} \left[\operatorname{En} + \frac{p}{\rho} \right]^{(n)}_{i-1}}{x_{i}} \right\}$$
(163)

where the subscript x has been dropped on Fr for clarity and the subscript i denotes the spatial position while the superscript

n denotes time. Upwind differencing demands that $\dot{m}_i > 0$ for the above formulation. If $\dot{m}_i < 0$, then i is replaced by i+1 and i-1 by i in the convective terms. It should be noted that this is unlikely to happen in the present case.

The finite-difference equations shown above are explicit in nature, i.e., all the values on the right-hand sides of equations (161), (162) and (163) needed to calculate the advanced n+1 time level are known. The stability of non-linear systems of equations is difficult to define; however, results from linear systems of each be applied and

$$Cr = \frac{\left[\dot{m}/\rho A + a\right]\Delta \tau}{\Delta x} \le 1$$
 (164)

$$\Delta \tau \leq \frac{|\dot{m}/\rho A|/\Delta x}{[|\dot{m}/\rho A|/\Delta x + a/\Delta x]^2}$$
 (165)

The latter equation is more restrictive and thus $\Delta \tau$ should be chosen such that equation (165) is satisfied for the smallest Δx and largest $\dot{m}/\rho A$ value.

The system of equations is specifically related to turbomachines by definition of Fr_i and f_i . For a compressor, these parameters can be defined from the temperature and pressure coefficients, i.e.,

$$\psi_{i}^{P} = \frac{2g_{c}^{JC}p}{(U_{R})_{i}^{2}} \quad T_{i-1} \left\{ \left(\frac{P_{i}}{P_{i-1}} \right)^{\frac{\gamma-1}{\gamma}} - 1 \right\}$$
 (166)

$$\psi_{i}^{T} = \frac{2g_{c}^{JC}p}{(U_{R})_{i}^{2}} \left\{ T_{i} - T_{i-1} \right\}$$
 (167)

where both $\psi_{\hat{\mathbf{i}}}^{P}$ and $\psi_{\hat{\mathbf{i}}}^{T}$ are unique functions of the flow coefficient φ where

$$\phi_{i} = \frac{(U_{x})_{i}}{(U_{R})_{i}} \tag{168}$$

Note that P and T denote the total pressure and temperature and can be related to p and t by means of

$$P = p \left\{ 1 + \frac{\gamma - 1}{2} M_{x}^{2} \right\}^{\gamma/(\gamma - 1)}$$
 (169)

$$T = t \left\{ 1 + \frac{\gamma - 1}{2} M_{x}^{2} \right\}$$
 (170)

where $M_{\rm X}=U_{\rm X}/a$ and $U_{\rm R}=2\pi r_{\rm T}N/60$ and denotes the rotor tip speed. Temperature and pressure coefficients for the J-85 compressor are given in references 97 and 98. The J-85 compressor utilizes stability bleeds and this can be accounted for by setting

$$\dot{m} = \dot{m}_{n-1} - (\dot{m}_{b1})_{n} \tag{171}$$

where (\dot{m}_{bl}) denotes the n-th stage bleed flow where it is assumed that this process does not affect the momentum balance.

The combustor is analyzed in an analogous manner with F and f determined from experimental pressure loss, heat addition and efficiency data. J-85 combustor data is given in reference 98.

The J-85 turbine has been modelled in reference 98 by means of an enthalpy and efficiency parameter, i.e.,

$$\frac{\hat{H}_{n} - \hat{H}_{n-1}}{T_{n-1}} = \phi_{1} \left\{ \frac{\hat{m}_{n-1} \sqrt{T_{n-1}}}{P_{n-1}}, \frac{N}{\sqrt{T_{n-1}}} \right\}$$
(172)

$$\eta_{n} = \phi_{2} \left\{ \frac{\dot{m}_{n-1} \sqrt{T_{n-1}}}{p_{n-1}}, \frac{N}{\sqrt{T_{n-1}}} \right\}$$
 (173)

The turbine cooling flow processes can be modelled by adding the cooling flow to the appropriate control volume and mixing the resulting streams to obtain an appropriate temperature.

The engine is terminated with an exhaust nozzle. This consists of a variable area passage with pressure loss given by a flow coefficient. There is no external heat addition and, thus, f is identically 0.

In the process of modeling the rotating components, an additional variable has been added -- the rotor speed N. The rotor dynamics are governed by the conservation of angular momentum and thus

$$\frac{dN}{d\tau} = \left(\frac{60}{2\pi}\right)^2 \left(\frac{J}{NI}\right) \quad \Sigma \dot{m} \Delta \hat{H} = \frac{N^{n+1} - N^n}{\Delta \tau}$$
 (174)

where $\Sigma \dot{\hat{m}} \Delta H$ denotes the net sum of enthalpy differences occurring across the turbine and compressor.

Structure of the J-85 Digital Simulation Computer Program

A computer program embodying the concepts of the previous section and following the structure of reference 98 was used for both steady-state and transient J-85 engine computations. This program is constructed in two major elements. The first consists of a steady-state computation which attempts to determine operating line and/or match points between the compressor and turbine. This is an iterative process and involves three nested iterative loops. The iteratively determined variables are:

- 1) Combustor total enthalpy
- 2) Combustor inlet pressure
- 3) The engine mass flow rate

The iterative procedure initially employed consisted of halvinginternal search technique and required approximately 2100 computations on the innermost variable, 150 computations on the second and 15 computations on the outermost variable at the design point condition.

The iterative procedure initially utilized in the program, was replaced with a multi-variable Newton-Raphson 99 iterative method. This technique uses Taylor expansions for the variables of interest, i.e.,

$$f^{(i)} (\alpha, \beta, \gamma) = f^{(i)} (x_{k}, y_{k}, z_{k}) + (\alpha - x_{k}) f_{x}^{(i)} (x_{k}, y_{k}, z_{k}) + (\beta - y_{k}) f_{y}^{(i)} (x_{k}, y_{k}, z_{k}) + (\gamma - z_{k}) f_{z}^{(i)} (x_{k}, y_{k}, z_{k})$$

$$i = 1, 2, 3$$
(175)

where x_k , y_k and z_k denote the three iterative variables—combustor total temperature, combustor inlet pressure, and the engine mass flow rate. The functions $f^{(i)}$ (x, y, z) denote differences in computed nozzle mass flow rates, turbine mass flow rates and combustor enthalpy, i.e.,

$$f^{(1)} = \frac{\dot{m}_{nz,x} - \dot{m}_{nz,1}}{(\dot{m}_{nz,x} + \dot{m}_{nz,1})/2}$$

$$f^{(2)} = \frac{\dot{m}_{tr,z} - \dot{m}_{tr,1}}{(\dot{m}_{tr,z} + \dot{m}_{tr,1})/2}$$

$$f^{(3)} = \frac{\hat{H}_{br,y} + \hat{H}_{br,1}}{(\hat{H}_{br,y} + \hat{H}_{br,1})/2}$$

The goal of the iterative process is to balance the mass flow rates and enthalpies thus making $f^{(1)} = f^{(2)} = f^{(3)} = 0$. If the values of x, y and z for which this occurs are denoted by α , β and γ , then

$$f^{(1)}(\alpha,\beta,\gamma) = f^{(2)}(\alpha,\beta,\gamma) = f^{(3)}(\alpha,\beta,\gamma) = 0$$
 (176)

Noting that $f_x^{(i)} = \frac{\partial f}{\partial x}^{(i)}$, $f_y^{(i)} = \frac{\partial f}{\partial y}^{(i)}$ and $f_z^{(i)} = \frac{\partial f}{\partial z}^{(i)}$, then equation (175) can be used to construct an iterative scheme

with the goal of finding α , β , and γ for which equation (176) is valid.

Equation (175) can be rewritten as

$$-f^{(i)}(x_{k}, y_{k}, z_{k}) = \Delta x f_{x}^{(i)}(x_{k}, y_{k}, z_{k}) + \Delta y f_{y}^{(i)}(x_{k}, y_{k}, z_{k}) + \Delta z f_{z}^{(i)}(x_{k}, y_{k}, z_{k}) \qquad i = 1, 2, 3$$

or in matrix form as

$$-[F] = [A] [\Delta x]. \tag{177}$$

[A] now denotes the partial derivative matrix with [F] denoting the function matrix and $[\Delta x]$ the step matrix. These take the form

$$[A] = \begin{vmatrix} f_{x}^{(1)} & f_{y}^{(1)} & f_{z}^{(1)} \\ f_{x}^{(2)} & f_{y}^{(2)} & f_{z}^{(2)} \\ f_{x}^{(3)} & f_{y}^{(3)} & f_{z}^{(3)} \end{vmatrix} \qquad [\Delta x] = \begin{vmatrix} \alpha - x_{k} \\ \beta - y_{k} \\ \gamma - z_{k} \end{vmatrix} \qquad [F] = \begin{vmatrix} f^{(1)} \\ f^{(2)} \\ f^{(3)} \end{vmatrix} \qquad (178)$$

Equation (177) can be solved for the matrix $[\Delta x]$ by multiplying both sides of the relationship by the inverse of [A], $[A]^{-1}$, and

$$[\Delta x] = -[A]^{-1}[F]$$
 (179)

This equation can be used to find successive values of x_k , y_k , z_k ,

$$x_{k+1} = x_k + \Delta x_k$$

$$y_{k+1} = y_k + \Delta y_k$$

$$z_{k+1} = z_k + \Delta z_k$$
(180)

with each value at successively smaller values of $f^{(i)}$.

The procedure is implemented in the following manner.

 Evaluate the coefficient matrix [A]. Since the functions f⁽¹⁾, f⁽²⁾ and f⁽³⁾ are not analytically defined, the partial derivatives must be determined numerically, i.e.,

$$f_{x}^{(1)}(x_{k'}, y_{k'}, z_{k}) = \left(\frac{\partial f}{\partial x}^{(1)}\right)_{x_{k'}, y_{k'}, z_{k}} = \frac{f^{(1)}(x_{k'}, y_{k'}, z_{k}) - f^{(1)}(x_{k-1}, y_{k'}, z_{k})}{x_{k} - x_{k-1}}$$

All nine terms must be defined and this requires 12 functional evaluations.

- 2) Invert the coefficient matrix [A] and solve equation (179) for the new [Δx] values. Note that the matrix [F] was evaluated in the course of defining [A].
- 3) Update the values x_{k+1} , y_{k+1} , z_{k+1} following equation (180).
- 4) Repeat this process, i.e., return to item (i) until f⁽¹⁾, f⁽²⁾ and f⁽³⁾ are less than a prescribed value.

This approach has been utilized in the previously described engine simulator with impressive results. As noted, the original iterative technique required 2265 functional evaluations to obtain a "converged" operating point. The Newton-Raphson method—as discussed above—required only three iterative passes or 36 functional evaluations. This is a two-orders—of—magnitude reduction in computing time and lends speed and versatility to the program.

The convergence process itself is second-order and this also speeds the computation. The iterative "track" is shown in Table 26. $f^{(1)}$, $f^{(2)}$ and $f^{(3)}$ are the previously defined variables, i.e., nozzle and turbine mass flow rate and combustor enthalpy, with x, y and z denoting the compressor mass flow rate, the turbine pressure, the combustor exit temperature pressure. As was previously noted, the convergence is second-order and proceeds rapidly.

The computer program using the previously discussed iterative procedure and mathematical framework of Section V.B.l is listed in references 100 and 101. The listings are supplemented with a users manual in reference 100.

5. Compressor Mapping Using a J-85 Turbine Engine

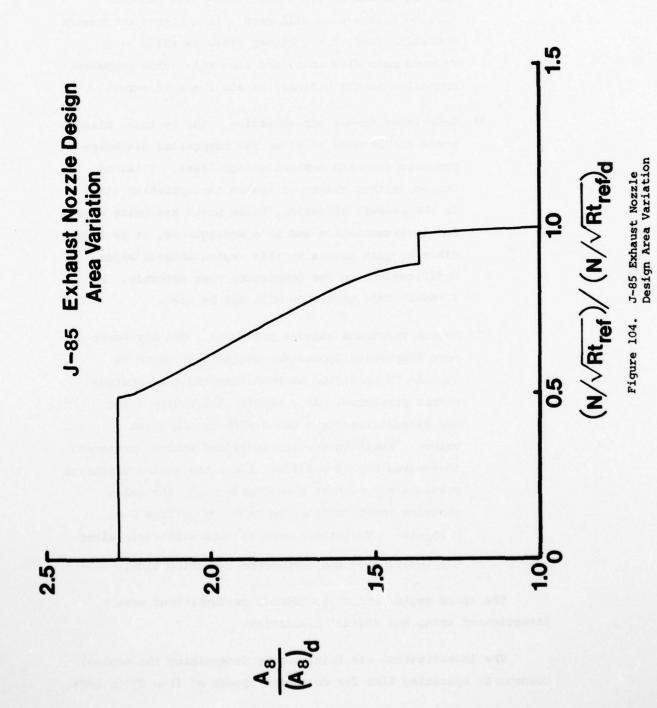
The computer program discussed in the previous section can be employed to predict the limits of compressor performance under differing engine geometric and environmental conditions. In particular, the following variables can be employed to create a series of steady-state compressor operating lines:

1) Exhaust nozzle area. The J-85 uses a variable nozzle area, i.e., A₈ = A₈ (N √Rt_{ref}). The design relationship is shown in Figure 104. This can be altered and will influence the location of the compressor operating line to some extent. The design or minimum nozzle area is 88.00 in² with the maximum nozzle area being 201.00. 102

TABLE 26

RESULTS OF NEWTON-RAPHSON ITERATION

Iteration Number	f(1)x10 ²	f(2) x10 ²	f ⁽³⁾ x10 ²	<u>x</u>	¥	<u>z</u>
1	1.467	2.171	0.366	43.500	35.000	2100.0
2	-0.506	-0.724	0.047	43.516	34.501	2123.7
3	-0.015	0.047	-0.004	43.509	34.781	2136.4



- 2) First stage turbine nozzle area. Three first stage turbine nozzle assemblies are currently available for the J-85 engine. These have areas of 32.000 in², 35.880 in² and 43.747 in² (102) with the latter being the design and/or production unit. The reduced turbine nozzle area will result in a higher compressor operating line, i.e., higher pressure ratio at a reduced mass flow rate, and thus will force compressor operation in the vicinity of stall and/or surge.
- 3) Compressor in--or out--bleeding. The customer bleed ports can be used to alter the compressor discharge pressure from its nominal design level. This, of course, either raises or lowers the operating line. In the present situation, these ports are being used for instrumentation and as a consequence, it is impossible to gain access to this region without major modifications to the compressor case assembly. As a result this technique will not be used.
- Aero Propulsion Laboratory engine test stand is capable of operation at both standard and subatmospheric pressures. As a result, the engine inlet and exhaust pressures can differ from ambient values. Furthermore, the inlet and exhaust pressures themselves may also differ, i.e., the engine discharge pressure may be near atmospheric while the inlet pressure can be maintained at values of from 7 to 8 lb_f/in². Variations such as this will again alter the location of the compressor operating line.

The above engine and environmental perturbations were investigated using the digital simulation.

The investigation was initiated by determining the nominal compressor operating line for corrected speeds of from 85 to 100%.

These calculations used the nozzle area variation of Figure 104 with a design point area of 88.00 in². The resulting pressure ratios and corrected mass flow rates are plotted in Figure 105. Other pertinent engine variables are given in Table 27.

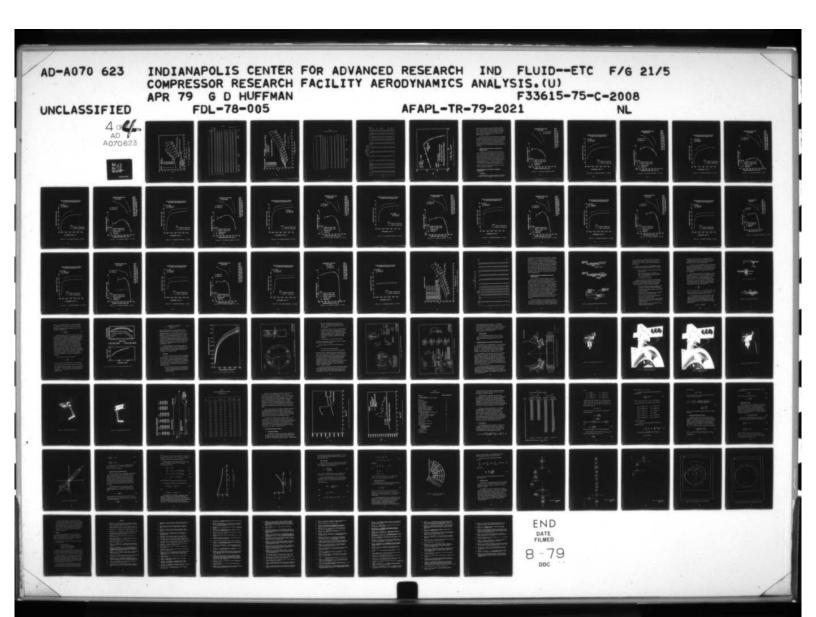
In addition to the design point conditions, a series of off-design points were investigated. These were generated using the turbine nozzles previously discussed and the variability of the exhaust nozzle. The upper portion of the compressor operating regime can be well covered using these variable geometry capabilities. A number of the conditions resulted in compressor surge or stall. This can be detected in the simulation by a rapid deterioration in the performance of one or more compressor stages. Using the surged conditions in conjunction with the shape of the constant speed lines, an estimated surge line was constructed.

The remaining portion of the operating map was generated in a similar manner. These results are plotted in Figure 106. The various component operating conditions are given in Table 28.

Following the computations of Tables 27 and 28 which employed variable turbine and exhaust nozzle areas, a series of calculations were carried out for variable, i.e., subatmospheric, inlet pressures. The previously discussed computer program was altered to reflect variable inlet and exhaust pressures. Equations were also developed to estimate the initial values of the iterative variables - thus speeding convergence. The updated listing of this program is presented in reference 101.

The results of these computations are shown in Table 29 and Figure 107. There is obviously little or no effect on compressor operation as a result of the different methods of generating parameter variability.

The test conditions themselves will be generated by installing a given turbine nozzle in the J-85 engine and then varying the



4 OF AD A A O 7 O 6 2 3



NATIONAL BUREAU OF STANDARDS MICROCOPY RESOLUTION TEST CHART

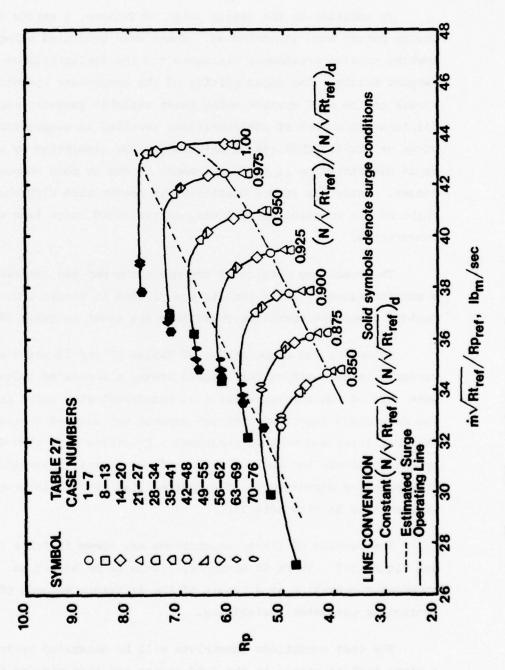


Figure 105. J-85 Compressor Performance as Determined with the Digital Simulation

TABLE 27

Engine Parameters

Component Exit Conditions

		m√Rt _{ref}									
	(NVRt ref	Rpref	A8	A ₅	T _C	P _c	Tbr	Pbr ,	T _{tr}	Ptr 2	
Ase*	ref	1b_/sec	in ²	in ²	•R	lbg/in2	•R	lbe/in2	•R	lbe/in2	Commen
	(NVRtref)d	m,									
	1.000	43.51	88.00	43.74	977	99.87	2121	92,38	1703	34.72	
	0.275	42.43	120.00	43.74	943	89.94	1807	82.40	1408	28.01	
	0.950	40.88	120.00	43.74	918	83.32	1693	76.09	1312	25.54	
	0.925	39.35	120.00	43.74	895	77.02	1695	70.48	1325	24.65	
	0.900	37.71	120.00	43.74	874	71.71	1670	65.72	1316	23.87	
	0.875	36.11 34.65	126.10	43.74	850 829	65.82	1588 1532	55.64	1211	20.74	
	0.850	36.87	88.00	43.74	1026	105.70	3316	101.30	2881	48.85	Surge
	0.950	36.20	88.00	43.74	997	98.55	3080	94.25	2661	44.73	Surge
0	0.925	34.37	88.00	43.74	973	90.93	3152	87.25	2741	42.70	Surge
1	0.900	32.16	88.00	43.74	953	83,60	3220	80.45	2819	40.42	Surge
2	0.875	29.91	88.00	43.74	933	76.71	3270	74.00	2880	38.38	Surge
3	0.850	27.21	88.00	43.74	915	69.63	3398	67.43	3017	36.49	Surge
	1.000	43.55	110.00	43.74	948	89.49	1652	80.85	1245	23.95	
5	0.975	42.35	110.00	43.74	957	94.86	2041	87.84	1637	33.05	
5	0.950	40.71	110.00	43.74	930	87.26	1895	80.51	1508	29.74	
7	0.925	39.19	110.00	43.74	907	80.68	1892	74.59	1517	28.53	
	0.900	37.55	110.00	43.74	885 866	75.00	1874	69.42 65.02	1512	27.37	
	0.875	35.85	110.00	43.74	851	70.09 66.68	1874	62.19	1525 1593	26.53 26.66	
)	1.000	34.21 43.56	110.00	43.74	945	88.31	1598	79.53	1193	19.69	
	0.975	42.48	145.00	43.74	927	84.69	1528	76.51	1146	22.07	
3	0.950	41.00	145.00	43.74	905	79.20	1471	71.42	1102	20.90	
	0.925	39.47	145.00	43.74	881	72.95	1465	65.89	1106	20.32	
	0.900	37.83	145.00	43.74	860	67.92	1459	61.46	1113	19.91	
	0.875	36.20	145.00	43.74	841	63.50	1453	57.59	1122	19.60	
	0.850	34.70	145.00	43.74	824	59.74	1460	54.35	1142	19.57	
	1.000	43.56	201.00	43.74	943	87.65	1566	78.78	1162	17.20	
	0.975	42.48	201.00	43.74	924	83.75	1516	75.48	1127	18.32	
	0.950	41.02	201.00	43.74	902	78.42	1449	20.56	1077	17.77	
	0.925	39.50	201.00	43.74	876 853	71.54	1394	64.30	1037 992	17.40	
	0.900	37.87 36.26	201.00	43.74	832	65.67	1332	58.91 54.72	980	17.10	
	0.850	34.79	201.00	43.74	815	57.22	1306	51.51	995	16.88	
	1.000	43.21	88.00	35.88	1009	112.50	1917	105.40	1462	31.76	
	0.975	41.68	120.00	35.88	986	104.90	1796	98.29	1358	27.05	
	0.950	39.89	120.00	35.88	961	97.03	1704	90.78	1285	24.78	
	0.925	38.56	120.00	35.88	933	88.62	1636	82.85	1234	23.59	
	0.900	37.04	120.00	35.88	907	81.33	1573	75.94	1186	22.56	
	0.875	35.45	126.10	35.88	882	74.55	1499	69.51	1130	20.99	
	0.850	33.96	134.40	35.88	860	68.85	1452	64.17	1099	19.88	
	1.000	37.82	88.00	32.00	1057	113.30	2079	107.80	1588	29.02	Surge
	0.975	36.29	120.00	32.00	1029	105.10	1951	99.98	1480	24.84	Surge
	0.950	34.81	120.00	32.00	1002	97.43	1859	92.56	1406	23.05	Surge
	0.925	34.44	120.00	32.00	973	90.97	1801	86.40	1363	22.41	Surge
	0.900	33.53	120.00	32.00	947 921	84.54 78.55	1730 1650	80.22 74.45	1308	21.70	Surge
	0.850	32.56 32.60	134.40	32.00	883	74.10	1506	70.03	1132	19.57	surge
	1.000	43.36	145.00	35.88	1001	109.10	1778	101.80	1326	20.23	
	0.975	41.81	145.00	35.88	982	103.80	1742	97.05	1306	22.72	
	0.950	50.01	145.00	35.88	958	96.16	1661	89.81	1243	21.32	
	0.925	38.65	145.00	35.88	930	87.91	1603	82.05	1201	20.54	
	0.900	37.11	145.00	35.88	905	80.72	1535	75.24	1150	19.87	
	0.875	35.51	145.00	35.88	880	74.06	1465	68.95	1098	19.31	
	0.850	34.05	145.00	35.88	857	68.12	1404	63.34	1053	18.97	
	1.000	43.36	201.00	35.88	1001	109.20	1778	101.80	1327	17.55	
	0.975	41.91	201.00	35.88	980	103.00	1701	96.12	1266	18.69	
	0.950	40.11	201.00	35.88	956 928	95.38	1622	88.92	1205	18.00	
	0.925	38.73 37.19	201.00	35.88 35.88	902	87.13 80.03	1562 1499	81.17 74.47	1161	17.61	
	0.900	35.57	201.00	35.88	878	73.48	1434	68.29	1067	17.01	
	0.850	34.11	201.00	35.88	855	67.64	1372	62.79	1023	16.84	
	1.000	38.88	145.00	32.00	1052	114.10	1988	108.20	1497	19.74	Surge
	0,975	36.83	145.00	32.00	1027	105.60	1909	100.30	1438	21.54	Surge
	0.950	35,28	145.00	32.00	1000	97.88	1825	92.89	1372	20.36	Surge
	0.925	34.80	145.00	32.00	972	91.18	1768	86.51	1330	19.90	Surge
	0.900	33.81	145.00	32.00	945	84.66	1702	80.26	1281	19.42	Surge
	0.875	33.95	145.00	32.00	905	80.09	1558	75.72	1168	19.14	
	0.850	32.67	145.00	32.00	882	74.04	1497	69.95	1123	18.85	
1	1.000	38.88	201.00	32.00	1052	114.10	1988	108.20	1497	17.29	Surge
	0.975	37.05	201.00	32.00	1026	105.80	1889	100.40	1419	18.20	Surge
	0.950	35.58	201.00	32.00	999	98.13	1795	93.05	1344	17.60	Surge
	0.925	35.17	201.00	32.00	970	91.35	1734	86.58	1296	17.36	Surge
,	0.900	34.15	201.00	32.00	944	84.78	1670	80.29	1249	17.12	Surge
	0.875	34.15	201.00	32.00	904	79.94	1529	75.49	1139	16.96	

*Cases 1 through 7 denote the nominal operating conditions

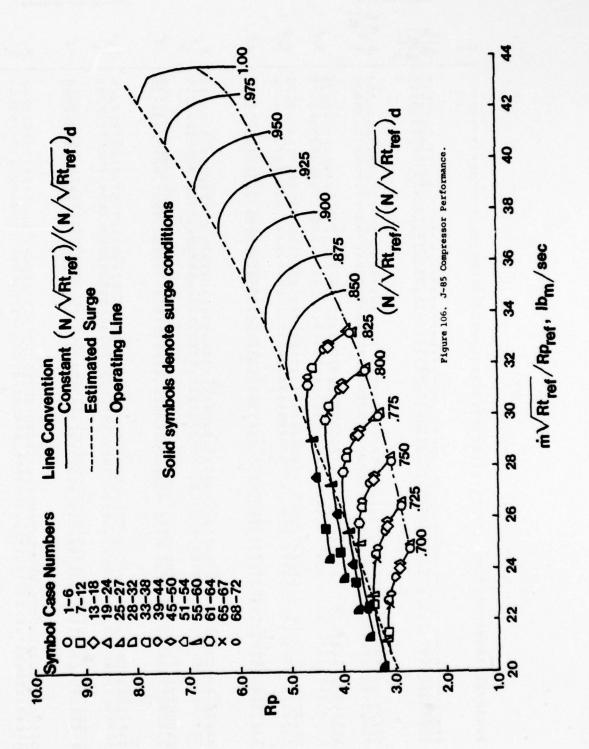


TABLE 28

J-85 COMPONENT OPERATING CONDITIONS

	Engine I	arameters						mponent Exit Con			
ase .	(N/\Rt ref)/(N/\Rt ref) d	mvRt ref	AR	As	T _C	Pc	T _{br}	br	Ter	P _{tr}	Comment
	ier ier d	m√Rt _{ref}	in ²	in ²	*R	Pc lbg/in ²	*R	lbg/in2	*R	lb _f /in ²	
	.825	33.20	140.8	43.74	808	56.31	1496	51.43	1188	19.67	
2	.800	31.73	145.9	43.74	789	52.10	1463	47.58	1171	18.83	
3	.775	29.99	150.0	43.74	771	48.57	1425	44.34	1149	18.16 17.61	
•	.750	28.27	154.2	43.74	755	45.29	1403	41.37 38.65	1142 1140	17.16	
5	.725	26.52	158.4	43.74	739 726	42.24 39.54	1385	36.28	1163	16.81	
6	.700	24.82	162.5	43.74	892	63.93	3435	62.03	3066	34.64	Surge
7	.825	25.58 24.65	88.0	43.74	867	59.35	3347	57.59	2993	32.74	Surge
9	.775	23.47	88.0	43.74	845	55.16	3224	53.47	2884	30.69	Surge
10	.750	22.52	88.0	43.74	823	51.48	3051	49.82	2729	28.81	Surge
11	.725	22,57	88.0	43.74	794	49.57	2788	47.82	2490	27.81	
12	.700	21.50	88.0	43.74	774	46.05	2648	44.35	2368	26.10	
13	.825	32.60	110.0	43.74	835	62.73	1976	58.70	1649	26.02	
14	.800	31.09	110.0	43.74	816	58.35	1973	54.69	1658	24.87	
15	.775	29.27	110.0	43.74	797	54.00	1902	50.57	1604 1576	23.52	
16	. 750	27.43	110.0	43.74	779	49.94	1857 1829	46.77	1562	21.34	
17	.725	25.65	110.0	43.74	762 745	46.25	1829	40.25	1564	20.52	
18	.700	23.98	110.0	43.74	807	42.89 55.97	1464	51.03	1159	19.29	
19	.825	33.22	145.0	43.74	789	52.16	1469	47.65	1176	18.89	
20	.800	31.73	145.0	43.74	773	48.88	1460	44.71	1182	18.48	
21	.750	28.20	145.0	43.74	757	45.79	1450	41.96	1187	18.11	
22	.725	26.41	145.0	43.74	743	42.87	1460	39.39	1211	17.78	
24	.700	24.70	145.0	43.74	729	40,18	1462	37.03	1227	17.47	
25	.825	33.32	201.0	43.74	797	53.57	1307	46.31	1009	16.76	
26	.800	31.83	201.0	43.74	779	49.94	1311	45.13	1026	16.59	
27	.775	30.11	201.0	43.74	764	46.91	1301	42.44	1031	16.42	-
28	.825	24.37	88.0	35.88	896	62.70	2653	60.64	2273	27.65	Surge
29	.800	23.57	88.0	35.88	871	58.36	2590	56.46 52.48	2225	26.44	Surge
30	.775	22.42	88.0	35.88	849	54.30	2489		2091	23.75	Surge
31	.750	21.30	88.0	35.88	828	50.58	2421	48.87	2013	22.67	Surge
35	. 725	20.23	88.0	35.88	853	47.19 66.94	2323	26.92	2329	23.11	our ge
33	.825	31.84	110.0	35.88 35.88	833	62.02	1327	58.49	1327	22.25	
34	. 800	30.32	110.0	35.88	814	57.34	1637	54.11	1321	21.31	
35	.775	28.34 26.42	110.0	35.88	797	53.03	1625	50.09	1325	20.50	
36 37	.750 .725	24.54	110.0	35.88	780	49.11	1626	46.46	1341	19.80	
38	.725	22.74	110.0	35.88	764	45.49	1644	43.13	1374	19.19	
39	.825	32.51	145.0	35.88	837	63.34	1 396	58.95	1060	18.67	
40	.800	31.02	145.0	35.88	817	58.71	1385	54.69	1064	18.28	
41	.775	29.15	145.0	35.88	799	54.54	1366	50.82	1062	17.89	
42	.750	27.25	145.0	35.88	782	50.57	1356	47.17	1069	17.53	
43	. 725	25.42	145.0	35.88	766	46.96	1359	43.88	1087	17.23	
44	.700	23.66	145.0	35.88	751	43.70	1378	40.93	1120	16.97	
45	.825	32.69	201.0	35.88	832	62.05	1310	57.49 52.90	978 959	16.60	
46	.800	31.26	201.0	35.88	810	57.14	1274	49.31	961	16.22	
47	. 775	29.42	201.0	35.88	793	53.24	1251	45.79	969	16.05	
48	.750	27.57	201.0	35.88	776 760	49.39 45.88	1245	42.60	977	15.91	
49	.725	25.76	201.0	35.88	744	42.70	1254	39.73	1004	15.79	
50	.700 .825	27.59	103.0	32.00	884	65.88	1821	62.96	1443	22.32	Surge
52	.800	26.15	103.0	32.00	862	60.70	1806	58.08	1446	21.48	Surge
53	. 775	24.18	103.0	32.00	842	55.76	1820	53.42	1475	20.58	Surge
54	.750	22.44	103.0	32.00	823	51.43	1821	49.32	1493	19.86	Surge
55	.825	28.86	110.0	32.00	879	66.84	1696	63.62	1320	21.38	Surge
56	.800	27.33	110.0	32.00	857	61.60	1702	58.72	1342	20.66	Surge
57	.775	25.36	110.0	32.00	838	56.71	1688	54.11	1347	19.90	Surge
58	.750	24.95	110.0	32.00	809	54.06	1584	51.46	1269	19.50	
59	.725	23.02	110.0	32.00	792	49.80	1582	47.48	1285	18.90	
60	.700	21.27	110.0	32.00	775	45.93	1613	43.93 64.67	1329	19.84	
61	.825	31.19	125.0	32.00	861	68.44	1476 1456	59.79	1113	19.29	
62	.800	29.73	125.0	32.00	840	63.24 58.44	1438	55.27	1113	18.74	
63	.775	27.78	125.0	32.00	821 804	53.96	1437	51.09	1128	18.27	
64	.750	25.84	145.0	32.00	836	62.59	1377	58.96	1037	17.94	
65	. 800	30.13	145.0	32.00	782	49.35	1349	46.61	1061	16.94	
66	.725	22.59	145.0	32.00	766	45.67	1364	43.23	1091	16.70	
68	. 825	31.52	201.0	32.00	857	67.87	1405	63.95	1049	16.58	
69	.775	28.50	201.0	32.00	812	56.87	1267	53.57	949	16.09	
70	.750	26.63	201.0	32.00	794	52.54	1253	49.33	953	15.93	
71	.725	24.80	201.0	32.00	776	48.60	1248	45.68	965	15.79	
	.700	23.03	201.0	32.00	760	45.01	1261	42.39	993	15.68	

TABLE 29

J-85 COMPONENT OPERATING CONDITIONS

 $t_2 = 519^{\circ}R$ $P_8 = 14.70 \text{ lb}_{g}/1n^2$

Case	N/V	P2 10 4/1n ²	Mark ref Rpref 1bg/in	<u>چ</u>	F	P C 10 4/1n ²	Tg &	Pbr 1b _f /4n ²	As tn2	* # *	Ptr 1b _f /1n ²	A ₈ tn ²	Comments
-	0.825	14.70	33.20	3.83	808	56.31	1496	51.43	43.75	1188	19.61	140.8	
2	0.825	14.70	25.58	4.35	892	63.93	3435	62.03	43.75	3066	34.64	88.0	Surge
	0.825	14.70		4.27	835	62.73	1976	58.70	43.75	1649	26.02	110.0	
*	0.825	14.70		3.81	807	55.97	1464	51.03	43.75	1159	19.29	145.0	
10	0.825	14.70		3.64	797	53.57	1307	48.31	43.75	1009	16.76	201.0	
9	0.825	14.70		4.27	968	62.70	2653	60.64	35.88	2273	27.85	88.0	Surge
1	0.825	14.70		4.55	853	66.94	1666	62.92	35.88	1319	23.11	110.0	
80	0.825	14.70		4.31	837	63.34	1396	58.95	35.88	1060	18.67	145.0	
6	0.825	14.70		4.22	832	62.05	1310	57.49	35.88	978	16.60	201.0	
10	0.825	14.70		4.48	884	65.88	1821	62.96	32.00	1443	22.32	103.0	Surge
11	0.825	14.70	28.86	4.55	879	66.84	1696	63.62	32.00	1320	21.38	110.0	Surge
12	0.825	14.70		4.66	198	68.44	1476	64.67	32.00	1117	19.84	125.0	
13	0.825	14.70		4.62	857	67.87	1405	63.95	32.00	1049	16.58	201.0	
14	0.825	10.98		3.96	816	43.48	1622	40.02	43.75	1310	16.17	201.0	
15	0.825	8.30		4.40	843	36.53	2146	34.41	43.75	1814	15.82	201.0	
16	0.825	11.20		3.93	814	44.06	1595	40.49	43.75	1284	16.21	201.0	
17	0.825	12.90		3.78	805	48.71	1433	44.32	43.75	1129	16.47	201.0	
18	0.825	9.35		4.47	885	41.81	2037	40.04	35.88	1657	15.67	201.0	Surge
19	0.825	11.57		4.40	843	50.94	1493	47.64	35.88	1154	16.06	201.0	
20	0.825	13.02		4.29	836	55.90	1381	51.98	35.88	1045	16.28	201.0	
21	0.825	10.10		4.44	887	44.86	1892	42.96	32.00	1512	15.61	201.0	Surge
22	0.825	10.89		4.55	879	49.56	1679	47.16	32.00	1305	15.77	201.0	Surge
23	0.825	13.03		4.63	658	960.36	1429	56.94	32.00	1072	16.02	201.0	

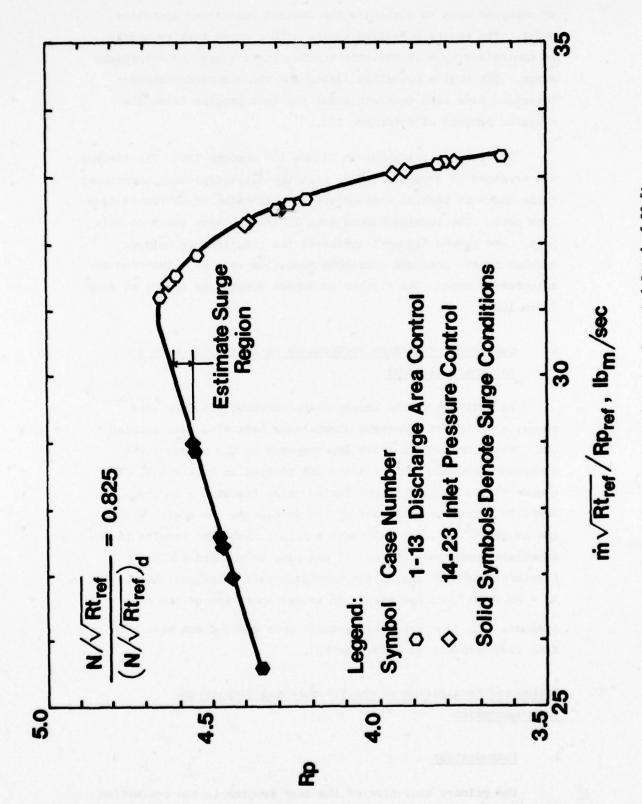


Figure 107. J-85 Compressor Operation at a Corrected Speed of 82.5%

afterburner area to determine the desired compressor operating point. The engine operating regime with a given turbine nozzle is controlled by both the exit turbine temperature and compressor surge. The engine operating limits and the compressor characteristics have been determined for the test program using the computer program of reference 101.

The results are shown in Figure 108 through 120. The figures are arranged in groups of two's with the first depicting compressor ratio and exit turbine temperature as a function of corrected mass flow rate. The turbine nozzle area limits are also shown on this plot. The second figure illustrates the relationship between turbine nozzle area and corrected mass flow rate as a function of afterburner area. The figures encompass compressor speeds of from 70 to 100%.

6. Compressor Transient Performance as Determined with a Mathematical Model

In addition to the steady-state calculations discussed above, a series of transient simulations have also been carried out. These trajectories are superimposed on the steady state compressor map of Figure 106 and are plotted in Figure 121. The engine component performance during these transients is shown in Table 30. Note that any attempt to accelerate the engine with the 35.88 in or 32.00 in turbine nozzle installed results in an immediate compressor surge. It can also be pointed out that accelerations with the design turbine nozzle installed, i.e., $A_5 = 43.74 \text{ in}^2$, do not result in surged operation of the compressor. The transient calculations were carried out with the fuel flow schedule of reference 103.

C. Design and Fabrication of the Pressure and Temperature Instrumentation

1. Introduction

The primary objective of the test program is the evaluation is achieved. However, wave attenuation occurs as a result of

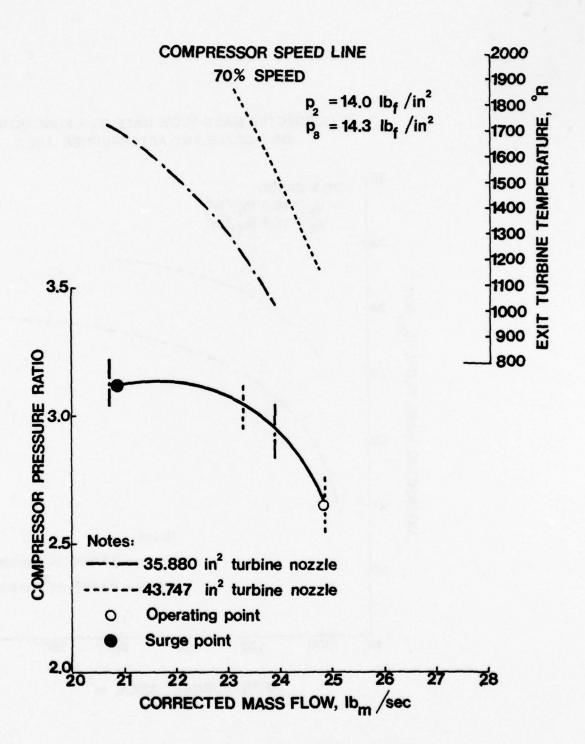


FIGURE 108a. J-85 COMPRESSOR PERFORMANCE 70% SPEED

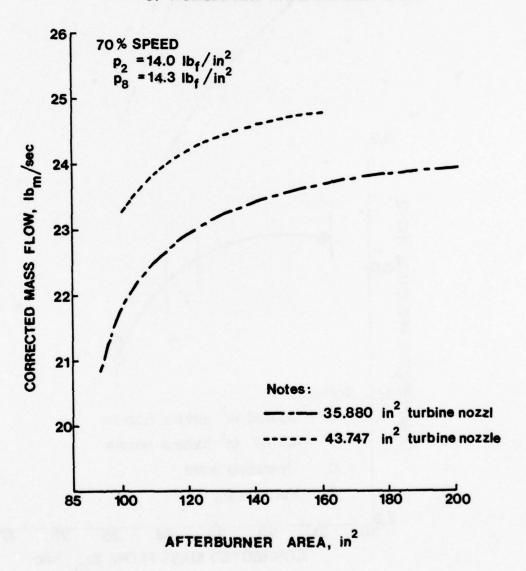


FIGURE 108b. J-85 COMPRESSOR PERFORMANCE. 70% SPEED

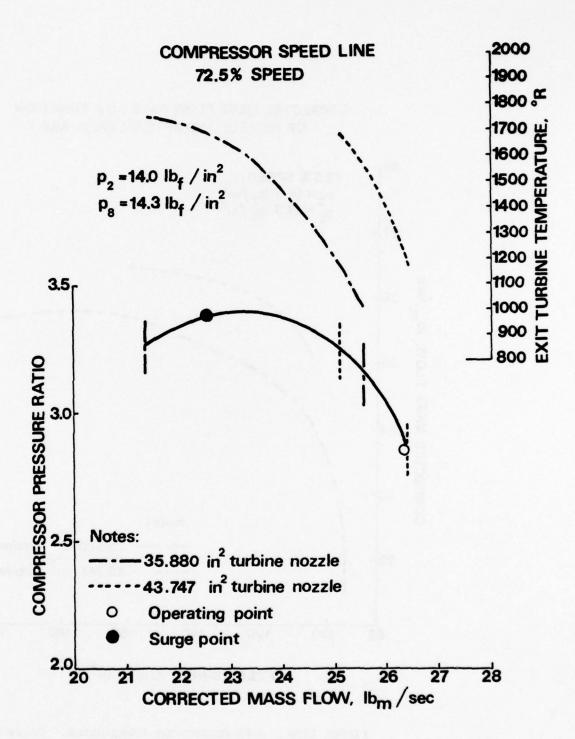


FIGURE 109a. J-85 COMPRESSOR PERFORMANCE. 72.5% SPEED

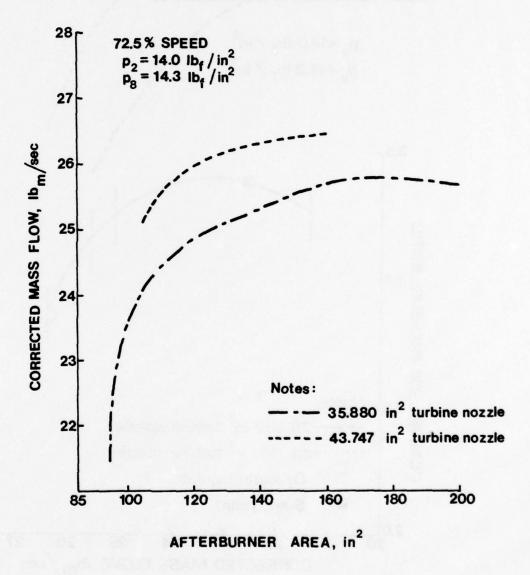


FIGURE 109b. J-85 COMPRESSOR PERFORMANCE. 72.5% SPEED

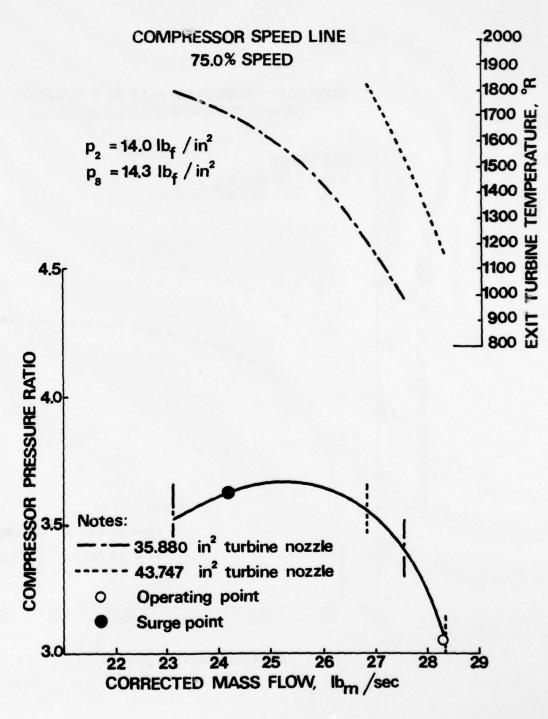


FIGURE 110a. J-85 COMPRESSOR PERFORMANCE. 75% SPEED

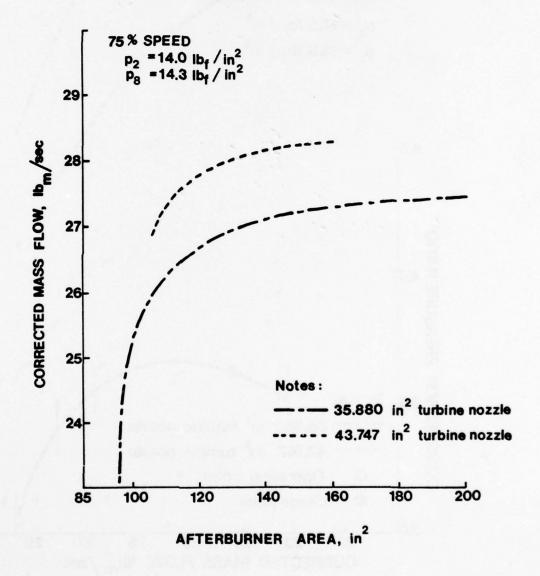


FIGURE 110b. J-85 COMPRESSOR PERFORMANCE. 75% SPEED

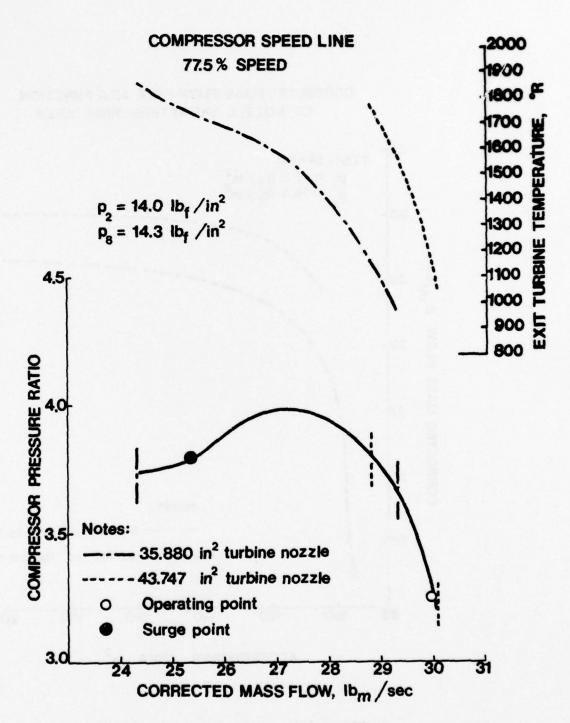


FIGURE 111a. J-85 COMPRESSOR PERFORMANCE. 77.5% SPEED

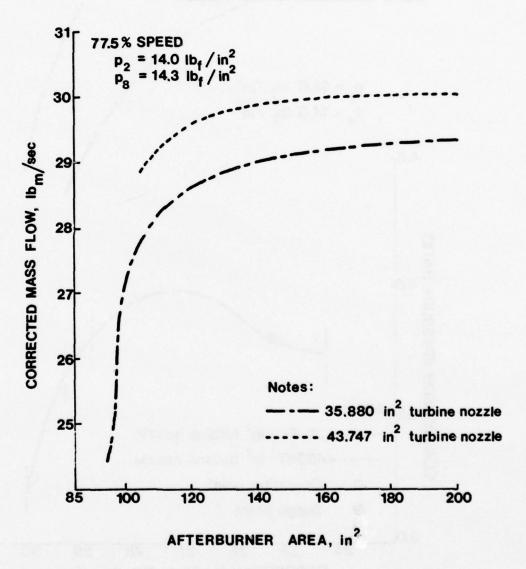


FIGURE 111b. J-85 COMPRESSOR PERFORMANCE. 77.5% SPEED

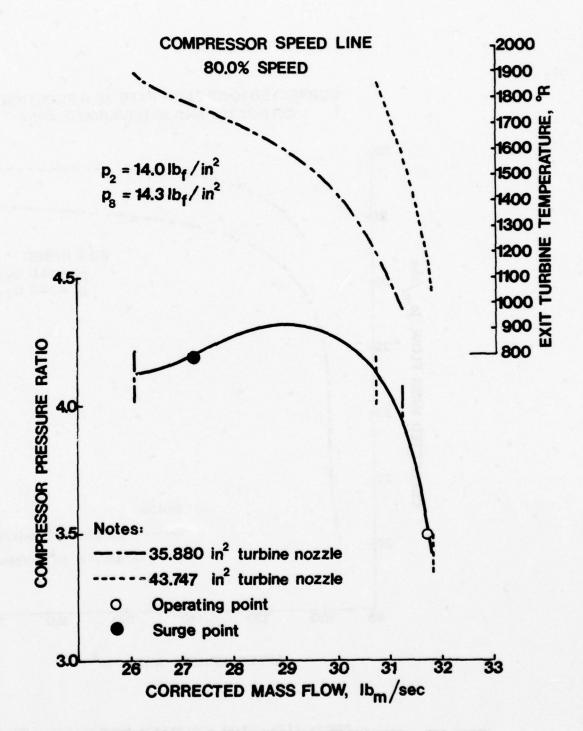


FIGURE 112a. J-85 COMPRESSOR PERFORMANCE. 80% SPEED

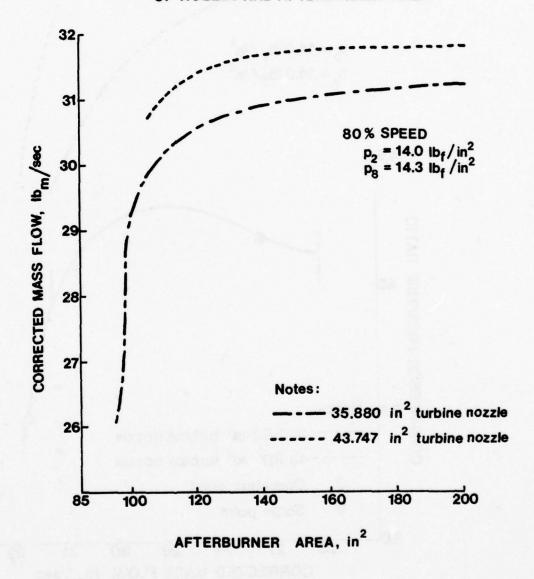


FIGURE 112b. J-85 COMPRESSOR PERFORMANCE. 80% SPEED

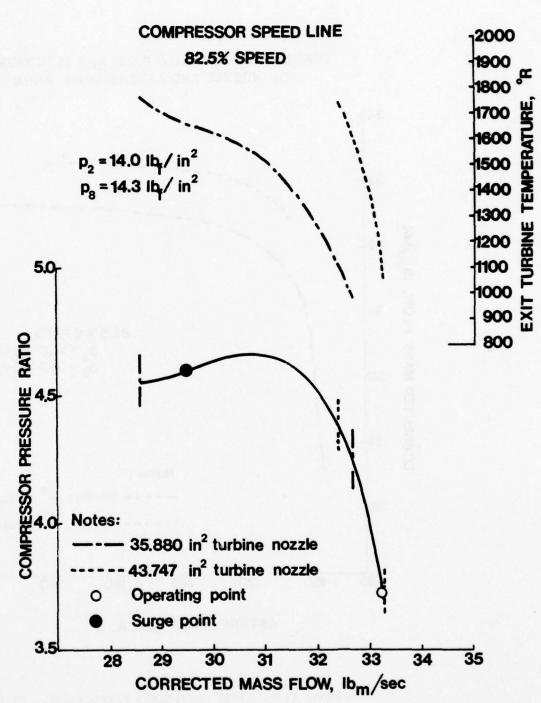


FIGURE 113a. J-85 COMPRESSOR PERFORMANCE. 82.5% SPEED

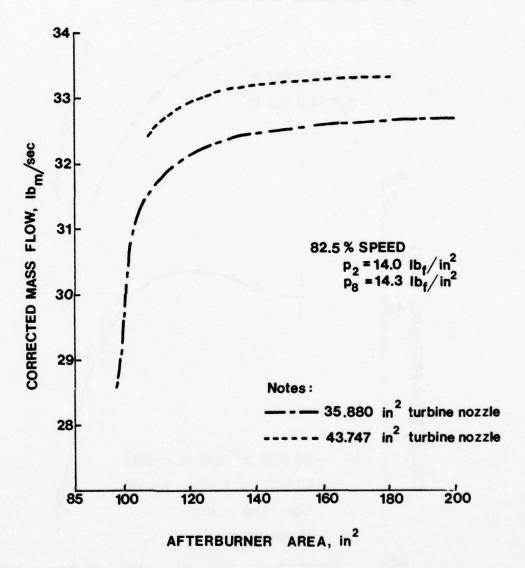


FIGURE 113b. J-85 COMPRESSOR PERFORMANCE. 82.5% SPEED

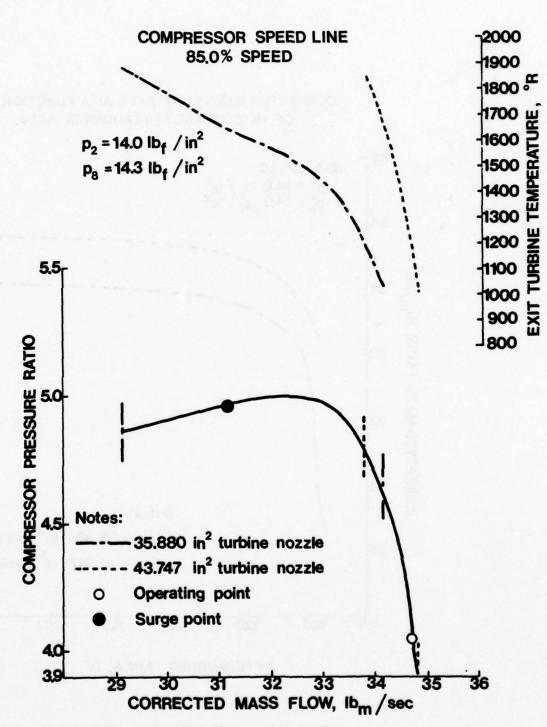


FIGURE 114a. J-85 COMPRESSOR PERFORMANCE. 85% SPEED

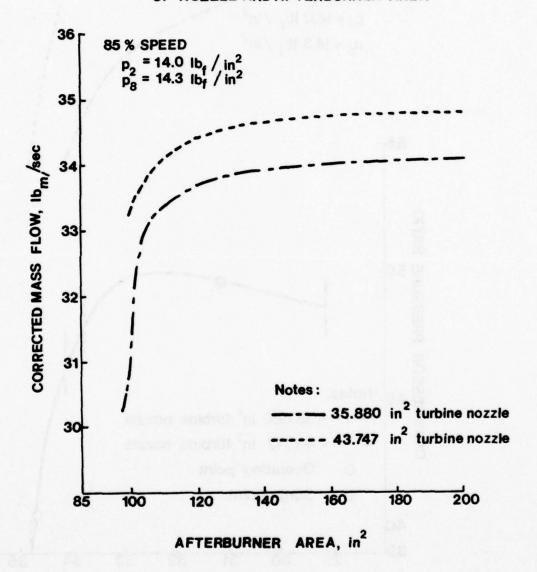
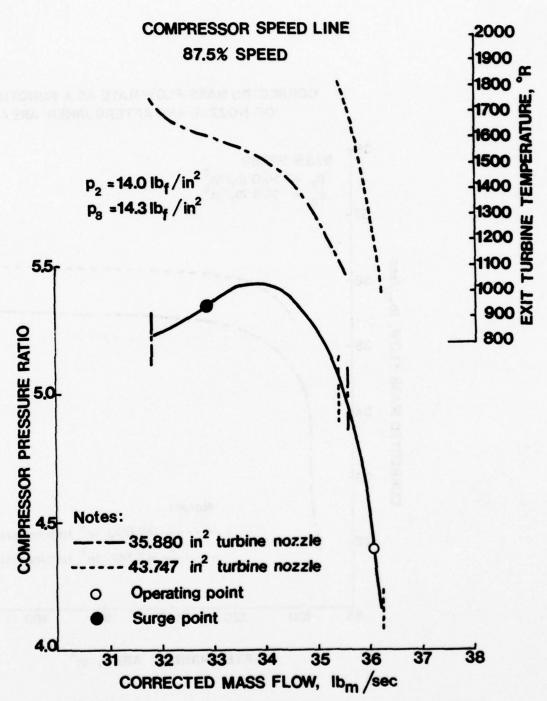


FIGURE 114b. J-85 COMPRESSOR PERFORMANCE. 85% SPEED



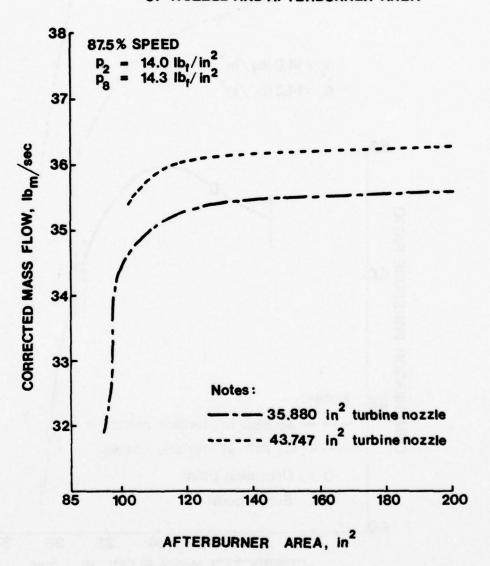


FIGURE 115b. J-85 COMPRESSOR PERFORMANCE. 87.5% SPEED

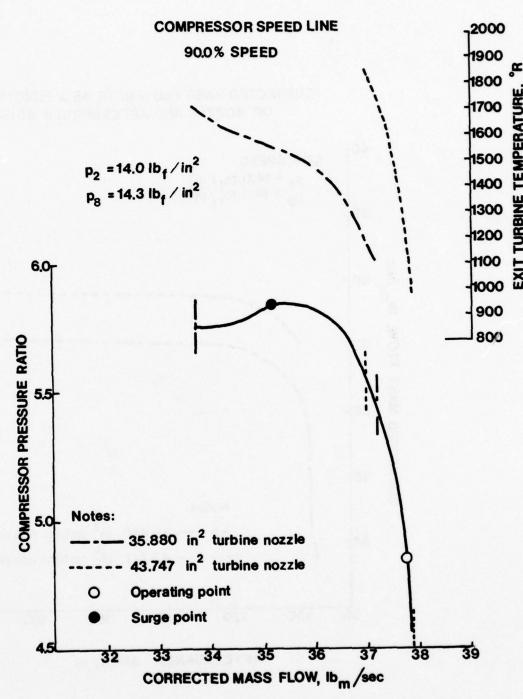


FIGURE 116a. J-85 COMPRESSOR PERFORMANCE. 90% SPEED

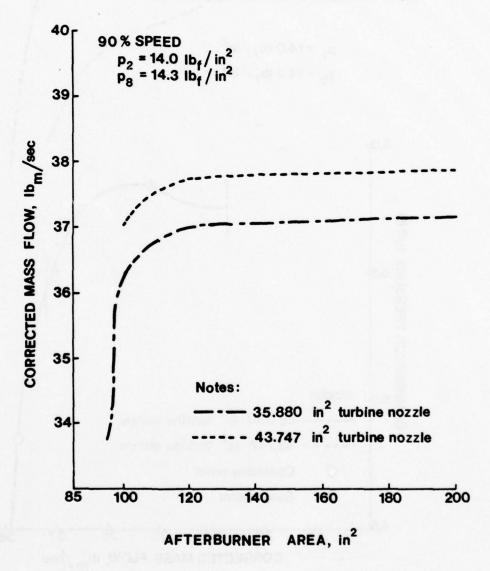


FIGURE 116b. J-85 COMPRESSOR PERFORMANCE. 90% SPEED

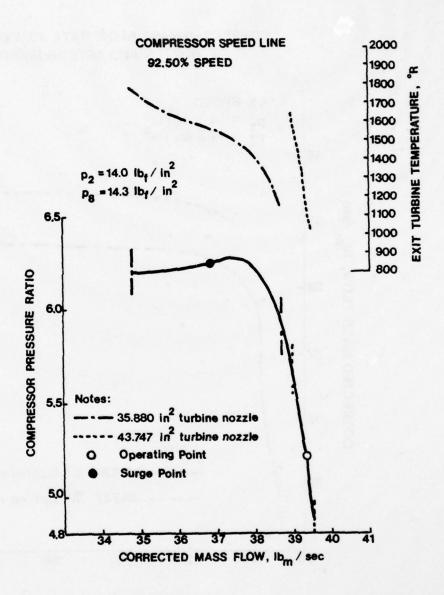


FIGURE 117a. J-85 COMPRESSOR PERFORMANCE. 92.5% SPEED

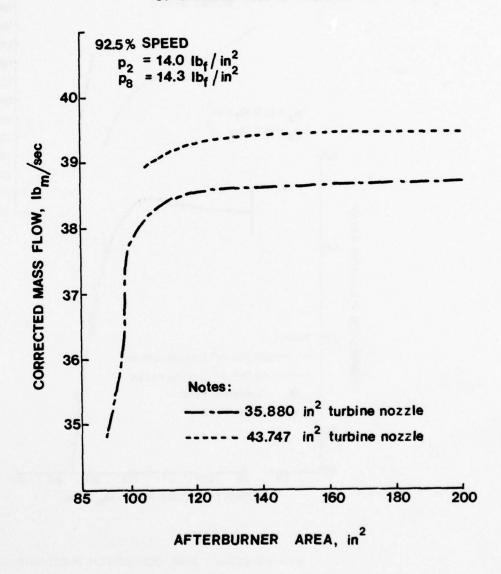


FIGURE 117b. J-85 COMPRESSOR PERFORMANCE. 92.5% SPEED

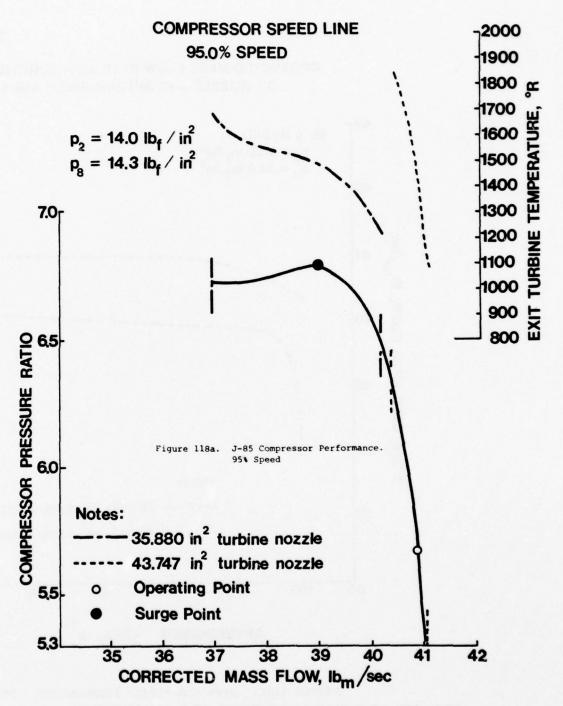


FIGURE 118a. J-85 COMPRESSOR PERFORMANCE. 95% SPEED

CORRECTED MASS FLOW RATE AS A FUNCTION OF NOZZLE AND AFTERBURNER AREA

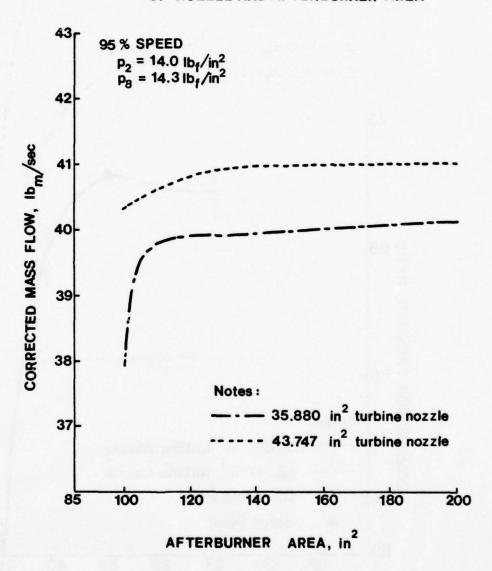
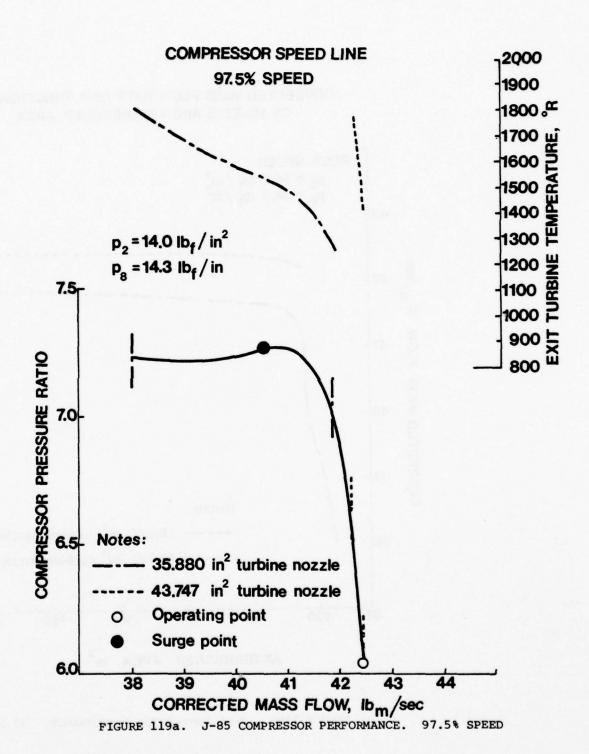


FIGURE 118b. J-85 COMPRESSOR PERFORMANCE. 95% SPEED



CORRECTED MASS FLOW RATE AS A FUNCTION OF NOZZLE AND AFTERBURNER AREA

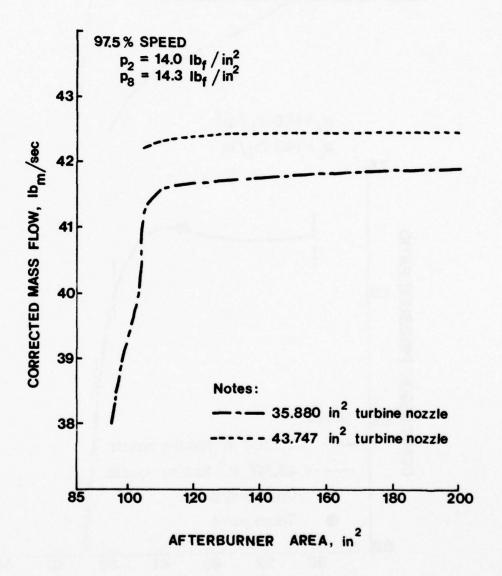


FIGURE 119b. J-85 COMPRESSOR PERFORMANCE. 97.5% SPEED

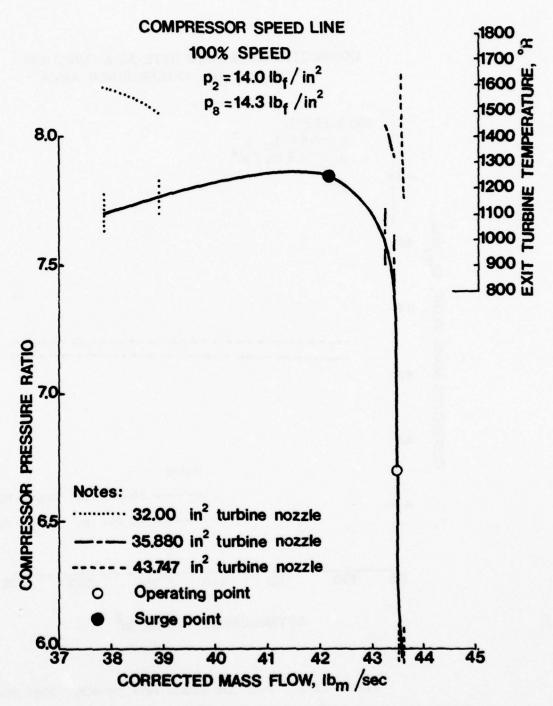


FIGURE 120a. J-85 COMPRESSOR PERFORMANCE. 100% SPEED

CORRECTED MASS FLOW RATE AS A FUNCTION OF NOZZLE AND AFTERBURNER AREA

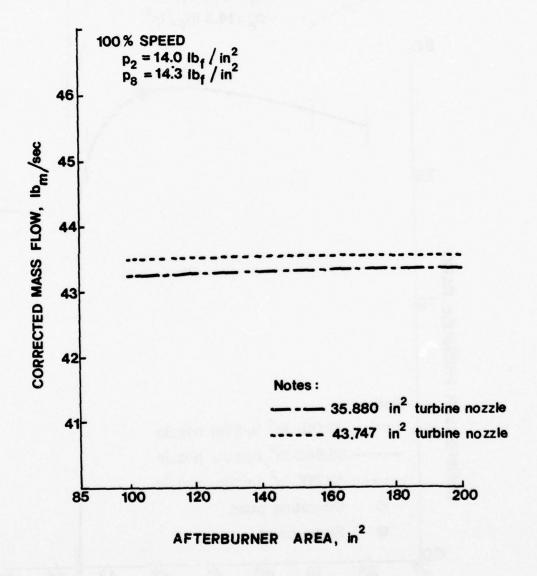
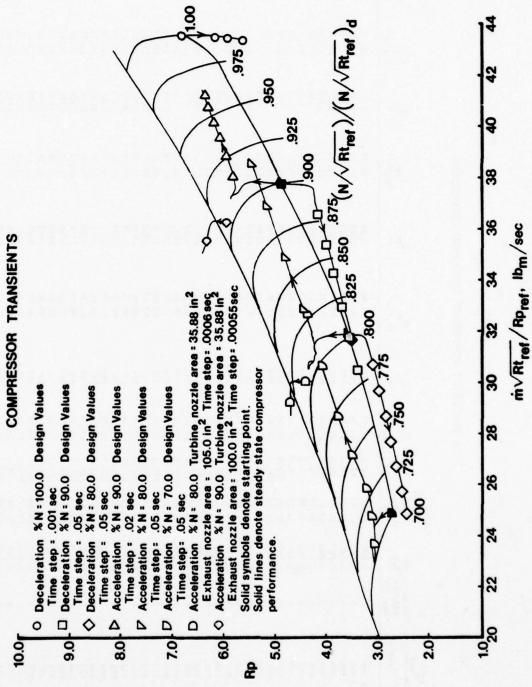


FIGURE 120b. J-85 COMPRESSOR PERFORMANCE. 100% SPEED



J-85 COMPRESSOR TRANSIENT PERFORMANCE

FIGURE 121.

TABLE 30

J-85 TRANSIENT COMPONENT OPERATING CONDITIONS

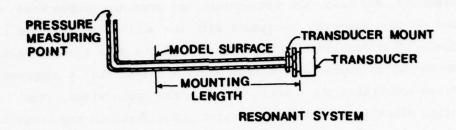
Comments																																					Surge	-	abine	
Ptr 1bf/in ²	35.08	30.84	28.76	23.99	20.80	10.05	19.54	19.12	18.73	18.90	17.65	17.42	17.22	16.85	16.68	16.53	23.71	29.26	29.90	30.53	31.57	31.98	18.71	21.98	23.18	24.45	25.58	17.72	17.79	18.15	18.62	19.26	19.99	20.90	23.22	23.50	24.41	28.18	28.50	*****
71.	1723	1549	1430	1325	951	941	937	929	922	1175	902	895	688	882	879	875	1317	1896	1999	2003	2000	2010	1163	1885	1919	1946	1954	9571	1700	1733	1773	1821	1843	1869	1401	1405	1449	1449	1454	200
P br 1b g/1n ²	92.39	75.95	73.25	65.73	54.41	50.26	48.34	46.17	44.11	47.58	40.61	38.96	37.46	34.61	33.29	32.01	65.74	80.47	82.25	84.00	10.00	88.19	47.58	61.82	29.99	71.57	75.60	35.28	43.19	45.62	48.66	52.47	56.65	61.46	59.57	65.62	68.40	80.83	89.05	20.46
Ta.	2149	1617	1509	1682	1207	1190	1173	1156	1140	1469	1110	1093	1066	1053	1042	1030	1668	2458	2464	2472	2483	2487	1451	2323	2376	2420	2442	1308	2040	2090	2153	2226	5269	2319	1729	1915	2119	1837	2026	05.43
P C 1D 2/1n ²	99.88	85.61	82.71	11.11	61.12	58.71	54.34	51.89	49.56	52.10	45.64	43.78	42.08	30.41	37.30	35.84	27.17	85.26	87.17	89.06	90.76	93.58	52.10	65.39	70.53	75.69	90.07	39.34	45.78	48.35	51.53	55.52	59.97	65.07	62.39	65.67	69.51	85.60	60.68	1.1
F. &	776	934	925	874	833	822	817	908	962	789	176	766	15/	740	732	724	874	920	927	934	144	953	789	845	998	887	908	171	760	773	789	805	823	844	838	847	861	922	932	010
As tu 2	43.74	43.74	43.74	43.74	43.74	43.74	43.74	43.74	43.74	43.74	43.74	43.74	43.74	43.74	43.74	43.74	43.74	43.74	43.74	43.74	43.74	43.74	43.74	43.74	43.74	43.74	43.74	43.74	43.74	43.74	43.74	43.74	43.74	43.74	35.88	35.88	35.88	35.88	35.88	22.00
A B Tu 2	88.0	88.0	88.0	120.0	120.0	120.0	120.0	120.0	120.0	145.9	145.9	145.9	145.9	145.9	145.0	145.9	120.0	120.0	120.0	120.0	120.0	120.0	145.9	145.9	145.9	145.9	145.9	162.5	162.5	162.5	162.5	162.5	162.5	162.5	105.0	105.0	105.0	100.0	100.0	100.0
Roref Roref 1b / sec	43.51	43.46	43.32	37.71	36.53	35.38	37.95	31.69	30.46	31.73	30.68	29.62	28.67	89.17	25.76	24.86	37.71	37.99	38.74	39.47	40.12	40.68	11.73	32.80	34.82	36.80	38.51	24.82	24.14	25.86	27.14	28.71	30.60	32.68	29.99	30.01	29.55	36.21	36.23	22.43
Time Sec.	0.000	0.007	0.003	0.00	0.050	0.100	0.200	0.250	0.300	0.000	0.050	0.100	0.150	0.200	300	0.350	0.000	0.020	0.040	0.060	0.080	0.100	0.00	0.050	0.100	0.150	0.200	0000	0.050	0.100	1.150	1.200	0.250	0.300	000.0	9000	.0012	0.000	.00055	*****
Accel. (A)/De- cel.(D)	۵	9 6	۵	a	٥	ه ه	0 0	۵	Q	Q	٥	٥	ء م	۵ د		۵۵	<	4	4	<	۷.		. «	<	*	<	۷,	٠.	< *	. «	. «	*	4	4	4	4	×	«	κ.	
N/Rtref	1.000	966.	995	006.	.881	.865	849	.815	. 799	.800	.783	.767	.752	181.	708	.693	006	.913	.923	.932	.942	.951	008	.827	.854	.882	116.	007.	907.	7.13	.751	.773	661.	.826	. 800	.801	.802	006.	106.	306.
Case		~ ~	4	2	91	- 0	0 6	10	11	12	13	14	15	170	18	19	20	21	22	23	57	57	27	28	53	30	31	32	34	35	36	37	38	39	40	41	42	43	44	7

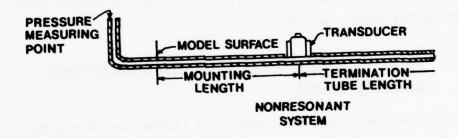
of compressor performance under transient conditions. Compressor performance will be monitored with temperature and pressure measurements, and thus, the temperature and pressure probes must have dynamic response consistent with the test objectives and the acceleration/deceleration capabilities of the J-85 turbine engine. The use of an engine as the test vehicle rather than a compressor per se constrains the number, location and probe sizes. The engine vibration field also dictates probe strength requirements. All in all, the probe design and fabrication is vital to the program and represents a compromise between oftentimes conflicting requirements. These topics will be discussed in greater depth in the following sections.

2. Frequency Response for the Temperature and Pressure Measuring Systems

The size, space and temperature limitations within the J-85 engine are such that the pressure transducers must be remotely connected to the pressure measurement point via a small tube. If the tube is terminated at the transducer location, a resonant system results. In this case, a pressure wave enters the tube and travels to the transducer. It is then reflected back toward the source and continues to oscillate back and forth in the tube. This causes a resonance condition—often called an "organ pipe" resonance—with a wave length equal to four times the connecting length for negligible end volumes. If the frequencies of interest are well below the resonant frequencies then acceptable data can be obtained with this approach. Erroneous amplitude and phase measurements will result, however, when the phenomenological frequencies approach the resonant frequency.

The resonant condition can be eliminated by providing an infinite tube. The technique is shown schematically in Figure 122. If the tube is infinitely long, i.e., length > > diameter, then the wave cannot be reflected forward and a nonresonant condition





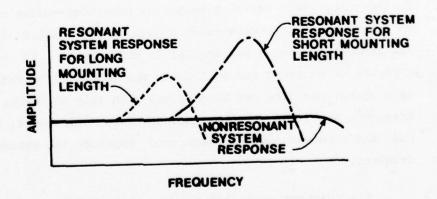


Figure 122. Resonant and Nonresonant Measuring Systems.

viscous effects and some reflection may occur since the tube is, of course, of finite length. In the latter case, the total measurement error is due to viscous and greatly diminished resonance effects.

Guidelines have been drawn for the design and fabrication of nonresonant pressure measurement systems. 104,105 In general:

- The cross-sectional area at all points in the system must be constant.
- 2) The tube internal passage must be smooth, i.e., burrs, steps, sharp edges or other discontinuities can create standing waves, etc.
- 3) All joints must be leak tight.

wilhelm in reference 104 carried out an extensive experimental evaluation of nonresonant pressure measuring systems with the objective of determining the sensitivity of the system to the above guidelines. He made the following observations:

- The response flatness was marginally improved at low frequencies by decreasing the tube inside diameter.
- The high frequency response improved as the connecting length was decreased.
- 3) Reflections were less pronounced in the low frequency range as the tube length was increased.
- 4) Use of an orifice at the end of the infinite tube improved the low frequency response.
- 5) Internal area changes introduced by various transducer mountings had no measurable effect on the amplitude frequency response.
- 6) Rubber and stainless steel tubing exhibited the same general response characteristics.

Furthermore it was noted that for all configurations having a 12" mounting length, there existed a 550 hz resonant point. This corresponded to an open organ pipe effect wherein the resonant wave length is equal to twice the mounting length.

As a result of the above considerations as well as discussions with other testing organizations, 106 the nonresonant approach was selected for the pressure measurements. This provided the ancillary advantage of placing the pressure transducer in a location remote to the sensing point and where it could be maintained at a constant temperature.

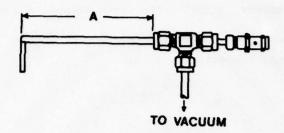
Two techniques were considered for the measurement of dynamic temperatures. The first utilized a hot wire anemometer in the constant current mode, 42 i.e., the probe resistance is determined and this can be related to the temperature provided the gas velocity is constant. This can be achieved through use of a sonic nozzle, i.e., the probe is aspirated. The sensing element is located just upstream of the throat in a constant velocity region as shown in Figure 123. The time constant is determined by the thermal inertia of the sensing element, i.e.,

$$\tau_{c} = \frac{\rho C_{p} d}{4h_{a}}$$

where ρ is the sensor density, C_p the sensor specific heat, d the sensor or wire diameter and h the heat transfer coefficient. The time constant typically has values of 10^{-4} - 10^{-5} sec. 108

The second approach utilized a miniature shielded thermocoupler. A sensor of this type is shown in Figure 124. This probe brings the fluid to rest adiabatically near the thermocouple junction. The probe itself is susceptible to both conduction and radiation errors. These factors reduce the measured temperature, and

$$t_{adb} = t(1 + r_f \frac{\gamma - 1}{2} M^2)$$
 (181)



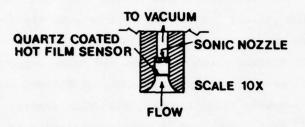


Figure 123. Aspirated Probe 107

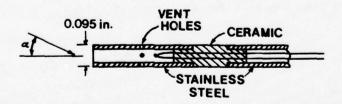


Figure 124. Shielded Thermocouple Probe 108

where t_{adb} is the measured temperature, t the static temperature, r_f the recovery factor, γ the ratio of specific heats and M the Mach number. The recovery factor can be further defined in terms of the total temperature, T, as

$$r_{f} = \frac{t_{adb} - t}{T - t}$$
 (182)

The shield and vent hole size can be chosen such that the gas is slowed to an optimum velocity, i.e., the heat gain by the thermocouple junction due to convection is just balanced by the heat lost at the junction due to thermal conduction down the probe supports. The shield itself will prevent radiant heat exchange between the junction and its environment, thus, reducing radiation errors. Gorlin and Slezinger 45 have shown that the optimum velocity is normally achieved when the outlet orifice or vent area is approximately 1/4 to 1/8 of the inlet area. The recovery factor for a probe using these design concepts is shown in Figure 125. Note that the recovery factor is reasonably constant over the velocity range of interest--300 to 460 ft/sec. Furthermore, the measurements are insensitive to yaw angle over the range of $\pm 10^{\circ}$. This is also true of the pressure probes. Both the resistance thermometer, i.e., hot wire anemometer, and the miniature thermocouple must be calibrated.

The time constant for the thermocouple is

$$\tau_{c} = \frac{mC_{p}}{h_{t}A} \tag{183}$$

where m is the mass of the sensing element, $C_{\rm p}$ the specific heat, $h_{\rm t}$ the overall heat transfer coefficient and A the heat transfer area. Equation (183) can be rewritten in terms of the thermocouple wire diameter d, the material density, ρ , and an empirical relationship for $h_{\rm t}$. One such formula has been given by Scadron and Warshawsky and

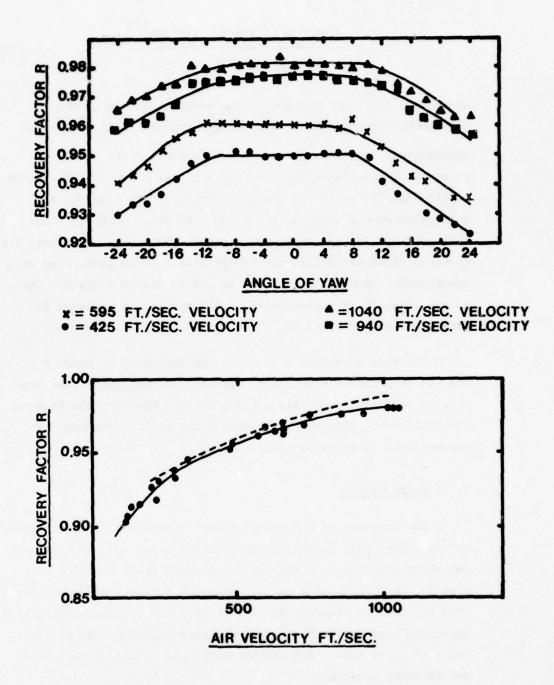


Figure 125. Recovery Factors for the Shielded Thermocouple Probe

$$\tau_{c} = \frac{4.05 c_{p} d^{3/2} [1 + (\gamma - 1) M^{2}/2]^{1/4}}{\sqrt{p_{M}} (T)^{0.18}}$$
(184)

where T is the time constant, ρ the average density of the thermocouple materials, C_p the average specific heat of the two thermocouple materials, d the wire diameter, T the total temperature, p the static pressure and M the Mach number. The above relationship is valid for Mach numbers of from 0.1 to 0.9 and a Reynolds number from 250 to 30,000. Equation (184) is shown in Figure 126 for the J-85 design point conditions. Note that the response times are relatively insensitive to Mach number for wire diameters of from 0.001 to 0.003 in. This figure indicates that a time constant of approximately 0.002 sec can be achieved for wire diameters of 0.001 in.

The time constants and, thus, the frequency response for the two temperature measurement systems are comparable when complexity is considered. Since the miniature thermocouple is more straightforward than the resistance temperature technique, it was employed in the subsequent design.

3. Probe Design

The location of the probes within the engine is constrained by the access port locations, the annulus size, and the combustor and strut locations. The overall instrumentation location relative to the outlet guide vanes, combustor diffuser and combustor cans is shown in Figure 127. Four radial and four circumferential locations were used. The radial stations were selected on the basis of equal area. Ten measurements will be made at each circumferential location:

 Five total pressures located at five circumferential locations. This spans two blade passages and should yield an accurate representation of the inviscid and viscous flow fields.

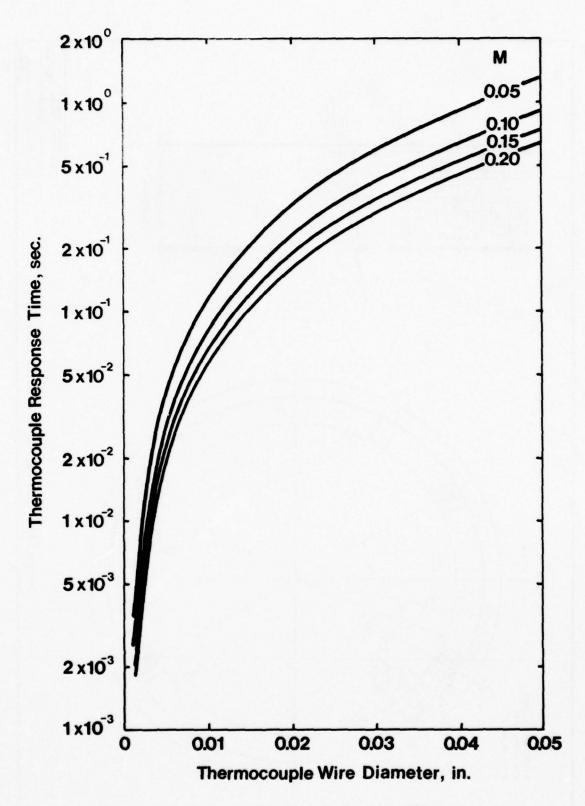
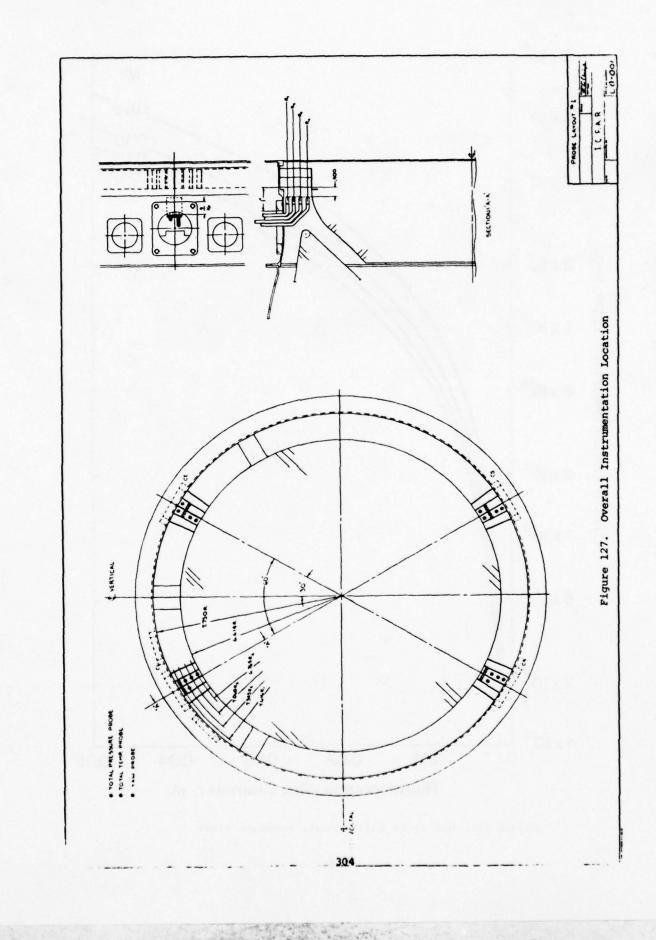


Figure 126. Miniature Thermocouple Response Times.



- 2) Three total temperatures located at three radial positions. The temperature field should be circumferentially uniform or well mixed, and, thus, only one is required.
- 3) A five-ported cone probe. This will be used to measure the flow angles in both the circumferential and radial direction. The flow should be nominally axial at the design point; however, the flow angle may vary slightly with off-design conditions. If warranted, the rake assemblies can be rotated to account for flow angle variations.
- 4) A static pressure tap located in the access cap.

The locations were changed from circumferential station to station so that all 20 locations were sampled.

The axial location of the probes was constrained by two factors:

- 1) The outlet guide vane generated wakes.
- 2) The diffusing flow passage upstream of the combustor.

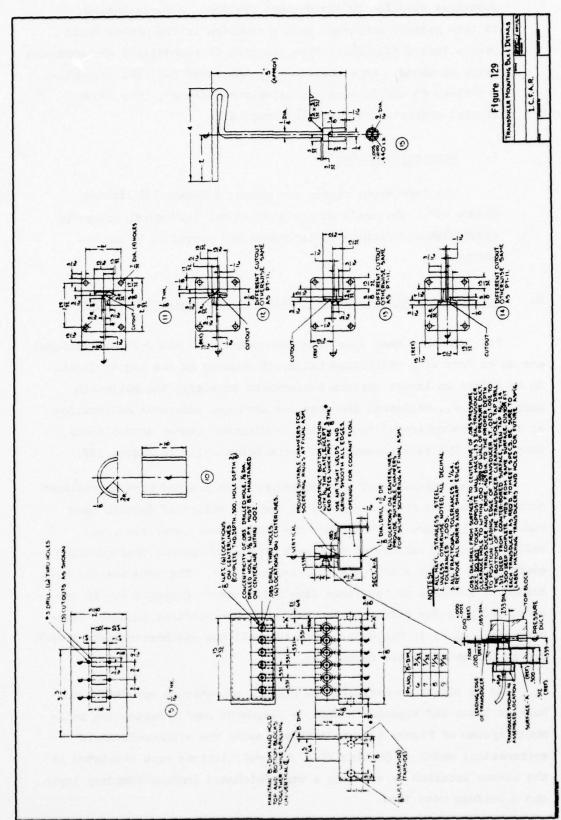
The former creates a circumferential flow non-uniformity while the latter yields a radial shift of streamlines. A far forward position is, thus, unacceptable as is a far aft location. As a result, the sensing location was positioned one chord length downstream of the outlet guide vanes. The preliminary design drawing for circumferential location 1 is shown in Figures 128 and 129.

All pressure sensing lines were the same length in the final design and maintained a uniform frequency response of approximately 1000 hz. Circumferential locations 2, 3 and 4 were similar to location 1 though not identical.

The four probe configurations for each circumferential location were originally designed to be reasonably similar. This was based on the premise that the engine accessory package located in the near vicinity of the lower access ports would be removed with its

FIGURE 128. PRESSURE & TEMPERATURE DETECTION ASSEMBLY

FIGURE 129. TRANSDUCER MOUNTING BLOCK



functions supplied by stand-alone systems. A re-evaluation of this premise indicated that a redesign of the probes would create less difficulties than removing or remodelling the accessory drive elements. As a consequence, the lower two rake assemblies, positions C3 and C4 were extensively redesigned. The reconfigured elements are shown in Figure 130.

Fabricated Probes

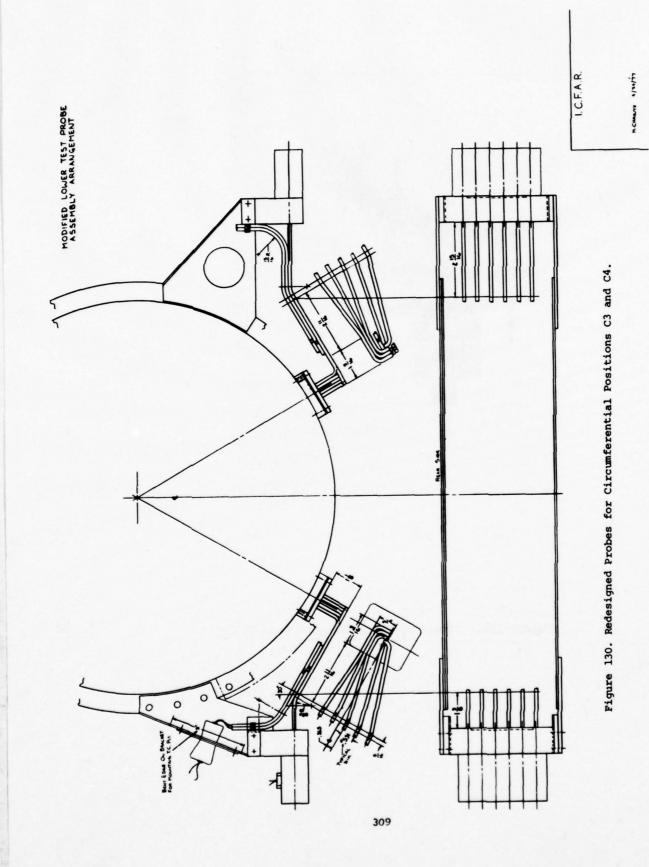
The fabricated probes are shown in Figure 131 through Figure 136. The units were evaluated for structural integrity under simulated engine environments and proved to be satisfactory.

D. Aerodynamic Analysis of the Bellmouth Flow Measuring System

All transient mass flow rate measurements in the J-85 test program are to be made with calibrated bellmouth located at the engine inlet. In an effort to insure maximum measurement accuracy, the bellmouth assembly, i.e., bellmouth and entrance section, underwent calibration at the Air Force Arnold Engineering Development Center at Tullahoma, Tennessee. The flow element is shown schematically in Figure 137.

Initial experimental investigations were plagued with measurement accuracy problems due principally to the low values of dynamic head and, thus, pressure differences. The measurement uncertainty was reflected in the calculated discharge coefficient and/or configuration coefficient values which generally exceeded one. The data scatter also tended to increase at the lower flow rates—again probably due to the decreased pressure differences. The bellmouth aerothermodynamic parameters are given in Table 31. Note that all the calibration data presented is for steady-state conditions.

In an effort to estimate the effects of entrance condition, turbulence level and Reynolds number on discharge coefficients, the bellmouth system of Figure 137 was analyzed using the viscous-inviscid mathematical model of Section III. The calculations were initiated at the screen location by assuming a zero thickness laminar boundary layer and a uniform core flow.



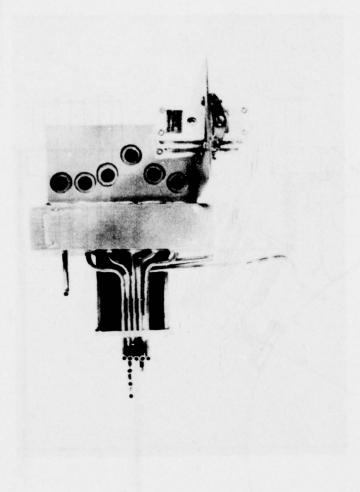


Figure 131. Probe Assembly for Position C1



Figure 132. Probe Assembly for Position Cl Installed in Compressor Case.

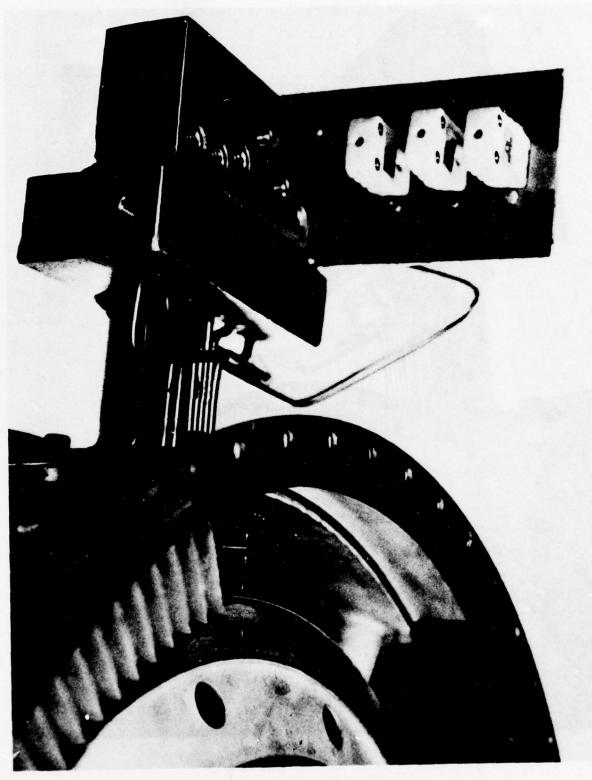


Figure 133. Sensor Location for Position Cl.

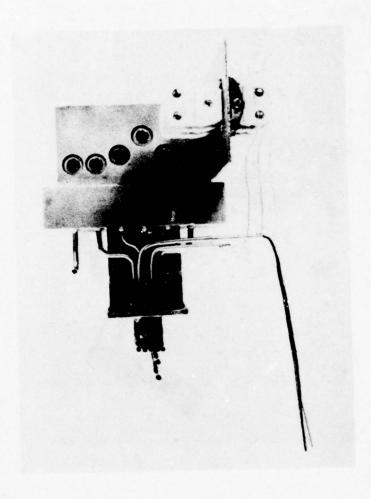


Figure 134. Probe Assembly for Position C2

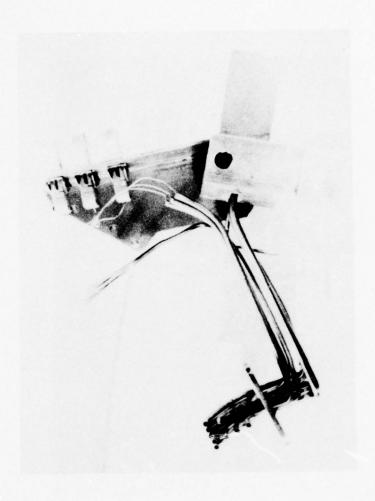


Figure 135. Probe Assembly for Position C3

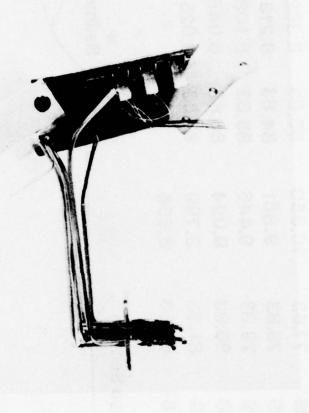


Figure 136. Probe Assembly for Position C4

FLOW SYSTEM COORDINATES

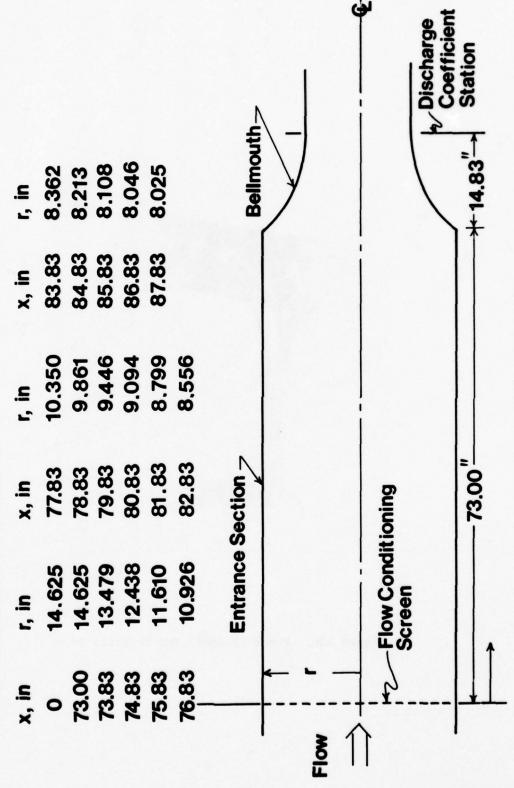


Figure 137. Bellmouth Assembly

TABLE 31

BELLMOUTH AEROTHERMODYNAMIC PARAMETERS

STEADY-STATE VALUES

Case	M _i	M _t	Re _t ×10 ⁵	T °R	lb _f /in ²	m lb /sec	C d mea
1	0.1158	0.4427	8.687	523.5	7.356	22.80	1.002
2	0.1103	0.3986	8.303	527.2	7.408	21.82	1.003
3	0.1012	0.3599	7.746	528.4	7.504	20.28	1.006
4	0.0913	0.3199	7.086	529.2	7.577	18.47	1.012
5	0.0766	0.2638	6.093	530.2	7.718	15.80	1.020
6	0.0709	0.2426	5.673	530.9	7.761	14.70	1.016
7	0.0631	0.2145	5.097	531.5	7.816	13.18	1.022
8	0.0583	0.1974	4.730	531.8	7.843	12.22	1.043
9	0.0521	0.1757	4.252	532.2	7.880	10.98	1.018
10	0.0627	0.2131	5.060	532.1	7.819	13.10	1.016
11	0.0705	0.2413	5.640	531.8	7.770	14.63	1.012
12	0.0772	0.2657	6.112	531.4	7.713	15.88	1.010
13	0.0839	0.2911	6.548	531.0	7.661	17.15	1.016
14	0.0889	0.3106	6.921	530.5	7.611	18.06	1.014
15	0.0992	0.3517	7.597	529.7	7.521	19.90	1.011
16	0.1064	0.3817	8.039	529.3	7.453	21.14	1.005
17	0.1156	0.4221	8.588	527.7	7.356	22.68	1.003
18	0.0523	0.1765	4.273	531.8	7.878	11.02	1.028
19	0.0608	0.2063	4.914	532.4	7.832	12.72	1.035
20	0.0678	0.2312	5.417	533.3	7.786	14.07	1.012

The results of the computations are plotted in Figure 138. The major difference in the two conditions, i.e., Tu = 0.5% and 1.0%, was the result of boundary layer development. When the throat Reynolds number is less than about 6 x 10⁵ and the turbulence level is less than 0.5%, the boundary layer remains laminar throughout the flow system—entrance region and bellmouth. The boundary layer will approach transition in the constant diameter section; however, the rapidly accelerated flow field in the bellmouth suppresses any tendency towards transition. On the other hand, if transition occurs in the entrance section, then the boundary layer will remain turbulent through the bellmouth.

The two curves of Figure 138 are typical of discharge coefficients for a range of turbulence levels. For example, the upper curve is qualitatively similar for all values $0 \le Tu \le 0.5$ % and the lower curve typifies results for 1% $\le Tu \le 5$ %. It should be pointed out that turbulence levels in the actual facility are probably from 2-5% and, thus, discharge coefficient values of 0.992-0.993 might be expected.

The measured and calculated values of discharge coefficients are plotted in Figure 139. The increased data scatter at the lower Reynolds numbers is clearly discernible. An ASME nozzle discharge coefficient is also included for comparison purposes. This relationship has been obtained from reference 52 and does not specifically relate to the given geometry. The difference between the two discharge coefficients is indicative of the effects of bellmouth geometry.

E. Data Processing and Analysis Program

Data Analysis Variables

The reduction and analysis of the pressure, temperature and flow direction data from the circumferentially mounted probes will be carried out using a computer program. The basic variables to be processed in this program are listed in Table 32. The measurements

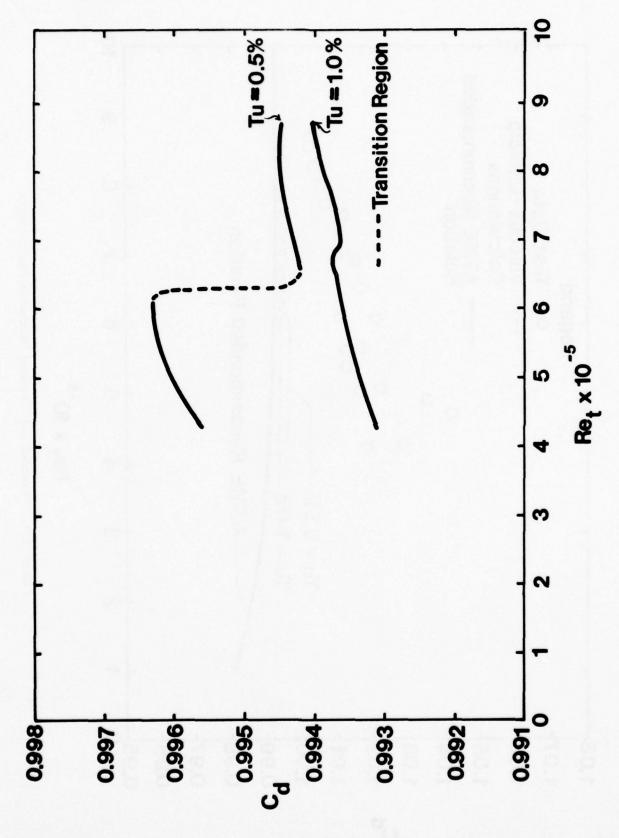
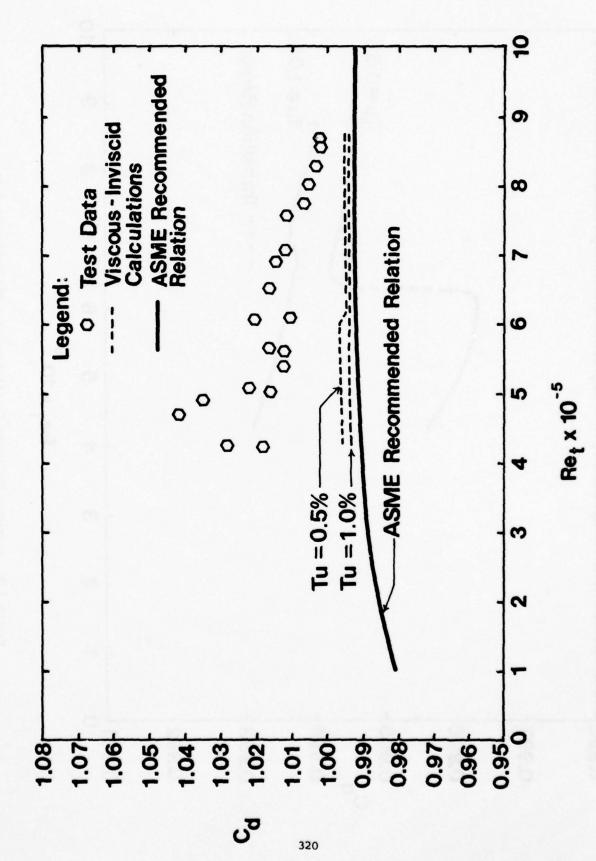


Figure 138. Computed Discharge Coefficients for the Bellmouth System



A. 4. 18.00

Figure 139. Measured and Computed Discharge Coefficients

TABLE 32
DATA ANALYSIS VARIABLES

Variable	Number of Measurements
Data Identification:	
Time, Day/Month/Year, Specific Comments	1
Time	1
Speed/Period	1
Dew Point Temperature	1
Venturi Temperature	4
Venturi Pressure	8
Bellmouth Temperature	16
Bellmouth Pressures: Steady-State	40
Bellmouth Pressures: Transient	20
Compressor Rotor/Case Clearance	12
Compressor Exit Temperature	12
Compressor Exit Pressure: Steady-State from Directional Probes	32
Compressor Exit Pressure: Steady-State	40
Compressor Exit Pressure: Transient	24
Bleed Door Temperatures	3
Bleed Door Pressures	6
Venturi Area	1
Venturi Discharge Coefficient	1
Bellmouth Area	1
Bellmouth Discharge Coefficient	1
Stall Indicator	
Wall Static Pressure	8
Differential Pressure	1
Fuel Pump Speed Stall Sensor	1
Bleed Door Position	2
	and the state of t
IGV Position	1
Fuel Valve Position	1

in general consist of both steady-state and dynamic temperatures and pressures. Compressor rotor-case clearance as well as the exit flow angle will also be measured.

As much redundancy as possible is being incorporated in the experiment. During steady-state operation, three separate mass flow rates will be measured. The principal measurement will be made with calibrated, universal venturi. Mass flow measurements will also be obtained with the calibrated bellmouth of Section V.D. Furthermore, the total and static pressures and temperatures measured at the compressor exit plane will be converted into velocities from whence a mass flow rate can be determined.

The bulk of the pressure measurements, i.e., all steadystate measurements, will be made with four Scani-valves.

The channel number, valve number and variable are listed in
Table 33. In Table 33, BMP denotes bellmouth pressure, CDP
denotes compressor discharge, S denotes static, T - total, W wall, R - rake, C - cobra and/or directional probe, VENT denotes
vent and BDP denotes bleed door pressure. With the aforementioned
symbol convention, BMPSWll denotes the bellmouth static pressure
at the wall - location 11, CDPTR34 denotes the compressor discharge total pressure for rake 3 radial position 4, etc.

Fluid Properties

The fluid flowing through the compressor is assumed to be an inviscid, thermally-perfect gas consisting of a mixture of atmospheric air and saturated water vapor. The gas properties are thus dependent on the amount of water vapor present. This can be related to the dew point temperature by means of

$$p_{v} = 3203.583 \exp \left\{ \frac{11.651 - (t_{dp}/100)}{(t_{dp}/100)} \sum_{i=1}^{8} f_{i}(6.087 - \frac{t_{dp}}{100})^{i-1} \right\}$$
(185)

TABLE 33

Valve 1

SCANIVALVE CHANNEL AND PRESSURE DESIGNATION

Valve 2

Valve 3

Valve 4

100 lb_f/in² gage 15 lb_f/in² absolute Low Pressures High Pressures High Pressures Low Pressures Vacuum lb lb_f/in² abs
85 lb_f/in² gage
CDPTRll CDPSl Channel 15 lb_f/in² abs 15 lb_f/in² abs
Atmospheric 1 lb_f/in² gage
BMPSR10 BMPTR10 1 BMPTR11 BMPSW11 CDPTR12 CDPS1 BMPTR12 CDPTR13 CDPS1 5 BMPSW12 BMPSW13 BMPTR13 CDPTR14 CDPS1 6 BMPSW14 BMPTR14 CDPTR15 CDPS1 CDPS2 BMPSR20 BMPTR20 CDPTR21 CDPS2 9 BMPSW21 BMPTR21 CDPTR22 CDPTR23 BMPTR22 CDPS2 10 BMPSW22 BMPTR23 CDPTR24 CDPS2 11 BMPSW23 BMPTR24 CDPS2 BMPSW24 CDPTR25 12 BMPTR30 CDPTR31 CDPS3 13 BMPSR30 BMPTR31 14 BMPSW31 CDPTR32 CDPS3 CDPS3 15 BMPSW32 BMPTR32 CDPTR33 BMPSW33 BMPTR33 CDPS3 CDPTR34 16 17 BMPSW34 BMPTR34 CDPTR35 CDPS3 BMPTR40 CDPS4 18 BMPSR40 CDPTR41 19 BMPSW41 BMPTR41 CDPTR42 CDPS4 CDPS4 20 BMPSW42 BMPTR42 CDPTR43 BMPSW43 BMPTR43 CDPTR44 CDPS4 21 CDPS4 BMPSW44 BMPTR44 CDPTR45 22 VENTP11 VENTP21 CDPTC10 CDPSC11 23 CDPSC12 24 VENTP12 VENTP22 CDPTC10 25 VENTP13 VENTP23 CDPTC10 CDPSC13 CDPSC14 26 VENTP14 VENTP24 CDPTC10 CDPSC21 27 CDPTC20 CDPSC22 28 CDPTC20 CDPSC23 29 CDPTC20 30 CDPTC20 CDPSC24 31 CDPTC30 CDPSC31 CDPSC32 32 CDPTC30 33 CDPTC30 CDPSC33 CDPSC34 34 CDPTC30 35 CDPTC40 CDPSC41 CDPTC40 CDPSC42 36 37 CDPTC40 CDPSC43 CDPSC44 CDPTC40 38 BDPTK1 BDPS1 39 40 BDPTK2 BDPS2 BDPS3 41 BDPTK3 42 43 44 45 46 47

Rough Vacuum

Rough Vacuum

Rough Vacuum

Rough Vacuum

^{*}Symbol definition is contained in the LIST OF SYMBOLS.

where

$$f_1 = -7.419242$$
 $f_5 = 1.042236 \times 10^{-4}$
 $f_2 = -1.651167 \times 10^{-1}$ $f_6 = 2.328538 \times 10^{-4}$
 $f_3 = -3.565700 \times 10^{-2}$ $f_7 = 7.411036 \times 10^{-5}$
 $f_4 = -1.489306 \times 10^{-3}$ $f_8 = 8.524197 \times 10^{-6}$

following Keenan et.al., reference 113. p_V denotes the partial pressure of water vapor and t_{dp} the dew point temperature. The partial pressure of air can be determined from p_V and the atmospheric pressure, p_{amb} , from

 $\mathbf{p}_{\mathbf{air}}$ and $\mathbf{p}_{\mathbf{v}}$ can be used to find the mass of each constituent per unit volume and

$$m_{air} = \frac{144p_{air}}{Ra_{air}t_{amb}}$$

$$m_{v} = \frac{144p_{v}}{R_{v} t_{amb}}$$

where $R_{air} = 53.37279 \frac{ft-lb_f}{lb_m - oR}$ and $R_v = 85.76068 \frac{ft-lb_f}{lb_m - oR}$

with

$$f_{air} = \frac{m_{air}}{m_{air} + m_{v}}$$
 (186)

where m air and m denote the air and vapor mass respectively.

The fluid density can now be written in terms of f_{air} , the fraction of gas by mass that is dry air, and

$$\rho = \frac{144p}{Rt} \tag{187}$$

where $R = R_{air} f_{air} + R_{v}(1 - f_{air})$.

The specific heat of the air-water vapor mixture can be determined from

$$c_{p} = \sum_{i=1}^{6} g_{i}(t/1000)^{i-1}$$
 (188)

with $g_i = (g_{air_i}) f_{air} + (g_v)_i (1 - f_{air})$. The coefficients $(g_{air})_i$ and $(g_v)_i$ refer to air and vapor and are defined as

$$g_{air_1} = 2.5037964 \times 10^{-1}$$
 $g_{v_1} = 4.348329 \times 10^{-1}$ $g_{air_2} = -8.081282 \times 10^{-2}$ $g_{v_2} = 1.098044 \times 10^{-1}$ $g_{air_3} = 2.312209 \times 10^{-1}$ $g_{v_3} = -5.229262 \times 10^{-1}$ $g_{air_4} = -3.416092 \times 10^{-1}$ $g_{v_4} = 1.018212$ $g_{air_5} = 2.749713 \times 10^{-1}$ $g_{v_5} = -7.923652 \times 10^{-1}$ $g_{v_6} = -8.554894 \times 10^{-2}$ $g_{v_6} = 2.272448 \times 10^{-1}$

following reference 114.

The enthalpy, H_{tl} , can now be defined in terms of the coefficients g_i and

$$H_{t1} = \int_{0}^{t} c_{p} dt = 1000 \sum_{i=1}^{6} \frac{g_{i}}{i} \left(\frac{t}{1000}\right)^{i}$$
 (189)

The first law of thermodynamics can be written as

$$dH_{t1} = tds + dp/\rho J$$

which reduces to

$$C_{p} \frac{dt}{t} = \frac{R}{J} \frac{dp}{p}$$

for an isentropic process. This can be integrated between the limits t_1 , t_2 and p_1 , p_2 yielding

$$\frac{p_2}{p_1} = \exp \left\{ \frac{J}{R} \left[g_1 \ln \left(\frac{t_2/1000}{t_1/1000} \right) \right] + \sum_{i=2}^{6} \frac{g_i}{i-1} \left[\left(\frac{t_2}{1000} \right)^{i-1} \right] \right\}$$

$$\left(\frac{t_i}{1000} \right)^{i-1} \right] \right\}$$
(190)

where J denotes the mechanical equivalent of heat and R the gas constant.

3. Mach Number and Velocity Calculation

The velocity and Mach number can be determined from the fluid property relations of the previous section and Bernoulli's equations. It is presumed that the total pressure, P, the static pressure, p, and the total temperature, T, are specified. The static temperature can be obtained by solving the isentropic pressure ratio relation iteratively, i.e., $p_2/p_1 = p/P$ and thus $t_2/t_1 = t/T$. The static and total enthalpies can be obtained and

$$U = \sqrt{2g_{c}^{J(H_{tl} - H_{tl})}}$$
 (191)

where H denotes the enthalpy corresponding to T and H $_{\mbox{tl}}$ st corresponds to t.

The Mach number is the ratio of the velocity, U, to the sonic velocity, a, and

$$a = \sqrt{g_{C} \gamma Rt}$$
 (192)

where γ is the ratio of specific heats and

$$\gamma = \frac{C_p}{C_p - R/J} \tag{193}$$

Five-Ported Cone Probe

The flow angles as well as intra-passage total and static pressures will be measured with a five-ported cone probe. The sensor is shown in Figure 140. The total pressure port is designated with a 1 while the side ports are numbered from 2 through 5. The radial and azimuthal flow angles are denoted as α and β with the included angle being γ^{*} . The total angle can be related to α and β via

$$\gamma^* = \tan^{-1} \sqrt{\tan^2 \alpha + \tan^2 \beta}$$
 (194)

The side-port pressure differences can be related to α and β by means of the calibration functions $\phi_1(\alpha)$ and $\phi_2(\beta)$, i.e.,

$$\frac{p_2 - p_3}{p_1 - p_8} = \phi_1(\alpha) \tag{195}$$

$$\frac{p_4 - p_5}{p_1 - p_s} = \phi_2(\beta) \tag{196}$$

where p_s^* denotes an effective static pressure and is $(p_2 + p_3 + p_4 + p_5)/4$. The actual total and static pressures can be correlated with the angle γ^* and

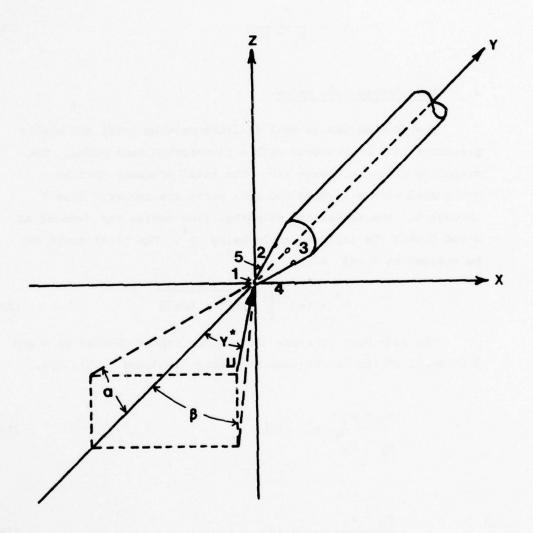


Figure 140. Five-Ported Cone Probe

$$\frac{p_1 - p_s^*}{p - p} = \phi_3(\gamma^*) \tag{197}$$

$$\frac{p_s^* - p_s}{P - p} = \phi_4(\gamma^*) \tag{198}$$

The flow angles and total and static pressures are determined by measuring p_1 , p_2 , p_3 , p_4 and p_5 and inverting the calibration functions ϕ_1 through ϕ_4 .

5. Recovery Factors for Thermocouple Probes

As noted in a previous section, thermocouple probes immersed in gas or liquid streams may attain thermal equilibrium at a temperature differing with that of the gas itself. At low airstream velocities, this temperature difference may be due to convection, conduction and/or radiation heat transfer between the thermocouple, gas stream and the external surroundings. For high Mach number gas flows, aerodynamic heating also comes into play and the indicated temperature must be corrected for this effect.

When negligible heat transfer to and from the external environment is presumed, i.e., aerodynamic heating only, the adiabatic temperature can be related to the recovery factor r_f^{63}

$$r_{f} = \frac{t_{adb} - t}{T - t}$$
 (199)

where t_{adb} denotes the adiabatic temperature with T and t specifying the total and static temperature respectively. The recovery ratio $r_{\rm r}^{-115}$ is similar and

$$r_r = \frac{t_{adb}}{T}$$
 (200)

where both r_f and r_r are functions of Mach number, flow angle, gas properties and probe geometry. Both r_f and r_r are determined by calibration with the above noted factors considered.

Following reference 115, the recovery ratio can be written in terms of calibration functions $\phi^{(1)}(M)$, $\phi^{(2)}(P/P_{ref})$, $\phi^{(3)}(T/T_{ref})$ and $\phi^{(4)}(\beta)$ as

$$r_f^{(1)} = \phi^{(1)}(M)$$
 (201)

$$r_r^{(2)} = r_r^{(1)} - (1 - r_r^{(1)}) \phi^{(2)} (P/P_{ref})$$
 (202)

$$r_r^{(3)} = r_r^{(2)} - (1 - r_r^{(2)}) \phi^{(3)} (T/T_{ref})$$
 (203)

$$r_r = r_r^{(3)} - (1 - r_r^{(3)}) \phi^{(4)}(\beta)$$
 (204)

where $\phi^{(1)}$ (M) and $\phi^{(4)}$ (β) are given in Figures 141 and 142.

 $\phi^{(2)}(P/P_{ref})$ and $\phi^{(3)}(T/T_{ref})$ can be approximated as

$$\phi^{(2)}(P/P_{ref}) = (P/P_{ref})^{-0.8} - 1$$
 (205)

and

$$\phi^{(3)}(T/T_{ref}) = (T/T_{ref})^{-0.3} - 1$$
 (206)

The determination of the adiabatic temperatures and Mach numbers is iterative in that the Mach number computation is dependent on the temperature and vice versa. This calculation is initiated by assuming that the indicated and adiabatic temperatures are the same and then computing the Mach number by means of Section V.E.3. With this Mach number value, the recovery ratios

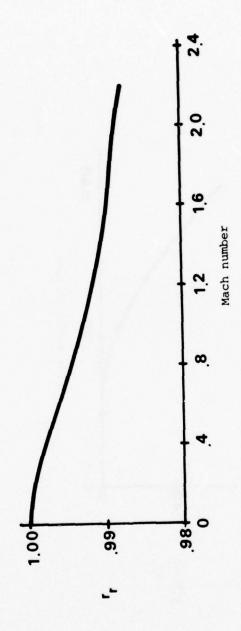


Figure 141. Recovery Ratio as a Function of Mach Number

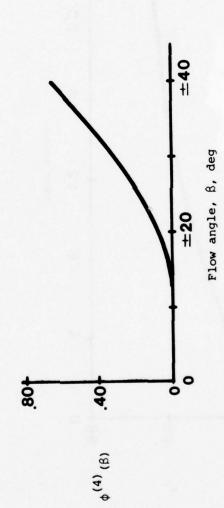


Figure 142. Recovery Ratio Function Variability With Flow Angle

are determined and an adiabatic temperature computed. This process is continued until successive temperature values agree to within prescribed limits.

Mass - Averaging

Compressor temperature ratios, pressure ratios, efficiencies, mass flow rates, etc., are computed using mass-averaged properties. Mathematically these are defined as

$$\langle \phi \rangle = \frac{\int_{A}^{f} \rho U \phi r dr d\theta}{\int_{A}^{f} \rho U r dr d\theta}$$
(207)

where the area of integration may consist of a complete circle or an annulus. Note that ϕ denotes an arbitrary property.

Since only point measurements are made, the integration process must be carried out numerically for a series of angular and radial locations. The integral $\iint \phi dA$ can be written as a A

double summation and

$$\int \int \phi dA = \sum_{i=1}^{I} \sum_{j=1}^{J} \phi_{ij}^{A}_{ij}$$
(208)

where

$$A_{ij} = \Delta r_i \Delta \theta_j / 16 \tag{209}$$

with

$$\Delta r_i = r_{i+1}^2 + 2r_i(r_{i+1} - r_{i-1}) - r_{i-1}^2$$
 1 < i < I

and

$$\Delta r_{1} = r_{2}^{2} + 2r_{2}r_{1} - 3r_{1}^{2}$$

$$\Delta r_{1} = 3r_{1}^{2} - 2r_{1}r_{1-1} - r_{1-1}^{2}$$
(210)

Furthermore,

$$\Delta\theta_{j} = \theta_{j+1} - \theta_{j-1}$$
 $1 < j < J$

and

$$\Delta\theta_{1} = \theta_{2} - \theta_{1}$$

$$\Delta\theta_{3} = \theta_{3} - \theta_{3-1}$$
(211)

 r_{i} denotes the radial location and θ_{j} the circumferential location. This is shown schematically in Figure 143.

7. Effective Wall Velocity

The boundary layers in turbomachines are normally turbulent and the velocity distribution can be approximated as

$$\frac{\mathbf{U}}{\mathbf{U}_{\infty}} = \left(\frac{\mathbf{y}}{\delta}\right)^{\mathbf{n}} \tag{212}$$

where U and U_{∞} denote the velocity and free-stream velocity respectively, y the distance from the wall, δ the boundary layer thickness, and n the profile exponent which is a function of Reynolds number.

In the mass-averaging process of the preceding section, the velocity in the vicinity of the wall must be included in the computations. Since the nearest measurement point may be well removed from the wall, considerable inaccuracy may result from assuming a linear velocity distribution, i.e., velocities varying from a measured value at the outermost radial

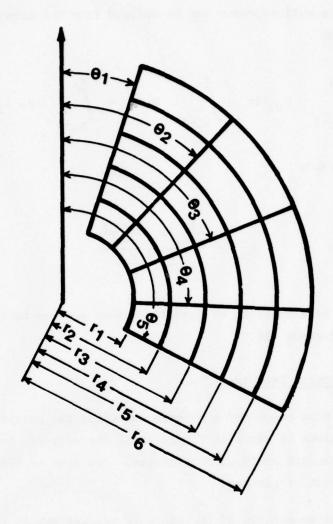


Figure 143. Grid System for Numerically - Averaging Variables

position to zero at the wall. This uncertainty can be minimized by defining an effective or wall slip velocity.

The wall velocity can be defined from the integral condition

$$\int_{\mathbf{r_o}-\delta}^{\mathbf{r_o}} \mathbf{u_{wl}} \mathbf{r} d\mathbf{r} = \int_{\mathbf{r_o}-\delta}^{\mathbf{r_o}} \mathbf{u} \mathbf{r} d\mathbf{r} = \int_{\mathbf{r_o}-\delta}^{\mathbf{r_o}} \mathbf{u_{\infty}} \left(\frac{\mathbf{y}}{\delta}\right)^{\mathbf{n}} \mathbf{r} d\mathbf{r} \qquad (213)$$

which yields

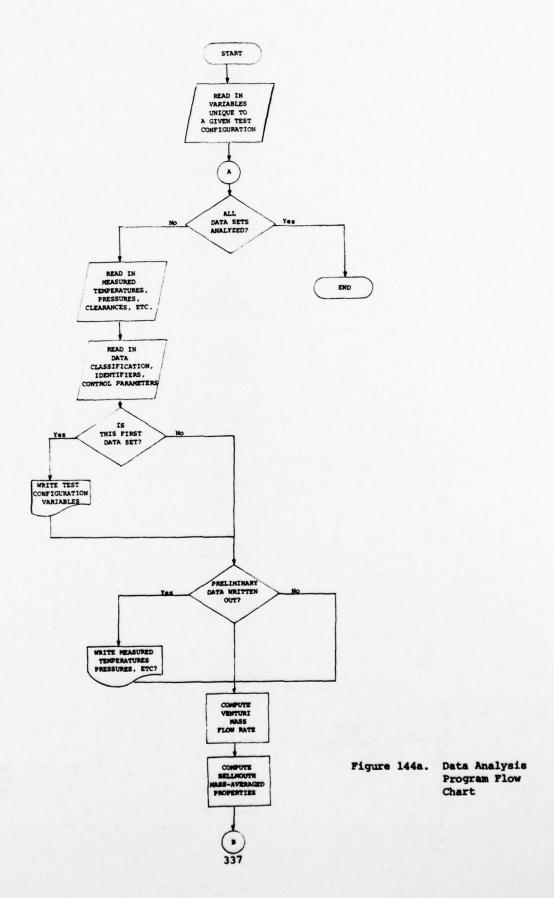
$$\frac{U_{w1}}{U_{\infty}} = \frac{\frac{1}{n+1} - \frac{(\delta/r_a)}{n+2}}{1 - \frac{(\delta/r_a)}{2}}$$
(214)

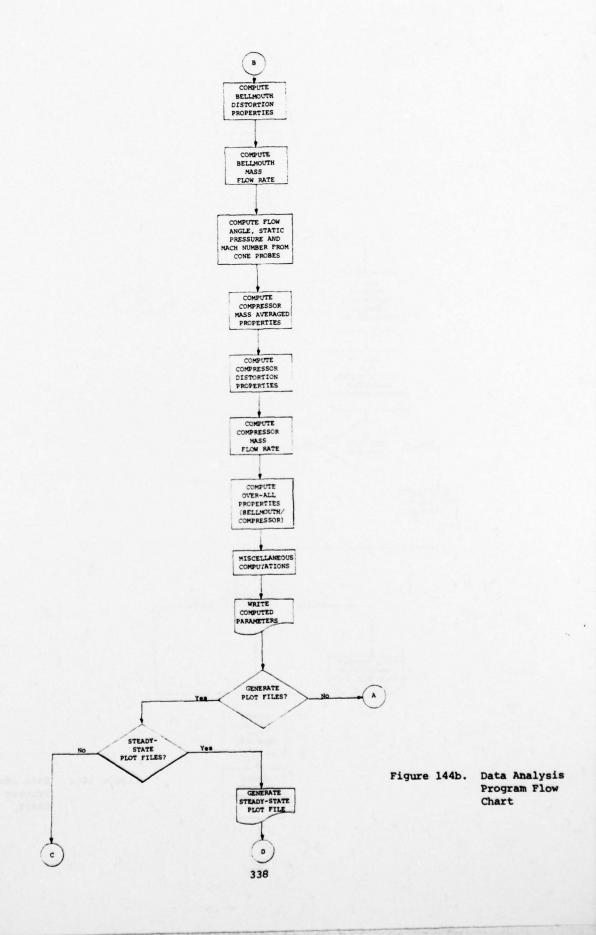
where n is a function of Reynolds number and can be obtained from reference 116.

8. Program Structure

A flow chart for a program embodying the previously described calculations is shown in Figure 144. The venturi, inlet and exit conditions are analyzed in sequence. The data is then either printed out or plotted.

The generation of the plots is carried out in two steps. First the isopleths are generated. A second series of subroutines "reads" the generated data and reorders the data in a form consistent with the circumferential and radial locations shown in Figures 145 and 146. Maximum and minimum values are then found and the data is rescaled to correspond to the physical size of the plots. Following this, linear interpolation or extrapolation is used to locate the isopleth value along a measuring station coordinate position.





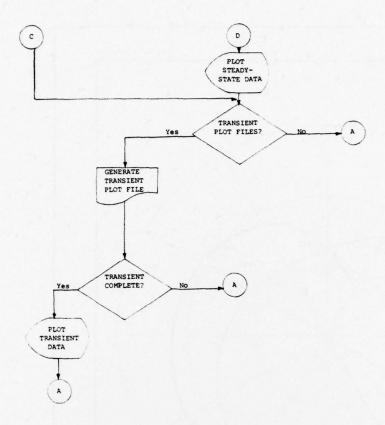


Figure 144c. Data Analysis
Program Flow
Chart

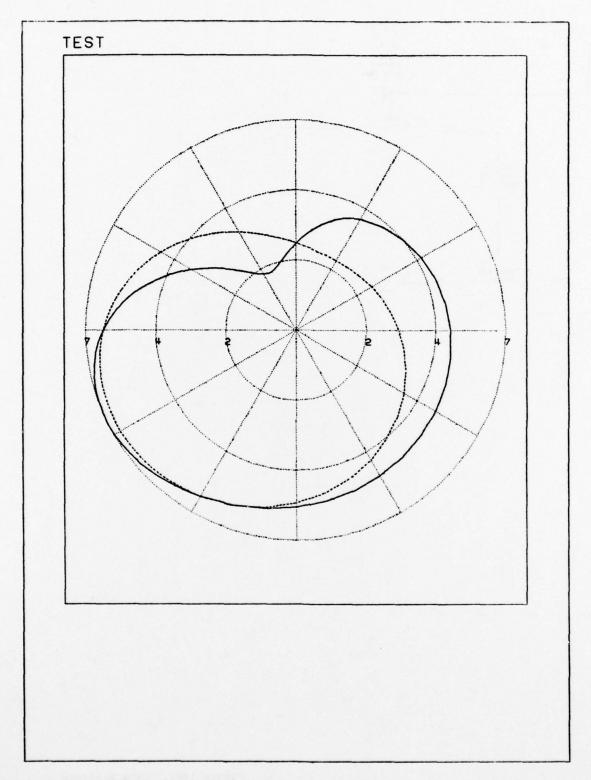


Figure 145. Typical Test Data Plot. Polar Coordinates.

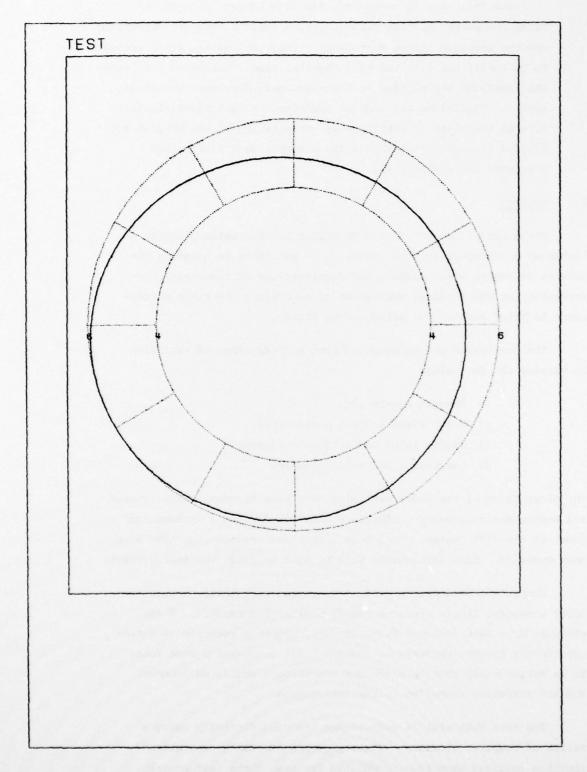


Figure 146. Typical Test Data Plot. Annular Polar Coordinates.

Once this step is completed, the grid system is plotted.

Using the point isopleth values, spline coefficients are determined and the isopleth curves formulated. These values are again scaled to be consistent with the plot physical size. Following this step, the isopleths are plotted on the previously developed coordinate system. Provisions are made to transfer the test identification data to the plots to permit ready coordination of the printed and plotted results. Flow charts and a source deck listing are presented in reference 117.

F. Summary

Transiently induced compressor stalls are currently plaguing a number of operational turbine engines. In an effort to quantify the effects of engine accelerations and decelerations on compressor performances, an experimental evaluation of compressor transient performance is being carried out using a J-85 engine.

The compressor can be operated over a broad range of variables by varying the following:

- 1) Exhaust nozzle area
- 2) First stage turbine nozzle area
- 3) Engine inlet and exhaust pressures
- 4) Compressor in-or-out bleeding

The first three of the above variables have been systematically altered and engine and compressor performance determined using a mathematical model of the J-85 engine. Transient compressor trajectories have also been computed. This information will be used to guide the test program.

Compressor performance will be monitored with total temperature, total pressure, static pressure and flow direction sensors. These elements have been designed with adequate frequency response to detect transiently induced performance changes. All probes have been found to be structurally able to withstand the turbine engine environment and are currently installed in the test engine.

The test data will be reduced and analyzed digitally using a series of computer programs. These programs including generalized plotting routines have been formulated for use in the test program.

REFERENCES

- Huffman, G. D., "A Technical Proposal for Compressor Research Facility Aerodynamic Analysis," Indianapolis Center for Advanced Research, Indianapolis, Indiana, Sept, 1974.
- "Design Requirements for the Auxiliary Air System," Report 78-M09-001, The Cadre Corporation, Atlanta, Georgia, October, 1973.
- Wennerstrom, A. J., "Summary Report," ARL/LF, August 19, 1974.
- 4. Wennerstrom, A. J., "Summary Report," ARL/LF, September 30, 1974.
- 5. "Standard Procedures for Rating and Testing Multistage Axial Flow Compressors," NACA TN 11 38, 1946.
- Dimmack, N. A., "A Compressor Routine Test Code," ARC R & M 3337, January, 1961.
- Pearson, H. and McKenzie, A. B., "Wakes in Axial Compressors,"
 J. R. Aero. Soc., Vol 63, p. 415, July, 1959.
- Prandtl, L., "Attaining a Steady Air Stream in Wind Tunnels," NACA TM 726, October, 1933.
- Tate, J. T. and Smith, R. E., "Normalized Testing Techniques to Determine Turbine Engine Stability Margins," AEDC-TR-71-249, January, 1973.
- 10. Susman, M. B. and Lampard, G. W. N., "A Possible Mechanism for Inlet/Engine Interactions Due to Inlet Flow Fluctuations," Proceedings of the Air Force Airframe Propulsion Compatibility Symposium, AFAPL-TR-69-103, June, 1970.
- Kimzey, W. F., "An Investigation of the Effects of Shock-Induced Turbulent Inflow on a YJ93-GE-3 Turbojet Engine," AEDC-TR-66-198, November, 1966.
- 12. Melick, H. C., "A Feasibility Study to Define Inlet Flow Quality and Development Criteria," AFAPL-TR-72-14, March, 1972.
- 13. Ammann, V. R., et.al., "Wind Tunnel Data Report 1/4 Scale Tailormate Forebody - Inlet Tests," USAF Contract No. F 33657-69-C-1209, General Dynamics Report FZT-587-004, February, 1971.
- 14. Farr, A. P., "Evaluation of F-15 Inlet Dynamic Distortion," AIAA Paper Number 73-784, August, 1973.
- 15. "Trip Report Visit to General Electric Company, Cincinnati, Ohio," Indianapolis Center for Advanced Research, September 20, 1974.

- 16. "Trip Report Visit to Pratt Whitney Aircraft, East Hartford, Connecticut," Indianapolis Center for Advanced Research, September 23, 1974.
- 17. "Trip Report Visit to NASA Lewis Research Center, Cleveland, Ohio," Indianapolis Center for Advanced Research, September 24, 1974.
- 18. "Trip Report Visit to Arnold Engineering Development Center, Tennessee," Indianapolis Center for Advanced Research, September 25, 1974.
- 19. "Trip Report Visit to McDonald-Douglas Aircraft Company, St. Louis, Missouri," Indianapolis Center for Advanced Research, September 26, 1974.
- 20. "Trip Report Visit to Boeing Aircraft, Seattle, Washington," Indianapolis Center for Advanced Research, September 27, 1974.
- 21. "Trip Report Visit to Detroit Diesel Allison, Indianapolis, Indiana," Indianapolis Center for Advanced Research, October 3, 1974.
- 22. "Trip Report Visit to General Electric Company, Lynn, Massachusetts," Indianapolis Center for Advanced Research, October 10, 1974.
- Abernathy, R. B., et.al., "Handbook Uncertainty in Gas Turbine Measurements," AEDC-TR-73-5, February, 1973.
- 24. Volluz, Navard Report 1488, Vol. 6, "Wind Tunnel Instrumentation and Operation."
- 25. "AF Technical Facility Capability Key," Air Force Systems Command, AFSCP 80-3, September, 1967.
- 26. Hardin, R. D. et.al., "An Inventory of Aeronautical Ground Research Facilities - Vol. II Air Breathing Engine Test Facilities," Prepared under Contract NAS2-5458, McDonnell Aircraft Company, October, 1970.
- Private Communication, R. J. Martin and M. A. Stibich, AFAPL, December 2, 1974.
- Dzung, L.S., <u>Flow Research on Blading</u>, Elsevier Publishing Company, New York, 1970.
- 29. deHaller, P., "Das Verhalten von Tragflugelgittern in Axial verdichtern und in Windkanal," <u>Brennstuff Warme Kraft</u>, Vol. 5, pp. 333-336, 1953.
- 30. Batchelor, G. K., The Theory of Homogeneous Turbulence. Cambridge University Press, 1960.
- Bird, R. B., et.al., <u>Transport Phenomena</u>, John Wiley and Sons, New York, 1965.

- 32. Schlichting, H., Boundary Layer Theory, McGraw-Hill Book Company, New York, New York, 1966.
- 33. Bradshaw, P. and Pankhurst, R. C., "The Design of Low Speed Wind Tunnels," <u>Progress in Aeronautical Science</u>, <u>Vol. 5.</u>, Pergamon Press, London, England, 1964.
- 34. Wieghardt, K. E. G., "On the Resistance of Screens," <u>Aeronautical</u> Quarterly, Vol. 4 p. 186, 1953.
- 35. Batchelor, G. K., Homogeneous Turbulence, Cambridge University Press, Cambridge, England, 1953.
- Schubauer, G. B. et.al., "Aerodynamic Characteristics of Damping Screens," NACA TN 20001, 1950.
- "Series 1050 Anemometer Systems," Thermo-Systems, Inc., St. Paul, Minnesota.
- 38. "Probes for Aerodynamic Measurements," United Sensor and Control Corporation, Watertown, Massachusetts.
- 39. "64 CBM Scanivalve," Scanivalve, Inc., San Diego, California.
- Bradshaw, P., An Introduction to Turbulence and its Measurement, Pergamon Press, Oxford, England, 1971.
- Collis, C. D. and Williams, M. J., "Two-Dimensional Convection from Heat Wires at Low Reynolds Number," <u>J. Fluid Mech.</u>, <u>Vol. 6</u>, p. 357, 1959.
- 42. Sandborn, V. A., Resistance Temperature Transducers, Metrology Press, Fort Collins, Co., 1972.
- 43. Huffman, G. D., "Eleventh Quarterly Report: Compressor Research Facility Aerodynamic Analysis," Contract Number F 33615-75-C-2008, Indianapolis Center for Advanced Research Report No. FDL-77-007, June, 1977.
- 44. Huffman, G. D., "Third Quarterly Report: Compressor Research Facility Aerodynamic Analysis An Assessment of Flow Quality Requirements for the Compressor Research Facility," Contract No. F33615-75-C-2008, Indianapolis Center for Advanced Research Report No. FDL-75-001, June, 1975.
- 45. Gorlin, S. M., et.al., "Wind Tunnels and Their Instrumentation," NASA TTF-346, 1966.
- Private Communication, R. J. Martin, AF Aero Propulsion Lab, February 12, 1975.
- 47. Townsend, A. A., "The Passage of Turbulence Through Wire Gauges," Quart. J. Mech. Appl. Math, Vol. 4, pp. 308-312, 1951.

- 48. Huffman, G. D., "First Quarterly Report: Compressor Research Facility Aerodynamic Analysis An Assessment of Flow Quality Requirements for the Compressor Research Facility," Contract No. F 33615-75-C-2008, Indianapolis Center for Advanced Research, December, 1974.
- Private communication, P. C. Tramm, Detroit Diesel Allison, June 10, 1975.
- 50. Schlichting, H. and Das, A., "On the Influence of Turbulence Level on the Aerodynamic Losses of Axial Turbomachines," in Flow Research in Blading, edited by L. S. Dzung, Elsevier Publishing Company, 1970.
- 51. Huffman, G. D., "The Effect of Free-Stream Turbulence Level on Turbulent Boundary Layer Behavior," in Boundary Layer Effects in Turbomachines, edited by J. Surugue, AGARD AG-164, December, 1972.
- 52. "Fluid Meters Their Theory and Application," Report of ASME Research Committee on Fluid Meters, American Society of Mechanical Engineers, 6th edition, New York, 1971.
- 53. Huffman, G. D., et.al., "Seventh Quarterly Report: Compressor Research Facility Aerodynamic Analysis," Contract Number F 33615-75-C-2008, Indianapolis Center for Advanced Research Report Number FDL-76-005, June, 1976.
- 54. Haering, G. W., et.al., "Eighth Quarterly Report: Compressor Research Facility Aerodynamic Analysis," Contract Number F 33615-75-C-2008, Indianapolis Center for Advanced Research Report Number FDL-76-007, September, 1976.
- 55. Huffman, G. D., et.al., "Tenth Quarterly Report: Compressor Research Facility Aerodynamic Analysis," Contract No. F 33615-75-C-2008, Indianapolis Center for Advanced Research Report No. FDL-77-005, March, 1977.
- 56. "Flow Measurement System. System Description," Report 78-M05-0004, The Cadre Corporation, Atlanta, Georgia, January, 1975.
- 57. "Design Notes, Flow Measurement System," Report DN-78-M05, The Cadre Corporation, Atlanta, Georgia, January, 1976.
- 58. "BIF Universal Venturi," Report 180-20-2, BIF, A Unit of General Signal, Providence, Rhode Island.
- 59. Halmi, D., "Metering Performance Investigation and Substantiation of the Universal Venturi Tube - Part I" ASME Paper, 73-WA/FM-3, 1973.
- 60. Halmi, D., "Metering Performance Investigation and Substantiation of the Universal Venturi Tube - Part 2," ASME Paper, 73-WA/FM-4, 1973.

- 61. Halmi, D., "C Evaluation Differences Between Mathematical and Physical Possibilities," ASME Paper, 74-WA/FM-2, 1974.
- 62. Private communication, E. W. Jehn, May, 1976.
- 63. Shapiro, A., The Dynamics and Thermodynamics of Compressible Fluid Flow, Vol. I, Ronald Press Company, New York, 1953.
- 64. Brune, G. W., et.al., "New Approach to Inviscid Flow/Boundary Layer Matching," AIAA Journal, Vol. 13, pp. 936-938, 1975.
- 65. Thwaites, B., ed. <u>Incompressible Aerodynamics</u>, Oxford at the Clarendon Press, 1960.
- 66. Bradshaw, P., et.al., "Calculation of Boundary Layer Developm at Using the Turbulent Energy Equation," J. Fluid Mechanics, Vol. 28, pp. 593-616, 1967.
- 67. Bradshaw, P. and Ferriss, D., "Calculation of Boundary Layer Development Using the Turbulent Energy Equation; Compressible Flow on Adiabatic Walls," J. Fluid Mechanics, Vol. 46, 1971.
- 68. Bradshaw, P. and Unsworth, K., "An Improved Fortran Program for the Bradshaw-Ferriss-Atwell Method of Calculating Turbulent Shear Layers," Imperial College Aero Report 74-02, February, 1974.
- 69. McNally, W. D., "Fortran Program for Calculating Compressible Laminar and Turbulent Boundary Layers in Arbitrary Pressure Gradients," NASA TN D-5681, May, 1970.
- 70. Cohen, C. B. and Reshotko, E., "The Compressible Laminar Boundary Layer with Heat Transfer and Arbitrary Pressure Gradient,"
 NACA TR 1294, 1956.
- 71. Thwaites, B., "Approximate Calculation of the Laminar Boundary Layer," Aero Quarterly, Vol. 1, pp. 245-280, 1949.
- 72. Sasman, P. K. and Cresci, R. J. "Compressible Turbulent Boundary Layer with Pressure Gradient and Heat Transfer," AIAA Journal, Vol. A., pp. 19-25, 1966.
- 73. Chang, P. K., Separation of Flow, Pergamon Press, Oxford, 1966.
- 74. Ferron, A. G., "Calibration Report on Four 48 in Universal Venturi Tubes Serial Numbers 48901 1, 2, 3, 4, Alden Research Laboratories, Holden, Massachusetts, April, 1977.
- 75. Mandel, John, The Statistical Analysis of Experimental Data, Interscience Publishers, New York, 1964.
- 76. Bradshaw, P. and Ferriss, D. H., "Applications of a General Method of Calculating Turbulent Shear Layers," <u>Journal of Basic Engineering</u>, <u>Trans. ASME</u>, <u>Series D.</u>, <u>Vol. 94</u>, #2, pp. 345-352, 1972.

- 77. Ferriss, D. H., "An Implicit Numerical Method for the Calculation of Boundary Layer Development Using the Turbulent Energy Equation," NPL Aero Report 1295, 1969.
- 78. Huffman, G. D., Unpublished report, Imperial College of Science and Technology, London, England.
- 79. Von Rosenberg, D. V., Methods for the Numerical Solution of Partial Differential Equations, American Elsevier Publishing Company, Inc., New York, 1975.
- 80. Patankar, S. V. and Spalding, D. B., Heat and Mass Transfer in Boundary Layers, Morgan-Grampian, London, 1967.
- 81. Richtmyer, R. D. and Morton, K. W., <u>Difference Methods for Initial Valve Problems</u>, Interscience Publishers, New York, 1967.
- 82. Meksyn, D., New Methods in Laminar Boundary Layer Theory, Pergamon Press, New York, 1961.
- 83. Bradshaw, P., "Calculation of Boundary Layer Development Using the Turbulent Energy Equation: III, Synthetic Starting Profiles," National Physical Laboratory, ARC 30-299, 1968.
- 84. Coles, D. E. and Hirst, E. A., Computation of Turbulent Boundary
 Layers 1968 AFOSR-IFP-Stanford Conference, Vol. II, Stanford
 University, 1969.
- 85. Huffman, G. D., et.al., "Optimization of Turbulence Models by Means of a Logical Search Algorithm," <u>Appl. Sci. Res.</u>, Vol. 27, pp. 321, 1973.
- Klebanoff, P. S., <u>Nat. Adv. Comm. Aero. Wash. Report.</u>, No. 1247, 1955.
- 87. Private communication, P. Bradshaw, Imperial College of Science and Technology, London, England, March, 1978.
- 88. Glushko, G. S., "Turbulent Boundary Layer on a Flat Plate in an Incompressible Fluid," NASA TT F-10, 080, 1965.
- 89. Granville, P. S., "The Calculation of the Viscous Drag of Bodies of Revolution," Navy Department Report 849, July, 1953.
- Van Driest, E. R., "On the Turbulent Flow Near a Wall," J. Aero. Sci., Vol. 23, p. 1007, 1956.
- 91. Cebeci, T. and Smith. A. M. O., Analysis of Turbulent Boundary Layers, Academic Press, New York, 1974.
- 92. Huffman, G. D. and Bradshaw, P., "A Note on von Karman's Constant in Low Reynolds Number Turbulent Flows," J. Fluid Mech., Vol. 53, p. 45, 1972.

- 93. Huffman, G. D., "A Re-examination of Some Retransitional Flows,"
 Paper presented at the Naval Postgraduate School and Naval Air
 System Command Workshop on Flow In Turbomachines, December, 1970.
- 94. Huffman, G. D., "Fourteenth Quarterly Report: Compressor Research Facility Aerodynamic Analysis," Contract No. F 33615-75-C-2008, Indianapolis Center for Advanced Research Report No. FDL-78-002, March, 1978.
- 95. Roache, P. J., Computational Fluid Dynamics, Hermosa Publishers, Albuquerque, New Mexico, 1972.
- 96. Kurzrock, J. W., "Exact Numerical Solutions of the Time Dependent Compressible Navier-Stokes Equations," CAL Report No. AG-2026-W-1, Cornell University, Ithaca, New York, 1966.
- 97. Willoh, R. G., and Seldner, K., "Multistage Compressor Simulation Applied to the Prediction of Axial Flow Instabilities," NASA TMX-1880, 1969.
- 98. Seldner, K., et.al., "Generalized Simulation Technique for Turbojet Engine System Analysis," NASA TN D-6610, 1972.
- 99. Private communication, J. Batka, March, 1976.
- 100. Huffman, G. D., et.al., "Ninth Quarterly Report: Compressor Research Facility Aerodynamic Analysis," Contract Number F 33615-75-C-2008, Indianapolis Center for Advanced Research Report No. FDL-76-009, December, 1976.
- 101. Huffman, G. D., "Thirteenth Quarterly Report: Compressor Research Facility Aerodynamic Analysis," Contract Number F 33615-75-C-2008, Indianapolis Center for Advanced Research Report No. FDL-77-013, December, 1977.
- 102. Private communication, F. R. Ostdiek, Air Force Aero Propulsion Laboratory, December 15, 1976.
- 103. Arnett, S. E., "Turbine Engine Control Synthesis," AFAPL-TR-74-113, December, 1974.
- 104. Wilhelm, W. E., "Investigation of Tubing Effects on Amplitude Frequency Response of Pressure Sensing Systems Using Nonresonant Terminations," NASA TM X-1988, 1970.
- 105. Kicks, J. C., "Development and Application of Ultraminiature Pressure Transducers for Use in Wind Tunnel Models, Section 2" Presented at the 15th National Instrument Society of America Aerospace Instrumentation Symposium, Las Vegas, Nevada, May 5-7, 1969.
- 106. Private communication, W. A. Kimzey, February, 1976.
- Ling, S. C. and P. G. Hubbard, <u>Journal Aeronautical Science</u>, Vol. 23, No. 9, 1956.

- 108. Hottel, H. C. and Kalitinsk, "Temperature Measurements in High Velocity Air Streams," <u>Journal of Applied Mechanics</u>, <u>Vol. 12</u>, A25-A32, No. 1, 1945.
- 109. Doeblin, E. O., <u>Measurement Systems</u>: <u>Application and Design</u>, McGraw-Hill Book Company, 1966.
- 110. Scadron, M. D. and Warshawsky, "Experimental Determination of Time Constants and Nusselt Numbers for Bare Wire Thermocouples in High Velocity Air Streams and Analytic Approximation of Conduction and Radiation Errors," NACA TN 2599, 1952.
- 111. Smith, A. M. O., "Transition Pressure Gradient and Stability Theory," Proceedings of the 9th International Congress of Applied Mech., Brussels, Vol. 4, p. 234, 1957.
- 112. Scanivalve Multiplexers Catalog, Scanivalve, Inc., P. O. Box 20005, San Diego, California 92120.
- 113. Keenan, J. H., et.al., "Steam Tables: Thermodynamic Properties of Water, Including Vapor, Liquid, and Solid Phases,"

 John Wiley and Sons (New York), 1969.
- 114. Hearsey, R. M., "Computer Programs for Single-Stage Axial Compressor Test Data Analysis," Aerospace Research Laboratories, WPAFB, Ohio, Vol. 1, ARL 73-0177, AD 776 791, December, 1973.
- 115. Stickney, T. M., "Recovery and Time Response Characteristics of Six Thermocouple Probes in Subsonic and Supersonic Flow," NACA TN 3455, 1955.
- 116. Knudson, J. G. and Katz, D. L., Fluid Dynamics and Heat Transfer, McGraw Hill Book Company, New York, New York, 1958.
- 117. Huffman, G. D., "Twelfth Quarterly Report: Compressor Research Facility Aerodynamic Analysis," Contract No. F 33615-75-C-2008, Indianapolis Center for Advanced Research Report No. FDL-77-009, September, 1977.